Development of Quantitative Techniques for the Study of Discharge Events During Plasma Electrolytic Oxidation Processes

Christopher S. Dunleavy, Trinity College
This dissertation is submitted for the degree of Doctor of Philosophy

University of Cambridge

Department of Materials Science and Metallurgy

Preface.

This dissertation is submitted for the degree of Doctor of Philosophy at the University of Cambridge. The research described herein was carried out by myself in the period from October 2006 to July 2010, under the supervision of Professor T.W. Clyne, in the Department of Materials Science and Metallurgy at the University of Cambridge.

To the best of my knowledge, the work described in this dissertation is original, except where due reference has been made to the work of others, and includes nothing which is the outcome of work done in collaboration except where specifically indicated in the text. No part of this dissertation, or any similar to it, has been, or is currently being submitted for any degree, or other qualification, at any other university. It is less then 60 000 words in length.

Christopher S. Dunleavy, July 2010.

Development of Quantitative Techniques for the Study of Discharge Events During Plasma Electrolytic Oxidation Processes

Christopher S. Dunleavy

Abstract.

Plasma electrolytic oxidation, or PEO, is a surface modification process for the production of ceramic oxide coatings upon substrates of metals such as aluminium, magnesium and titanium. Two methodologies for the quantitative study of electrical breakdown (discharge) events observed during plasma electrolytic oxidation processes were developed and are described in this work.

One method presented involves direct measurement of electrical breakdowns during production of an oxide coating within an industrial scale PEO processing arrangement. The second methodology involves the generation and measurement of electrical breakdown events through coatings pre-deposited using full scale PEO processing equipment. The power supply used in the second technique is generally of much lower power output than the system used to initially generate the sample coatings.

The application of these techniques was demonstrated with regard to PEO coating generation on aluminium substrates. Measurements of the probability distributions of discharge event characteristics are presented for the discharge initiation voltage; discharge peak current; event total duration; peak instantaneous power; charge transferred by the event and the energy dissipated by the discharge.

Discharge events are shown to increase in scale with the voltage applied during the breakdown, and correlations between discharge characteristics such as peak discharge current and event duration are also detailed. Evidence was obtained which indicated a probabilistic dependence of the voltage required to initiate discharge events. Through the scaling behaviour observed for the discharge events, correspondence between the two measurement techniques is demonstrated. The complementary nature of the datasets obtainable from different techniques for measurement of PEO discharge event electrical characteristics is discussed with regards to the effects of interactions between concurrently active discharge events during large scale PEO processing.

Acknowledgements.

I gratefully acknowledge the financial support of the Engineering and Physical Sciences Research Council. I am also grateful for the additional funding provided each year by the Department of Materials Science and Metallurgy. Thanks are due also Professor A.L. Greer for provision of office, laboratory and workshop facilities within the department. I would also like to thank Trinity College for the excellent graduate accommodation from which I benefited greatly during my studies.

I would like to thank my supervisor Prof. T.W. Clyne for all his advice and input to the project. In particular for his having created in the Gordon lab an environment which is not only welcoming but also a place in which creative thinking can thrive. Elsewhere in the department the project would not have gotten very far without the assistance of Kevin Roberts and Les Allen, who seem to never lack for a plan to bypass or resolve any experimental difficulties. The frequent assistance of Keith Page and Maddy MacElroy, and their patience with my deviant requirements for electronics with crucial to the success of the project. A good deal is owed to Keronite Plc for the loaning of PEO processing equipment and raw materials for processing. I was also thankful for the assistance of Simon Griggs with SEM facilities. Special mention must be made of James Curran, for many, many useful discussions and a surplus of mad ideas.

Within the Gordon lab many people have helped me along the way. Special thanks go to Julien, Sandra and Erica for performing the sacred rituals of coffee machine maintenance. The original three postdocs, Athina, Jin and Igor, now all moved on to better things, for help settling in and getting started. Helen and Jiu Ching for finishing before me. Andy and Sonya for hanging around the computer room and chatting almost as much as I do. Liza for returning to study PEO despite the detonation of her part III practical, and Maya who can understand the pain of running long experiments on the process lab mezzanine. James Dean is just generally a great guy to have around the lab, and naturally I could never forget The Jeff.

Outside the lab, much appreciation is directed towards all those I've known through First and Third, for all the cold mornings,maths chat and mighty victories. Long suffering friend Steph, without whom I would be less addicted to caffeine, but would know less of the brains of rats. I must thank the guys from MK, Jonny, Ruari and Dave for helping me escape from Cambridge for short periods for time to time, and Rik and Emily in London for the same. Finally Hannah for coffee, care, and moral support throughout the thesis.

Contents

Nomenclature.

Abbreviation	Meaning
PEO	Plasma Electrolytic Oxidation
DC	Direct Current
AC	Alternating Current
PBC	Pulsed Bi-polar Current
SEM	Scanning Electron Microscopy
TEM	Transmission Electron Spectroscopy
EDX	Energy Dispersive X-ray spectroscopy

Symbol	Meaning
V	Voltage
I	Current
j	Current density / subscript index
R	Resistance
G	Logical variable utilised in discharge indexing
H	Variable utilised in discharge indexing
F	Variable utilised in discharge indexing
ρ	Resistivity
σ	Conductivity
r	Radius
I_{step}	Minimum resolved current shift
V_{step}	Minimum resolved voltage shift
I_{shift}	Threshold current shift for indexing of discharge event
I_{base}	Baseline current level between discharge events
V_{init}	Voltage at initiation of discharge event
I_{peak}	Maximum current reached by discharge event
d_{sing}	Total duration of single current peak discharge event
P_{peak}	Peak instantaneous power reached by discharge event
Q_{sing}	Charge transferred by a single current peak discharge event
E_{sing}	Energy dissipated by a single current peak discharge event
V_{peak}	Voltage applied when discharge reaches peak current
R_{peak}	Resistance of the discharge at the point of peak current

Notation

In this text it was sometimes required to discuss array variables of between one and three dimensions. The convention adopted was that, A_j, for example, indicates the j^{th} element of vector A. Likewise $B_{j,m}$ represents the j^{th} entry of column m of the array B.

In the appendices, numerous variables were used which will be differentiated by superscript, for example I_j^{one} and I_m^{two} refer to the j^{th} element of the vector I^{one} and m^{th} element of the vector I^{two}. The number of variables required to describe the data post-processing is large, and it would not be appropriate to describe all such variables here. Descriptions of each variable used can be found in the accompanying text throughout the appendices.

Chapter 1

Introduction.

The process which is the topic of this work is a surface modification technique known as plasma electrolytic oxidation (PEO), micro–arc oxidation (MAO), spark anodising or anodic spark anodising. In this work I shall use the terminology plasma electrolytic oxidation for the reason that this has become the dominant term in the literature over the previous decade.

The PEO process is used to generate or deposit coatings, often largely composed of ceramic oxides, onto the surfaces of light metals such as aluminium, magnesium and titanium. During processing the substrate is submerged in an aqueous electrolyte and connected to the output of a high voltage power supply. The balance between deposition of material from the electrolyte, and generation of coating material by oxidation of the substrate material, depends upon several factors. Some examples include the nature of the substrate; the chemical composition of the electrolyte used and the specific electrical parameters of processing. The nature of the power supply used can be simple direct current (DC); alternating current (AC) or pulsed direct current in the form of pulsed bi–polar current (PBC).

In this work the objective has been to develop and apply techniques which would allow a greater understanding of the process mechanisms, with a focus upon the plasma discharges which are the most prominent feature of the PEO process. Before reviewing the existing literature data relating to the plasma discharges, a brief overview of the main features of PEO processing and coatings is provided for the reader not familiar with the topic.

1.1 PEO processing.

Plasma Electrolytic Oxidation (PEO) processing involves the submersion of the metallic substrate in an aqueous electrolyte. Aluminium, titanium and magnesium have attracted the most interest, but do not represent an exhaustive list of the

materials which can be processed in this fashion. The process cell is completed by a counter-electrode, often made of stainless steel, and usually of greater surface area than the substrate. A high voltage power supply is used to apply a voltage between the substrate and counter-electrode. The nature of the voltage waveform depends upon the type of power source used, DC, AC or PBC.

The application of voltage across the process cell causes current to flow, and the native oxide of the substrate thickens by a process similar to conventional anodising. The voltage rises rapidly as the oxide layer thickens, and once the applied potential difference has reached several hundred volts, electrical breakdowns of the growing oxide begin to manifest as bright visible sparks on the substrate surface. Shortly after this the rate of voltage increase slows dramatically, and the process enters a more steady state situation of slowly increasing applied voltage. An example of the behaviour of bulk electrical parameters from PEO processing of aluminium alloy is reproduced in Figure 1.1 [**1**].

Processing after the point of the voltage slope transition is dominated by the visible sparks which cover the substrate surface. A good example of the appearance of the sparks during processing, and the variation seen with processing time, was published by Yerokhin et al in one of the early works to apply video imaging to the analysis of the PEO process [**2**].

A figure from that work is reproduced in Figure 1.2 for illustrative purposes. This reproduced figure shows the main features observed in the substrate appearance during PEO processing. Figure 1.2 panel (a) shows the sample 30 s into processing. Intense gas evolution is seen on the substrate surface but not discharges as yet. Panel (b) shows the situation 10 minutes into processing, the substrate surface is covered by a large number of small bluish white discharges. These appear short lived and evenly spread across the sample surface. As the process continues, the discharges appear to become brighter and larger. They also appear to be less numerous, and to persist for longer in some locations. This behaviour is seen in panel (c) of Figure 1.2, from 35 minutes into processing. Further continuation of processing leads to the discharges appearing to be less frequent and larger still. The evolution of large quantities of gas on the substrate surface is evident at all times during PEO processing. The discharges are also observed to change colour as coating proceeds, taking on a more yellowish appearance, as displayed in panel (d) from 65 minutes into processing.

These visually apparent discharges on the substrate surface are believed to be an essential part of the coating formation process. The development and application of techniques to allow for detailed quantitative study of these discharges was the principle aim of the present work. The existing literature data on these discharges

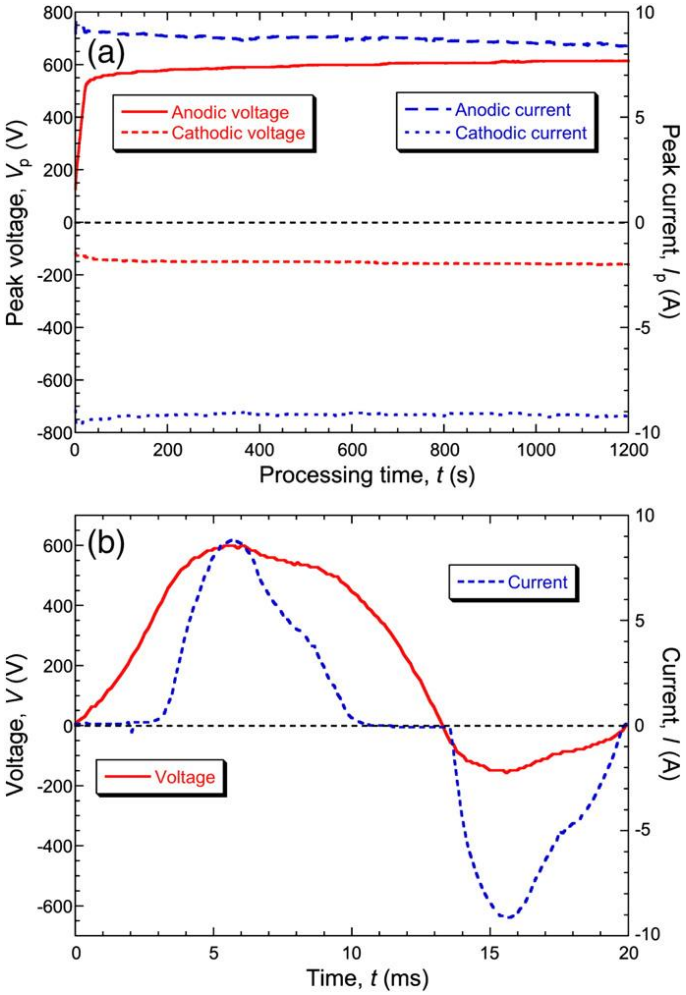

Figure 1.1: *(a) Typical variation of the peak anodic and cathodic voltage and current during the first 20 min of PEO processing and (b) voltage and current waveforms during a single cycle, after 10 min of processing. Figure and caption reproduced from Dunleavy et al* [**1**]

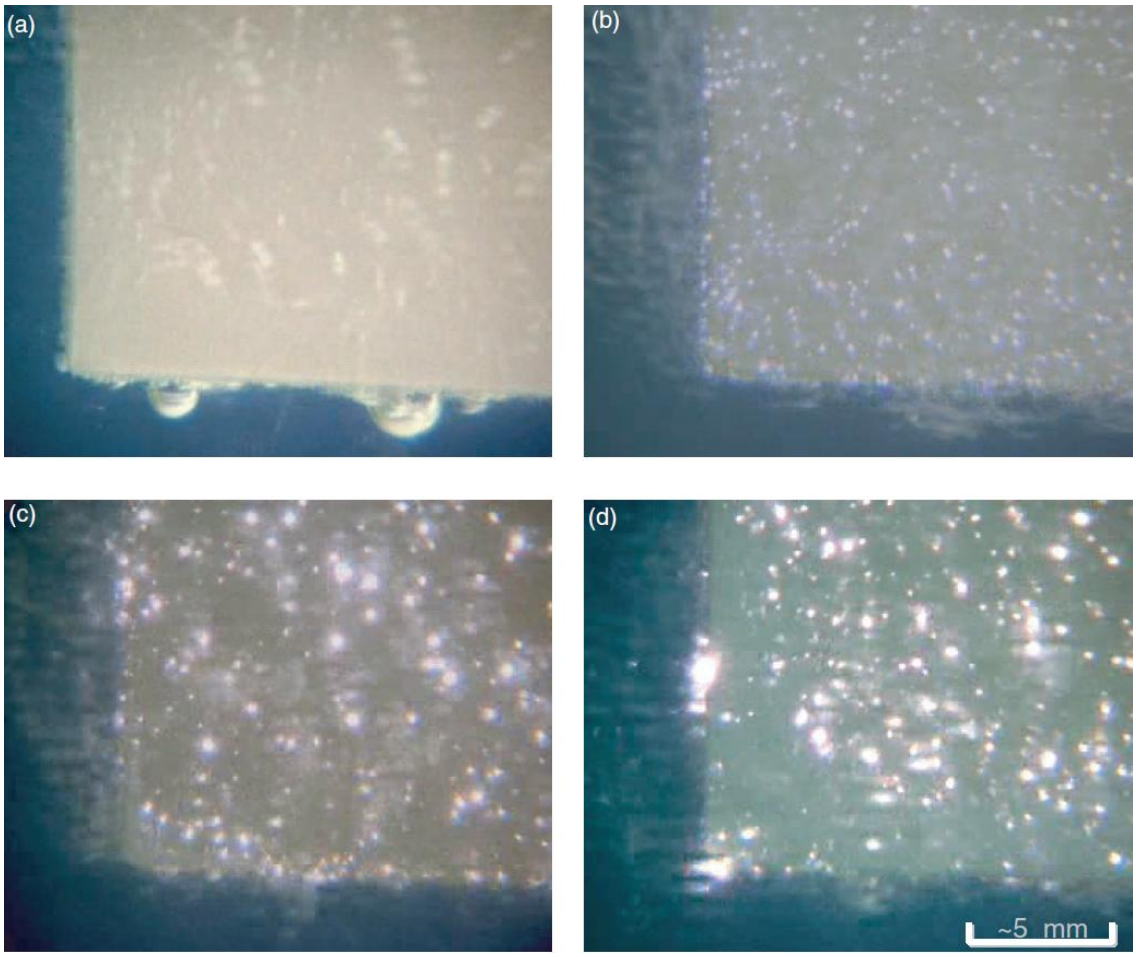

Figure 1.2: *Sample surface appearance at various stages of the coating formation process: (a) 0.5 min; (b) 10 min; (c) 35 min and (d) 65 min. Figure and caption reproduced from Yerokhin et al* [**2**].

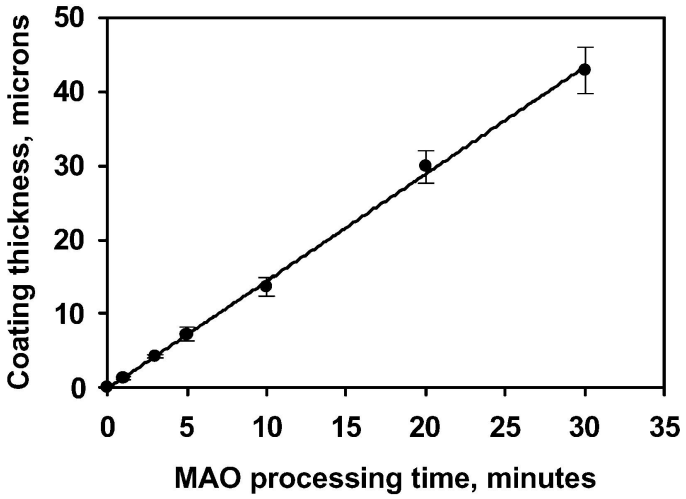

Figure 1.3: *Influence of MAO treatment time on coating kinetics. Caption and figure reproduced from Sundararajan and Rama Krishna* [**3**]. *MAO stands for Micro-Arc Oxidation, an alternative name to PEO for this process.*

will be summarised in chapter 2.

1.2 PEO coatings.

In general PEO coatings can be produced to thicknesses of up to several hundred μm. The rate of coating thickening is often found to be approximately linear for processing to less than 60 minutes, as seen in a typical example of coating growth kinetics originally published by Sundararajan and Rama Krishna [**3**], and reproduced in Figure 1.3. The precise rate of coating growth is found experimentally to vary with such factors as the substrate material; the electrolyte composition; the current density and the frequency of the process waveform applied. It is interesting that such thickening rates can be sustained for prolonged periods, especially given the low rate of voltage variation typically observed throughout most of processing (e.g. Figure 1.1, panel (a)).

The coating exterior surfaces tend to present a characteristic appearance, an example of which is displayed in Figure 1.4. The coating surface contains many pores of varying scales. Some of the larger pores are surrounded by comparatively smooth, nearly circular regions, of what looks to be re-solidified coating material. These pores are often referred to as 'craters' or 'discharge channels' in the literature, and are believed to be associated with the plasma breakdown events. Radial cracks are often seen in these smooth regions, radiating outwards from the central pore. These cracks are thought to be related to rapid cooling of molten coating material. The regions of rougher looking material interspersed with the smooth regions are

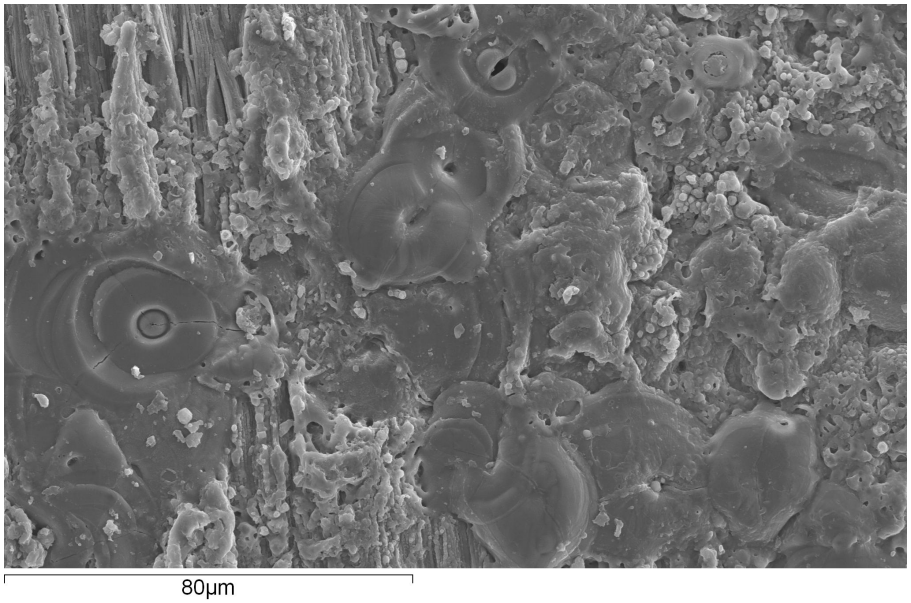

Figure 1.4: *Typical surface morphology observed for a PEO coating on aluminium. The coating displayed is approximately* 20 μm *in thickness.*

also fairly typical. The characteristic surface appearance of PEO coatings implies locally high temperatures; high cooling rates and growth of new coating material at discrete locations. This is one of the reasons why it is conventionally assumed that the visually observed sparks play a significant part in the coating growth mechanism.

1.3 PEO coating applications.

The intention of any surface modification process is that it should provide some functional enhancement of the substrate surface properties. In general for PEO of aluminium and magnesium substrates, the intent is to generate hard coatings which will improve the wear properties of the substrate. The PEO processing of titanium is often undertaken with the intent of generating titania layers, thought to improve the bio-compatibility of substrates, for use in prosthetic bone replacement implants. The functional properties of PEO coatings are not the subject of this work, and will not be discussed in detail.

The principle attraction of PEO coatings over conventional anodising processes are that coatings generally contain greater fractions of crystalline Al_2O_3 and MgO, which can impart high hardness to the coatings. Aluminium PEO coatings produced by Curran and Clyne were measured by nano-indentation to have hardnesses around 20 GPa [**4**]. Hardness values for coatings produced on magnesium by Arrabal et al were found to be in the range from 2.0 to 4.4 GPa [**5**]. Such values enable

replacement of steels by lighter metals in high performance applications where the bare aluminium or magnesium would not be tribologically suitable. The relatively high levels of fine interconnected porosity found in PEO coatings, typically 20% according to investigations by Curran and Clyne [**6**], afford the coatings good lubricant retention in sliding friction applications.

1.4 Research aims.

The central theme of this work is the study of the plasma discharge events, or sparks, observed on the substrate surface during PEO processing. In my work I have only studied coatings produced on aluminium, using only one chemical formula of aqueous electrolyte. Almost all the coatings studied were produced (or in the process of being produced) using a 50 Hz AC power supply. The specific data presented is then necessarily limited in scope, nonetheless certain underlying trends representative of general physical scaling of PEO discharge events were obtained. The purpose of this work was to develop and then validate quantitative techniques which can be applied to the study of discharges during PEO processes in general. In this respect the work was successful, and whilst the techniques presented in later chapters have definite limits, with minor adjustments to experimental parameters there are no inherent barriers to wider application.

1.5 Document overview.

Chapter 2 presents a brief review of background literature on PEO coatings, and of the quantitative data available in the literature on the properties of PEO plasma discharge events.

Chapter 3 describes the experimental equipment and procedures utilised in this work. Two experimental methodologies will be introduced. The first, referred to as 'in-situ monitoring' experiments, relates to measurement of discharge event electrical properties during coating deposition. The second, referred to as 'single discharge' testing, uses a low power DC supply to generate discharge events through pre-deposited PEO coatings at a low enough rate that the properties of individual events may be measured. The computer processing of the data obtained is briefly discussed, but for full details the reader will have to turn to **Appendix A** and **Appendix B**.

Chapter 4 presents results of the 'in-situ monitoring' experiments. The accuracy and reliability of the technique will be discussed, and distributions of individual discharge event properties as a function of processing time will be presented. The

discharge event initiation voltages; peak discharge currents; event durations; peak power levels; charge transferred by individual events and the energy dissipated by events will be detailed.

Chapter 5 introduces measurements from 'single discharge' testing of pre-deposited coatings. This data is complementary to that obtained from monitoring of bulk PEO processing. Unexpected behaviour of the observed breakdown voltages of PEO coatings will lead to a discussion of the probabilistic nature of discharge event initiation for PEO coatings.

Chapter 6 brings together the results obtained from **chapter 4** and **chapter 5** to examine scaling effects observed for the discharge events. Comparisons between the two datasets will be presented and discussed. The physical scaling of the discharge events will be discussed, and shown to apply to both 'in-situ' and 'single discharge' datasets. The importance of applied voltage to the plasma discharge development will be demonstrated. It will also be shown that the current profiles of discharge events exhibit remarkable self-similar scaling between events which develop to different values of the peak discharge current.

Chapter 7 contains a brief review of the major implications and results from this work.

Chapter 2

The Plasma Electrolytic Oxidation Process.

In this chapter the literature information relating to discharge events during plasma electrolytic processing will be reviewed. Most of the information relates to aluminium and alumina coatings, which are the focus of this work. Some studies of titanium and magnesium PEO processing have reported results relevant to the consideration of discharge event properties, and have also been included in the discussion.

2.1 Reported properties of discharge events during plasma electrolytic oxidation.

2.1.1 Experimental approaches.

The literature information relating to discharge events observed during PEO processing is substantially incomplete. Researchers have applied four main experimental approaches to the investigation of the properties and distributions of discharge events on the substrate surface during processing. These approaches will be briefly discussed, and the results obtained will be discussed in the subsections which follow.

Optical imaging.

Optical imaging of a substrate under processing conditions yields information about the spatial distribution of discharge events, and how this distribution changes with the duration of processing. With appropriate high speed imaging equipment (< 100 μs exposure time) information about the discharge durations can be obtained [**5**].

If the spatial resolution is sufficient, the results of optical monitoring can also provide valuable information about the physical scale of plasmas associated with discharge events. Studies performed using longer exposure times than 100 μs cannot provide reliable data on event durations [**2, 7, 8, 9**], however these works should not be discounted from serious consideration. Imaging on timebases of ms provides information about the persistence of discharge events at, or close to, a particular point. The distribution of discharging behaviour across the substrate surface can also be obtained from optical imaging at low frame rates. Understanding such localisation of discharge events is at least as important as understanding the individual events, if a complete understanding of PEO coating growth and microstructural development is to be obtained.

In recent work published by Arrabal et al [**5**], optical imaging was synchronised to recording of the bulk current and voltage process waveforms. This allowed the authors to correlate the discharging activity with the bulk current response, and also to identify the voltage required to initiate discharging behaviour on the substrate. Such experiments can allow the discharge events to be better understood within the context of the wider processing.

Electrical monitoring.

Electrical measurements of discharges allow for certain properties of discharge events to be directly obtained. Properties such as the duration; the discharge current; the instantaneous power; the total charge transferred and the energy dissipated by a discharge can be measured. Unlike optical imaging approaches, the measurement of discharge event properties electrically will usually exert some degree of influence upon the system being investigated.

Therefore with electrical monitoring of discharge events, careful consideration of the relationship of results obtained to more regular PEO processing is essential. Some studies have been performed on the terminal stages of conventional anodising at low current densities [**10, 11, 12**], and an article by Bao Van et al measured discharges on a pin-head sized area exposed to the electrolyte [**13**].

References to studies not available in the English language literature are encountered in some publications investigating PEO. Many of these Russian language journals are not translated for English publication, however interesting values have been quoted by other researchers. Where appropriate in the discussion which follows I have included such values with explicit referencing of both the work which cites the reference, and the source of the original material which is being cited.

Optical spectroscopy.

Another source of information about conditions in the plasmas associated with breakdown events is spectral analysis of light emitted by the discharges. The spectral region of interest is the visible to near-UV. Information about the constituents of the plasma can be obtained through identification of emission lines of ionic, atomic and molecular components in the plasma.

Information about the electron temperature and number density in the plasma can be obtained from analysis of the continuum background emission from free-free electron transitions [**1, 14**]. In studies with finer wavelength resolutions, such information can also be obtained from broadening of spectral lines and examination of the relative intensities of transitions between bound states of atomic or ionic species [**1, 14, 15**]. Logging of the relative intensities of emission lines as a function of processing time has been performed [**15, 16, 17**], and provides information about changes in the typical discharge plasmas as the coating thickens.

Microstructural characterisation.

The last general approach, and that most often applied to PEO processing, is the characterisation of the coating microstructure by microscopy, x-ray diffraction and other related techniques. Whilst no direct dynamical information about the discharging phenomena may be obtained via such techniques, analysis of PEO coatings produced in a wide variety of experimental conditions, and to varying thicknesses, can allow important inferences to be made about the conditions during formation of the coating material.

2.1.2 Durations of discharge events.

An early work by Bao Van et al used an oscilloscope to capture the current signals from several discharges generated on the exposed point of a nickel plated steel needle [**13**]. They reported some properties of two events visible in the oscilloscope trace reproduced in Figure 2.1. The events had durations of ~ 200 μs and were separated by a period of ~ 350 μs.

A record of a similar event, but much shorter at ~ 1 μs duration, was presented in more recent work by Kasalica et al [**10**]. This work related to the end stages of more conventional anodising of an aluminium substrate, and as such the discharge event captured is probably a good representation of the initial discharges during PEO processing.

Application of high speed video imaging in the range of 5400 to 20 000 frames per second was reported by Arrabal et al for PEO processing of pure magnesium and

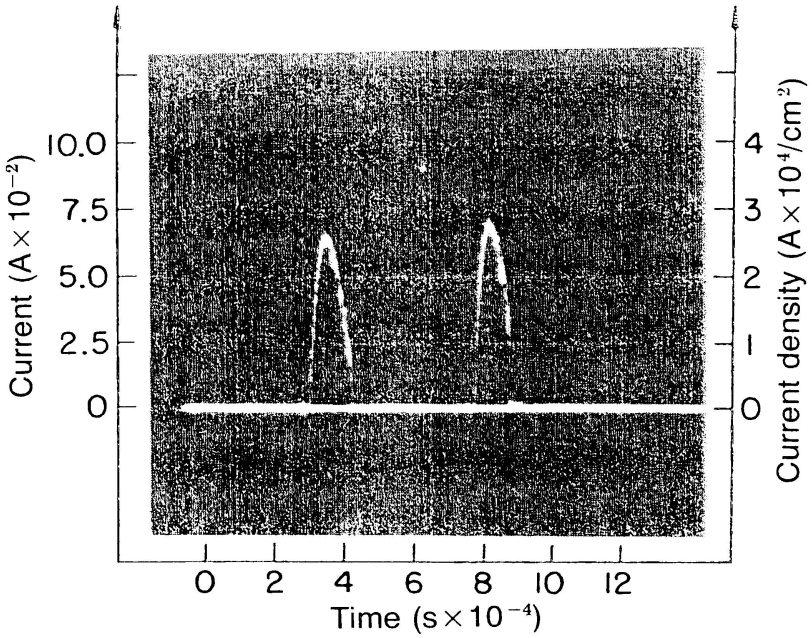

Figure 2.1: *Traces of single spark reaction on tip of stainless steel needle. Figure and caption reproduced from Bao Van et al* [**13**]

a range of magnesium alloys [**5**]. In this optical study lifetimes of the shortest lived discharges were found to be in the range $\leq 50 - 185$ μs, and the average lifetime was estimated as $500 - 1100$ μs.

Discharge lifetimes in the range of $\sim 10 - 100$ μs were reported in work by Dunleavy et al [**1**], which applied two different methodologies. The first was low power DC processing of pre-deposited PEO coatings on aluminium. The second involved monitoring the current through a small aluminium area (500 μm diameter) which was processed in parallel with a larger area under more standard coating growth conditions.

Several sources quote discharge duration values from papers published in Russian. Typical durations in the range $100 - 500$ μs are quoted by Terleeva et al [**18**], with reference to a book published by Bakovets et al [**19**]. It is not clear whether this value was derived from electrical monitoring or high speed image capture. It is also not stated which substrate these values refer to, though aluminium is perhaps the most likely given the longer history of PEO on aluminium.

A similar range of $10 - 100$ μs was quoted by Long et al [**20**] and attributed to Snezhko and Chernenko [**21**]. Values of typical current from the study by Snezhko and Chernenko are also quoted, which implies that this range was determined by electrical monitoring. Information on the substrate metal was not provided.

A shorter range of $10 - 20$ μs was stated by Gnedenkov et al [**22**], with reference to a book by Gordienko and Gnedenkov relating to processing of titanium [**23**]. The Gordienko and Gnedenkov value is most likely to be derived from electrical monitoring as Gnedenkov et al also quote values for typical event currents and power levels.

A study which applied video imaging to study discharge lifetimes by Golovanova and Sizikov [**24**] was cited by Yerokhin et al [**2**] as having ascertained the discharge lifetime to be ≤ 7.5 ms, the upper bound is presumably determined by the temporal resolution obtainable from the imaging system used.

Imaging of titanium PEO processing by Matykina et al [**8**] used a camera system with 10 ms exposure time and a 40 ms shutter interval. Probability distributions of apparent discharge lifetimes were presented for three values of the applied voltage, each corresponding to a later time during processing. The discharge apparent lifetimes were reported as $\sim 35 - 100$ ms at 300 V, $\sim 35 - 260$ ms at 370 V and $\sim 100 - 800$ ms when the applied voltage had reached 430 V.

Given the temporal resolution in this study, and considering the other values quoted in the literature for discharge lifetimes, it is unlikely that the discharge lifetimes quoted by Matykina et al [**8**] represent single discharge events. More likely the slow sampling rate and long exposure time for each image allows a prolonged series of much shorter discharge events, occurring at the same point on the surface, to appear in the images as a single long-lived event. Whilst such slow (relative to the discharge lifetime) video imaging cannot yield usable data on the discharge durations, the results suggest increasing persistence and localisation of discharge events as coating progresses.

An estimate of the discharge lifetime is made by Yerokhin et al [**2**] in an optical imaging study of aluminium PEO processing, though not from the individual frames themselves. The video was taken at only 24 Hz, when the processing was AC with frequency 50 Hz. The authors instead identified the apparent area under discharge from the video stills. They then estimated the current density through each discharge and used that to estimate the time required to raise the local volume of coating to a temperature great enough to cause alumina to melt. They reported values in the range $0.25 - 3.5$ ms.

The literature data on discharge event durations is summarised in Table 2.1. With the exception of studies which used inappropriate measurement time-scales, the consensus appears to be discharge event lifetimes of the order tens to hundreds of μs.

Substrate	Technique	Duration / μs	Source
nickel plated steel	electrical	~ 200	[**13**]
aluminium	electrical	~ 1	[**10**]
magnesium	optical	$50 - 1100$	[**5**]
aluminium	electrical	$10 - 100$	[**1**]
		$100 - 500$	[**19**]
	electrical	$10 - 100$	[**21**]
titanium	electrical	$10 - 20$	[**23**]
		≤ 7500	[**24**]
titanium	optical	$35\,000 - 800\,000$	[**8**]
aluminium	theoretical	$250 - 3500$	[**2**]

Table 2.1: *Summary of the discharge duration data from literature sources.*

2.1.3 Discharge event currents.

The discharges visible in Figure 2.1 from Bao Van et al [**13**] reach peak currents of 52 mA and 70 mA. The corresponding peak power reached by the 70 mA discharge is quoted to be 35 W, given the applied voltage of 500 V. The calculated energy transferred by this event was quoted as 2.9 mJ. By assuming that the area of the discharge was identical to that of the exposed nickel plated needle, 17.8 μm in diameter, they estimated discharge current densities for the two events of 2.1×10^8 A.m^{-2} and 2.83×10^8 A.m^{-2}.

The discharge event plotted in an article by Kasalica et al [**10**] is reproduced in Figure 2.2. The peak current reached by the discharge event is ~ 1 mA. The average energy quoted for the discharge events was ~ 0.2 μJ. Based on analysis of the observed pores in the coating exterior surface, the authors estimate a discharge current density of $\sim 10^9$ A.m^{-2}.

The current density of discharge events reported by Yerokhin et al [**2**] varied with duration of processing. Starting from $\sim 5 \times 10^4$ A.m^{-2} one minute into processing, the current density, calculated from analysis of video stills at 24 Hz, was seen to drop to $\sim 2 \times 10^4$ A.m^{-2} after 80 minutes of processing.

The individual discharge current quoted by Terleeva et al [**18**] is 100 mA, cited from Bugaenko et al [**25**] and Polyakov and Bakovets [**19**]. Also cited by Terleeva et al are values of the current density in discharge events. Values of 3×10^8 A.m^{-2} and 1×10^7 A.m^{-2} were referenced to Snezhko [**26**]. A separate value of 2×10^8 A.m^{-2} was attributed to Markov and Mironova [**27**]. Discharge current densities reported by Terleeva et al [**18**] for three experimental systems are in order of magnitude agreement at $0.2 - 2 \times 10^8$ A.m^{-2}. These were estimated from the total sample

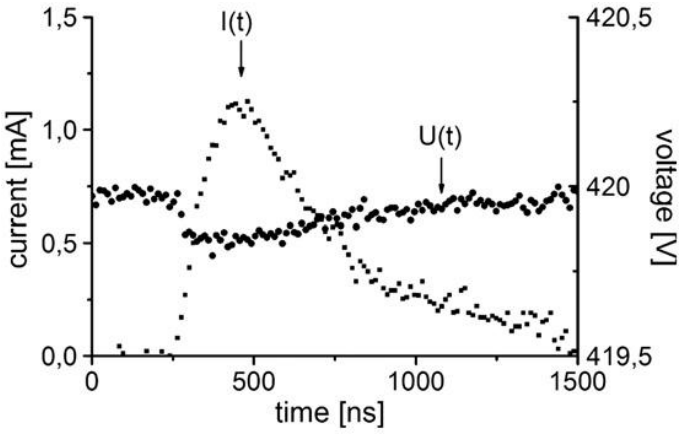

Figure 2.2: *Current and voltage variation during one breakdown event. Caption and figure reproduced from Kasalica et al* [**10**]

current rather then directly measured.

Discharge currents in the range $1 - 10$ mA for PEO of titanium were quoted by Gnedenkov et al [**22**], with reference to Gordienko and Gnedenkov [**23**]. Other values quoted from Gordienko and Gnedenkov were instantaneous discharge powers in the range $0.2 - 1.0$ W.

Further values for discharge current are found in work by Dunleavy et al [**1**]. The values for the peak currents reached by individual events were seen to span the range of currents from ~ 8 mA to ~ 40 mA, as illustrated in Figure 2.3. A summary of the available literature data may be found in Table 2.2. The literature data indicate discharge currents of the order tens to a few hundred mA, and current densities for the discharge of the order 10^8 A.m^{-2}.

2.1.4 Spatial scale of discharge events.

Literature data on the size of the plasmas resulting from breakdown events are in the range from tens to several hundred μm. Probability distributions of the apparent diameter of discharge events during PEO of titanium were presented in an imaging study by Matykina et al [**8**], and these are reproduced in Figure 2.4. The reported scale of discharge diameters spans the range from ~ 80 μm up to > 370 μm.

As was discussed in subsection 2.1.2, the temporal resolution of this study was not ideal. However even if several events occurred during the 10 ms exposure time, the apparent size of the event would still represent the diameter of the largest plasma which occurred, provided that the repeated events initiated at or close to the same location on the sample. The minimum spatial resolution claimed in this study was 40 μm.

Such values for the discharge diameter are in broad agreement with the earlier

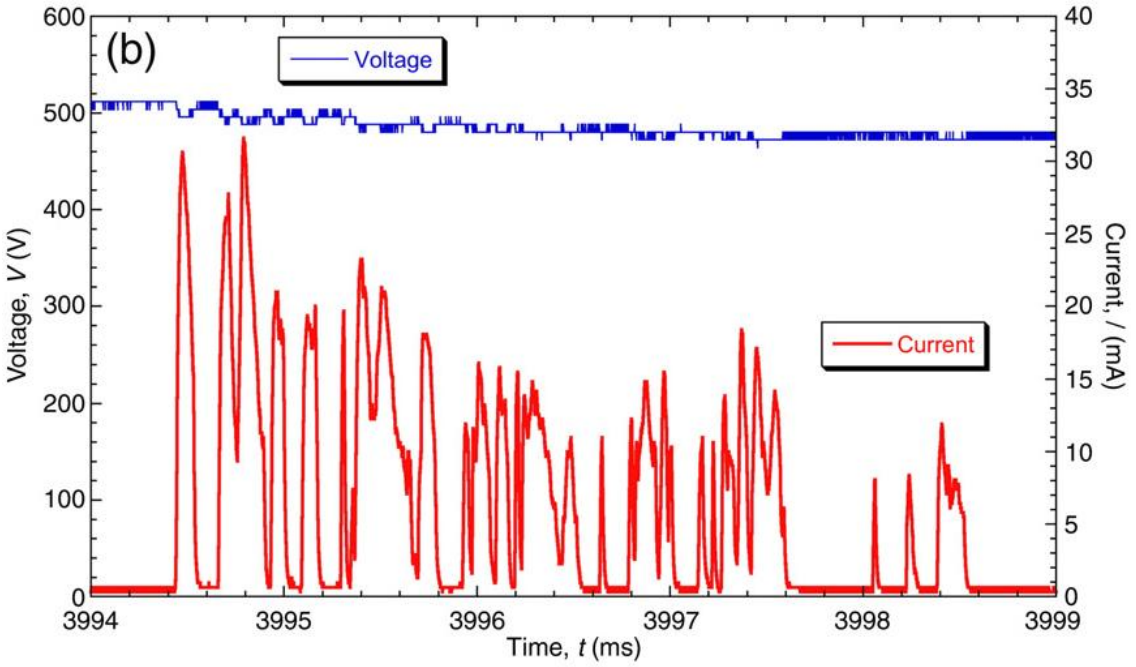

Figure 2.3: *A sequence of discharge events recorded during low power DC processing. Reproduced from Dunleavy et al* [**1**].

Substrate	Discharge current / mA	Discharge current density / A.m^{-2}	Source
nickel plated steel	70, 52	2.1×10^8, 2.83×10^8	[**13**]
aluminium	~ 1	$\sim 1 \times 10^9$	[**10**]
aluminium		2×10^4–5×10^4	[**2**]
	100		[**19**]
	100		[**25**]
		3×10^8, 1×10^7	[**26**]
		2×10^8	[**27**]
		0.2–2×10^8	[**18**]
titanium	1–10		[**23**]
aluminium	8–40		[**1**]

Table 2.2: *Summary of the discharge current data from literature sources.*

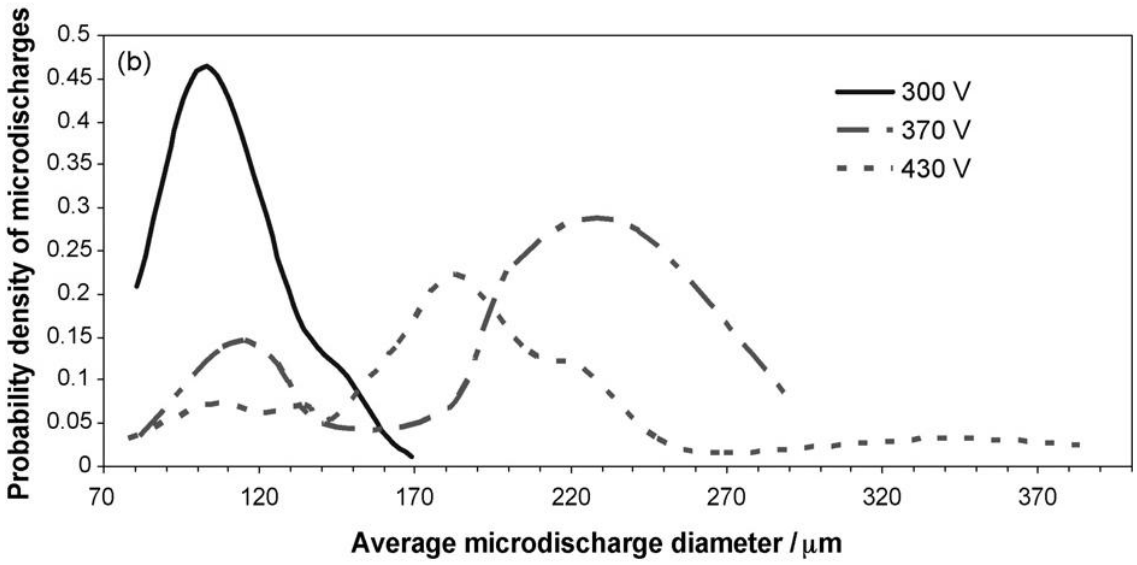

Figure 2.4: *Microdischarge characteristics during PEO treatment of titanium at* 20 $mA.cm^{-2}$ *in 0.026 M* Na_3PO_4*: (b) microdischarge diameter. Caption and figure reproduced from Matykina et al* [**8**].

video imaging studies by Yerokhin et al [**2, 7**]. In these works the most common events at all times of processing were found to have a mean diameter of ~ 160 μm. These were termed 'small' by the authors. It should be noted that the authors reported the apparent cross sectional areas of events, I have assumed circular symmetry to estimate diameters. Also studied were 'medium', 'large' and 'very large' breakdown events, with average apparent diameters of ~ 340 μm, ~ 540 μm and ~ 1000 μm respectively.

Results of both studies by Yerokhin et al are summarised in Table 2.3. The much larger apparent sizes of some events recorded in these two studies, compared to the Matykina et al study, could be due to a number of factors. The camera capture rate of 24 Hz is slower than the 10 ms exposure time in the work by Matykina et al. Secondly the processing was continued for a longer period of time, and the largest events only became significant after 35 minutes of coating deposition. In addition the substrate metal studied by Yerokhin and co-workers was aluminium, not titanium, which is potentially significant. The most prevalent events, with average apparent diameters of 160 μm and 340 μm, are in good agreement with the results obtained by Matykina et al.

Time / min	'small'	'medium'	'large'	'very large'
1	0.96	0.04	0	0
15	0.8	0.18	0.01	0.01
25	0.73	0.23	0.02	0.02
35	0.67	0.27	0.02	0.04
65	0.77	0.11	0.08	0.04

Table 2.3: *Fractional distributions of discharge populations from Yerokhin et al* [**2, 7**].

2.1.5 Discharge event spatial density.

The number of discharge events active at any given time can be estimated from optical imaging studies of PEO processing. Comparison between studies is possible if the quoted density of discharges per unit area is divided by the camera exposure time used, yielding a rate of discharging per unit area.

Matykina et al [**8**] report discharge densities of $\sim 5 \times 10^6$ m^{-2}.s^{-1} after about 160 s, rising to to $\sim 2 \times 10^7$ m^{-2}.s^{-1} after 900 s of processing. The maximum population density seen was $\sim 3 \times 10^7$ m^{-2}.s^{-1} around 760 s into processing. These results were for a frame exposure time of 10 ms and DC processing of titanium.

Yerokhin et al [**2, 7**] report comparable values, though showing a different trend. They found discharge densities of $\sim 6 \times 10^7$ m^{-2}.s^{-1} around 10 minutes into processing, falling gradually to $\sim 2.6 \times 10^7$ m^{-2}.s^{-1} after 60 minutes. This work related to processing of aluminium and used a frame rate of 24 Hz, corresponding to a frame time of 41.7 ms.

An indication of the effect of current density on the breakdown event frequency is provided by the study of Moon and Jeong [**9**]. Current densities of 5 and 10 A.dm^{-2} were applied in PEO processing of aluminium. The exposure time used was 30 ms. For processing with 5 A.dm^{-2} the discharge density was found to be $\sim 1.7 \times 10^7$ m^{-2}.s^{-1} after about 30 s, falling off to $\sim 3.3 \times 10^6$ m^{-2}.s^{-1} after 300 s.

Greater initial discharge densities were seen for processing using a current density of 10 A.dm^{-2}, with $\sim 5 \times 10^7$ m^{-2}.s^{-1} after 60 s, falling to $\sim 3.3 \times 10^6$ m^{-2}.s^{-1} after 300 s. Such values are consistent with Matykina et al [**8**] and Yerokhin et al [**2, 7**].

The high speed optical studies by Arrabal et al [**5**] utilised a frame rate of 5400 frames per second to study the processing of pure magnesium and several alloys. The exposure time of 185 μs makes this one of the most reliable information sources, however the discharge densities reported are significantly greater than the other optical studies. Instantaneous discharge rates spanning the range 10^8 m^{-2}.s^{-1}

to 10^9 $m^{-2}.s^{-1}$ are reported.

The discrepancy could be due to the exposure time being shorter in the work of Arrabal et al [**5**]. If many discharge events occur close to a single location in rapid succession, then with an exposure time of many ms these will appear as a single event, reducing the apparent discharging rate. The difference of $\sim 10^2$ in apparent rate between the results of Arrabal et al and the other optical studies is probably related to the similar $\sim 10^2$ difference in frame rate, and the fact that the exposure time of 185 μs is similar to both the discharge event lifetime and the separation between discharge events (see subsection 2.1.2). The value obtained by Arrabal et al is likely the most accurate reflection of discharge event rate. Comparison to the slower optical studies is suggestive that clustering of events around specific active locations is likely.

2.1.6 Discharge plasma composition.

Based on indexing of emission lines, the plasma composition is found to be dominated by atomic and singly ionised species [**1, 5, 10, 14, 15, 17**]. Molecular OH has also been reported by some studies [**1, 5, 15, 17**]. Doubly ionised Al has been reported by Klapkiv et al [**14**]. In addition to O, H and the substrate material, signatures of alloying elements in the substrate, and elements incorporated from the electrolyte are also observed. These results support a view that the discharge events provide a mass transport pathway through the coatings as they grow, because optical emissions are observed from elements only present in the substrate.

2.1.7 Discharge plasma temperature.

Several studies have applied optical spectroscopy to estimate the plasma electron temperature. Klapkiv et al used the relative intensity of atomic and ionic emission lines to estimate temperatures in the range 3500 to 12 000 K [**14**]. The wide spread was attributed by the authors to the existence of a hot core and cooler periphery region in the discharge plasma.

Such results are supported by several independent measures in an article by Dunleavy, Golosnoy et al [**1**]. Temperatures of ~ 3500 K were derived from the intensity ratio of the Balmer H_α (656.3 nm) and H_β (486.1 nm) emission lines; analysis of intensity of the recombination continuum and from the relative intensities of the OH molecular rotation lines. Temperatures of $\sim 16\,000 \pm 3500\ K$ were estimated from emission lines of singly ionised magnesium (which originated from the substrate alloy), and confirmed by examination of singly ionised silicon ions.

Further confirmation of these temperature ranges was provided in a more ex-

tended spectroscopic study by Hussein et al [**15**]. This work monitored specific spectral lines over 60 minutes of PEO processing. Temperatures ranging from 4500 to 10 000 K were reported based on intensity ratios of emission lines from atomic aluminium species.

Electron temperatures in the range from 3000 to 16 000 K are reported for the plasmas associated with PEO discharges. Whether the high and low temperatures calculated from different portions of the spectrum correspond to a hot core and cooler periphery of each event; to a hot initial stage which expands and cools, or to entirely seperate events, is not possible to say at present.

2.2 Bulk electrical properties of PEO processing.

Bulk current and voltage waveforms for PEO processing, and properties such as the peak current and voltage during each process cycle, are important parameters from a quality control perspective. An example of both the process waveforms at one time, and the behaviour of maximum and minimum current and voltage with time of processing is reproduced in Figure 2.5 from work relating to aluminium by Yerokhin et al [**2**]. An additional example was given in the introductory chapter in Figure 1.1.

In the article from which Figure 2.5 is reproduced, the coating thickness is reported to increase between 20 and 80 minutes from 18.9 ± 3.4 to 80.4 ± 5.0 μm, an increase of a factor of approximately 4 times. The voltage did not undergo an increase in proportion with the thickness. One interpretation of this is that the applied voltage is primarily developed over a relatively thin internal region of the coating. This idea will be discussed further in relation to coating porosity (subsection 2.3.4) and internal structure (subsection 2.3.3).

The behaviour of bulk current and voltage shown in Figure 2.5 and Figure 1.1 is typical for PEO processing, showing a rapid initial rise of the voltage, which after a short time slows to a reduced rate of increase for the rest of processing. There are examples in the literature of different behaviours of current and voltage characteristics, for instance Arrabal et al report a substantial (100–150 V) decrease in magnitude of the applied voltage for processing of magnesium alloys beyond 400 s [**5**].

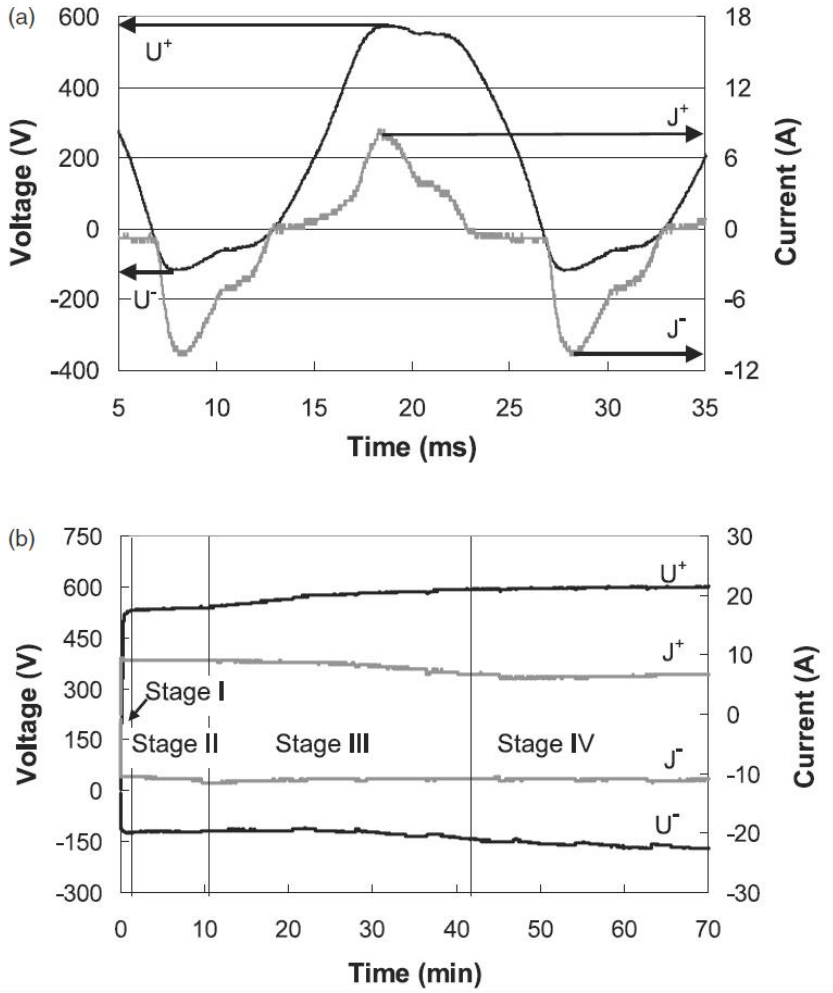

Figure 2.5: *Typical diagrams representing (a) the shape of amplitude modulated current and voltage signals in AC PEO and (b) amplitude dependences of current and voltage pulses on the time of PEO treatment. Figure and caption reproduced from Yerokhin et al* [**2**].

2.3 Structural features of PEO coatings.

2.3.1 Growth rates and thicknesses of PEO coatings.

An attractive feature of the PEO process is that reasonably high, and often linear, growth rates can be sustained until thicknesses up to several hundred μm are reached. Growth rates and processing conditions for articles which reported linear growth of PEO coatings are summarised in Table 2.4. Though conditions vary widely, in general the growth rates range from several hundred nm to a few μm per minute of PEO processing.

The data in Table 2.4 comes from processing using DC or low frequency (50–100 Hz) current sources. The maintenance of such growth rates when the existing coating is tens of μm thick has informed the generally held view that the discharge events provide pathways for mass transport through the growing oxide coatings. More direct evidence of this from the literature is discussed in subsection 2.3.6.

Not all studies have reported constant growth rates for PEO coatings, though in many cases the thickening rate is linear for some initial period of the processing [**17, 20, 32, 33**]. In these studies the growth rates were of the same order of magnitude as those reported in Table 2.4, but changed noticeably at some point during processing. As yet no consistent trends emerge from the studies which report non-linear coating growth, and the underlying causes of such variations are not known.

The important information from literature growth rates is that deposition of PEO coatings can proceed at rates from several hundred to a few thousand nm per minute, until coatings are over 100 μm in total thickness. At the same time the voltage applied does not increase in proportion to the coating thickness (section 2.2). The implications of this will be discussed further in subsection 2.3.3 and subsection 2.3.4.

2.3.2 Exterior surfaces of PEO coatings.

SEM imaging of coating free surfaces is amongst the most common characterisation techniques applied, and the majority of articles written about PEO include one or more SEM images of the coating exterior. This has been a productive source of indirect information about conditions during processing, with inferences being made from observation of surface features. For example there are always pores, or craters, on the surface, and these are usually associated with the discharge events.

Electrolyte /g.l^{-1}	Substrate	j /A.m^{-2}	time /min	rate /μm.min^{-1}	source
alkali silicate	Al 7075	3000	30	1.45	[**3**]
1–2 KOH & 3–5 Na_2SiO_3 & 3–5 $Na_4P_2O_7$	Al 6082	1000	100	1.00	[**4**]
2.8 KOH & 5.3 Na_2SiO_3	99.99% Al	500	90	0.57	[**28**]
KOH & Na_2SiO_3	Al 2214-T6	3800	200	0.80	[**16**]
KOH & Na_2SiO_3	Al 6082	1500	150	0.67	[**29**]
		2700	150	1.17	
$NaWO_3$ & Na_3PO_4	Al LD31	800	180	0.36	[**30**]
2.8 KOH & 5.3 Na_2SiO_3 with 10 ZrO_2	99.99% Mg	2000	40	0.95	[**31**]
			40	1.10	
2.8 KOH & 5.3 Na_2SiO_3	Mg WE43-T1	3000	40	0.43	[**32**]
9.5 Na_3PO_4 & 52.5 NH_4OH	Mg WE43-T1	3000	40	0.70	[**32**]

Table 2.4: *Summary of linear coating growth behaviours for PEO processing which have been reported in the literature, j is the applied current density.*

2.3.2.1 Appearance of coating surfaces.

PEO coatings on aluminium display a characteristic surface appearance, of which the micrographs reproduced in Figure 2.6 are a typical example. The coatings at all times exhibit pores (craters) on scales from a few hundred nm up to a few μm. These pores are often surrounded by relatively smooth regions of material, which are speculated to be formed from the re-solidification of molten material after a discharge event.

Cracks radiating from the craters have been attributed to thermal shock caused by rapid quenching [**4**]. Evidence of melt flow and solidification would suggest that temperatures in the region of the discharge reach several thousand Kelvin. This is consistent with the plasma temperature estimates from spectral studies [**1, 14, 15**]. The increasing scale of surface features with processing time is usually attributed to increased intensity and power of discharge events as coating proceeds.

2.3.2.2 Discharge channel sizes and populations.

Sundararajan and Rama Krishna [**3**], and Shen et al [**34**] studied variation in the diameters of open pores (craters) with processing time. Both studies found an approximately linear increase in channel diameter with processing time. Sundararajan and Rama Krishna found the diameter to vary from $\sim 1.4\ \mu$m after 1 minute, to $\sim 2.4\ \mu$m after 30 minutes of processing. This related to the 5 largest pores observed in each micrograph. This represents an upper bound on discharge channel scale, as smaller pores were still present. The trend found in this study is reproduced in Figure 2.7.

Shen et al [**34**] found the diameter to increase from $\sim 1\ \mu$m after 1 minute to $\sim 9\ \mu$m after 36 minutes of processing. This is a much larger increase than reported by Sundararajan and Rama Krishna [**3**]. However it is not clear from the methodology of De-Jiu et al exactly which channel diameters they have included, and no errors are estimated for their channel diameter measures. It is unlikely the numbers plotted represent a mean, as micrographs in the same article indicate that much smaller pores are present for all times of processing.

Estimates of the number of discharge channels per unit area have also been published. For aluminium processing Sundararajan and Rama Krishna report a density of $\sim 1.1 \times 10^{16}\ \mathrm{m}^{-2}$ after 1 minute, falling with processing time to $\sim 5 \times 10^{14}\ \mathrm{m}^{-2}$ after 30 minutes [**3**]. Studies of PEO on aluminium were also published by Shen et al [**34**] and Curran and Clyne [**4**]. Shen and co-workers report lower discharge channel populations, of $\sim 3.8 \times 10^{11}\ \mathrm{m}^{-2}$ at 1 minute, falling to $\sim 1 \times 10^{10}\ \mathrm{m}^{-2}$ after 36 minutes.

Curran and Clyne [**4**] found a population density of $\sim 1.4 \times 10^{10}\ \mathrm{m}^{-2}$ for a

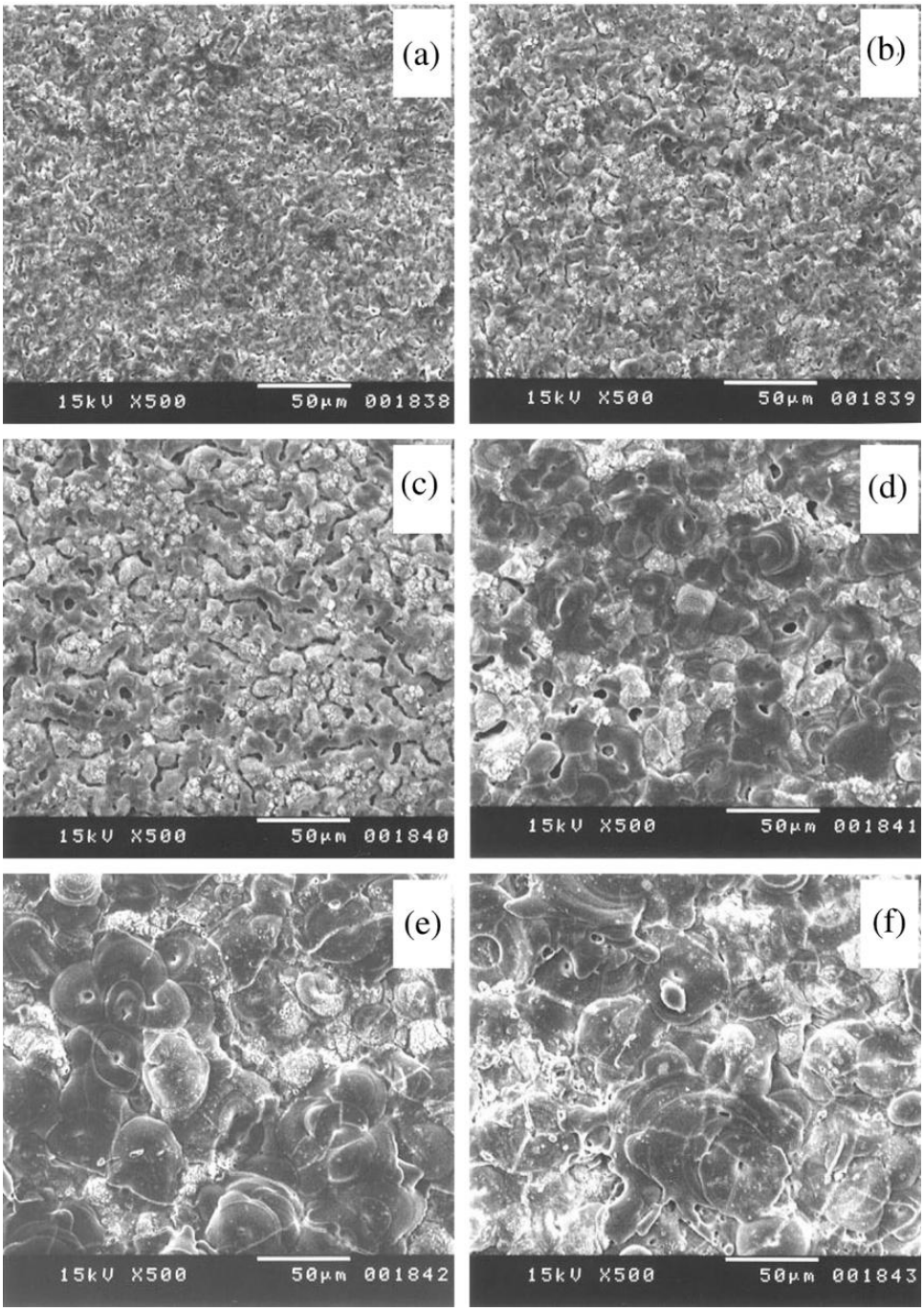

Figure 2.6: *Secondary electron images of MAO coating surfaces at 500× magnification processed for (a) 1; (b) 3; (c) 5; (d) 10; (e) 20 and (f) 30 min. Figure and caption reproduced from Sundararajan and Rama Krishna* **[3]**, *substrate material was aluminium.*

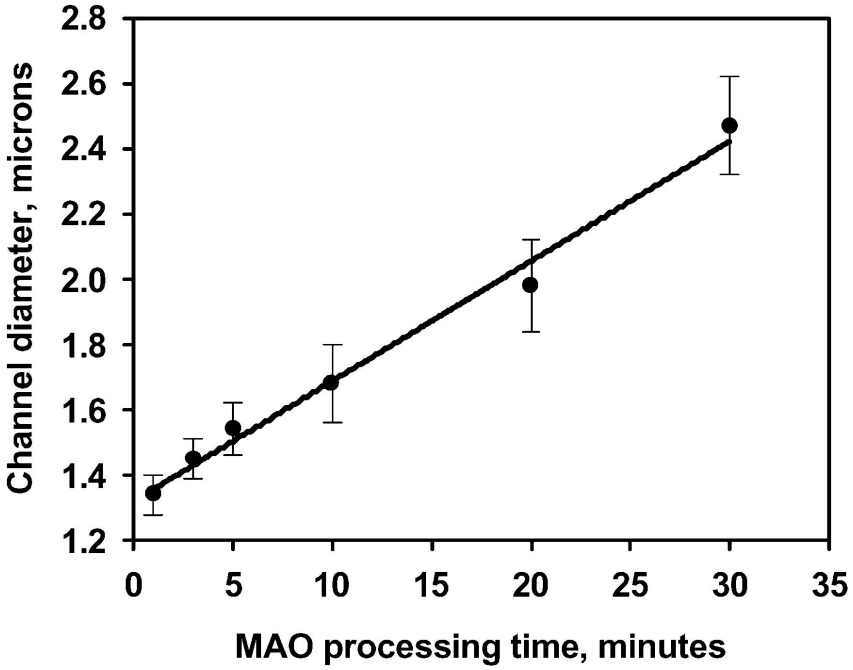

Figure 2.7: *Variation in diameter of the microarc discharge channels as a function of MAO processing time. Figure and caption reproduced from Sundararajan and Rama Krishna* [**3**].

5 μm coating (approximately 5 minutes processing), falling to $\sim 1 \times 10^9\ m^{-2}$ when a coating thickness of 40 μm had been reached. Thereafter the crater population density remained approximately level to a thickness of 100 μm (about 100 minutes processing). For PEO processing of titanium, Matykina et al found pore population of $\sim 3.5 \times 10^{11}$ m^{-2} 2 minutes into processing, which was observed to fall to $\sim 1 \times 10^{11}$ m^{-2} after 15 minutes [**8**].

With the exception of Sundararajan and Rama Krishna, the literature data indicates the pore population density to be in the range from 10^9 to 10^{11} m^{-2}. The information about visible crater (pore) populations, when combined with estimates of dynamic discharging rates, can enable estimates to be made of the period for which surface features persist before being overlaid by subsequent discharging activity. For example with a discharging rate of 1×10^8 m^{-2}.s^{-1} and a crater population of 1×10^{10} m^{-2}, you would expect the lifetime of a particular surface feature to be roughly 100 s. All studies reported significant decreases in the number of pores visible on the coating exterior with increased thickness.

2.3.2.3 Surface roughness of coatings.

Increases in exterior roughness of PEO coatings with processing time are well known, and evident upon examination at the human scale by eye and touch. Some authors

have quantified these changes in surface roughness, which are thought to provide an indirect measure of the scale and uniformity of discharging activity.

The characterisation study by Sundararajan and Rama Krishna included quantification of the coating roughness [**3**]. They report a linear increase in the coating arithmetic roughness from ~ 0.3 μm just after commencement of processing, to ~ 2.2 μm when the coatings were about 40 μm thick after 36 minutes processing.

The authors also quantified the typical diameter of the smooth regions of apparently re-solidified material surrounding discharge craters, finding ~ 15 μm at 5 minutes into processing, then a rough linear increase to ~ 35 μm after 30 minutes. They speculate that growth of the coating is by flow of molten material out of the discharge channel, which spreads to form the smooth regions which they refer to as 'pancakes'. The authors speculate that increases in the mean 'pancake' diameter, when coupled with the decrease in crater population density, may be the cause of the increased roughness seen with thickening of the coatings.

Comparison can be made with the study by Curran and Clyne [**4**], who reported arithmetic roughness ~ 1.5 μm for a 5 μm coating, which increased until levelling off at ~ 8 μm from 80 μm to 100 μm of coating thickness. Jin et al reported a linear increase in the observed arithmetic roughness of PEO coatings [**30**]. They found an increase from ~ 1.3 μm for 15 μm coatings to ~ 4.5 μm when the coating was more then 65 μm in thickness. Data from Curran and Clyne [**4**] and Jin et al [**30**] are in reasonable agreement with Sundararajan and Rama Krishna [**3**].

The 'pancake' concept of Sundararajan and Rama Krishna was adopted by Jaspard-Mecuson et al [**16**], they reported initial diameters for the smooth surface regions of ~ 15 μm after 10 minutes processing. This then rose in roughly linear fashion to ~ 110 μm after 140 minutes of conventional PEO processing. The implied value of ~ 30 μm after 35 minutes processing compares reasonably with the values reported by Sundararajan and Rama Krishna [**3**]. They also report on an experimental set of processing conditions which they state displayed reduced intensity of discharging when observed visually. For this experimental process they found the 'pancake' diameter to be roughly constant at around 20 μm throughout.

The trends in surface roughness are related to increases in the scale of surface features as PEO coatings thicken. In the context of information on size and prevalence of discharge channels (subsubsection 2.3.2.2), and if feature size is assumed proportional to some energy input from processing, the literature data suggests greater local intensity of processing at a reduced number of sites as coating proceeds.

2.3.3 Coating interior microstructures.

PEO coatings are often reported to show a two layer structure, with an outer layer described variously as porous or friable, and an inner layer described as dense, compact or functional. Such a structure has been reported for Aluminium by Guan et al [**35**], Jaspard-Mecuson et al [**16**], Gu et al [**36**], Long et al [**20**], Yerokhin et al [**2, 33**] and Xue et al [**37**]. For magnesium processing, two layer structures are reported by Arrabal et al [**5, 31, 32**]. In relation to titanium, a two layer structure was reported by Teh et al [**38**].

There are certainly differences in the coating morphology through the cross section, as seen in Figure 2.8, reproduced from [**4**]. However, there is no clear boundary between two regions of coating, what change there is happens gradually between the substrate and the free surface. Claims of obvious two layer structures in the literature are sometimes tenuous, and the relative thickness of 'porous' and 'functional' layers is often used as a parameter to quantify the relative quality of different processing conditions. Using a subjective measure like this for such purposes is not ideal.

Some studies have used TEM imaging to focus on the boundary between the coating and substrate. This interface is important for coating corrosion performance and adhesion to the substrate. A thin, typically several hundred nm thickness, barrier layer of amorphous material has been reported at the substrate-coating interface for aluminium by Monfort et al [**28**], for titanium by Matykina et al [**39**] and for magnesium by Arrabal et al [**5**].

The interpretation of these authors is that much of the coating thickness is permeable to the electrolyte via a network of surface connected porosity, and that only this internal region presents a barrier to electrical conduction and corrosion of the substrate. This is a reasonable conjecture, especially as the voltage required to cause breakdowns through a coating during PEO does not double with the coating thickness (see section 2.2). It makes sense that the majority of the applied voltage be dropped over some thinner internal region of the coating, with discharge events possibly initiated at this internal barrier. This is consistent with the observation that PEO coating rates can remain reasonably constant to thicknesses in excess of 100 μm. The conjecture that the majority of the coating be permeable to the electrolyte relies upon a high level of surface connected porosity in the coating, which will be discussed in subsection 2.3.4.

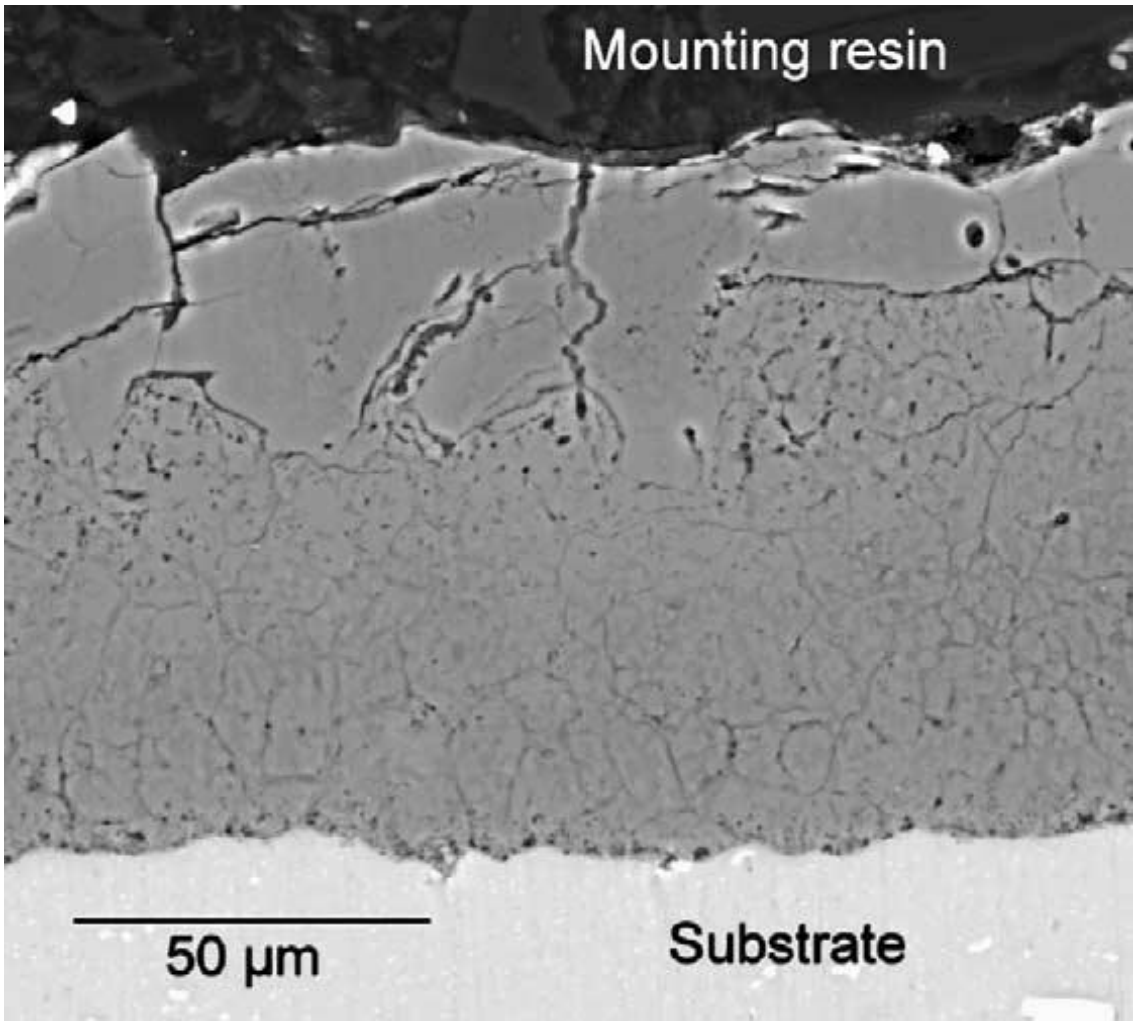

Figure 2.8: *Back-scattered SEM micrograph of a polished cross-section through a* 100 *µm thick coating, showing surface cracks, shrinkage pipes and an extensive network of micro-defects. Figure and caption reproduced from Curran and Clyne* [**4**].

Technique	Porosity
free standing bulk density	$42 \pm 12\%$
attached bulk density	$50 \pm 14\%$
mercury porosimetry	$17 \pm 7\%$
nitrogen adsorption	$20\%\star$

Table 2.5: *Summary of the porosity measurements reported by Curran and Clyne* [**6**]. $\star$ *this value is an estimate assuming cylindrical pores of 30 nm diameter, as nitrogen adsorption measures specific surface area.*

2.3.4 Coating porosity.

Dietzel et al studied porosity of coatings on magnesium indirectly by examination of coating surfaces after either chemical etching or electro-deposition of copper, which was preferentially deposited at sites of pores in the coating surface [**40**]. They quote pore numbers in the range of $\sim 5 \times 10^6$ m^{-2} to $\sim 6 \times 10^7$ m^{-2}, though no fraction of porosity is quoted. The pore density identified is much lower than that quoted by other studies.

An estimate of the porosity as less than 10% was reported by Yerokhin et al from analysis of polished cross-sections [**33**]. This estimate is probably too low as polished cross-sections do not represent the most reliable approach to measurement of porosity. Much of the porosity may not show up clearly, and the polishing process can result in sample porosity being filled in with material dislodged from elsewhere on the sample surface.

The most expansive study of porosity was published by Curran and Clyne [**6**]. They estimated the porosity for coatings on aluminium by measurement of the bulk density of both attached PEO coatings and coatings detached by dissolution of the substrate. Porosity was also measured using mercury intrusion porosimetry and isothermal nitrogen adsorption. A summary of the measured porosity values may be found in Table 2.5.

The fraction of surface connected porosity was estimated by comparison of the skeletal density, as measured by Archimedian displacement, He pycnometry or mercury porosimetry, with the theoretical skeletal density from the phase proportions measured by X-ray analysis. A summary of the skeletal densities reported by the authors is found in Table 2.6.

Porosity values from bulk density measurements are probably the least reliable. The coating dimension was measured for free standing coatings with a micrometer, and for attached coatings by eddy current thickness gauge. These techniques are not sensitive to the surface roughness of the coatings, and will tend to measure the

Technique	Skeletal Density / g.cm^{-1}
theoretical	3.63 ± 0.2
Archimedian	3.73 ± 0.02
He pycnometry	3.498 ± 0.004
mercury porosimetry	3.609 ± 0.004

Table 2.6: *Summary of the skeletal density measurements reported by Curran and Clyne* [**6**].

thickest points on the area tested. This will lead to an overestimate of the thickness and porosity. The values from mercury porosimetry, and estimated from nitrogen adsorption, around 20%, are probably the most accurate reflection of the coating porosity.

The similarity reported between the theoretical skeletal density from X-ray analysis and the three different experimental measurements is evidence of low levels of occluded porosity in PEO coatings. This implies that the majority of porosity in PEO coatings is connected to the coating surface. This would allow for infiltration of the electrolyte into the bulk of the coating during processing, and is consistent with the conjecture in subsection 2.3.3.

2.3.5 Phase constitution.

The crystalline phases, and the relative fractions of each present, are thought to be influenced by the heating effects of the plasma discharges during processing. For aluminium the most common constituents have been often confirmed to be α and γ-alumina [**2, 3, 4, 28, 29, 30, 33, 35, 36, 37, 41, 42, 43**]. Other polymorphs of alumina, such as δ and θ-alumina, were detected in some of these studies, and aluminosilicate phases such as mullite were detected in some of the studies which utilised electrolytes with a high concentration of Na_2SiO_3.

Crystalline phases detected in PEO coatings on magnesium included MgO, Mg_2SiO_4, $MgSiO_3$ and $Mg_3(PO_4)$ [**5, 32**]. For titanium the main phases identified are anatase and rutile forms of TiO_2 [**44**]. Anatase and rutile were also seen in selected area electron diffraction analysis by Matykina et al [**39**]. Other works in addition have no doubt found similar phases to those mentioned, the papers referenced in this work correspond to studies where some emphasis was placed on process mechanisms, and not tribological or biomaterials applications.

The α-alumina structure is the stable form of Al_2O_3 [**45**]. There are a number of structurally similar transition alumina polymorphs, and these may co-exist within a single sample at a given temperature and pressure [**45, 46, 47, 48**]. This makes

single crystal samples of transition aluminas difficult to achieve, and as a result the exact structures of γ, δ and θ-alumina structures are not completely resolved. All are based roughly around face centred cubic arrangement of the oxygen anions, with the different symmetries being realised by differing arrangements of the Al cations.

The γ-alumina phase may be formed from thermal oxidation of aluminium; heating of aluminium hydrates; transformation of amorphous Al_2O_3 and from quenching of alumina melt [**45**]. Most of these routes could be feasible in the PEO process. Furthermore, γ-alumina can also be directly formed during anodising of aluminium under certain conditions, and is associated with oxygen generation [**28, 43**].

Once γ-alumina has been formed, it may be transformed into α-alumina either directly, or via intermediate transformation to δ then θ-alumina [**45, 48**]. The temperature required for transformation of γ to δ is ~ 1023 K, for δ to $\theta \sim 1273$ K and above ~ 1473 K any of the transition aluminas can undergo transformation to the stable α form.

The existence of α-alumina in PEO coatings is indicative of local temperatures in the coating reaching at least ~ 1473 K. The existence of δ and θ-alumina polymorphs is not unfeasible given the possible transformation routes between γ and α-alumina. Generation of α-alumina in PEO coatings is usually attributed to thermal annealing effects of the discharges. Knowledge of the physical scale of events, and of the energy and power delivered to individual plasma discharges is thus crucial; if the thermal fields in PEO coatings near to a discharge event are to be calculated to allow testing of this hypothesis.

Relative fractions of phases at different depths below the free surface of a ~ 70 μm PEO coating were measured using X-ray spectroscopy and Rietveld refinement for PEO coatings on aluminium by Curran and Clyne [**4**]. The results are reproduced in Figure 2.9; the content of α-alumina is seen to be highest in the outer 30–40 μm of the coating.

By contrast, Xue et al [**37**] found the opposite trend, with the lowest content of the α phase at the coating surface, $\sim 12\%$. The proportion rose with depth below the coating free surface to $\sim 56\%$ when 50 μm from the interior boundary with the substrate. In both cases the authors attribute the higher content of α-alumina to greater thermal effects of the discharges, though there is clearly a discrepancy in their assumptions about where in the coating system heat loss will be a minimum.

It seems unlikely that thermal effects in the two experiments would be substantially different with depth into the coating. It is possible that another factor is responsible for the observed phase distributions, possibly the concentrations of alloying elements. Impurities are said by Levin and Brandon [**45**] to have a bearing on transition temperatures and stability of transition aluminas. Curran and Clyne

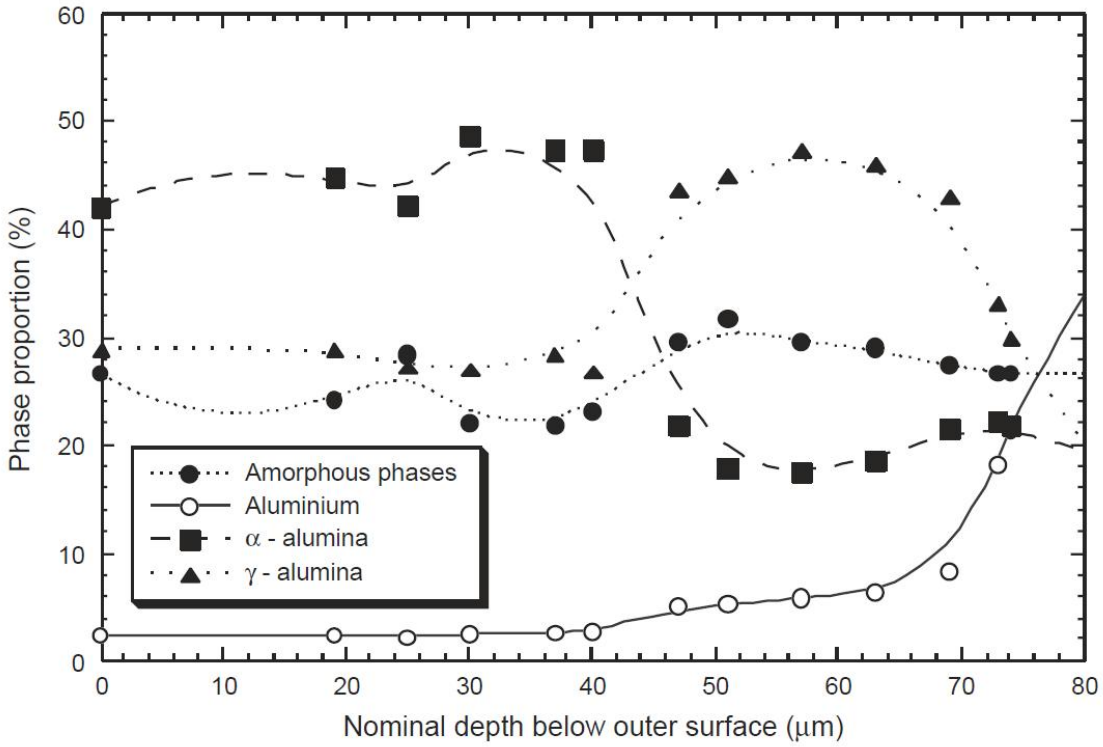

Figure 2.9: *X-ray diffraction data in the form of a plot of the phase proportions against the nominal depth below the free surface for surface scans during the progressive polishing of a* 100 μm *thick coating. Figure and caption reproduced from Curran and Clyne* [**4**].

[4] used Al 6082, Xue et al [37] used Al 2024, which contains substantially more Cu then the 6082. Without detailed information about differences in discharge event power levels between different processing systems, further progress in understanding the phase proportions is difficult.

2.3.6 Elemental distributions.

The distribution of atomic elements within PEO coatings is not uniform, and often EDX mapping of elemental compositions has been used to gain insight into the discharge and coating growth mechanisms. The first work to fully realise this potential was published by Monfort et al [43]. The authors processed aluminium sequentially in first an electrolyte containing Na_2SiO_3, then a second containing $(NH_4)_2\,HPO_4$. They applied EDX mapping of the coatings formed to examine the distributions of silicon and phosphorous within the coatings.

They present maps showing that silicon was primarily present in the outer parts of coatings when samples were processed only in the silicate containing electrolyte. For coatings produced only in the phosphate electrolyte the phosphorous was found predominantly in the interior regions of the coatings. Most significantly the authors demonstrated that when a sample coated for 30 minutes in the silicate electrolyte was processed for just 15 s in the phosphate containing electrolyte, phosphorous could be found at some locations near to the substrate-coating boundary. A reproduction of these elemental maps is in Figure 2.10 for reference.

This provides valuable evidence that the PEO discharge events provide a mass transport pathway between the electrolyte and the coating interior. Similar results for sequential processing of magnesium alloy were reported by Arrabal et al [32], and for titanium by Matykina et al [49]. The tendency for silicon to be found in the coating exterior was further confirmed in studies by Monfort et al on aluminium [28], and Arrabal et al for another study of magnesium [5].

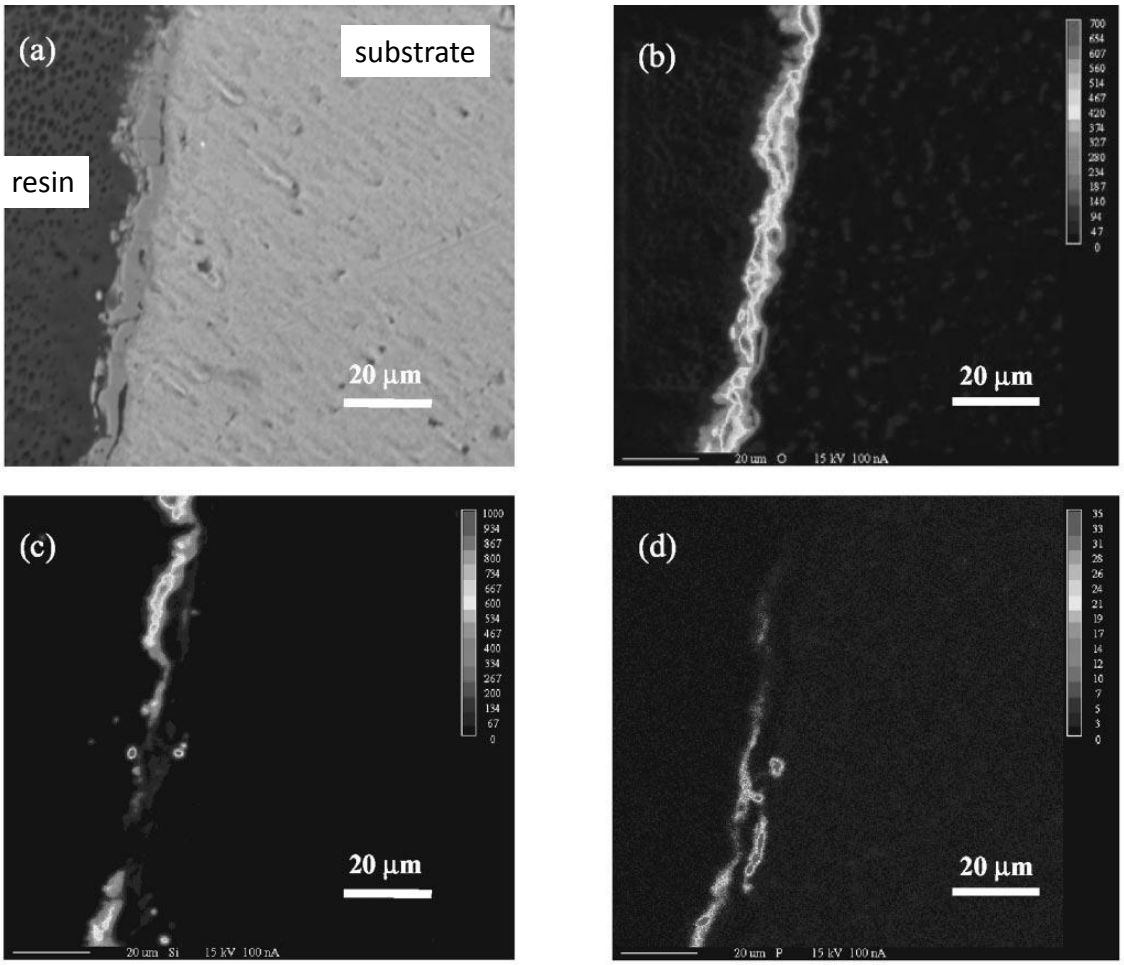

Figure 2.10: *EPMA of the coating formed on aluminium for 1800 s at* 5 $A.dm^{-2}$ *in 0.05 M KOH + 0.025 M* $Na_2SiO_3.10H_2O$ *electrolyte at 293 K and then for 15 s in 3 M* NH_4OH *+ 0.05 M* $(NH_4)_2\,HPO_4$ *electrolyte at 293 K. a) Backscattered electron image, b) oxygen, c) silicon, and d) phosphorus. Figure and caption reproduced from Monfort et al* [**43**], *annotations added for additional context.*

Chapter 3

Methodology.

3.1 PEO Processing Equipment.

Two methodologies which enable quantitative information on the discharge event properties to be measured are presented in this work. The first involves monitoring the current passing through a small area, exposed to PEO processing in parallel with a larger area. This approach relies upon the existence of a well defined probability of breakdown per unit time and area. By using a small enough area, the possibility of two or more events being active concurrently on the small area is reduced. This allows individual breakdown events to be resolved in the current signal. This method will be referred to as 'in-situ monitoring' experiments, as the data is recorded during a full scale application of the PEO process. This work was inspired by the work of Bao Van et al [**13**].

The second methodology takes a different approach to reduce the probability of concurrent discharge events. Testing is performed on coatings pre-deposited by conventional 50 Hz PEO processing. Small test wells are created on the sample surface, then filled with a sample of an electrolyte to be tested with the coating. The substrate metal is raised to a high positive voltage, as during PEO processing, whilst the electrolyte is held at ground potential. Breakdown events are initiated when the potential difference becomes large enough. The incidence of concurrent events is reduced by using power supplies which are not capable of supplying large currents for continuous periods. The current loading causes the applied voltage to drop once an event has initiated, reducing the probability of a second event initiating until after the first has terminated, and the applied voltage recovered. Capacitors placed in parallel with the sample under test can provide an additional store of charge and energy, reducing the magnitude of the drop in applied voltage during a discharge event.

These experiments will be referred to in this text as 'single discharge' experi-

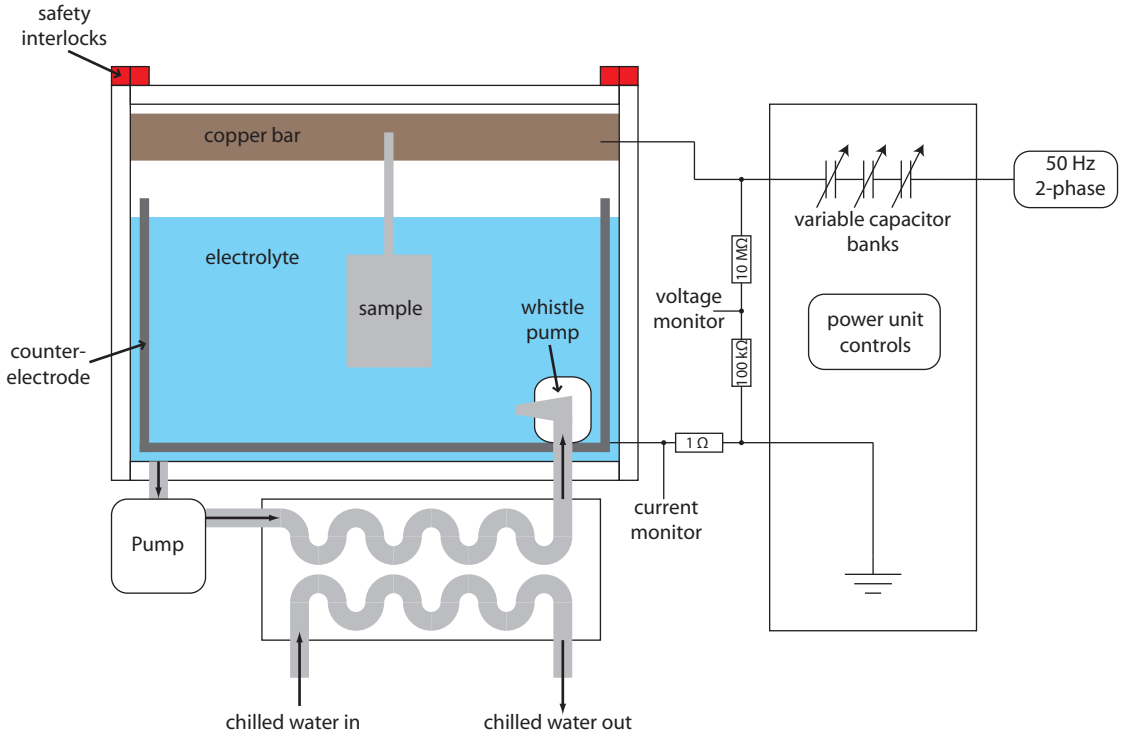

Figure 3.1: *Schematic of the 10 kW 50 Hz AC PEO processing unit used in this research.*

Figure 3.2: *Photograph of the 10 kW 50 Hz AC PEO processing unit used in this research.*

ments. This is not always accurate, as for some experiments a significant population of the discharge events recorded appear to be the superposition of two separate current peaks. The name is used here in preference to the terminology of 'small area DC testing', which was used in a previous publication [**1**]. This is because it would be confusing to refer to these experiments as small area, when the monitored area is several orders of magnitude larger then that used for the in-situ experiments.

The same PEO processing unit was used for both in-situ monitoring experiments and to generate samples used for single discharge testing. The supply is depicted schematically in Figure 3.1, and a photograph is presented in Figure 3.2. The power unit is a 50 Hz fixed frequency unit operated from 2-phase UK mains supply. Banks of capacitors can be switched in and out of series with the process tank, in steps

of 2 μF. The capacitors limit the charge which can be supplied during each 50 Hz cycle, and in addition enforce balance of the charges supplied during positive and negative polarisation of the sample. In standard operation the electrolyte is kept at ground potential, and the sample is connected to the power supply output.

It should be noted that no bias of the voltage is applied directly by the power unit. Greater voltages are generally reached under positive polarity, however this is due to the interaction of the substrate-coating-electrolyte system with the power supply. Application of the power supply to substrates which are inert to PEO processing, for example stainless steel, results in symmetric voltage waveforms. Examples of the process current and voltage waveforms from this unit may be found in Figure 1.1.

The electrolyte used for all processing and testing was a commercial electrolyte of approximate composition 1–2 g.l^{-1} potassium hydroxide (KOH), 3–5 g.l^{-1} sodium silicate (Na_2SiO_3) and 3–5 g.l^{-1} tetra-sodium pyrophosphate ($Na_4P_2O_7$). The electrolyte used had conductivity of $\sigma = 5.1 \pm 0.1$ mS and pH of 10.9 ± 0.1.

The electrolyte was pumped through a heat exchanger to prevent large temperature rises during processing, and passed back into the tank through an aerating pump. The cooling water passed through the heat exchanger varied in temperature from ~ 16°C to ~ 18°C. Electrolyte temperature was logged along with other experimental parameters. Temperature was measured by a sensor in the processing tank, connected to a readout on the supply control unit.

The coatings produced by this 50 Hz PEO processing unit have been well characterised previously [**4, 6**]. The processing frequency is fixed at 50 Hz, and all that can be set on the unit are the time of processing and the capacitance, which as previously mentioned influences the current density. It should be stressed that the capacitance setting does not actually control the current density to a precise level.

Some modifications to the basic unit were made to allow direct logging by oscilloscope of the bulk current through the process tank and the voltage between the output and ground. A 1 Ω resistor was included in the return path to ground, allowing the current to be monitored via the voltage developed over the resistor. The voltage was monitored by a 100$\times$ attenuation potential divider built in between ground and the power supply output. When bulk waveforms were being logged, the monitoring box was connected to a Picoscope 5203 PC USB oscilloscope, controlled using a laptop computer.

3.2 In-situ Discharge Monitoring Experiments.

The general geometry of the samples used for in-situ current monitoring is shown schematically in Figure 3.3. The sample consists of a cylinder of aluminium 6082 alloy with diameter of 10 mm, with one or more fine wires of 99.5% purity aluminium running parallel. The assemblage of large and small areas was mounted in a cold setting acrylic resin (Epofix), to provide electrical insulation from the electrolyte. Electrical connection of the large area was through a 4 mm threaded stainless steel rod, connected to the power supply output (Figure 3.1) by a brass clamp. Full details of the relative scale of small and large areas of the in-situ samples can be found in subsection 3.2.1. The small and large areas are connected via an extended pair of wires, twisted together to reduce noise in the current signal. The twisted pair extended out of the processing tank and was passed through a non-contact current probe as a coil of 4 turns.

This current probe operated by electromagnetic induction, and 4 turns of the signal wire were passed through the probe to increase the current sensitivity. The probe used was a Tektronix P6021 current probe. The coupling into the oscilloscope was set to a sensitivity of 1 mV per 2 mA, so with the enhancement provided by using 4 turns of the signal wire, this gave a sensitivity of 2 mV per 1 mA. Working by electromagnetic induction, the probe requires a changing current signal to function, and with the settings used the low frequency cut off was 400 Hz.

The short ($\sim$ 100 μs) current pulses which were measured in this work principally contain frequency components greater than 400 Hz. However, the current gradient is low, and temporarily zero, in the region of the peak discharge current. During this period the signal in the current probe displays decay similar to a resistor-inductor circuit (LR), leading to distortions of the measured baseline level. This phenomenon is referred to as LR 'droop', and the effect may be corrected for. This correction was made in the present work, and full details of the procedure may be found in Appendix B.

Monitoring of the current passing through the small area was performed using a Picoscope 5203 USB oscilloscope, controlled by a laptop computer. The voltage between ground (electrolyte) and the sample was monitored using the built in 100$\times$ attenuation potentiometer, depicted in Figure 3.1. The oscilloscope had two data channels, so the small area current and the bulk processing current were not recorded in the same experiment, as one channel was reserved to monitor the applied voltage.

The sampling rate used in the in-situ experiments was 500 kHz, one sample every 2 μs. Data was recorded in 20 s continuous sections, and after each section the internal memory of the oscilloscope was filled. There was then a period of $\sim$ 2.7 s 'dead time' during which the oscilloscope memory was transferred to the laptop

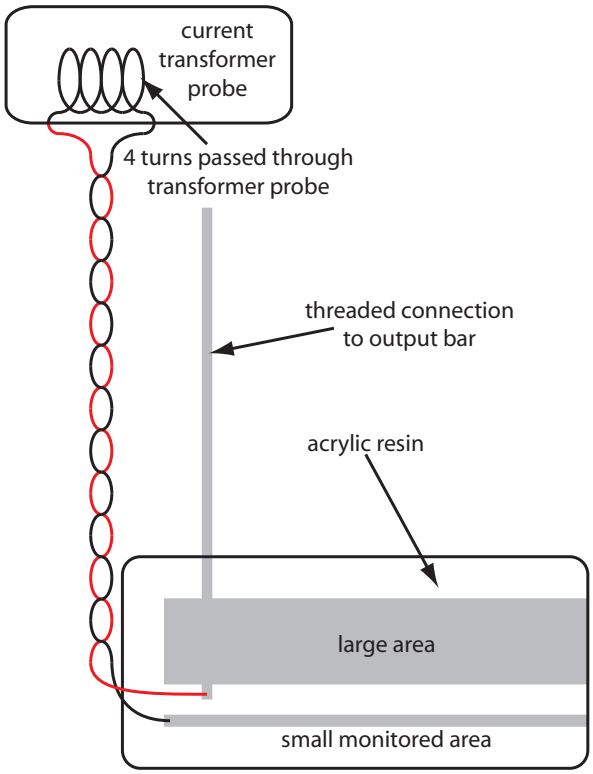

Figure 3.3: *Schematic of the sample geometry used for small area in-situ discharge monitoring.*

memory. This could not be repeated indefinitely, and periodically the processing had to be stopped to allow the data in the laptop memory to be written to the hard disc. As a result in-situ experiments were conducted as a sequence of 150 s segments of PEO processing. During each processing segment, 7 oscilloscope buffers were taken, 6 spanning 20 s and one spanning ~ 13.8 s. The total period which was not recorded was ~ 16.2 s, meaning that coverage during in-situ experiments was $\sim 89.2\%$.

The duration of the interruption between process segments was always more then 120 s, but never more then 180 s. Interruptions to PEO processing are generally of minimal impact once processing is resumed, however some effect of this procedure upon the discharging behaviour might be expected. This procedure of logging, stopping, then re-starting the processing was repeated until the desired duration was reached. Full details of the durations of each experiment may be found in subsection 3.2.1.

The main purpose of the in-situ experiments was to obtain information representative of bulk PEO processing. This is why a small area was monitored in parallel with a larger area. It was desired to understand the properties of breakdown events which occurred as part of a larger ensemble of active discharge events, spread across the exposed substrate surface. Whilst the data obtained during any given experimental run will not be representative of the wider process at that time (due to the small area sampled), across multiple repeats the measured properties should converge to a distribution which is representative of the individual discharge properties across the whole sample at that point in time. The validity of this assumption will be discussed in chapter 4.

The elongated shape of the in-situ samples, 120 mm in length, was chosen to allow many repeats to be performed in rapid succession. After each experimental run a Struers Secotom-10 precision saw was used to cut off the front 3–4 mm of the sample. The cut off was kept for analysis by microscopy, and the newly exposed surface ground with 800 grade SiC grit paper. The newly resurfaced sample was then used for another experiment. The front face of the sample was always positioned at a distance of 40 mm from the stainless steel counter electrode.

3.2.1 Variations of discharge characteristics with processing time and effects of monitored area size.

The purpose of this experiment was firstly to measure the properties of PEO discharge events during processing of an aluminium substrate, for periods up to 40 minutes of processing. Samples with several different sizes of small area were produced to confirm that rates of activity seen scaled with the size of the area moni-

Name	Al_01	Al_02	Al_03	Al_04	Al_05	Al_06
Small area / m $\times 10^{-7}$	1.96	1.96	3.93	3.93	5.89	0.113

Table 3.1: *Sizes of small areas for in-situ experiments.*

tored. If this was not the case, then data obtained from the small area could not be taken as representative of the properties of discharge events anywhere beyond the monitored area.

For this experiment six samples were produced with the general form depicted in Figure 3.3. The large area in each case was a cylinder of 6082 aluminium alloy with diameter 10 mm. The samples measured 120 by 50 by 20 mm in total. The designations of these samples and the sizes of the small areas used for each are outlined in Table 3.1. For samples Al_01 to Al_05, the small areas were composed of either one, two or three wires of diameter 500 μm and composed of 99.5% purity aluminium. For sample Al_06 the small area was composed of a single 120 μm diameter wire, formed by swaging down one of the 500 μm diameter wires.

As was described in section 3.2, for monitoring of discharge events each sample was sequentially processed for 150 s segments, with logging of both small area current and applied voltage at a rate of 500 kHz. The overall coverage of sampling was $\sim 89.2\%$. Some of the experimental runs did not follow this procedure. For one experimental run with each of samples Al_01, Al_04 and Al_05, the bulk processing current and not the small area current was logged. This was done for a processing time of 40 minutes, and was important as the oscilloscope used (Picoscope 5203) meant that bulk process current, small area current and applied voltage could not all be logged at the same time. A summary of the total duration of processing for each of the experimental runs, with each of the samples Al_01 to Al_05, is presented in Table 3.2.

After each experimental run the front facing 3–4 mm of the samples was cut off, and the section kept for microscopy. The off cuts from experimental runs with samples Al_02 and Al_03 were used to examine changes in the surface appearance of the small monitored area with process time. These off cuts were subsequently re-mounted and cross-sectioned to allow the thickening rates of coatings on the small and large areas to be compared. The data from all experimental runs required extensive post-processing before discharge properties could be obtained. The full details of this process are presented in Appendix B. At the start and end of each experimental run the electrolyte conductivity and pH were measured using a dual probe Jenway 430 pH-conductivity meter. The electrolyte had conductivity of $\sigma = 5.1 \pm 0.1$ mS and pH of 10.9 ± 0.1. Electrolyte temperature was also recorded at the start and end of each 150 s processing segment.

Experimental run	Al_01	Al_02	Al_03	Al_04	Al_05
run 1	35	2.5	unusable	40	40
run 2	40	5	2.5	40	40
run 3	40	10	5	40	40
run 4	bulk log	15	10	bulk log	bulk log
run 5	unusable	20	15	40	40
run 6	unusable	25	20	40	40
run 7	40	30	25		40
run 8	40	35	30		
run 9		40	35		
run 10			40		

Table 3.2: *Times of processing for in-situ samples. All times are in minutes, 'bulk log' represents that the experimental run was used to log bulk process current. Several experimental runs were rendered unusable due to technical difficulties.*

The sample with the smallest monitored area, Al_06 with a single 120 μm wire as small area, was made after the conclusion of data processing for the other five samples. It was specifically produced to allow resolution of the very smallest discharge events which occur during processing. In addition to the smaller monitored area, the current monitoring arrangement was physically altered for this sample. Instead of 4 turns of the signal wire being passed through the current probe, as depicted in Figure 3.3, ten turns were used with sample Al_06. This increased the current sensitivity of the probe to 5 mV per 1 mA. Logging with this sample was not as comprehensive as the other samples, but was conducted at greater sampling rates, typically 62.5 MHz.

3.3 Single Discharge Experiments.

Whilst the properties of breakdown events recorded during PEO processing are of obvious interest, the occurrence of each event as part of a wider set of discharges presents several problems when it is desired to understand the underlying physical principles. For such studies the 'single discharge' techniques were developed.

The concept of the single discharge experiments is to generate breakdown events as close as can be managed to one at a time. Samples used were pre-deposited PEO coatings of varying thicknesses. Using pre-deposited coatings has several advantages, the most important of which is that the electrolyte used for the testing need not be the same electrolyte as was used to generate the coating in the first place. Whilst in this work the same electrolyte was used for all processing and testing, the

techniques developed could readily be applied to testing of standard coatings using a range of electrolyte compositions.

The general form of samples for single discharge testing is described in subsection 3.3.1. Over the course of this work, two different power supplies were used to generate breakdown events during single discharge testing. These power supplies are described in subsection 3.3.2 and subsection 3.3.3. The first power supply was used to generate one of the two large datasets of discharge properties presented in this work, discussed in detail in chapter 5. The second power supply was used to generate calibration data, which was used to develop a correction procedure for the current probe data from in-situ monitoring experiments.

3.3.1 Small area general set-up.

The single discharge experiments all use the same sample preparation route. The cleaned and dried surface of the PEO coated part is divided into many small and separate wells. Each of these wells is formed by attaching a 15 mm length of cylindrical PVC tubing, with internal diameter of 6 mm, to the sample surface. The tubes are bonded to the coating using a small quantity of cyanoacrylate adhesive. Grid arrangements of the testing wells were used. After attachment of the PVC tubes, the waterproofing of each was made certain by painting PVA adhesive around the exterior of each well at the join to the substrate. A photograph of a sample prepared in this way is presented in Figure 3.4.

Once the sample is prepared, the basic procedure for generating the breakdown events is the same regardless of the power supply used. The well to be tested is filled by pipette with a sample of the desired electrolyte solution. The coated substrate is connected to the output of the power supply, and the electrolyte grounded by inserting a counter-electrode in the form of a 1 mm diameter wire of 99.5% pure aluminium. The counterelectrode wire was connected to the system ground. The general set-up for single discharge testing is depicted schematically in Figure 3.5.

When the power supply is switched on the applied voltage climbs rapidly until breakdowns of the coating begin to be observed. The precise duration of testing in each experiment is detailed in section 3.4, but no sample was subjected to single discharge testing for more then 60 s. In the sections which follow, the power supplies used for these experiments will be described, and the capabilities of each briefly explored.

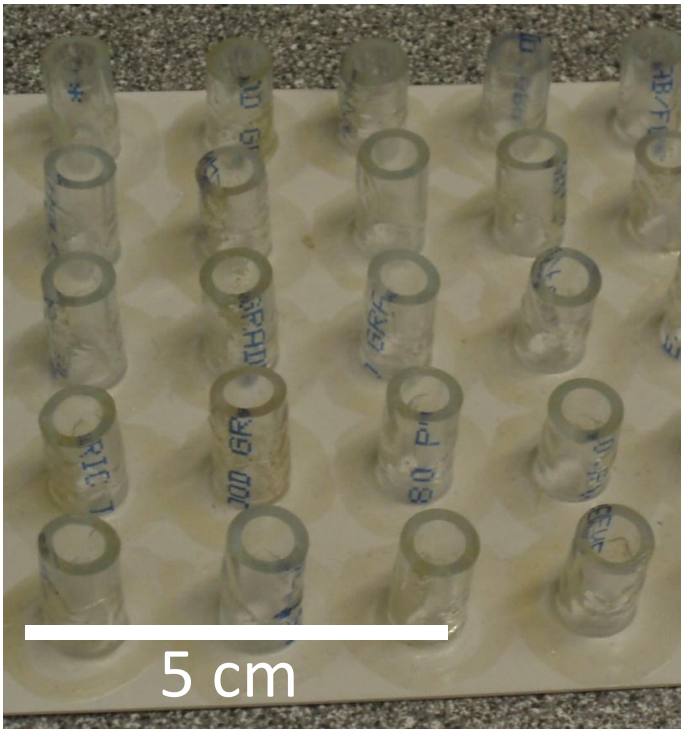

Figure 3.4: *A photo of part of a PEO coated substrate prepared for single discharge testing. This particular sample was not used for the present work, however the form of sample is identical.*

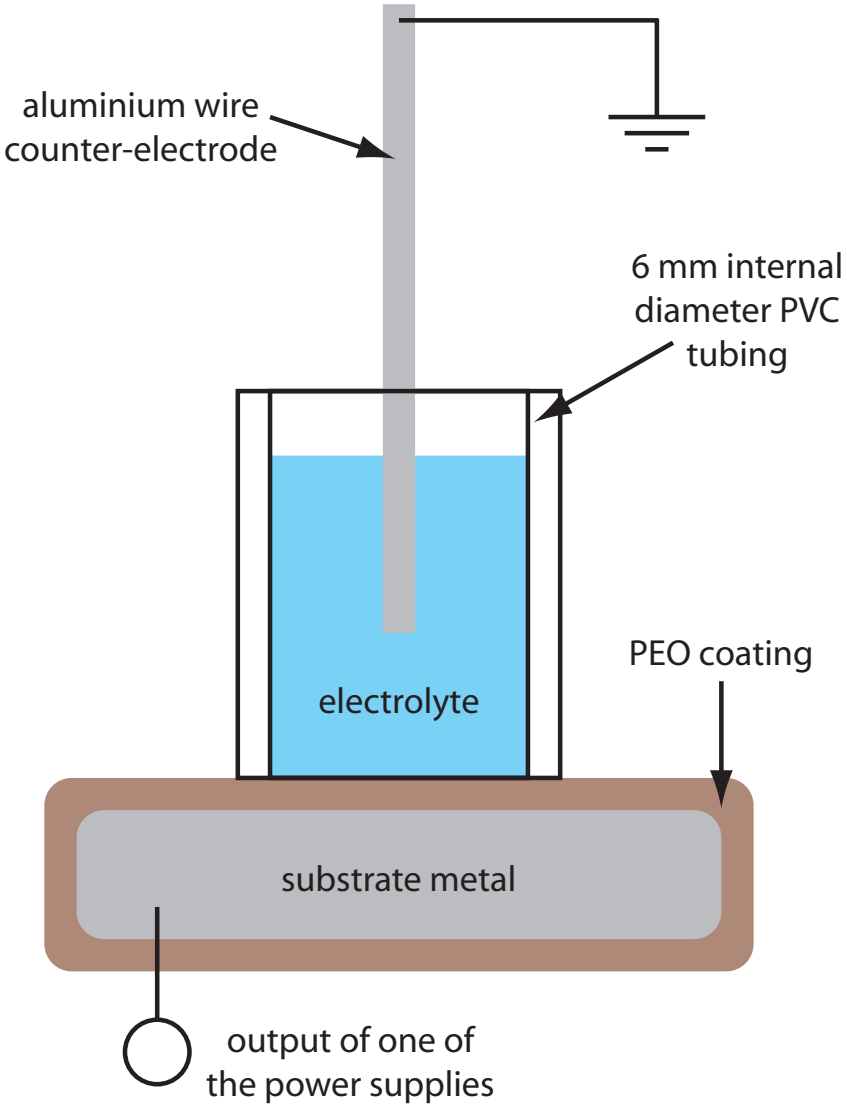

Figure 3.5: *General setup for small area experiments.*

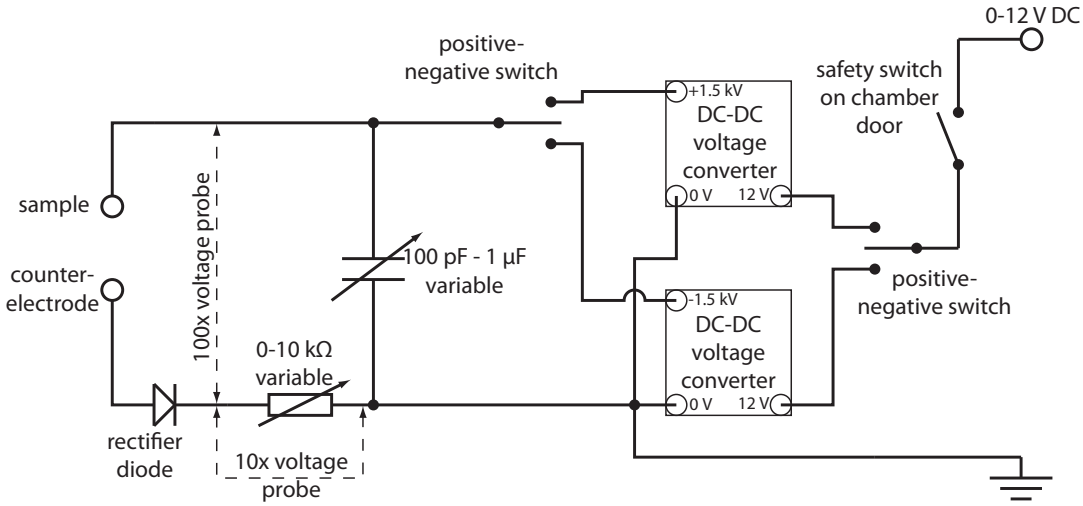

Figure 3.6: *Low power 1500 V power supply used for some of the small area experiments.*

3.3.2 Single Discharge Machine MK I.

Chronologically this supply was the first to be applied, and provided the first measurements of the electrical properties of individual breakdown events. The supply is depicted schematically in Figure 3.6, and inspiration was drawn from the supply used by Kadary and Klein for their studies of discharging towards the end of stable anodising [**11, 12**]. The supply differs from Kadary and Klein in that it is able to operate to potentials of up to 1500 V.

The construction of the circuit is reasonably simple. The DC–DC converter steps up the input 0–12 V to 0–1500 V. The converter output is linearly related to input voltage for input greater then 1.2 V. The capacitor was not a single variable capacitor. A wide range of different capacitances could be installed by plugging them into the circuit. Capacitances in the range 100 pF to 1 μF were available, all were of the ceramic disc and plate design, due to the requirement for the capacitors to operate up to 1500 V.

Voltage was measured with a 100× attenuation probe (Tektronix P5100) connected across the sample. The current was determined by monitoring the voltage developed over a variable resistor placed in series with the sample. The current was then found as $-$V/R with V the voltage, R the resistance and the negative sign due to the location of the scope grounding (both oscilloscope probes had to be grounded at the same voltage). The rectifier diode was not originally part of the circuit, however significant spikes of negative current were seen after the end of each

discharge event, despite positive polarisation of the sample. The diode was included to suppress this behaviour, which was likely a resonance relating to the capacitance and the comparatively large change in current once an event has initiated.

The low power output of the DC–DC converter used, just 1.5 W continuous, meant that the voltage across the sample could not be sustained once an event initiated. The parallel capacitance in the circuit served as a store of charge and energy which could be supplied to breakdown events. Even with a large capacitance in parallel, the terminal voltage on the supply always drops when a breakdown event initiates (see Figure 6.4). This is due to the high internal resistance of the converter, and the large change in resistivity of the load from $> 10^5\ \Omega$ with no active discharge to $\sim 10^4\ \Omega$ when the discharge current peaks (see Figure 5.4). The size of the voltage drop over the course of a discharge event could be reduced by increasing the capacitance, but never totally removed (see Figure 6.4).

The drop in voltage during breakdown events, typically in the range from 8 to 100 V, will naturally have an effect upon the measured electrical characteristics of the discharge events. Initially, the intention was to perform experiments on different coating thicknesses using a series of increasing capacitances, to see whether the measured properties reached limiting values as the capacitance was increased. As will be discussed in chapter 5 and chapter 6, the interpretation of the data was not quite so simple.

3.3.3 Single Discharge Machine MK II.

The second single discharge supply used was a combination of a commercial 650 V, 200 mA supply (FUG Elektronik MCP-140-650MOD) with a simple RC circuit. The circuit is practically identical to the first supply, with a parallel capacitance and a variable resistor to measure the current. The arrangement of the oscilloscope probes was different in this case however, and the voltage over the current monitoring resistor has to be subtracted from the voltage measurement to obtain the potential difference across the sample. The other change is the inclusion of a 50 kΩ variable resistor between the supply and the capacitor. This can be set to prevent the power supply from being overloaded when a breakdown event initiates. The voltage over the sample still drops, however the terminal voltage on the supply remains constant.

The voltage output and current limit of the supply were controlled using an analog controller linked to the signal generator on the Picoscope 5203. The power supply was also safety interlocked via the analog controller. The arbitrary waveform generator on the Picoscope could in theory be used to control the supply voltage output, however in practice the slow response time of the power unit means that control at frequencies more then a couple of hertz is not viable. A limitation with

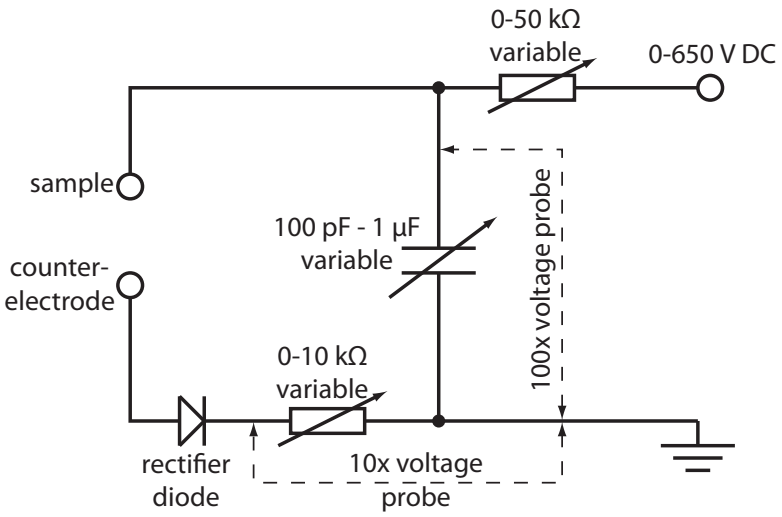

Figure 3.7: *Additional circuitry used in conjunction with a 650 V, 200 mA, power supply used for some of the small area experiments.*

this supply is that it only goes up to 650 V, minus any drop in potential across the 50 kΩ resistor.

3.4 Single discharge experiments performed.

Two experiments will be discussed in this work. The first resulted in a large dataset which will be analysed and discussed in detail in chapter 5 and chapter 6. The second did not result directly in useful data on discharge event properties, however it was required in order to correct the data from in-situ monitoring. As was mentioned in section 3.2, the current probe used electromagnetic induction to generate a signal, and suffered from signal distortion when applied to measuring one-off pulses like the discharge events. By recording the current signals from discharge events more directly without this distortion, and concurrently recording the signal from the current probe with distortion, a correction procedure could be produced.

3.4.1 Coating thickness and test circuit capacitance effects.

This experiment applied single discharge testing to seven different thicknesses of pre-deposited coating. This was to investigate changes in discharging behaviour with variation of the coating thickness. The different capacitances were used as it was initially felt that discharge event properties would saturate at physically limiting values of the system as the capacitance was increased. The actual behaviour was markedly different, and will be discussed in chapter 5 and chapter 6.

6 mins	12 mins	18 mins	24 mins	30 mins	36 mins	42 mins
637 Ω	509 Ω	464 Ω	340 Ω	279 Ω	279 Ω	233 Ω

Table 3.3: *Resistances used for current monitoring during single discharge testing with a range of capacitances and coating thicknesses.*

Samples were produced by coating rectangular sheets of aluminium 2024 alloy, of dimensions 38 by 45 mm and 1 mm thickness. Two samples were coated for each time of 6, 12, 18, 24, 30, 36 and 42 minutes. The substrates were coated using the 50 Hz machine detailed in section 3.1 using an initial RMS current density of 1500 $A.m^{-2}$.

Once coated, the samples were prepared for testing by attachment of 8 sections of PVC tubing to one of the large flat coated surfaces, as described in subsection 3.3.1. Seven wells on each sample were then used for single discharge testing, with a different capacitance for each. The seven values used were 5.5, 14.3, 33.3, 100, 200, 500 and 1000 nF, spaced roughly equally on a base ten logarithmic scale. The 8^{th} test well was used as a test to determine an appropriate setting for the current measurement resistor. The electrolyte used for the single discharge testing was a sample of the electrolyte from the processing tank, which had been stored after all the substrates had been coated.

Each combination of coating thickness and capacitance therefore had two repeats. Each test was conducted for a total period of 60 s after initiation of discharging. The testing was broken down into 10 s segments. During each 10 s segment the current and voltage were recorded at 1 MHz using a Picoscope 5203 oscilloscope controlled from a laptop computer. The data obtained was analysed according to the procedures detailed in Appendix A.

The resistance of the variable resistor used to measure the discharge current was different for each different thickness of coating, details of the test resistances used are presented in Table 3.3. Different values were used to obtain a signal across the monitoring resistor in the range 0–20 V for all thicknesses of coating tested. As will be shown later in section 5.2, these resistances were all well below the minimum resistances of typical discharge events, and so loading effects of the test resistor would not be expected to be significant.

Test wells were only attached to one 38 by 45 mm side of the coated samples, and the other coated side was reserved for microscopy of the coating free surfaces, and sectioning to determine the coating thickness.

3.4.2 Generation of dataset for calibration of in-situ current probe.

The data used to calculate the correction to be applied to the current probe data was generated using the power supply detailed in subsection 3.3.3. The electrolyte used was the same electrolyte as for all other experiments. The test coating used was a 153 by 101 by 1 mm aluminium 1050 sample, coated for 10 minutes. It was a spare from a different experimental set, the results of which will not be included in this work. Three of the test wells on this sample were used to generate calibration data.

Recording of data was at 500 kHz, for 5 segments of 20 s each, and for each of the three test wells used. One channel of the oscilloscope recorded the voltage over the variable resistor, set to 200 Ω, the other channel recorded the data from the Tektronix P6021 current probe. Four loops of the signal wire, in series with the measurement resistor, were passed through the current probe. This was in fact the exact same coil as was used for in-situ monitoring experiments.

This dataset then comprised two sets of measurements of the same current signal. The current measured from the variable resistor had no distortion, and was compared to the current probe data to produce a correction function for the in-situ data. The procedure for this is discussed in Appendix B.

3.5 Microscopy and sample preparation.

3.5.1 Cold mounting of samples

Cold mounting was used for two purposes. Firstly to mount samples for sectioning and microscopy, and secondly to create the samples for in-situ discharge monitoring experiments. In both cases the system used was a commercial 2 component liquid acrylic resin sold under the brand name Epofix. The two liquids were mixed in disposable plastic beakers inside the hood of a fume cupboard. The pot life of the mixture is long, as the resin takes ~ 24 hours to cure at room temperature. The resin is transparent when set, and shows low volume contraction upon curing. The samples to be embedded were placed inside pre-greased rubber moulds for easy extraction of the set samples. When the sample was to be used for microscopy, the moulds were placed inside a sealed container and cycled between atmosphere and vacuum several times to remove air bubbles in the resin that were introduced while stirring the resin mixture.

3.5.2 Hot mounting of samples.

When the samples to be mounted were not likely to be damaged by heat or suffer from significant thermal mismatch with the mounting resin, hot mounting presses were used to mount samples for examination. The presses used were a Buehler Metaserv and a Buehler Simplimet, and the powdered resin used was either transparent or conducting, depending upon the requirement for the specific sample.

3.5.3 Sample sectioning.

When it was required to cut a section through a sample mounted for microscopy, this was performed using a Struers Secotom-10 precision saw. Typical cutting speeds in the range $0.005 - 0.03\,\mathrm{mm.s^{-1}}$ were used, with a 2200 RPM alumina wheel of thickness ~ 1 mm. The saw had a computerised micrometer mount for accurate positioning of the sample prior to sectioning. The same saw was used to cut 3–4 mm off the ends on samples for in-situ monitoring between experiments, to expose a fresh surface for subsequent experimental runs.

3.5.4 Polishing procedures.

Polishing procedures vary much depending upon the application and personal preferences. It was found that the following procedure provided adequate surfaces for microscopy. The samples were first ground with SiC papers, starting with 500 grade; then 800; then 1200 and finally 4000 grade. Between moving to the next grinding stage the samples were briefly inspected by optical microscope to confirm the removal of large scratches from the previous stage. Following grinding, the samples were polished using first 6 μm and then 1 μm diamond suspensions, applied to the polishing cloth in aerosol form. Soft polishing cloths were not used, owing to the tendency for the softer substrate to be preferentially removed by the polishing, meaning the coating and substrate were not at the same height. Alcohol based lubricant was used for polishing, and water for the grinding stages.

3.5.5 Optical microscopy.

Optical microscopy was performed using Olympus BHM and Zeiss Axiolab microscopes, each fitted with a Moticam 1000 digital camera connected to a PC. Determination of scales in the images was performed using images captured with the same systems of a calibration graticule.

3.5.6 Scanning electron microscopy.

Free surfaces of coatings were examined by scanning electron microscopy in secondary electron mode. A JEOL 5800LV SEM and a JEOL 6340F FEGSEM were used for this purpose. No complications to usual SEM procedures were experienced, with the exception of samples embedded in cold mounting resin (such as the in-situ samples). Such samples required exposure to vacuum in a separate system for up to 24 hours prior to examination by SEM, in order to thoroughly outgas any residual volatiles.

3.6 Processing of data.

A major challenge in this project was to develop computer procedures to reliably identify and measure the discharge events recorded during experimentation. In total across both in-situ and single discharge experiments approximately 5 million individual discharge events were measured, this quite clearly was not done manually! As with any automated data analysis, it is important to understand how reliable the analysis is, and what the limitations may be. However, the general reader may not be interested in the precise functioning of the algorithms used. To this end a brief description of the functions of data handling algorithms will be given here, along with a few figures to illustrate the algorithm functions. A detailed discussion of each part of the data processing is provided at the end of this text in Appendix A for single discharge data and Appendix B for in-situ monitoring. The procedures were different due to the baseline correction required for the current probe data from in-situ experiments.

3.6.1 Analysis of single discharge data.

A sample of the single discharge data obtained is presented in Figure 3.8. The short lived current peaks corresponding to discharge events can be clearly seen, separated by periods of low baseline current ($\sim$ 1 mA). The slight decrease in voltage over each event can also be seen in the figure. One of the events appears to be a superposition of at least two current peaks. Such multiple peak events probably correspond to two spatially separate discharge events that happen to overlap in time. Such multi-peak events were common for some combinations of low coating thickness and high circuit capacitance.

For analysis of discharge event properties, it is desirable to only consider events comprised of a single current peak. To this end, the computer processing is required to outline not just the start and end points of discharge events, but also the number

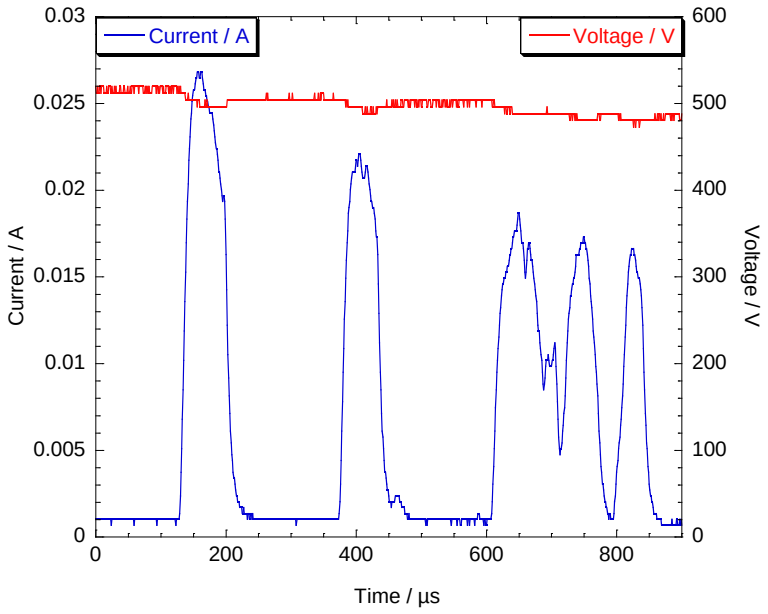

Figure 3.8: *Sample current and voltage data from single discharge experiments, taken from an 18 minute coating tested with 200 nF circuit capacitance.*

of discrete current peaks within each event. Detailed discussion of the procedures used can be found in Appendix A.

Procedures were developed which allowed for the automated estimation of the baseline current level, I_{base}, and a current threshold value, I_{shift}. These were used to identify regions of interest. These regions of interest were expanded by a combination of procedures involving local current, voltage and current gradient thresholds, until discharge events were indexed from initiation to termination. The discharge locations were indexed in a vector, G, which took the value 1 if that sample was part of a discharge event, and 0 otherwise.

Two values of importance are I_{step} and V_{step}. The data recorded by the oscilloscope is 8-bit, meaning that only 127 distinct values can be resolved between 0 and the maximum range set. The variables I_{step} and V_{step} then represent the minimum detectable shift in current or voltage respectively. V_{step} was 7.87 V for all data, and I_{step} varied with the size of resistor used, according to the expression $I_{step} = (20/127)/R$, with R the resistance used. The value of 20 is present as the current data was recorded from 0–20 V across the measurement resistor.

The positions of internal peaks and troughs within each outlined region were indexed in the vector F. This variable took the value 1.0 at current peaks, and 0.5 at troughs. A peak, or trough, was defined relative to the scale of the event in question. If the maximum current during an event is I_{max} and the minimum I_{min},

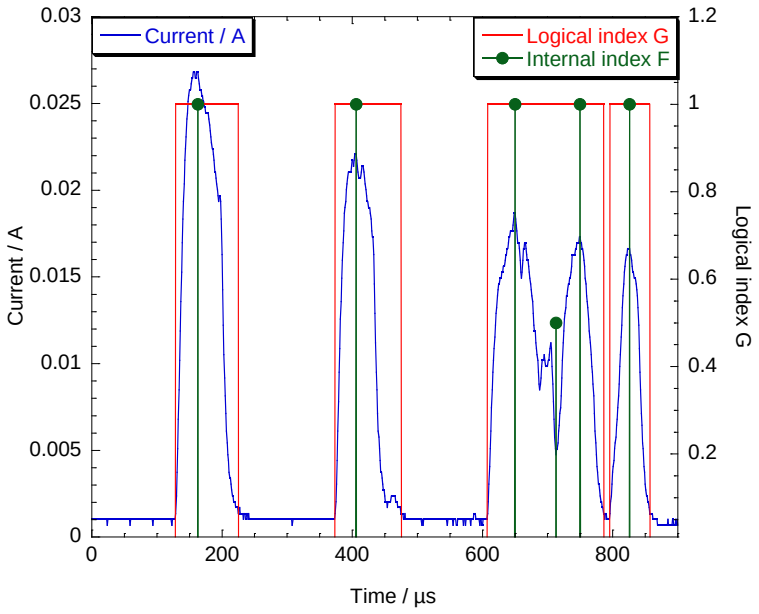

Figure 3.9: *The representative section of experimental data, showing current, logical indexing vector G and internal peak indexing vector F.*

then the scale of variation required for a peak or trough to be identified was the larger of $0.2 \times (I_{max} - I_{min})$ or $5 \times I_{step}$. The final results of indexing procedures are demonstrated for the same section of data as in Figure 3.8 in Figure 3.9.

Once events had been indexed and listed, measurements could be made of the discharge event properties. The data was first separated into two lists, one contained all indexed discharge events, the second only events comprised of a single current peak. It is primarily the latter dataset which will be of interest. Important measurements that were made included the peak current, I_{peak}; the initiating voltage, V_{init}; the duration, d_{sing}; the peak power, P_{peak}; the charge, Q_{sing}, and energy, E_{sing}, associated with each event. The charge and energy were calculated from trapezium rule integration over the event duration, and the baseline current was subtracted from the current values prior to any calculations. Other measurements were made, and are detailed in Appendix A, however those mentioned in this section are those of greatest interest.

It should be borne in mind that no events were included which showed a value of I_{peak} less than $5 \times I_{step}$. Also, the minimum error on currents is I_{step}, on voltages is V_{step} and in time, the indexing is not accurate to more than plus or minus the sampling interval of $\delta \mathrm{t} = 1 \times 10^{-6}$ s.

3.6.2 Analysis of in-situ monitoring data.

Procedures for the in-situ data are broadly similar, as the events being indexed are essentially the same. Before any events can be indexed however, the signal from the current probe must be corrected for the distortion of the baseline level. The data obtained as described in subsection 3.4.2 was used to directly calculate a frequency response function relating the signal from the current probe to the actual current (as measured by the voltage over the 200 Ω resistor). The discussion in this section will not go into many details, and the interested reader can find a complete description of the data processing for in-situ experiments in Appendix B.

The current peak associated with a discharge event can be viewed as a wave-packet, and as such it will contain amplitude across a wide range of frequencies. Some of the signal amplitude will be at frequencies below the frequency cut off of the current probe, and it is the distortion of these low frequency components which leads to the distortion of the signal. Once the frequency response had been calculated using the calibration data, the current probe signal from each process cycle could be readily corrected.

This involved isolating the period of positive polarity during each cycle in the in-situ monitoring records, then applying the fast Fourier transform to compute the discrete Fourier transform of the current data. The current signal in the frequency domain is then multiplied at each frequency by the corresponding value of the frequency response function. Application of the inverse Fourier transform brings the signal back into the time domain.

An example of the correction procedure, as applied to a section of the calibration data (so the corrected current can be compared to the resistor based measure) may be found in Figure 3.10. The current measured from the resistor and from the current probe are both plotted, as is the corrected signal from the current probe. The agreement seen is good, but of course it is far from perfect, and this leads to a greater level of uncertainty when compared to the single discharge data. On the other hand, the in-situ data is a closer analogy to actual PEO processing, and so the data obtained is more representative than that from single discharge experiments.

An example of the in-situ experimental data, and the corrected small area current, is plotted in Figure 3.11. There does appear at first to be a slight problem with the correction, in that the data seems to be superposed on a low 'hump'. This 'hump' is real however, and probably corresponds to a non-discharge component of current (see Appendix B). The rough signal in the region preceding the large discharge events is not noise, and typically is only present in the early part of each process cycle. It could be small discharge events that are poorly resolved using the parameters used for the bulk of the in-situ work. The presence of very small dis-

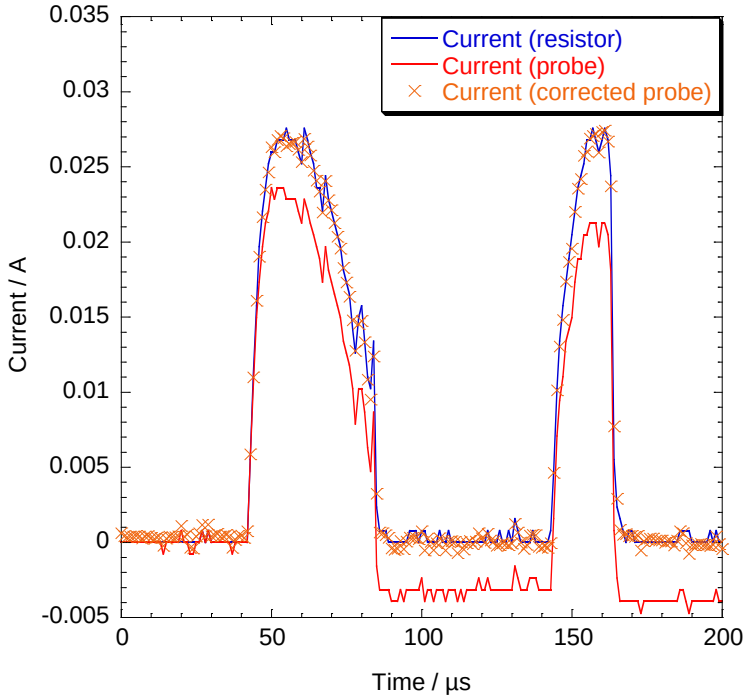

Figure 3.10: *Section of calibration data showing the current measured via a known resistance, using the current probe, and the corrected current probe signal.*

charges, and discharges during negative polarisation of the sample, will be discussed in section 4.3 and section 4.4 respectively.

Once the baseline level has been corrected, a series of routines broadly similar to the single discharge case are applied to identify the discharge events and measure the relevant properties. The indexing of the large events seen in Figure 3.11 can be seen in a zoomed-in view in Figure 3.12. The internal indexing of multiple peak events is also performed, though multi-peak events were rarer than for the single discharge experiments. This is probably a result of the much smaller area being monitored in this case.

The event properties are then calculated from the indexed discharge events. The same properties as were outlined in subsection 3.6.1 were calculated for in-situ monitoring data, and the data was again broken down into all events, and the subset which displayed a single current peak. One important difference is in the range of events included; only events which exceeded 10 mA base to peak were included. This was because the hump like feature during every cycle, when combined with the error incurred from the correction procedure, meant that a reliable indexing of events smaller than about 6–8 mA was elusive.

The bar was set at 10 mA for safety, operating under the principle that it is

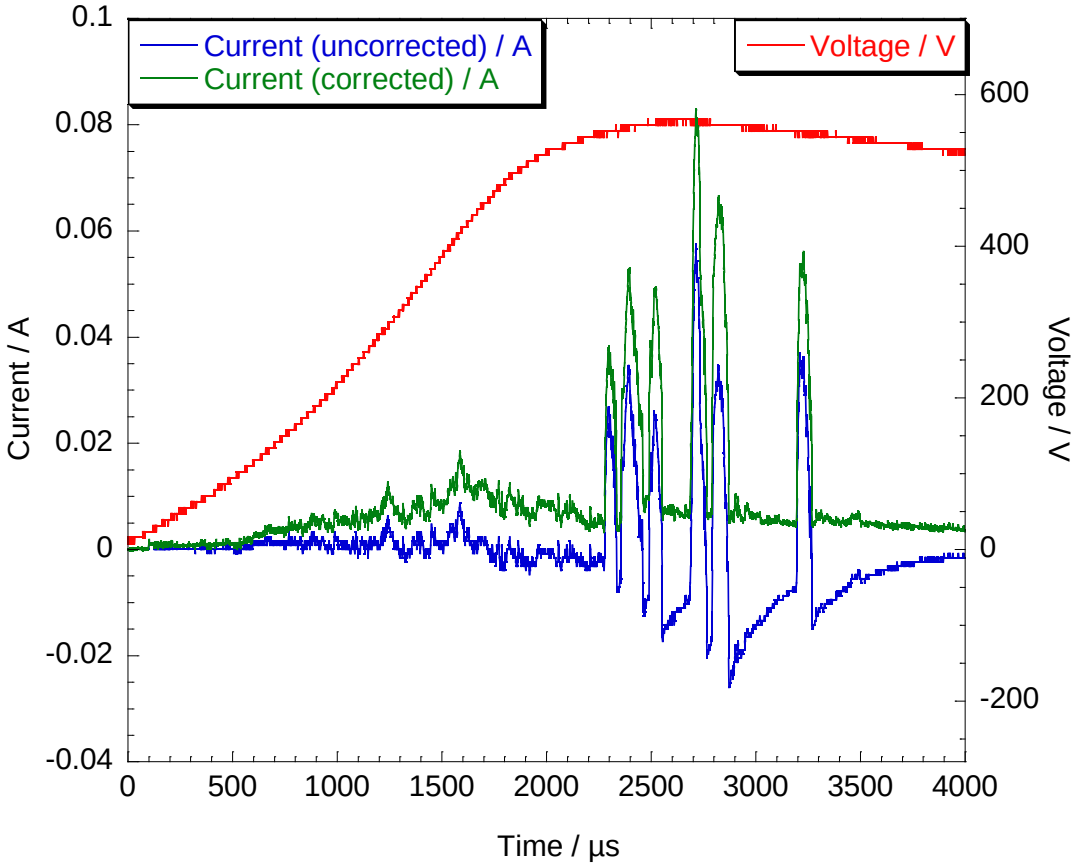

Figure 3.11: *Comparison of the uncorrected and corrected current signal for one processing cycle. Note that the full period of positive polarity is not displayed to allow better resolution of discharge features during the active period.*

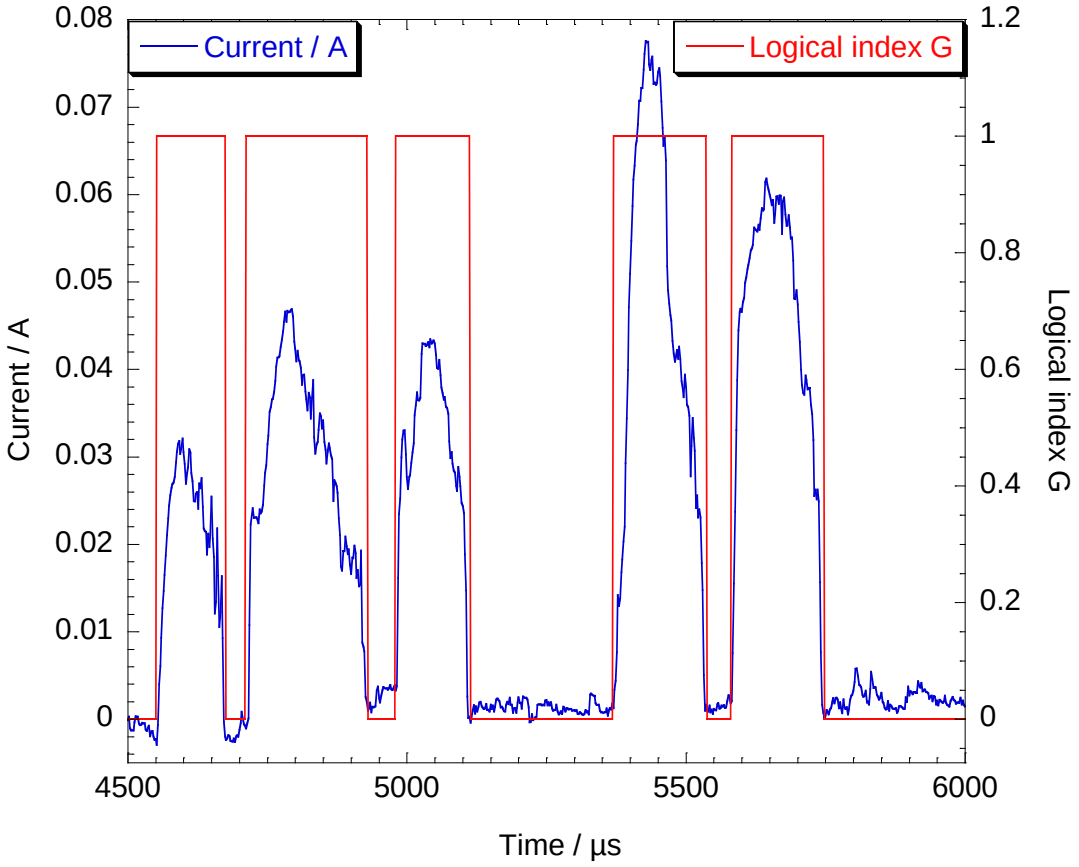

Figure 3.12: *Example of the completed indexing for a zoomed-in section of the example cycle from Figure 3.11.*

better to be able to trust a reduced range of application than to leave coverage wider but unreliable. The reader should not forget though that the in-situ data reported only relates to events larger then 10 mA. This is not an inherent limit, and with small changes to this methodology the coverage can be extended down to smaller discharge events. Some steps in that direction have been taken, and will be discussed in section 4.3.

3.6.3 Averaged development profiles of discharge events.

The average current at times after the initiation of a discharge event was also calculated, for both single discharge and in-situ data. The calculation of average current development profiles was broken down by initiating voltage and duration. For example, if we wanted the average current profile for an event initiated at 520 V, which lasted for 50 μs, the algorithm would locate every discharge event which met those two criteria. Then for every time point between initiation and termination it would calculate the mean and standard deviation of the current at that time point after initiation, using all the events which met the criteria as a sub-dataset. This allows a reasonable measure of the average 'shape' of discharge events to be estimated.

As mentioned previously this was done for each combination of V_{init} and d_{sing}. This was performed for both the current and the voltage during discharges, and corresponding standard errors were also calculated. Full details may be found in Appendix A, and examples of the procedure output will be presented and discussed throughout chapter 6.

Chapter 4

Evolution of Discharge Events During Coating Production.

4.1 In-situ monitoring with scaling of monitored area.

The results of in-situ monitoring experiments can provide much information about the process, however it must first be considered just how representative the data from the small area can be of the wider PEO process. To this end, before the results of individual discharge measurements are presented, the processing of the small area will be discussed in more conventional terms.

4.1.1 Coating development on the small area.

As the small area was processed to longer times, the coating increased in thickness as is normal for PEO processing. What was different was that the scale of the small area exposed to processing was not constant. This arose from the progressive failure of the resin in which both small and large areas were mounted.

At the edges where the substrate was in contact with the resin, any discharge event which occurred would cause local destruction of the shielding resin. This would in turn expose more of the substrate wire to the electrolyte. An example cross section can be seen in Figure 4.1. The destruction of the resin and the penetration of processing down the sides of the substrate are evident in the figure.

It is worth noting that whilst the polymeric resin failed in this fashion, it has better performance than might be expected. A chemically setting and low temperature curing ceramic cement containing TiN was also tried (Ceremabond 865 from Aremco). Though such a material has a higher operating temperature (1923 K), and so might be expected to perform better than the resin, the thermal shocking

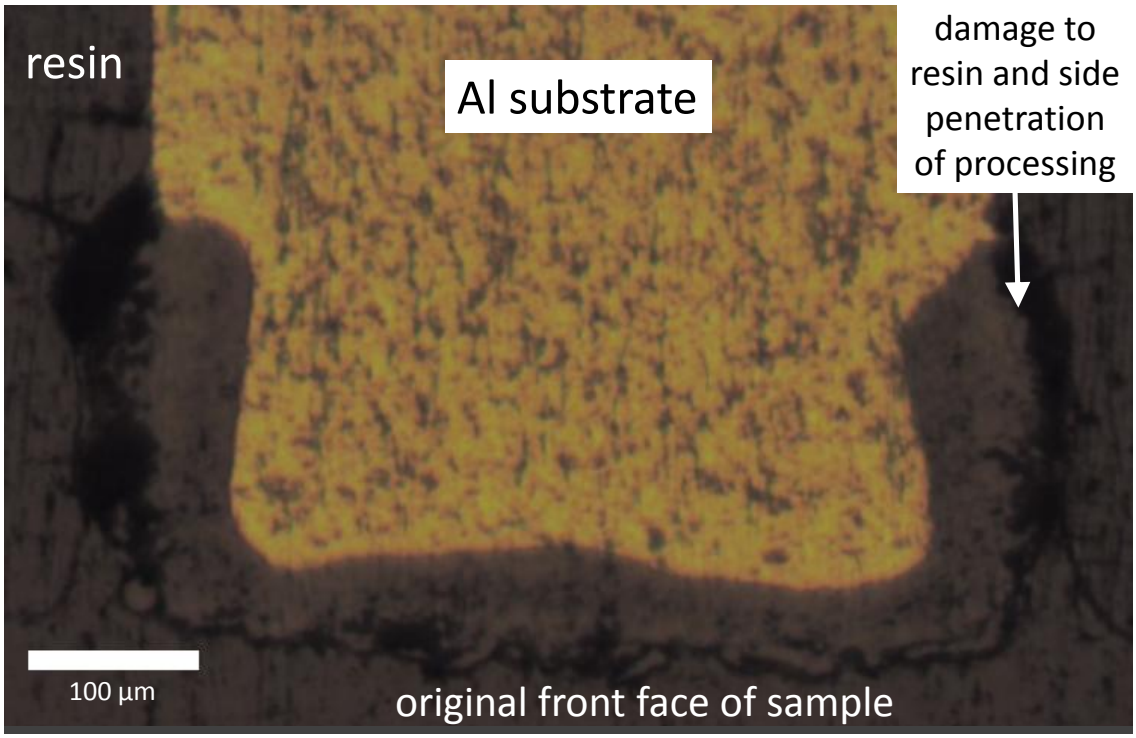

Figure 4.1: *One example of the sectioned small area after 15 minutes of processing. Obtained from optical microscopy of a polished cross section.*

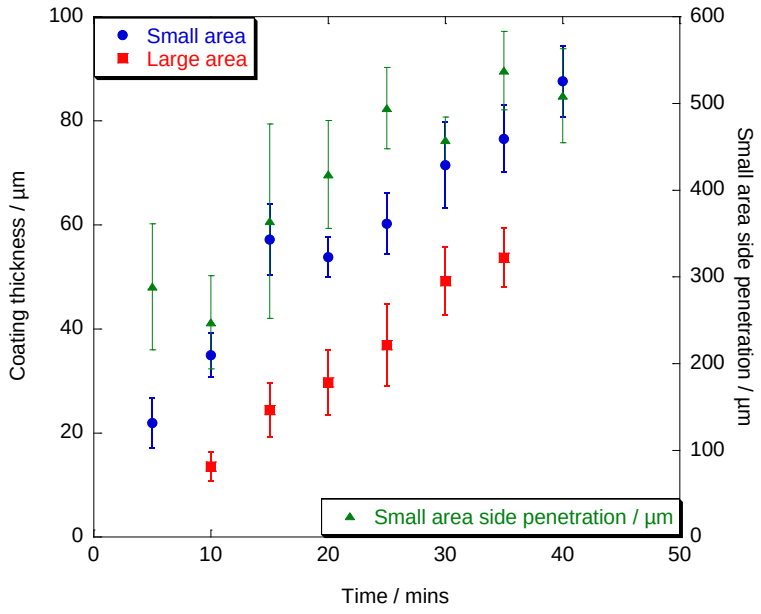

Figure 4.2: *Development of coating thickness on small and large areas with processing time. Determined from examination of polished optical cross sections.*

associated with the discharging behaviour caused the ceramic shielding material to rapidly fail by cracking.

4.1.2 Thickness development and surface appearance.

As samples were sectioned for every 5 minute period of processing up to 40 minutes, the development of the coating thickness on the small and large areas can be determined and compared. The progressive failure of the sample shielding can also be examined. These properties are plotted in Figure 4.2. The small area coating thickness seems to develop at a slightly faster rate than the thickness on the large area at long times, but the main discrepancy is within the first few minutes. The thickening rate in the very early stages of processing must therefore be significantly larger for the small area. Both thicknesses display the linear coating growth expected for 50 Hz PEO processing, as was discussed in subsection 2.3.1.

The progression of shielding side penetration is less regular than that of the thickness, but still shows a clear trend with coating time. The initial period of processing again shows faster progression. A linear fitting to the side penetration data can then be used to estimate the total size of the small area exposed to the electrolyte, being the original area plus the additional area in the form of a cylinder exposed by degradation of the resin shielding.

Before moving on to utilise the small area variation estimate, the surface appear-

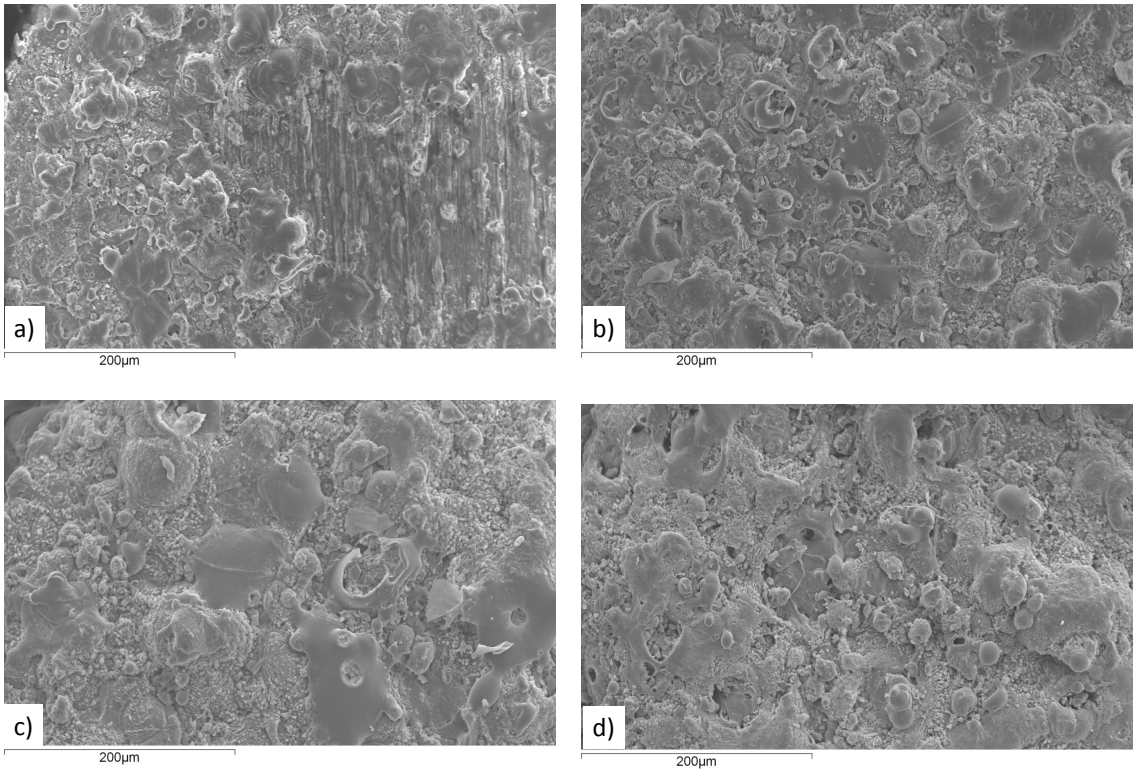

Figure 4.3: *SEM images of the coating free surfaces after a) 5, b) 15, c) 25 and d) 35 minutes.*

ances of the PEO coatings deposited on the small monitored area shall be briefly considered . SEM images of the coating free surface are presented in Figure 4.3. The surface morphologies are seen to be typical for PEO processing of aluminium.

4.1.3 Comparison of charge delivered to small and large areas.

The surface structures are typical of PEO coatings on aluminium (see subsection 2.3.2). How representative the small area is of the bulk processing of the wider sample is yet to be made clear. This can be examined by using the estimates of total exposed area, derived from a linear fitting to the progressive shielding penetration plotted in Figure 4.2. The charge delivered per positive cycle, per unit area, for both the small and large areas is plotted in Figure 4.4. This figure was compiled from averaging across all the samples in the set Al_01 to Al_05, and all experimental runs (see subsection 3.2.1). Average values for each 150 s process section are what is plotted. Large area charge delivered was calculated from the experimental runs which logged bulk current (see Table 3.2). The charge per cycle per unit area is

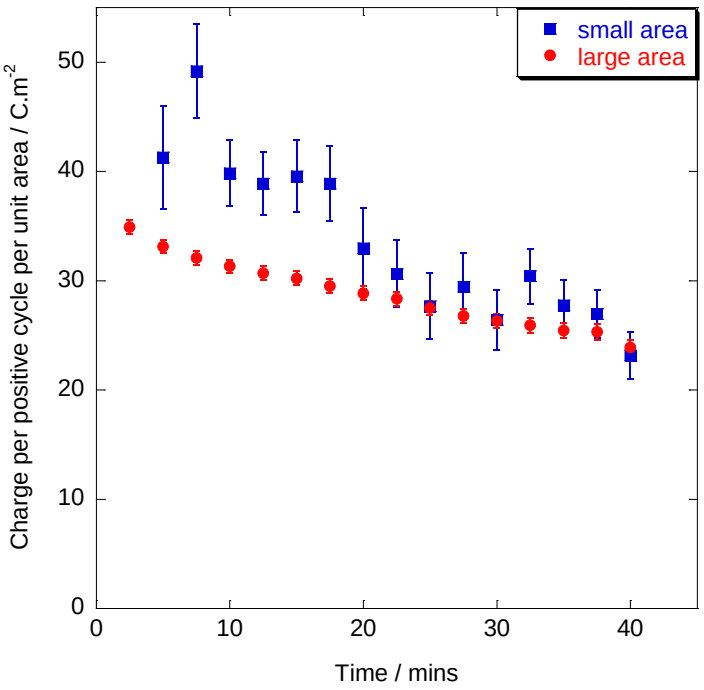

Figure 4.4: *Plots of the charge per positive cycle per unit area delivered to small and large areas.*

elevated for the small area at all times, and is particularly pronounced for about the first 20 minutes of processing. This appears to be in good agreement with the relative thickening rates observed.

From the consideration of thickening rates in Figure 4.2 and charge delivered in Figure 4.4, is is apparent that the small area is not entirely representative of the bulk processing behaviour. However the information indicates that what is seen on the small monitored area represents PEO processing at a current density that is slightly enhanced with respect to the rest of the substrate.

4.1.4 Cumulative charge of indexed discharge events.

An important test of whether the data can be taken as representative of the wider sample is whether or not the discharge activity seen scales with the size of the monitored area. We would expect that the discharging activity on the samples Al_03 and Al_04 with two 500 μm wires as small area would be approximately twice that seen for the samples with only one wire, Al_01 and Al_02. The sample with three wires, Al_05, would be expected to show approximately three times the activity.

One way to visualise the discharging activity is to plot the cumulative charge

delivered by indexed events against the time of processing. This may be done for each distinct experimental run. No two experimental runs are the same, as at any given point the discharging occurs in a stochastic and unpredictable fashion with such small areas. However when many experimental runs are plotted in this fashion, as in Figure 4.5 and Figure 4.6, the overall trends become more evident.

In can be seen most clearly in Figure 4.5 panel a) that discharging activity on a small scale does not occur in a continuous fashion. Rather it occurs in interspersed periods of high and low discharging activity. This can also be seen in the samples with 2 or 3 wires as the small area However the larger area being monitored increases the probability of one of the sampled areas being active at any given point. This leads to cumulative charge plots which are more continuous in appearance and which appear to show less variation between experimental runs.

Panel b) of Figure 4.6 plots the averages of all continuous experimental runs for each of the 1 wire, 2 wire and 3 wire samples. The average plots for 2 and 3 wire samples are also plotted normalised by division by a factor of either 2 or 3 as appropriate. From the normalised plots it can be seen that with two wires as the small area, the cumulative charge in discharges increases approximately twice as rapidly, and with three wires the rate of increase is tripled. This is not exact however, and the 2 wire normalised plot is higher then the single wire average. The triple wire data is again slightly above the double wire values. This slight enhancement over that expected is possibly due to edge effects, known to increase discharging intensity around the edges of samples.

4.1.5 Discharging rates.

The data on cumulative charge with processing times appears to support the conclusion that the discharging activity scales with the area being monitored. Further evidence is provided by analysis of the overall rates of recorded discharges, plotted in Figure 4.7. This demonstrates that the discharge activity seen does scale with the size of the area monitored.

When combined with the information in Figure 4.2 on thicknesses and Figure 4.4 on the charge transfer per process cycle, it is possible to state that the information gathered from in-situ monitoring of a small area can be taken to be representative of the wider bulk processing. Subject of course to the condition that the experiment be repeated a sufficient number of times, due to the stochastic nature of the discharging behaviour.

Having demonstrated that the discharging activity scales with the size of area monitored, no distinction will be made in the following discussions between data obtained from experimental runs with single, double or triple wire samples. All

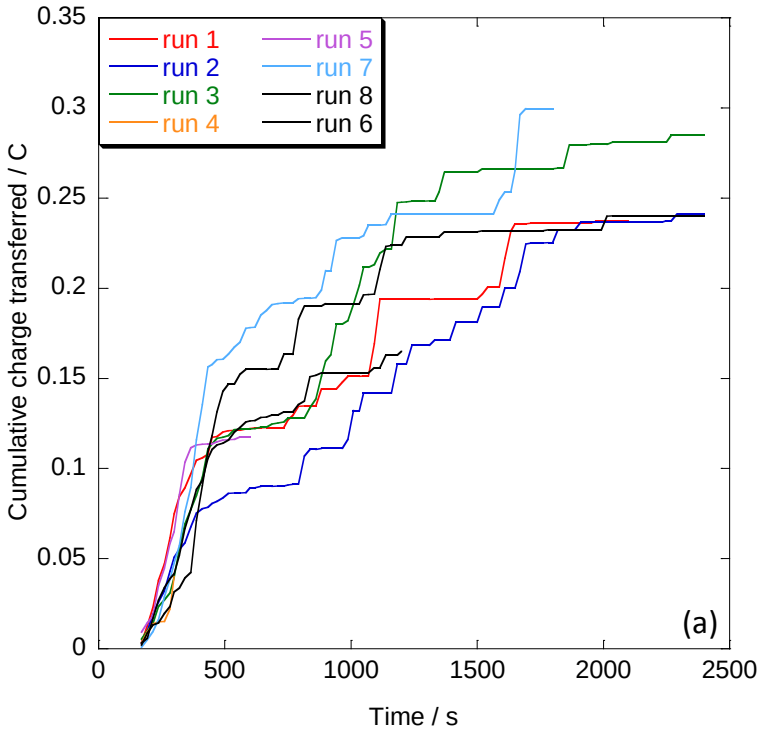

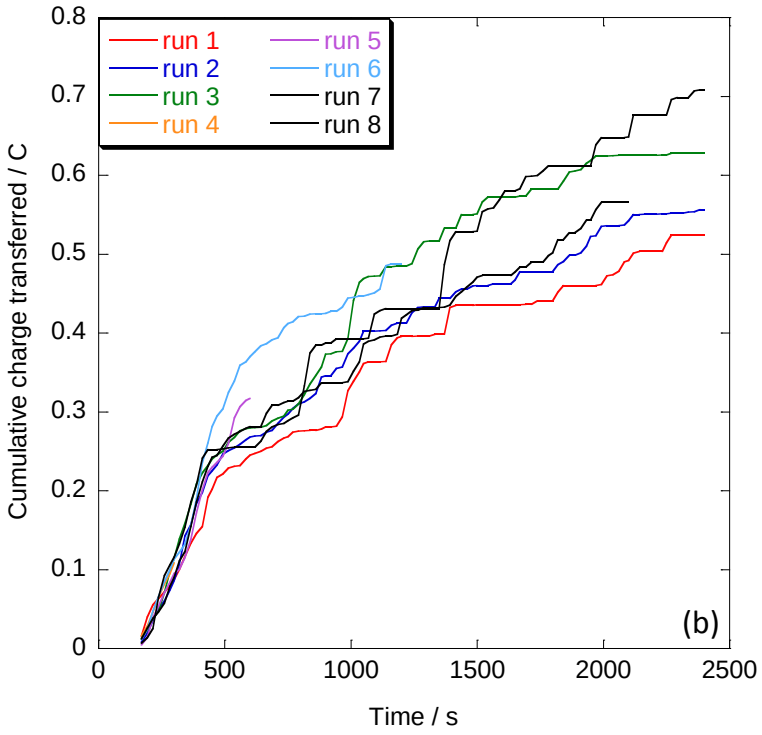

Figure 4.5: *Cumulative charge delivered by indexed discharge events for multiple experimental runs for (a) 1 wire samples and (b) 2 wire samples.*

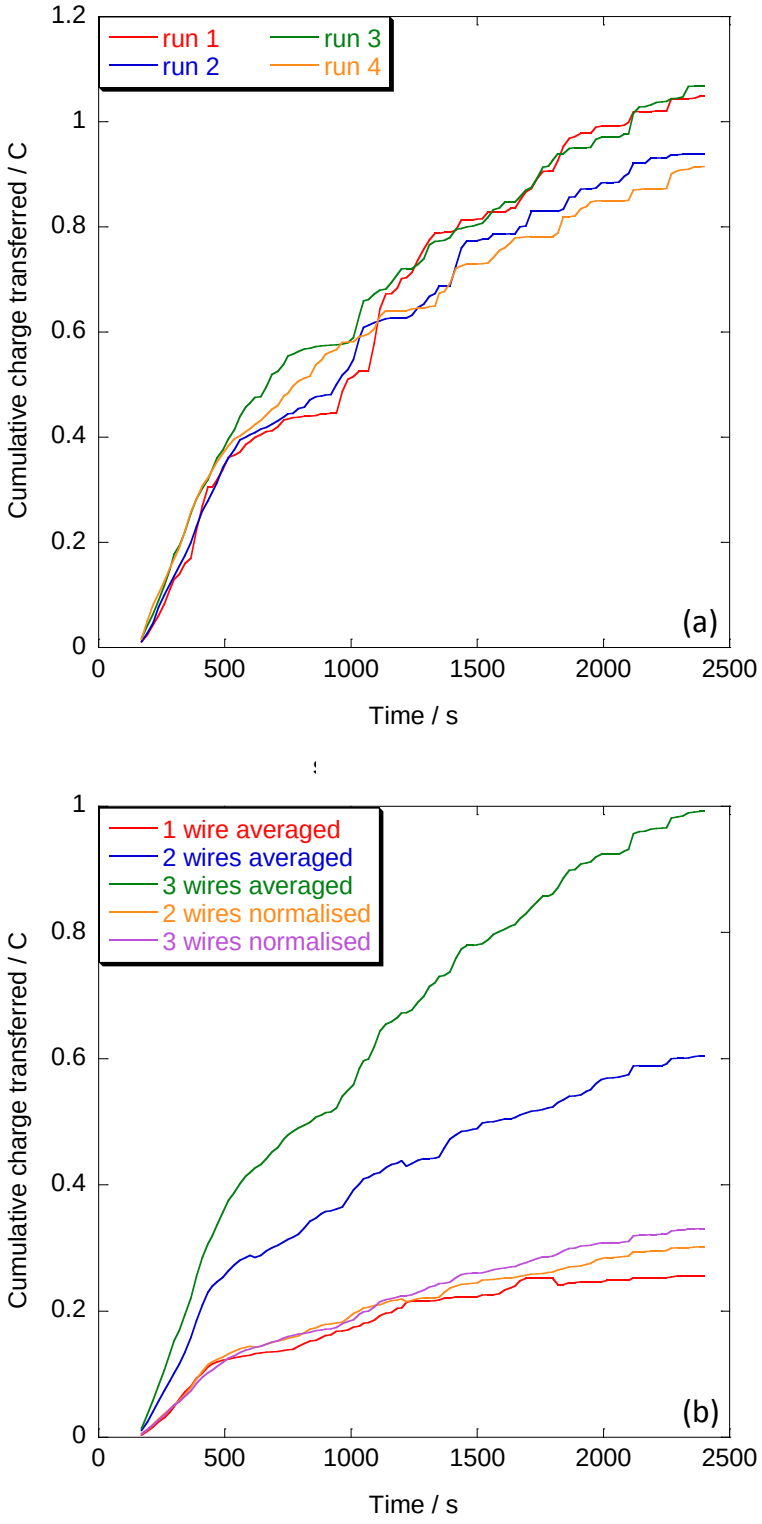

Figure 4.6: *Cumulative charge delivered by indexed discharge events for multiple experimental runs for (a) 3 wire sample and (b) sample averages and normalised plots.*

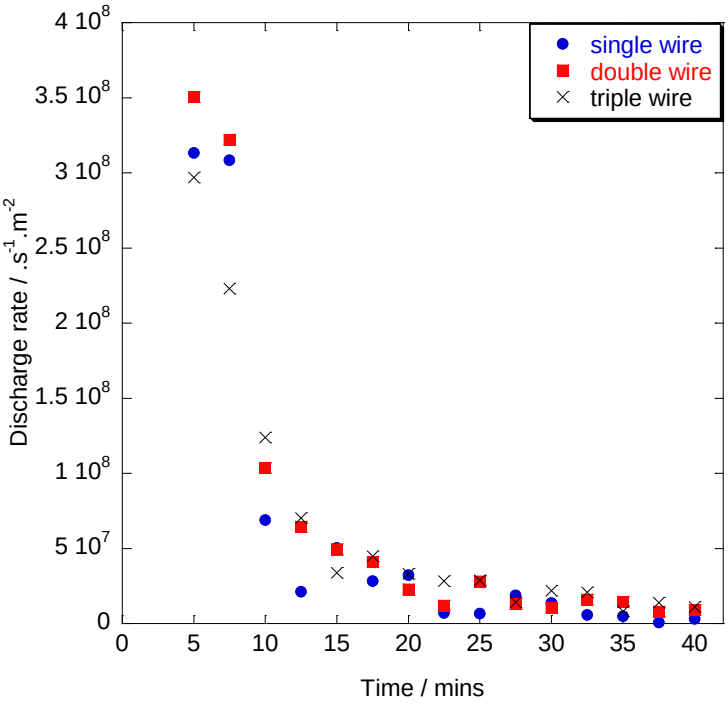

Figure 4.7: *Average discharging rates as events per unit time per unit area for in-situ samples with a single, double or triple* 500 μm *wire as the small area. Rates are an average of the total number per unit time over the 2.5 minutes prior to the marked point.*

events recorded at a certain time into processing will be taken together to be representative of that time period, once they have been combined to produce average values and distributions.

Before proceeding to discussion of the single event properties, it is worth placing the discharging rates per unit area plotted in Figure 4.7 within the context of the literature values for discharge rates. The rates derived from low speed optical imaging studies are found to be a factor of ten lower than in the present work at equivalent durations of processing [**2, 7, 8, 9**]. This is probably because the imaging speed in these works was insufficient to capture the discharging behaviour accurately when clustering of discharge events in considered.

For some of the alloys they tested, the data from the high speed study of Arrabal et al is in order of magnitude agreement with the present work, at around 10^8 $m^{-2}.s^{-1}$ [**5**]. Values up to the order of 10^9 $m^{-2}.s^{-1}$ were reported in the same work, and this shows that the difference between different substrates could be pronounced in some cases.

4.2 Properties of individual events recorded during in-situ monitoring of the PEO process and variation with processing time.

The properties of events seen at any given point in time were observed to vary over a wide range. Given this, to calculate mean event properties would be to omit most of the important details of the discharging behaviour. The rates of discharging behaviour were also decreasing with processing time. In order to account for the variation of event properties seen at any time, for the statistical spread of measured properties and also for the variations in discharging rate, a specific form of plot will be used to present the single discharge data.

These plots will be of the 10^{th} to the 90^{th} percentiles of the data in each time region. The width of time regions will vary to ensure that there are 50 000 measured events during each time region. The plots will be in the form of step plots, which make the width of each time region clear, in addition to the value of the relevant percentile of the measured event property at that time.

At no time should the reader forget that the measured properties refer only to those events which exceeded 10 mA from base to peak, and for which the data was processed as described in Appendix B. Furthermore, whilst 2 666 611 events were indexed in total across all experimental runs with the samples Al_01 to Al_05, only 2 351 508 were in the form of individual events which occurred during process

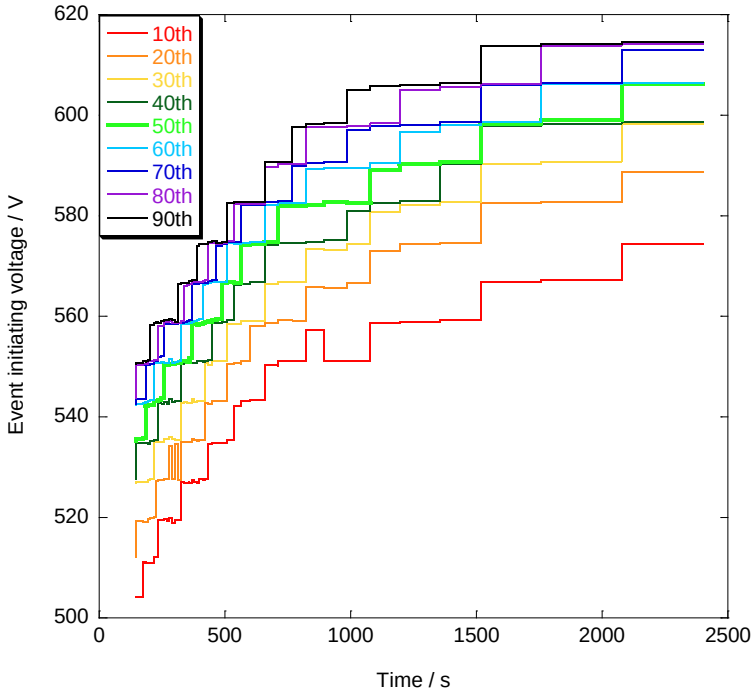

Figure 4.8: *Variation of the distribution of V_{init} with time of processing. Variable step length indicates the diminishing rate of discharging.*

cycles in which the current probe signal was less then the maximum range. These represented 98.53% of all single peak events, the remaining 1.47% having occurred during process cycles in which the maximum current range set on the oscilloscope (100 mA) was exceeded. Current data from such cycles could not be properly corrected for the baseline distortion due to truncation of one or more peaks.

4.2.1 Event initiating voltages.

The event initiating voltages, V_{init}, will be considered first, and the distributions can be seen plotted in Figure 4.8. The step-like appearance of this plot is due to the 8-bit nature of the original voltage data, with $V_{step} = 7.87\ V$. At all times the shape of the distribution is seen to be asymmetric, with greater width down to lower voltages, and rapid drop off in the distribution above the median.

The rate of increase of V_{init} slows between 700 to 1000 s into processing. At about the same time the width of the distribution is seen to increase. Whether these slight changes in the V_{init} distribution are significant is hard to say, as it cannot be determined from this data alone whether the changes are due to the processing or the equipment used.

What is clear from the V_{init} distributions presented in Figure 4.8 is that discharge

events are initiated across a range of applied voltages at all times of processing. This distribution moves upwards in voltage as the coating thickens, but as can be seen from comparison with Figure 4.2, this increase is not in proportion to the coating thickness.

4.2.2 Discharge event peak current.

The peak current reached by discharge events, I_{peak}, is a key measure of discharge scale and intensity. It also offers an opportunity for comparison with the literature records. The distributions of I_{peak} with processing time are plotted in Figure 4.9. The distributions are seen to be relatively broader than for V_{init}, with a noticeable shift in both distribution width and median value around 700 to 1000 s into processing. Beyond 1000 s there is no significant increase in the median value of I_{peak}, with the only change being a gradual widening of the distribution.

This shift in the distribution occurs at around the point in processing when it was observed that the visual appearance of the processing undergoes a noticeable change. The change seen through this period is from a blue-white appearance of the discharges to a more orange-yellow character. Such a transition has often been reported in the literature [**2, 7, 9, 16, 17**]. Whether the shift in the median and distribution width of the discharge peak event currents is related to such an apparent change in visual appearance is not possible to say conclusively.

One point of interest from Figure 4.9 is that the low current end of the I_{peak} distribution never shows any significant increase over the duration of processing. It should also be remembered that the distribution has been artificially curtailed at 10 mA, and so probably continues down to lower values of the discharge peak current for all times. The implication of this is that whilst the largest discharges, and the discharges on average, show increased current as the coating thickens, the smallest events remain of a similar scale throughout.

The range of currents seen in Figure 4.9 is from the cut off at 10 mA up to 110 mA. Referring back to Table 2.2, such values are in agreement with quoted literature values for the scale of discharge currents [**10, 13, 19, 23**]. The advantage of the in-situ monitoring dataset over the literature values is that the present work provides much more information than just an order of magnitude. The great variety of values seen at all process times underlines the requirement for datasets of PEO discharge properties to be presented as statistical distributions, based upon large numbers of measurements. In fact examination of Figure 4.9 suggests that still further repeats would be of value.

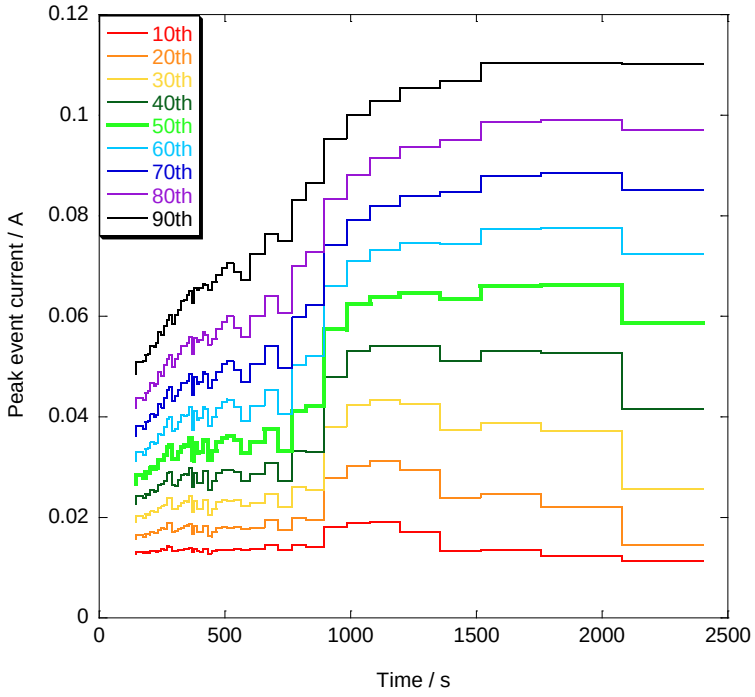

Figure 4.9: *Variation of the distribution of I_{peak} with processing time.*

4.2.3 Discharge event durations.

Distributions of the discharge event durations, d_{sing}, may be found in Figure 4.10. The form of the distributions is broadly similar to that of the event peak currents. A shift in the distribution width and median value is again seen as 1000 s of processing is approached, though in the case of the durations the median value sustains an increase as the distribution widens with processing time beyond 1000 s. The lower end of the d_{sing} distribution does not display any trend with the coating thickness.

The values seen are from ≈ 30 μs up to almost 400 μs. Such values are in good agreement with many of the studies summarised in Table 2.1. The major discrepancies are from comparison with studies by Matykina et al [**8**] who reported discharge durations in the hundreds of ms, and Golovanova and Sizikov [**24**] who reported less than 7.5 ms, which was presumed to be an upper bound. The disagreement with these studies is readily explained by the inappropriate measurement timebase employed, and good agreement is seen with studies which had better temporal resolution [**5, 10, 13, 19, 21, 23**]. For the higher end of the discharge current densities considered by Yerokhin et al, they calculated ~ 250 μs [**2**], also in good agreement with the findings of the present work.

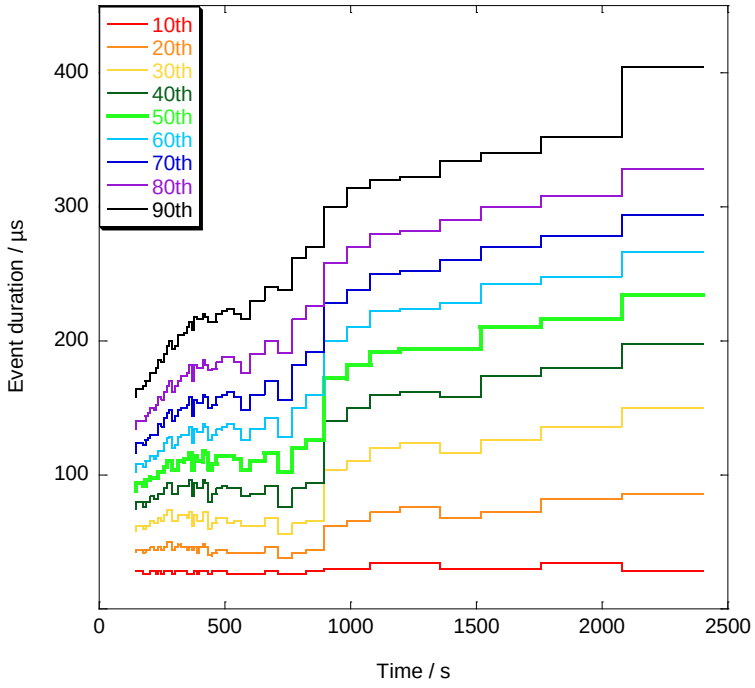

Figure 4.10: *Variation of the distributions of d_{sing} with processing time.*

4.2.4 Peak instantaneous power levels.

It should not be surprising that the peak power, P_{peak}, reached by individual discharge events follows the trends of the I_{peak} and V_{init} distributions. The P_{peak} distributions are presented in Figure 4.11. The power levels are large, though generally not sustained for more then a few μs. If the discharge current is all passing through a hole in the coating of similar dimension to the craters observed in the exterior surfaces of PEO coatings (see subsubsection 2.3.2.2), then the power density in the region of the discharge event will be very large.

The value of peak power quoted by Bao Van et al for one of the discharges they observed was 35 W [**13**]. This value is well within the range seen in the present dataset, and close to the median value beyond about 1000 s. The range reported by Gordienko and Gnedenkov was $0.2 - 1.0$ W [**23**]. This is not within the range of values plotted in Figure 4.11. The present dataset contains no information on events less then 10 mA base to peak, however events spanning the range quoted by Gordienko and Gnedenkov [**23**] were observed in the single discharge dataset, discussed in chapter 5. Such small events do exist in the in-situ dataset, though they are not resolved in the bulk of the results some information is available in section 4.3.

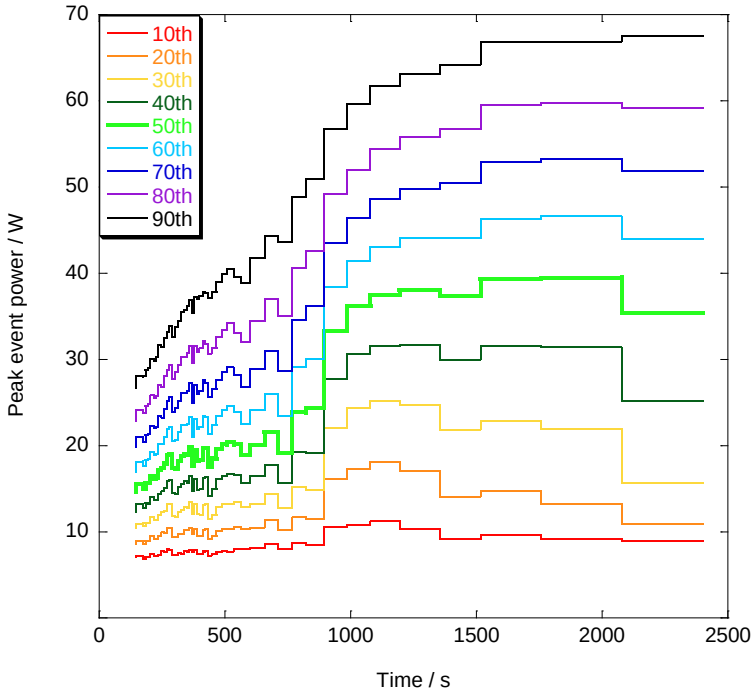

Figure 4.11: *Variation of the distributions of P_{peak} with processing time.*

4.2.5 Charge and energy of individual discharges.

The distributions of both charge transferred, Q_{sing}, and energy dissipated, E_{sing}, by individual events are little different in form and variation, following closely from the I_{peak} and V_{init} distributions. The precise values are nevertheless of interest, given the previous lack of information with regard to these properties. The Q_{sing} distributions are found in Figure 4.12 and the distributions of E_{sing} values are presented in Figure 4.13.

Typical events are seen to transfer from a few to a few tens of μC of charge. Typical energy dissipation is from a few mJ to about 13 mJ. It should be borne in mind that the precise volume within which this energy is dissipated will depend upon such parameters as the electrolyte and plasma electrical conductivities, and on the geometry of the event in terms of size and scale.

Few values are available in the literature for comparison, though Bao Van et al reported the energy of a single measured event to be 2.9 mJ [**13**], which is in good agreement with the distributions presented in Figure 4.13. Another value reported by Kasalica et al was 0.2 μJ, much lower than typical values seen in the present work [**10**]. The distribution of the event energy dissipations in the present work does extend all the way down to ~ 1 μJ however, so even this low value is not far outside the range observed.

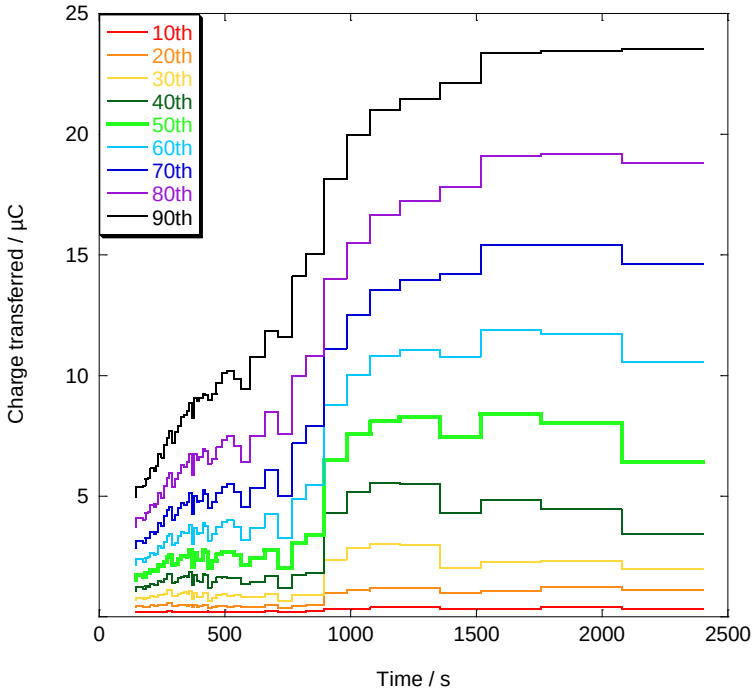

Figure 4.12: *Variation of the distributions of the Q_{sing} with processing time.*

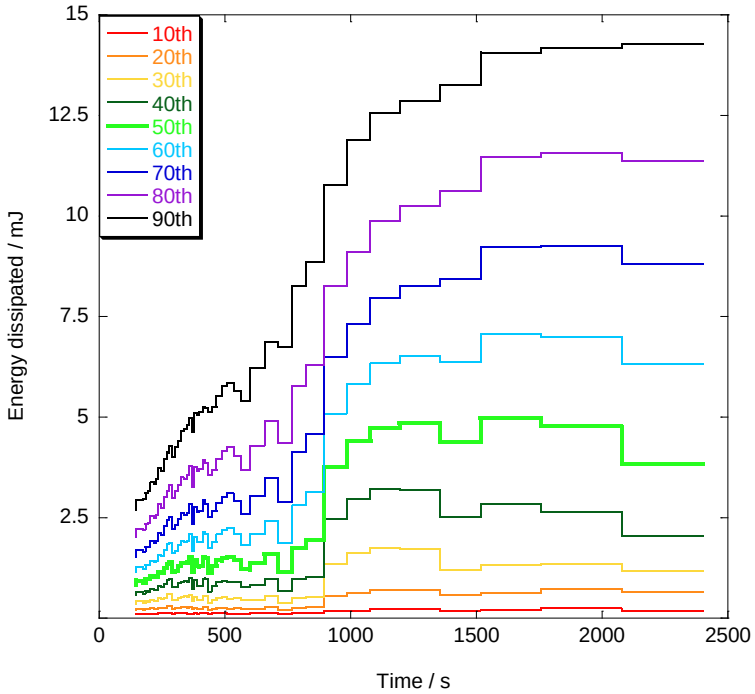

Figure 4.13: *Variation of the distributions of E_{sing} with processing time.*

4.3 Small current (< 10 mA) events.

The limits applied to the data obtained by in-situ monitoring, in the form of the cut off below 10 mA, are not inherent to the technique. Use of more sensitive detection arrangements, and smaller monitored areas can allow for information about the smallest events during PEO processing to be obtained.

As was described in subsection 3.2.1, one additional in-situ sample was produced, using a single 120 μm wire as the small area. This sample was used for some limited in-situ monitoring, and the coil passed through the current probe was increased from four turns to ten, increasing the sensitivity of the current probe to 5 mV per 1 mA. Experiments were also conducted at a faster logging rate of 62.5 MHz. A sample of the data from this more sensitive version of the in-situ monitoring experiment, from about 6 minutes into processing, is presented in Figure 4.14.

The data in Figure 4.14 has not had the frequency response correction applied. This is as the fine detail would likely be lost during the process. The events captured in this instance are small, meaning the effect of LR droop is minimal.

A selection of very low amplitude events is seen. Such events are commonplace throughout the duration of PEO processing. Events this small could not be reliably resolved in the original in-situ monitoring experiments, though they could be identified before and after the peak activity periods in some cycles. It is likely that the 500 μm wires used originally represented an area too large to ensure that no events as small as those seen in Figure 4.14 initiated concurrently. This is I believe the source of the 'noisy' region seen in many of the in-situ current traces. Though relatively small, such events were numerous, and the discharges shown in Figure 4.14 still reach peak instantaneous powers in the range 1–2 W.

Whilst it is unfortunate that such detail was not resolved in the main experiments, this data demonstrates that the capabilities of the technique go far beyond what has been achieved so far. There is a trade-off however: although smaller areas ensure that even the weakest of discharge events can be isolated, a great many more repeats will be required before information representative of the wider processing can be obtained.

4.4 Occurrence of electrical breakdowns during cathodic polarisation of the substrate.

Using the same modified in-situ monitoring set-up described as for the data presented in section 4.3, observations of the current during cathodic polarisation of the sample were made and are presented in Figure 4.15. It should again be noted

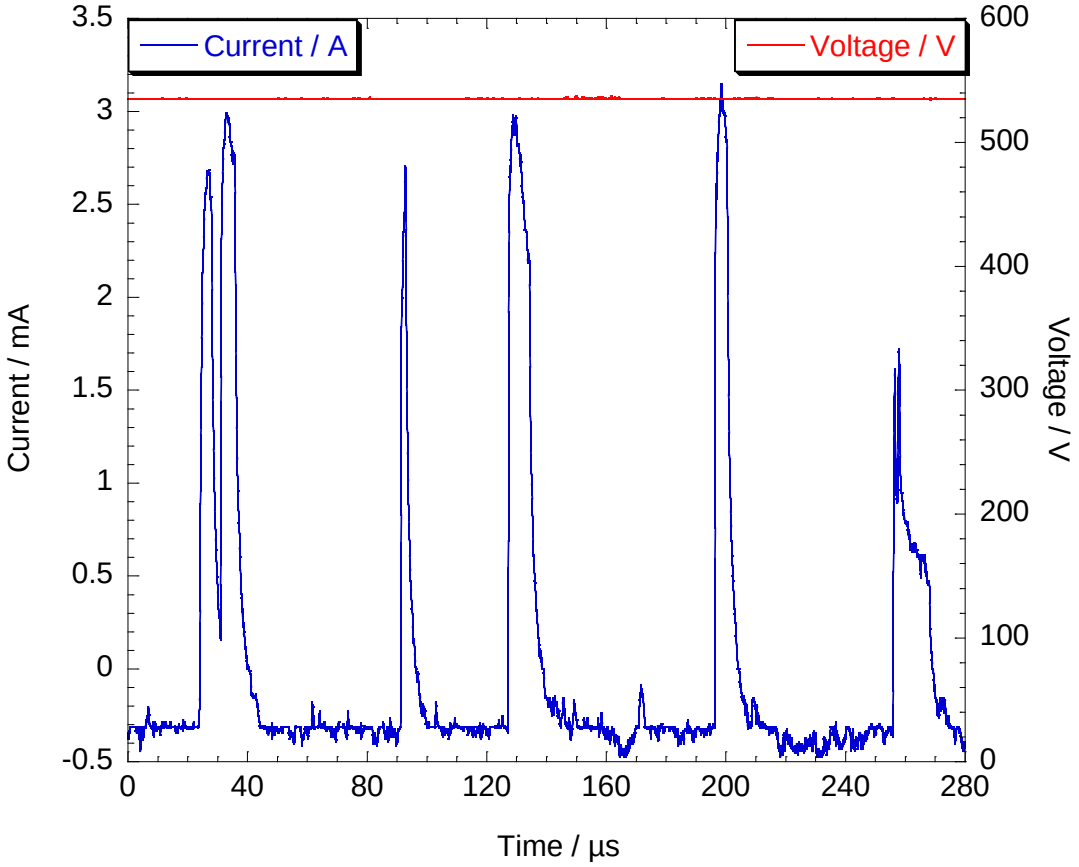

Figure 4.14: *Example of the sensitivity which can be achieved for in-situ monitoring experiments, taken from about 6 minutes into processing. Note that no correction for the inductive effects of the current probe has been applied to this data.*

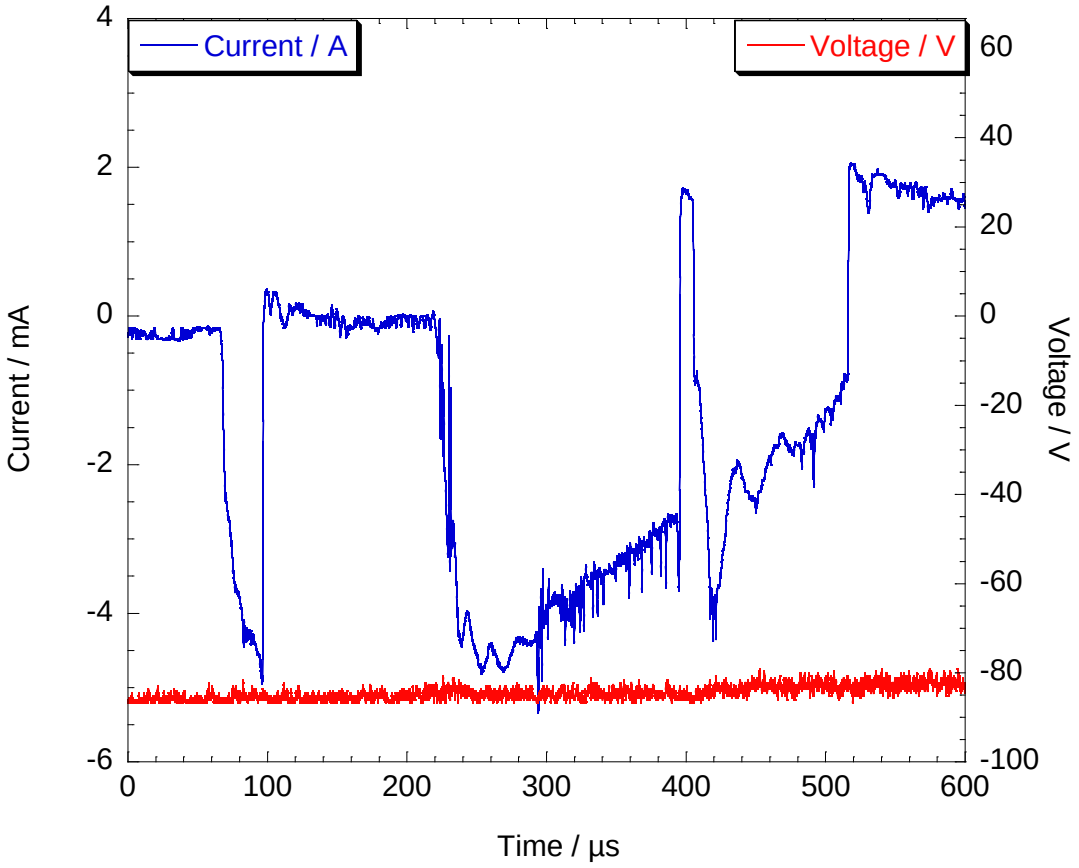

Figure 4.15: *Example of some apparent electrical breakdown events during cathodic polarisation of the substrate, taken at a point about 3 minutes into processing. Note that no correction for the inductive effects of the current probe has been applied to these data.*

that no frequency response correction has been made to this data, which is why the baseline level shows distortion in the figure. There are features in the plot which look very similar to the discharge events during positive polarisation of the sample.

Such discharging behaviour during the negative portion of the process cycle was observed to be reasonably common during the the first 5–6 minutes of processing. No such breakdown events during cathodic polarisation were seen beyond 7 minutes into processing in the present work. Whilst no firm conclusions can be drawn based on the available evidence, the indications are that electrical breakdowns do occur during cathodic polarisation of the substrate during PEO processing, though it appears that such events are only seen in the very early stages of coating development.

Chapter 5

Single Discharge Experiments.

In this chapter the results of single discharge testing of coatings pre-deposited using the 10 kW industrial supply detailed in section 3.1 are presented. Coatings were produced to multiples of 6 minutes from 6 up to 42 minutes as detailed in subsection 3.4.1. The thickening rate of the pre-deposited coatings for single discharge testing will be discussed first, followed by the experimental results obtained from the experiments.

A series of increasing capacitances were used for each different thickness as it was originally thought the discharge event properties such as peak current and duration would increase with capacitance until they reached a saturation value which could be regarded as representative of the large scale processing. As shall be described below, this was not observed, however the technique proved useful nonetheless, and fundamental aspects of PEO discharging behaviour were extracted from the data. To briefly re-state, the circuit capacitances applied in parallel with the samples took the values 5.5, 14.3, 33.3, 100, 200, 500 and 1000 nF, spaced roughly equally in the values of logarithm base ten.

5.1 Coating thickness development.

Before considering the properties of individual discharge events recorded during the experiments, the thickness and structure of the coatings used for single discharge testing will be briefly considered. The coating free surfaces were examined by SEM, one such image of a coating deposited for 30 minutes is presented in Figure 5.1. Such images confirm that the coatings generated are regular PEO coatings, as described in the literature (subsection 2.3.1).

The coating thickness was determined by optical microscopy of polished cross sections. Several such cross sections were joined together by correlating the edges until a region of coating just over 500 μm in length was in a single image. The

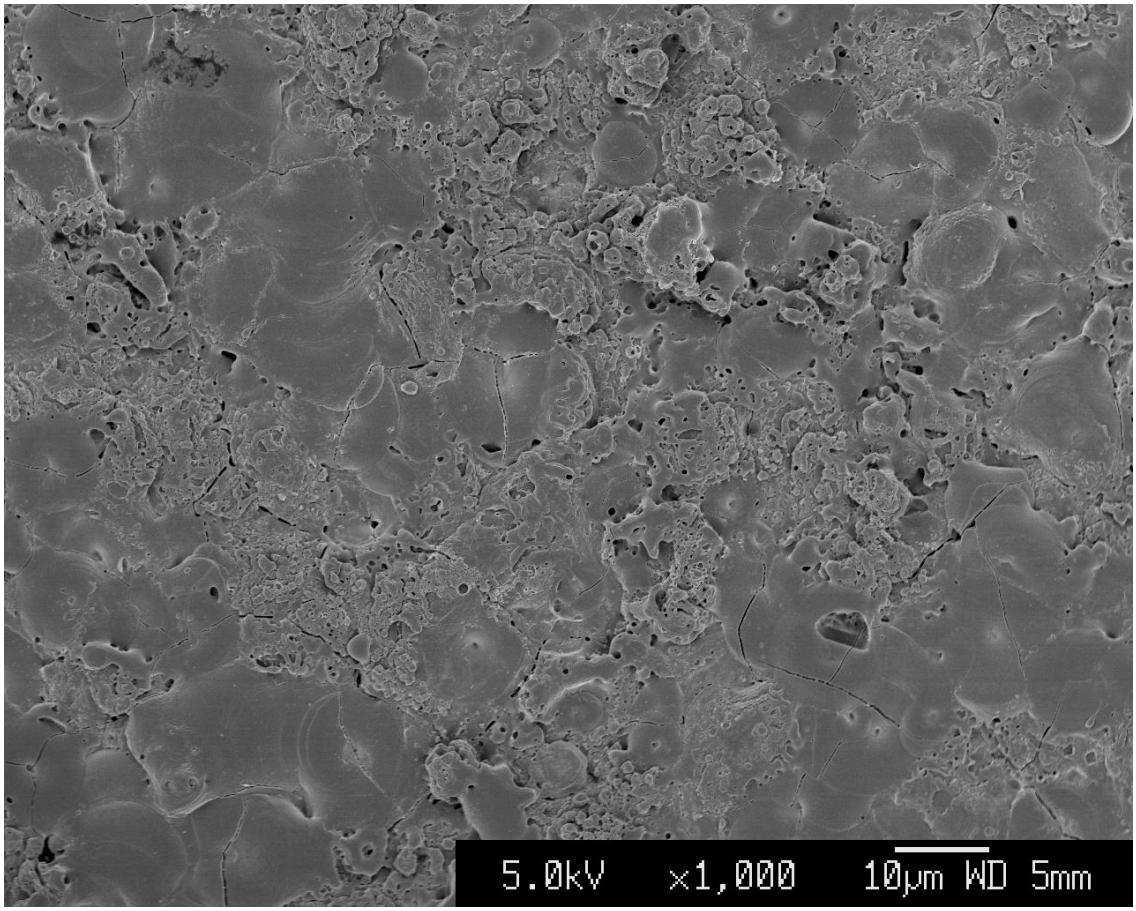

Figure 5.1: *FEGSEM secondary electron image of the exterior surface of a PEO coating deposited for 30 minutes.*

coating thicknesses were then determined by thresholding the images by grayscale value and subsequent computer analysis. The progression of coating thickness with time of processing is displayed in Figure 5.2, and some examples of the variability of coating thickness across the 500 μm section examined are presented in Figure 5.3.

The free surface image in Figure 5.1 is included not because anything novel may be learned from it, but rather to reassure the reader familiar with PEO coating technology that the coatings used for this experiment are fairly standard looking aluminium PEO coatings. The reader less familiar with PEO coatings should note the typical surface features visible. Many pores or 'craters' can be seen, the latter being surrounded by smoother regions which appear to be re-solidified coating material. The craters are often postulated to be the locations of recent discharge events.

The smooth regions are often interrupted by cracks, many of which are seen to run radially away from the central pore. Such features are thought to be generated

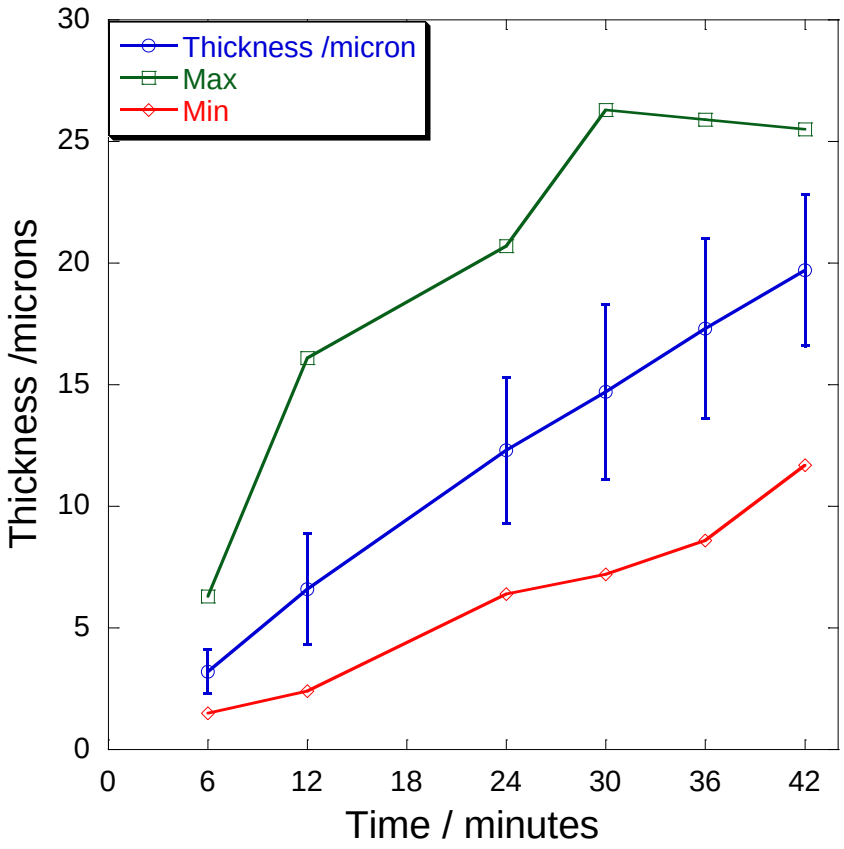

Figure 5.2: *Development of the coating thickness with time of processing for single discharge samples. The line labelled thickness is the mean thickness, and the error plotted represents standard deviation of the thickness. Minimum and maximum thickness values observed are also plotted for reference.*

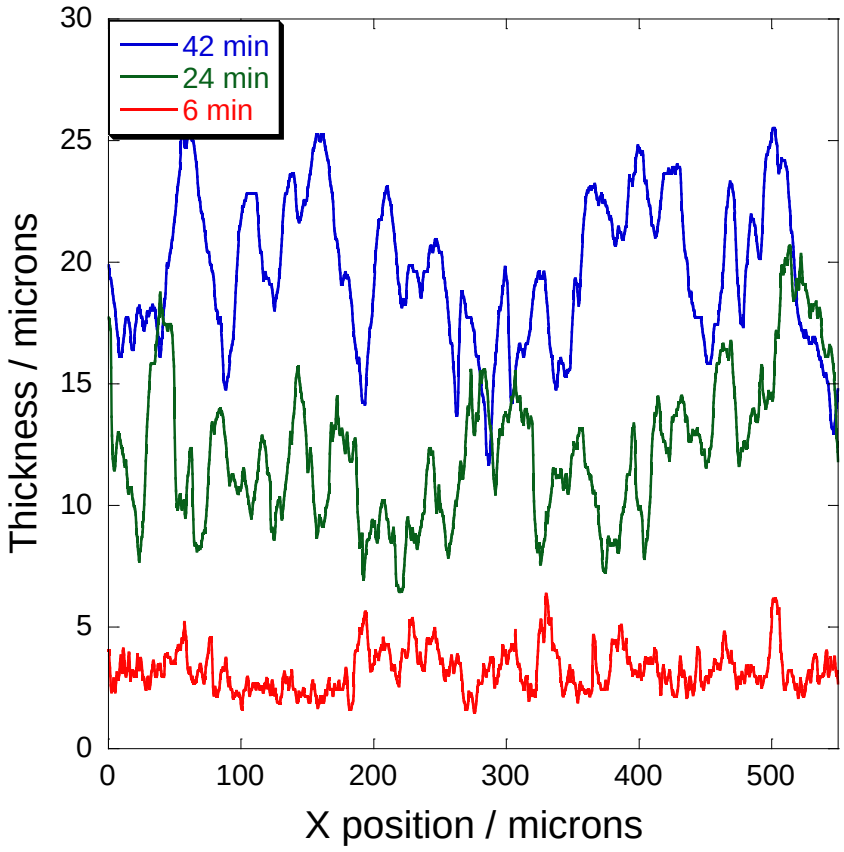

Figure 5.3: *Variability of the coating thickness for some of the coatings over the examined* 500 μm *length of coating. Measured from analysis of optical micrographs of polished cross sections.*

6 mins	12 mins	18 mins	24 mins	30 mins	36 mins	42 mins
637 Ω	509 Ω	464 Ω	340 Ω	279 Ω	279 Ω	233 Ω

Table 5.1: *Resistances used for current monitoring during single discharge testing with a range of capacitances and coating thicknesses.*

by differential thermal stresses experienced during rapid cooling of the coating material in the aftermath of a discharge event. The rougher material interspersed with the smooth re-solidified patches is also penetrated by numerous pores. All of these pores and surface cracks are thought to be connected to the sub-surface porosity known to be present in PEO coatings at levels around 20% [**6**].

From Figure 5.2 it can be seen that the coating growth rate is roughly linear with processing time, as has often been reported in the literature (subsection 2.3.1). The minimum and maximum coating thicknesses also follow the same general trend, though a slight increase in the variability of the thickness is seen with increasing process time as well. Such an increase in roughness has been reported in the literature (subsubsection 2.3.2.3), and can be visualised readily from the thickness profiles plotted in Figure 5.3.

5.2 Discharge event resistance at peak current.

Before considering the measured properties of single discharges, it must first be considered what the loading impact was of the variable resistance inserted to monitor discharge current. Any inserted resistance incurs some loading of the circuit being tested, causing deviations from the behaviour that would be observed in the absence of the test resistance. In order that the loading not impact the observed currents significantly, the monitoring resistance should be of much smaller magnitude than the minimum resistance seen in the circuit being investigated. In this case, this means that the resistances applied should be considerably smaller than the resistance seen for discharge events at the point of peak current, R_{peak}. The values of test resistance used for the coatings processed for different durations were as in Table 5.1, reproduced from subsection 3.4.1.

The median values of the dynamic resistance of discharge events at peak current, R_{peak}, is plotted as a function of I_{peak} value in Figure 5.4. The series in this plot were calculated for each coating thickness (and hence for each value of the current monitoring resistance), using data from all circuit capacitances used. From Figure 5.4 three things can be seen. Firstly the current monitoring resistances used were all at least an order of magnitude lower than the minimum resistances seen

Capacitance	6 mins	12 mins	18 mins	24 mins	30 mins	36 mins	42 mins
5.5 nF	194 223	146 214	155 768	62 819	39 946	53 219	40 525
14.3 nF	152 243	138 025	116 490	108 519	40 230	54 080	30 459
33.3 nF	140 147	141 054	130 663	56 669	43 247	40 089	27 200
100 nF	122 128	112 521	122 339	29 196	44 887	35 447	27 873
200 nF	109 867	114 761	100 108	47 501	42 573	38 431	21 862
500 nF	120 722	96 827	97 702	43 739	42 581	33 501	27 203
1000 nF	89 263	87 893	83 201	45 061	45 898	40 884	28 450

Table 5.2: *Table of the number of single peak discharge events recorded for each combination of coating process time and circuit capacitance.*

for even the largest discharge events. Secondly R_{peak} values show strong variation with I_{peak}. Finally, there is no discernible difference in the dependence of R_{peak} on I_{peak} with the coating thickness, the values from different thicknesses are all seen to lie along slightly different sections of the same relationship.

This figure is getting a bit ahead of the discussion, and is included in this section rather than in chapter 6 in order to demonstrate that the resistances used to monitor discharge current had negligible impact on the event development observed. The scaling relationships of discharge events will be discussed further in chapter 6.

5.3 Event average properties.

We shall first consider the average values of important discharge properties measured for each combination of circuit capacitance and coating thickness. The different coatings will be referred to in this section, and those that follow, by the time of processing not the thickness. It should nevertheless be understood that 'thicker coatings' refers to longer times of processing, as evidenced in Figure 5.2.

Also, all properties referred to in this discussion will be measured from single peak discharge events, not the multi-peak events, except where explicitly specified. This is as the multi-peak events possibly represent concurrent events at two or more points on the sample surface, which happen to overlap in time. The multi-peak events are still of interest in certain discussions relating to the initiating voltage however. The precise number of single peak events recorded and used in subsequent calculations is outlined in Table 5.2 and the fraction of all recorded events which were single peak may be found in Table 5.3.

The fraction of single peak events is seen to be greatest for thicker coatings from Table 5.3, and the rate of discharging is seen to be generally lower for coatings

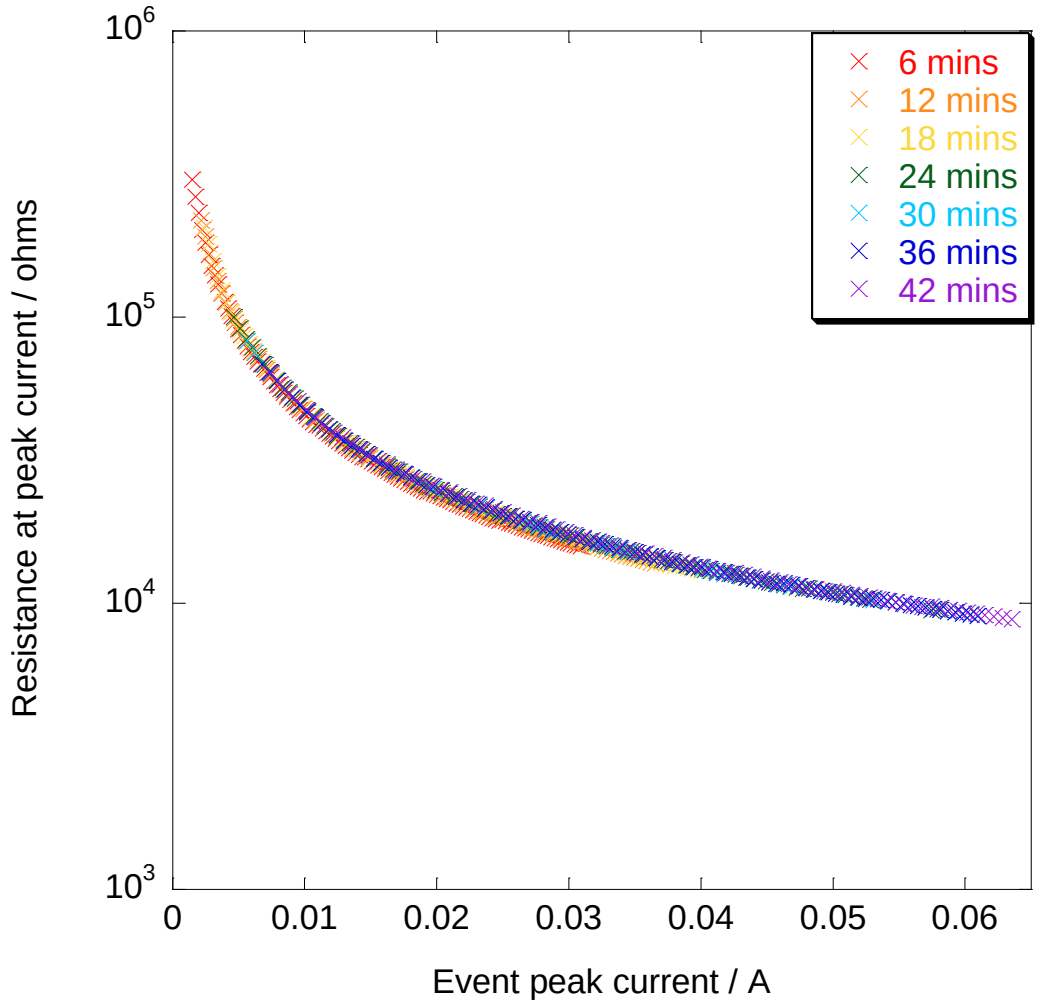

Figure 5.4: *Dynamic resistance of discharge events at the point of peak current, R_{peak}, as a function of discharge peak current, I_{peak}. The width of the distribution of R_{peak} values at each I_{peak} value was found to be too small to be resolved if plotted on the figure.*

Capacitance	6 mins	12 mins	18 mins	24 mins	30 mins	36 mins	42 mins
5.5 nF	0.46	0.47	0.67	0.96	0.98	0.99	0.99
14.3 nF	0.46	0.56	0.76	0.94	0.98	0.99	0.99
33.3 nF	0.48	0.62	0.78	0.97	0.98	0.98	0.99
100 nF	0.50	0.64	0.79	0.96	0.97	0.97	0.98
200 nF	0.52	0.66	0.79	0.93	0.95	0.97	0.98
500 nF	0.58	0.67	0.77	0.90	0.92	0.93	0.94
1000 nF	0.56	0.69	0.79	0.89	0.91	0.91	0.92

Table 5.3: *Table of the fraction of all recorded discharge events which were composed of a single current peak, for each combination of process time and circuit capacitance.*

formed to longer times in Table 5.2. The concurrent decrease in incidence of multiple peak events at the same time as the rate of discharging drops is consistent with the multi-peak events being separate discharges operating at different locations.

The event average properties are presented in Figure 5.5 for V_{init}, I_{peak}, d_{sing} and P_{peak}. The data for Q_{sing} and E_{sing} may be found in Figure 5.6. The value plotted is the median for all properties except V_{init}, where the mean value is used in preference.

This choice of average relates to distribution widths and the number of distinct values spanned by the distribution of event properties. For V_{init} the number of distinct values was low so the mean was judged a better measure. All the other properties show wide distributions and are often asymmetric about the peak value, as such the median was judged more representative in those cases. More detailed probability histograms will be presented later in Figure 5.7 to Figure 5.12, which will allow the reader to judge these choices of average measure.

The data presented in Figure 5.5 and Figure 5.6 give an immediate overview of the data obtained from the single discharge experiments. Something perhaps unexpected can be seen immediately, namely that the mean value of V_{init} is seen to decrease with the circuit capacitance. It is not obvious why the circuit capacitance used should have an impact on the coating breakdown strength.

Whilst a larger capacitance will provide a greater reserve of charge and energy to develop a discharge once it initiates, such factors cannot influence the physical system prior to initiation of the event. A possible explanation is that breakdown of PEO coatings has a stochastic dependence as well as a voltage dependence. This hypothesis will be discussed in greater detail later, at present it will be useful to continue with discussion of the observed discharge properties.

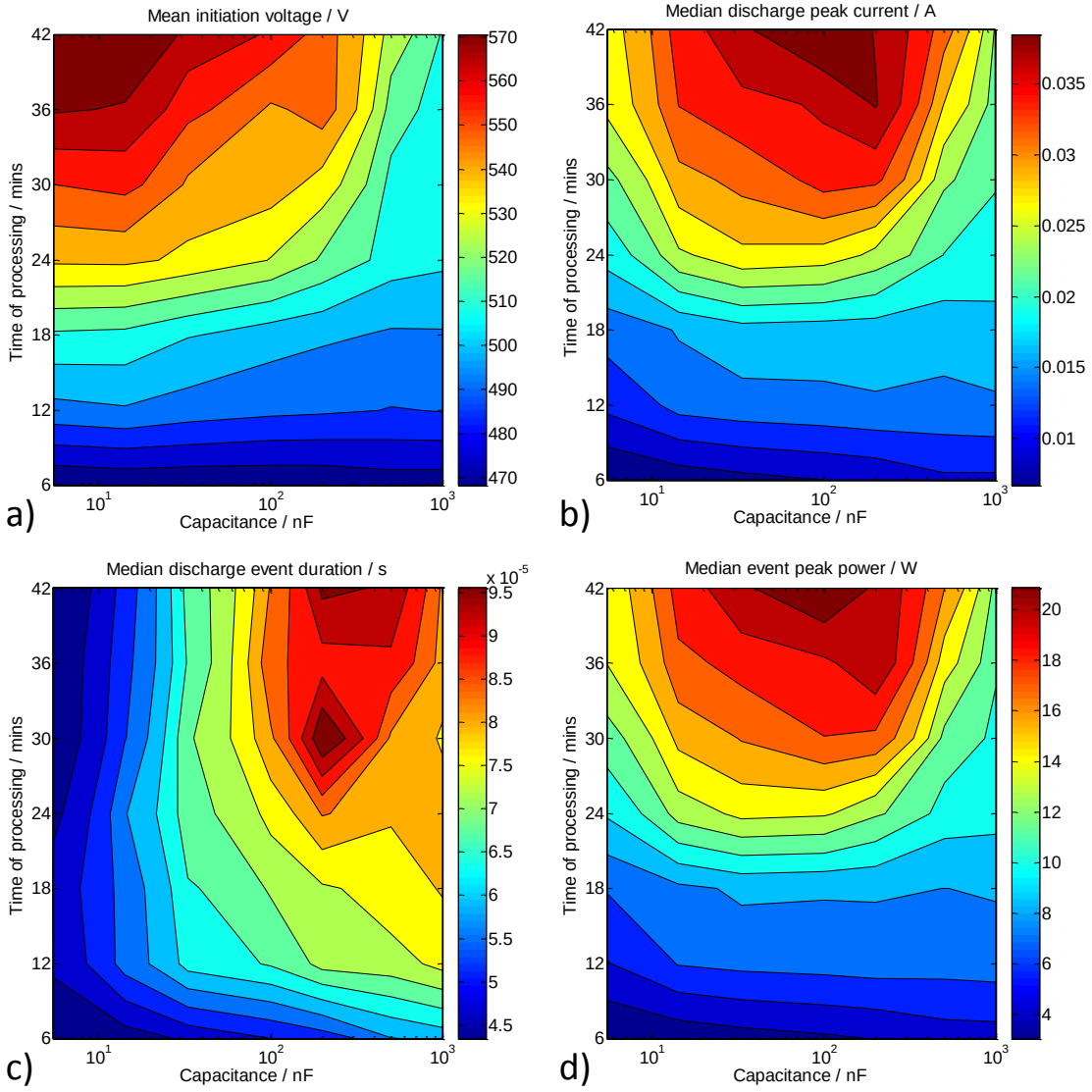

Figure 5.5: *Panel (a) shows the mean values of V_{init} for each combination of coating processing time and circuit capacitance; (b) the median values of I_{peak}; (c) the median values of d_{sing} and (d) the median values of P_{peak}.*

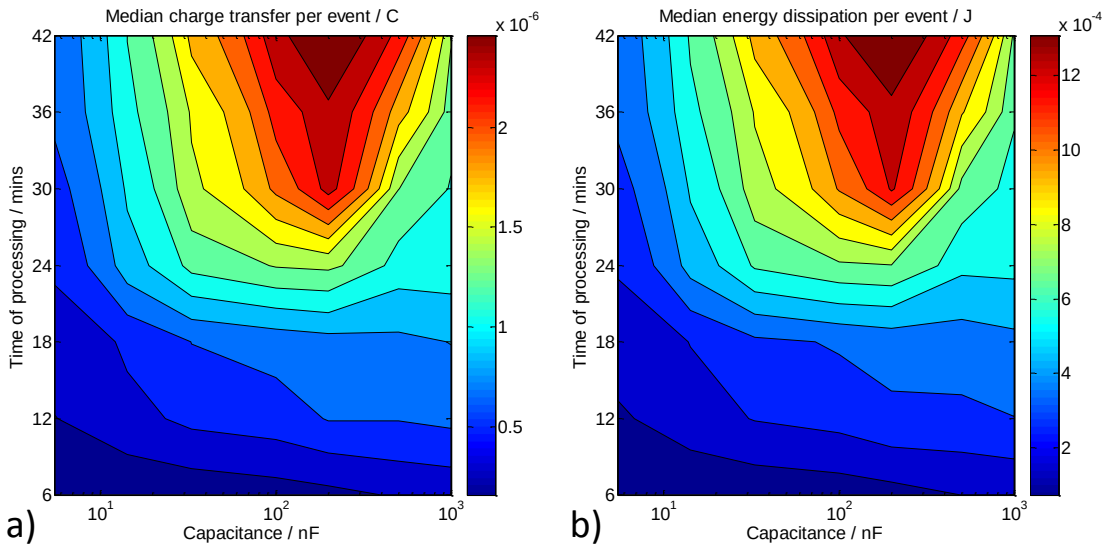

Figure 5.6: *Panel (a) shows the median Q_{sing} for each combination of processing time and circuit capacitance tested. In panel (b) the values of median E_{sing} are plotted.*

5.4 Discharge event probability histograms.

Whilst the average values of a particular event property are of interest, the distributions are poorly characterised by a single number. In this section histograms of the discharge event properties will be presented, normalised by total number so that the value of each bin range represents the probability of a discharge event property taking a value in that range.

Comparisons will made to highlight the variation of the event property distributions with processing time and with circuit capacitance. In each figure, panel (a) will show variation with processing time for a fixed capacitance of 200 nF, and panel (b) will display variations with circuit capacitance for a coating processed for 30 minutes.

When considered in conjunction with Figure 5.5 and Figure 5.6, the probability histograms should allow the reader a clear overview of the properties of the discharge events recorded in this experiment. Figure 5.7 shows probability histograms for V_{init} for selected combinations of capacitance and processing time; Figure 5.8 shows I_{peak} data; Figure 5.9 shows d_{sing} data; Figure 5.10 shows P_{peak} data; Figure 5.11 the Q_{sing} data and Figure 5.12 the histograms of E_{sing} values.

The histograms show the same trends as the property averages. Circuit capacitance is seen to cause a decrease in the observed distribution of V_{init} values, especially for the thicker coatings. For a fixed circuit capacitance, V_{init} distribu-

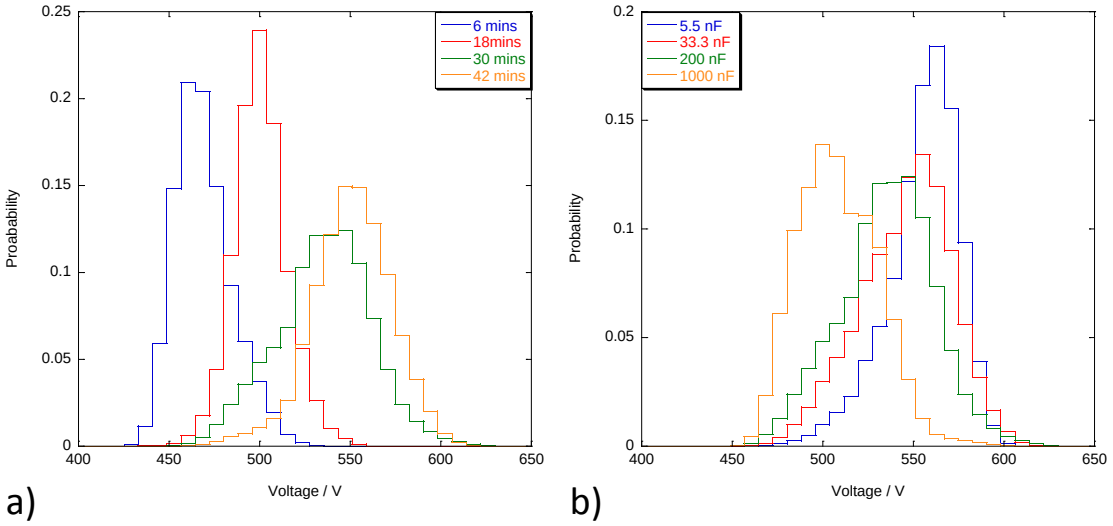

Figure 5.7: *Probability histograms of V_{init} values, using bin widths of 7.87 V. Panel (a) shows variation with processing time for a fixed capacitance of 200 nF, panel (b) shows variation with capacitance for a 30 minute coating.*

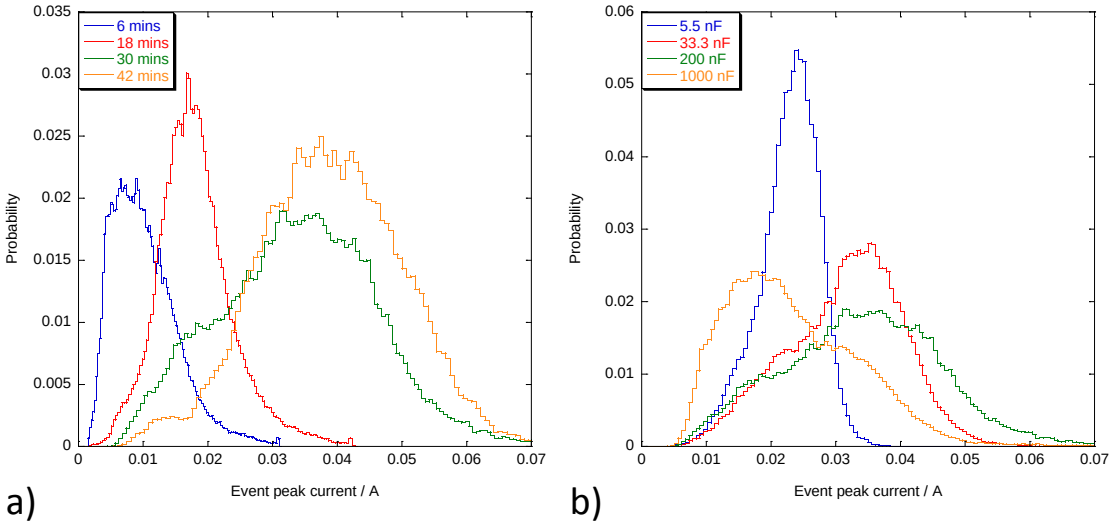

Figure 5.8: *Probability histograms of I_{peak} values, bin width was variable and took the values 0.25, 0.34, 0.56 and 0.68 mA for 6, 18, 30 and 42 minutes processing respectively. Panel (a) shows variation with processing time for a fixed capacitance of 200 nF, panel (b) shows variation with capacitance for a 30 minute coating.*

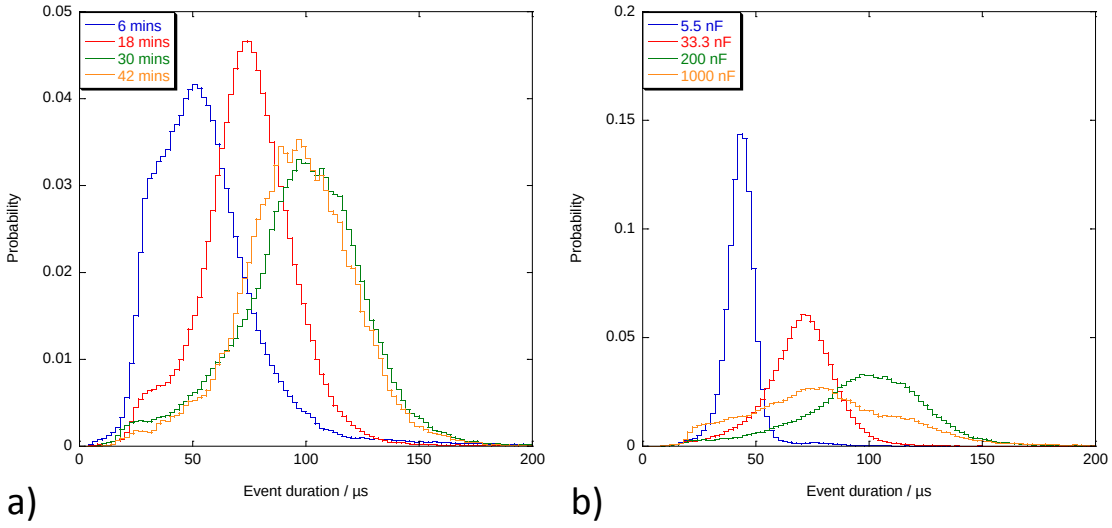

Figure 5.9: *Probability histograms of d_{sing} values, with bin width of 2 µs. Panel (a) shows variation with processing time for a fixed capacitance of 200 nF, panel (b) shows variation with capacitance for a 30 minute coating.*

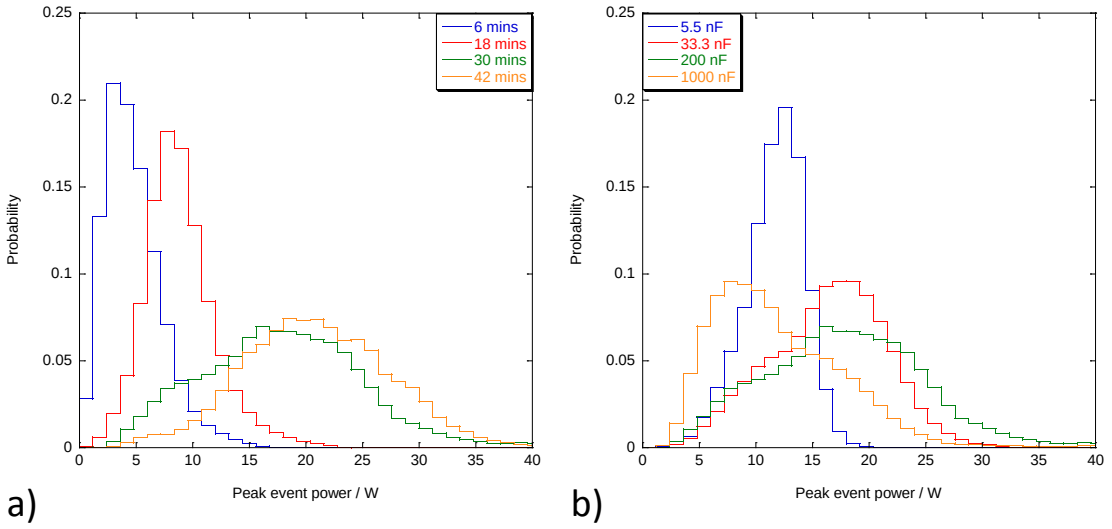

Figure 5.10: *Probability histograms of P_{peak} values, with bin width of 1.2 W. Panel (a) shows variation with processing time for a fixed capacitance of 200 nF, panel (b) shows variation with capacitance for a 30 minute coating.*

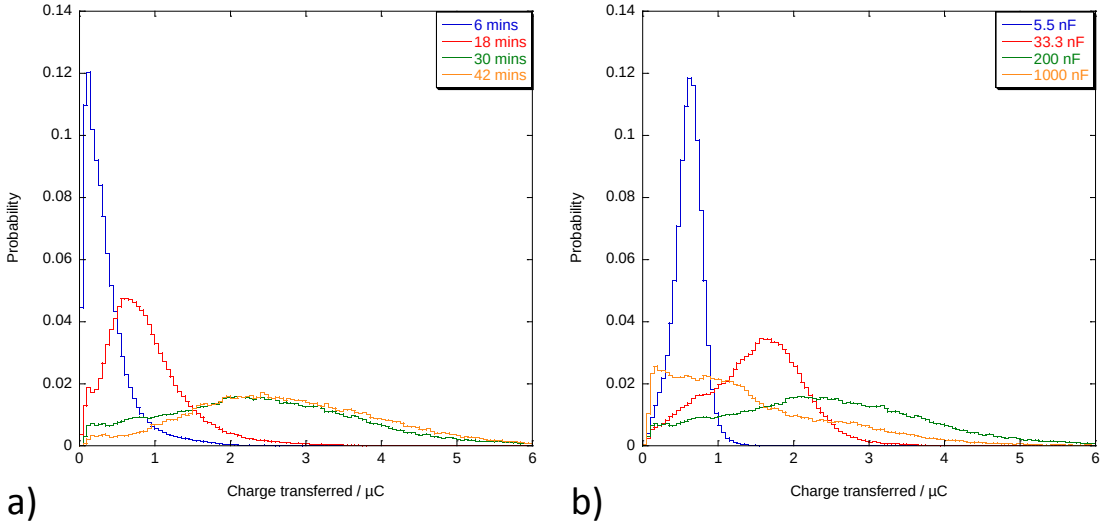

Figure 5.11: *Probability histograms of Q_{sing} values, with bin width of 50 nC. Panel (a) shows variation with processing time for a fixed capacitance of 200 nF, panel (b) shows variation with capacitance for a 30 minute coating.*

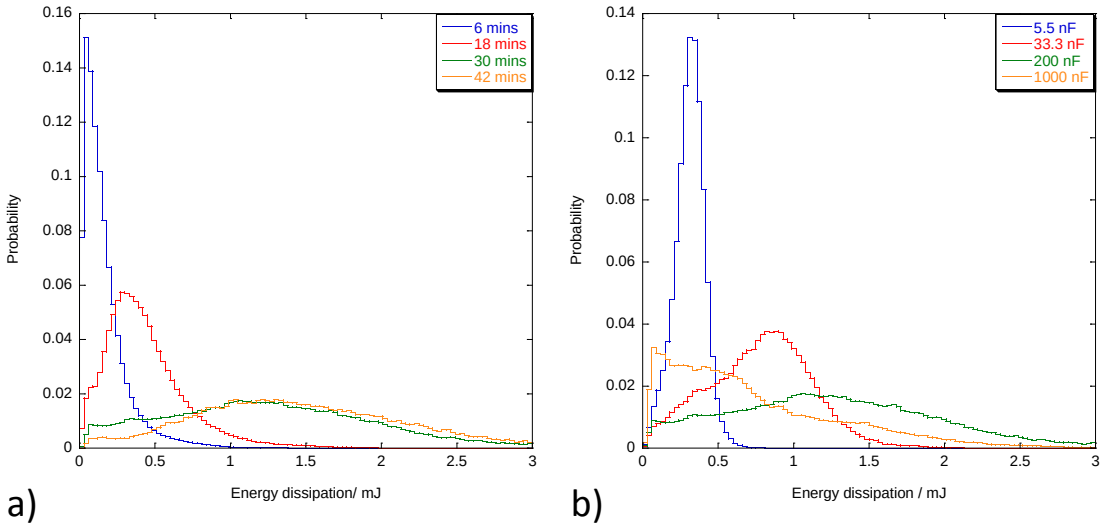

Figure 5.12: *Probability histograms of E_{sing} values, with bin width of 30 μJ. Panel (a) shows variation with processing time for a fixed capacitance of 200 nF, panel (b) shows variation with capacitance for a 30 minute coating.*

tions rise with increased coating process time. The I_{peak} and d_{sing} distributions are seen at first to increase with circuit capacitance, however beyond about 200 nF the property distributions are seen to move back down to lower values. For fixed capacitance both I_{peak} and d_{sing} distributions showed sustained increases with coating thickness. Other key parameters follow the trends set by peak current and duration.

Comparison with in-situ monitoring data (section 4.2) shows that the single discharge data from this experiment do not give an accurate reflection of the properties of discharge events observed during bulk PEO processing, at least when the raw measurements are considered. It will be shown in chapter 6 that when two property correlations are considered, such as variation of d_{sing} with I_{peak}, the correspondence is good. Furthermore it will be shown that some information obtained from single discharge testing, relating to the scaling behaviour of the discharge events, cannot be obtained from in-situ monitoring as easily.

In order to get to that point, it is important to develop an understanding of why the measured properties from single discharge experiments behave in the observed fashion. The key to understanding the observed distributions lies in understanding why an increased circuit capacitance causes a shift to lower V_{init} values. It will then be shown in chapter 6 that applied voltage is a key parameter for the development of discharge events during PEO; not only in single discharge testing but in bulk processing also.

5.5 Clustering behaviour of discharge events.

In order to understand the behaviour of the event initiating voltages, there is another aspect of the discharge behaviour which requires discussion, specifically the tendency of discharge events to occur in clusters or sequences. For reasons discussed shortly in subsection 5.5.3, the author believes these clusters of discharge activity to represent a series of discharge events at, or close to, the location of the primary event in each cluster. An example of an extended segment of single discharge data from a 42 minute coating with a 1000 nF circuit capacitance, in which two clusters are evident, is presented in Figure 5.13.

This behaviour was also seen in the in-situ monitoring experiments for the plots of cumulative charge transfer plotted in Figure 4.5 and Figure 4.6. The tendency seen was for events on the small area to occur during periods of high activity, separated by periods of little or no discharging.

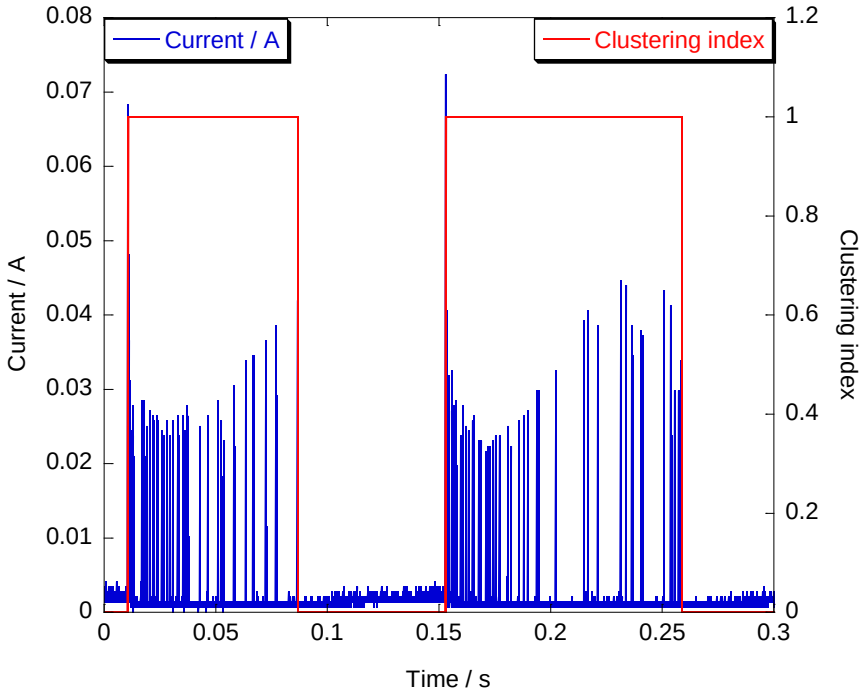

Figure 5.13: *Example of a section of data containing two clusters of discharge events. The second axis plots the indexing of such discharge clusters for visual reference.*

5.5.1 Definition of a cluster.

For the purposes of examining clustering behaviour it was necessary to develop some criteria to assign discharge events as belonging to clusters. A typical separation, T_{sep}^{avg}, was defined by dividing the total time recorded, which was 10 s, by the number of discharge events within that 10 s segment. Then if the initiation to initiation time between two events was less then T_{sep}^{avg}, those two events were assigned to be part of the same cluster. This process of adding events to clusters continues until no more events satisfy the criteria. All remaining discharge events at this point are taken to be clusters of a single event. For this analysis all indexed events, not just single peak events, must be used.

The clustering index is plotted in Figure 5.13 for comparison with the current data. Once clusters had been identified, each discharge event was assigned an integer number which represents the order in which that event occurred within the relevant cluster. A question of immediate relevance is how many clusters were identified, and how many discharge events were in them? The number of clusters identified for each combination of process time and capacitance can be found in Table 5.4.

The number of clusters is only part of the picture; the mean number of events in each cluster is another key parameter. A table of the mean number of events per

Capacitance	6 mins	12 mins	18 mins	24 mins	30 mins	36 mins	42 mins
5.5 nF	137053	128579	99490	16948	6243	8035	5150
14.3 nF	103342	97505	59563	44979	5832	11243	3790
33.3 nF	80279	84096	60971	18067	9935	9418	4792
100 nF	56977	56929	57425	7402	15275	10993	9155
200 nF	40821	49180	40296	15733	14673	13550	6584
500 nF	23509	32219	33388	11288	11226	8183	6178
1000 nF	18165	23553	23791	10093	9636	5237	4711

Table 5.4: *Table of the number of clusters of discharge events recorded for each combination of capacitance and process time.*

Capacitance	6 mins	12 mins	18 mins	24 mins	30 mins	36 mins	42 mins
5.5 nF	3.0	2.4	2.6	4.2	6.0	6.9	11.0
14.3 nF	3.0	2.6	2.8	3.5	6.9	5.4	7.6
33.3 nF	3.9	2.7	2.6	3.8	4.4	6.2	6.5
100 nF	4.4	3.1	2.6	4.6	3.7	4.2	3.9
200 nF	5.0	3.4	3.3	3.9	3.1	3.4	4.1
500 nF	7.1	4.0	3.7	5.4	5.0	5.2	5.7
1000 nF	8.6	4.9	3.8	5.8	6.2	6.6	7.5

Table 5.5: *Table of the mean number of discharge events per cluster for each combination of capacitance and process time.*

cluster is presented in Table 5.5. It should be remembered this is only information about clusters as they were defined earlier, ie according to a measure which is not without problems.

Some measure of the clustering behaviour is required, however using the typical separation I_{sep}^{avg} is not always ideal. For example if all events occur roughly spaced by a mean separation I_{sep}^{avg} but with finite standard deviation, this will generate a large number of spurious clusters of 2 or 3 members. However, as the number of events added becomes larger, the likelihood of the cluster being the result of a chance occurrence of discharges reduces considerably.

To try and account for such factors, a further measure of clustering may be calculated as a bound on the clustering tendency of the discharge events. This was taken to be the 90^{th} percentile of numbers of event per cluster, after removal of clusters containing less then 3 events. The results of this are displayed in Table 5.6. The 90^{th} percentile was chosen as a measure of upper bound on the clustering as it is less sensitive to outliers then the maximum value.

Capacitance	6 mins	12 mins	18 mins	24 mins	30 mins	36 mins	42 mins
5.5 nF	8	8	10	25	32	30	47
14.3 nF	9	8	12	21	32	25	32
33.3 nF	10	8	10	27	33	41	26
100 nF	13	9	9	30	29	24	24
200 nF	14	11	13	23	27	17	21
500 nF	24	14	15	37	38	41	54
1000 nF	29	18	17	42	57	55	55

Table 5.6: *Table of the* 90^{th} *percentile of the number of discharge events per cluster, after removal of clusters less than 3 in number, for each combination of capacitance and process time.*

5.5.2 The tendency towards clustering.

Taking Table 5.5 and Table 5.6 together, events appear to show a tendency towards a greater probability of clustering for increases in the process time of the sample coating. The same tendency is seen for increased circuit capacitance, though not as strongly as for process times.

An increase with circuit capacitance makes sense, and might be expected given that the applied voltage will decrease less over the course of an event with a larger capacitance, as it will buffer the supply against the current loading of the discharge more effectively. This will leave the voltage after termination of each event higher than it would be for a smaller circuit capacitance, potentially increasing the probability of a subsequent breakdown event.

The estimated increase in the extent of clustering with coating process time may be taken in the context of bulk PEO processing. Many authors have noted that the discharge events have a tendency to become localised around certain sites as processing proceeds, and generally appear by eye or by low speed optical imaging to be longer lived and less mobile [**2, 7, 8, 9, 16**]. These empirical observations are consistent with the information in Table 5.5 and Table 5.6.

Furthermore there does appear to be a transition in the upper bound of the discharge numbers per cluster between 18 and 24 minutes. Whether the changes in discharge event property distributions seen around similar process times in section 4.2 are related to such a step change in the likelihood of event clustering, possibly at a localised site, is not possible to say absolutely from the present data. The timings are compelling however, especially given the changes in the visual appearance and colour of discharge events typical around 15-20 minutes into processing.

5.5.3 Likelihood of sequential events in clusters being spatially related.

It is the authors opinion that these long clusters of discharge events represent successive events occurring at or near to the location of the primary event in each cluster. This is based primarily upon the observations of V_{init} values of events during clusters. A plot of the mean decrease in voltage between the primary event and the initiation of the n^{th} event in a cluster is shown in Figure 5.14 for data from the 1000 nF circuit capacitance.

It is seen that within each cluster, successive events occur at progressively lower voltages. In one sense this is not surprising as the events occur in rapid succession, and the capacitor cannot recharge much between termination of one and initiation of the next. What is surprising is that the events keep initiating at voltages much lower than that of the primary event. It should be remembered that prior to the primary event the sample had been exposed to a higher voltage for a much longer period, compared to the separation of events within the cluster.

This may be indicative of the first event somehow priming the discharge site and allowing subsequent discharges at the same location to initiate at lower voltages. This cannot be confirmed with the present dataset however. Whether such priming is in the form of changes to the local structure of the coating, or whether it relates to slight changes in the local composition of the electrolyte, or even persistence of elevated temperatures at the discharge site is not possible to say.

It is worth referring back to the in-situ monitoring data, which showed discharging at later times in processing during periods of elevated activity spread across multiple process cycles (see Figure 4.5 and Figure 4.6). Given the small area being monitored, such periods of activity probably correspond to discharges at, or close to, a single location. The persistence across multiple process cycles at 50 Hz is suggestive of a structural origin for the discharge clustering, as any thermal or electrolyte effects would tend to be interrupted by the cycling of applied voltage.

Each event in such clusters is nevertheless associated with a distinct plasma, as was confirmed by experiments in which a photo-multiplier module recorded concurrently with electrical monitoring, described in a previously published paper [**1**].

5.6 Relation of the initiating voltage and circuit capacitance

Having established that the voltage tends to drop over the course of a cluster of discharge events, and that clustering is favoured by thicker coatings and larger

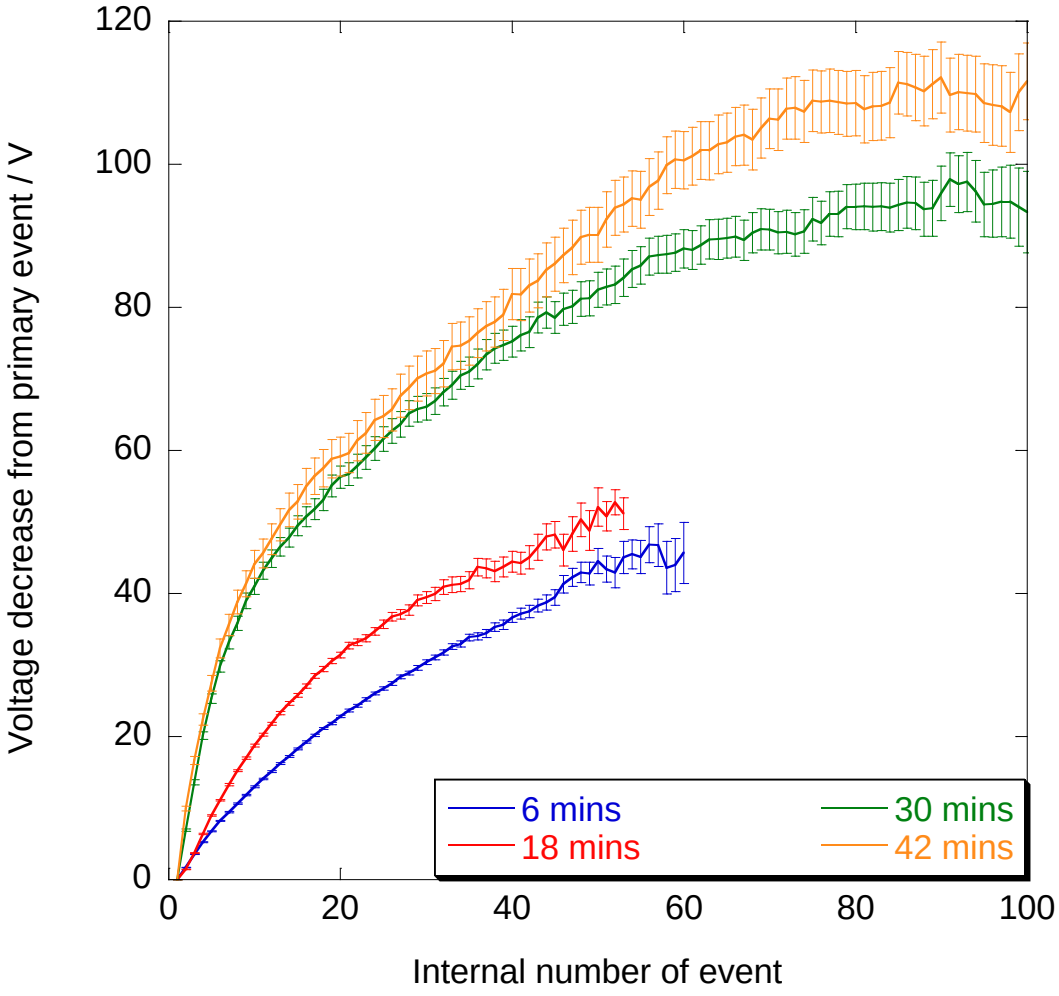

Figure 5.14: *Mean decrease of applied voltage between initiation of primary event in cluster and the n^{th} event in the same cluster. Error bar is the standard error on the mean.*

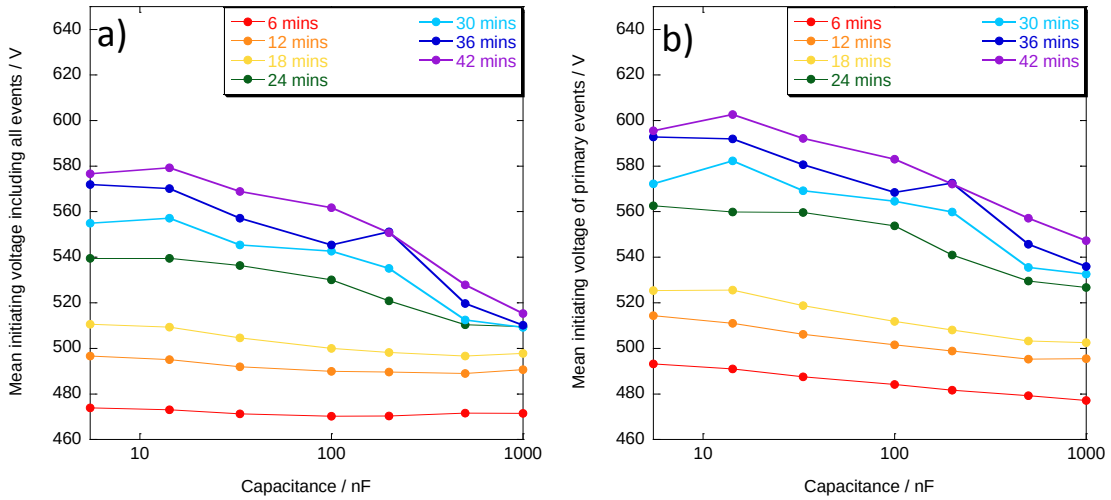

Figure 5.15: *Mean V_{init} values taken from (a) all indexed discharge events (including multi-peak) and (b) only those discharge events which were first in the respective cluster. Errors on the mean values are too small to plot, distribution widths are similar to those seen in Figure 5.7 and widths are not plotted for clarity of presentation.*

capacitances, it is possible to ask whether the previously noted decrease in V_{init} with capacitance, seen in Figure 5.5 and Figure 5.7, is related to the clustering behaviour. It is possible that the mean V_{init} values were skewed by inclusion of data from events at later stages of the discharge clusters, which become more sustained with increased capacitance.

A comparison is presented in Figure 5.15 of the mean V_{init} values for all indexed discharge events (not just the single peak events) in panel (a), whilst panel (b) shows the same information when only the primary event in a given cluster is included. It can be seen that inclusion of more than the primary event does tend to cause a lowering of the mean V_{init} for discharges. However, the observed decrease with capacitance remains, and furthermore is even more pronounced for the thinner coatings than when all events were considered.

The question is now quite pressing as to why the circuit capacitance used should affect the initiating voltages of discharge events. One of the physical parameters which the capacitance can influence prior to onset of breakdown is the ramping rate of the voltage. Larger capacitors do not just reduce the voltage decrease during an event, the rate of recharging after event termination will also be reduced.

This point is illustrated by Figure 5.16. This figure plots for each 10 μs possible separation period from the end of one cluster to the initiation of the next, the mean

V_{init} which was observed. Only 10 μs separation periods for which there were at least 10 values were included.

From Figure 5.16 it can be seen how the recharging rates varied with the circuit capacitance. This confirms that, for example, a 12 minute coating which broke down at 490 V with a 1000 nF circuit capacitance will have been exposed to that voltage for a significantly longer period than a 12 minute coating through which a discharge event was initiated at the same voltage using a 5.5 nF circuit capacitance.

It is the author's feeling that the breakdown behaviour of PEO coatings displays a significant stochastic component. Rather than there being a well defined breakdown strength for any given coating, the author would propose that there is instead a probability of breakdown per unit time and area, which is a strong function of the applied voltage and the existing coating structure. Therefore any given coating, if exposed to a constant voltage, would show greater probability of breakdown the longer the time for which it was exposed. For the present there is not sufficient data to rigorously test such a hypothesis, though the experimental data from the single discharge testing with different circuit capacitances does strongly suggest some form of probabilistic dependence of the breakdown upon the applied voltage.

The consideration of event initiation is further complicated by the fact that one may never cause electrical breakdown through the same PEO coating twice. The nature of the process is that the local micro-structure is re-configured every time a discharge occurs. Indeed if the discharges had no effect on the micro-structure the growth of the coatings would never deviate from regular anodising.

High roughness and porosity levels also contribute to the uncertainty. The surface connected nature of the porosity [**6**] means it is likely that electrolyte penetrates into the interior of the coatings, much closer to the metal than the bulk thickness would indicate. Even if this were not the case, the surface roughness would mean that the precise field strength at any point on the surface would be highly variable. Finally the roughness of the coatings and structural flaws in the coating (such as the visible craters on the coating surface) mean that there will be no shortage of sites at which electrical breakdown will occur more readily.

At the present stage, the data recorded has been insufficient to study the initiation step of the discharges in detail. As such this text will not speculate as to the precise nature of the physical processes which lead to the initial electrical breakdown of the coating. Instead the discussion will consider in some detail the development of discharge events after they have initiated. In chapter 6 it will be shown that once the initial breakdown has occurred, the subsequent development of the discharge event is heavily dependent upon the applied voltage. Once such relationships have been understood, it will be possible to understand the trends observed with coating

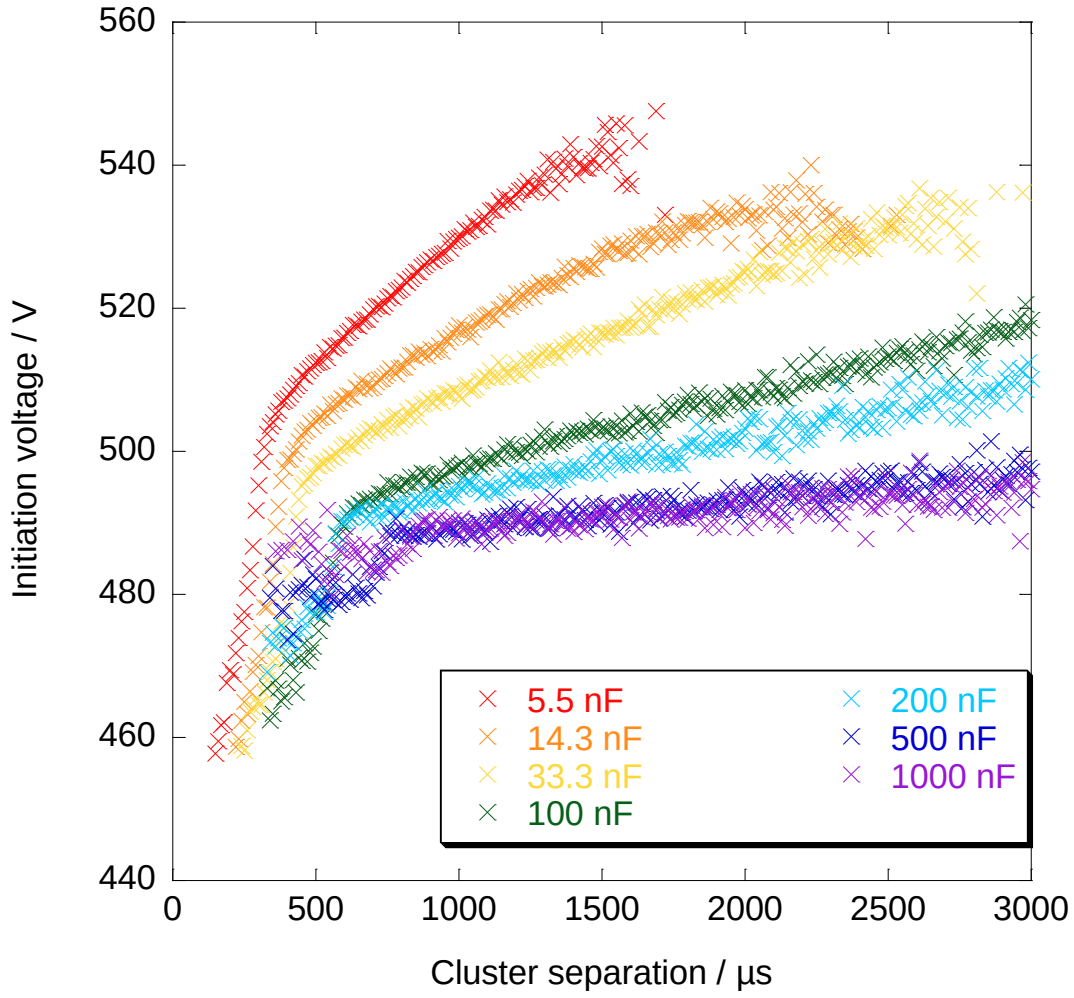

Figure 5.16: *Plot of the mean V_{init} for each 10 μs period after termination of previous event cluster. Only separation bins containing 10 initiated clusters were included. This data corresponds to the 12 minute coating.*

thickness and circuit capacitance for the I_{peak}, d_{sing}, P_{peak}, Q_{sing} and E_{sing} values measured from single discharge testing.

Chapter 6

Scaling Effects for Discharge Events.

So far many measurements of the discharge properties have been presented, but nothing has been presented to tie the measurements together into a more cohesive framework. The hints of some underlying principles have already been seen, especially in the single discharge data. Examination of Figure 5.5 and Figure 5.6 is suggestive of a link between the initiating voltage and the peak discharge current. This will provide a starting point for this discussion of the scaling behaviour of PEO plasma discharges.

6.1 Correlations between initiation voltage and peak current in single discharge data.

Correlations between single peak discharge event V_{init} and I_{peak} were performed by breaking down each dataset into subsets corresponding to a certain value of V_{init}. Recall that the voltage was recorded as 8-bit data over a range of $\pm$1000 V, and the minimum resolved voltage shift was 7.87 V. For each V_{init} value a list was generated of the I_{peak} values of all events which initiated at that voltage. This list of current values was then used to calculate every tenth percentile of the I_{peak} distribution at the specified V_{init}. Only voltages at which a minimum of 100 events initiated were included in such analyses.

The results of such calculation, for an 18 minute coating and a 200 nF circuit capacitance are displayed in Figure 6.1. Once the effects of the spread in V_{init} values are accounted for in this fashion, the distribution of I_{peak} values at each voltage is found to be quite narrow and symmetric, in contrast to the distributions seen in Figure 5.8.

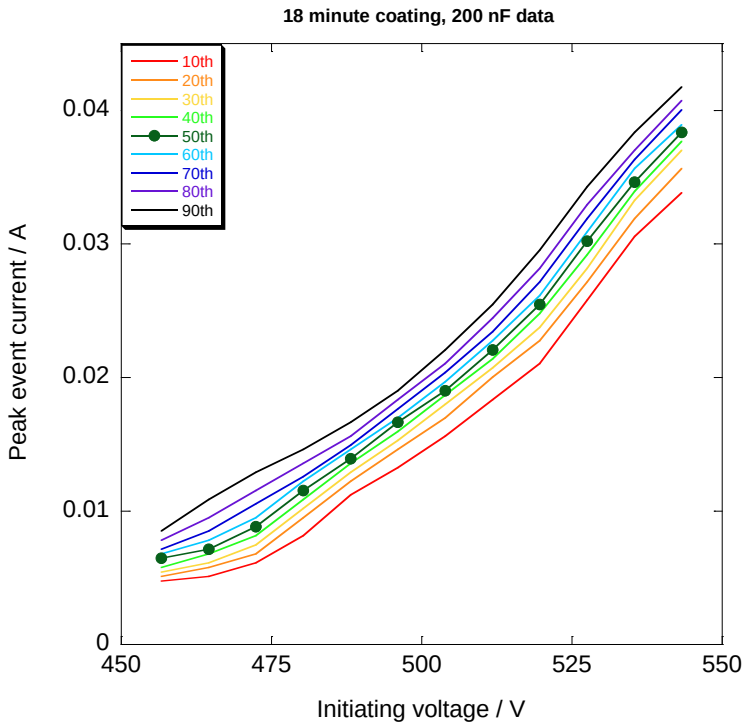

Figure 6.1: *Percentiles of the I_{peak} distribution for each voltage at which more then 100 events were observed to initiate. Data is from a coating processed for 18 minutes and taken with a 200 nF circuit capacitance. Voltage bin width was the minimum resolved value of 7.87 V.*

A strong correlation of the I_{peak} distribution with V_{init} is also seen in Figure 6.1. Similar calculations can be performed on all other combinations of capacitance and processing time, and these are plotted in Figure 6.2 and Figure 6.3. However, in these figures only the median I_{peak} is plotted, with error bars representing the upper and lower quartile I_{peak} values for each V_{init}.

Evident from the figures is the lack of sensitivity to the prior coating thickness, once the event has initiated. Overlap of the correlation plots from coatings of different thickness, using the same circuit capacitance, is well within the bounds of the uncertainty brought about by the distribution widths. The increase in I_{peak} with V_{init} is more pronounced for larger circuit capacitances, as shown most clearly in the summary plot of Figure 6.3, panel (d).

Two points should be made at this time. Firstly, despite tending towards linearity in the I-V plots for greater voltages, this is not indicative of a region of constant resistance of the discharge-electrolyte system, as a projection of the linear region towards zero current will not intersect the origin.

Secondly it should be borne in mind that whilst the discharge events develop to

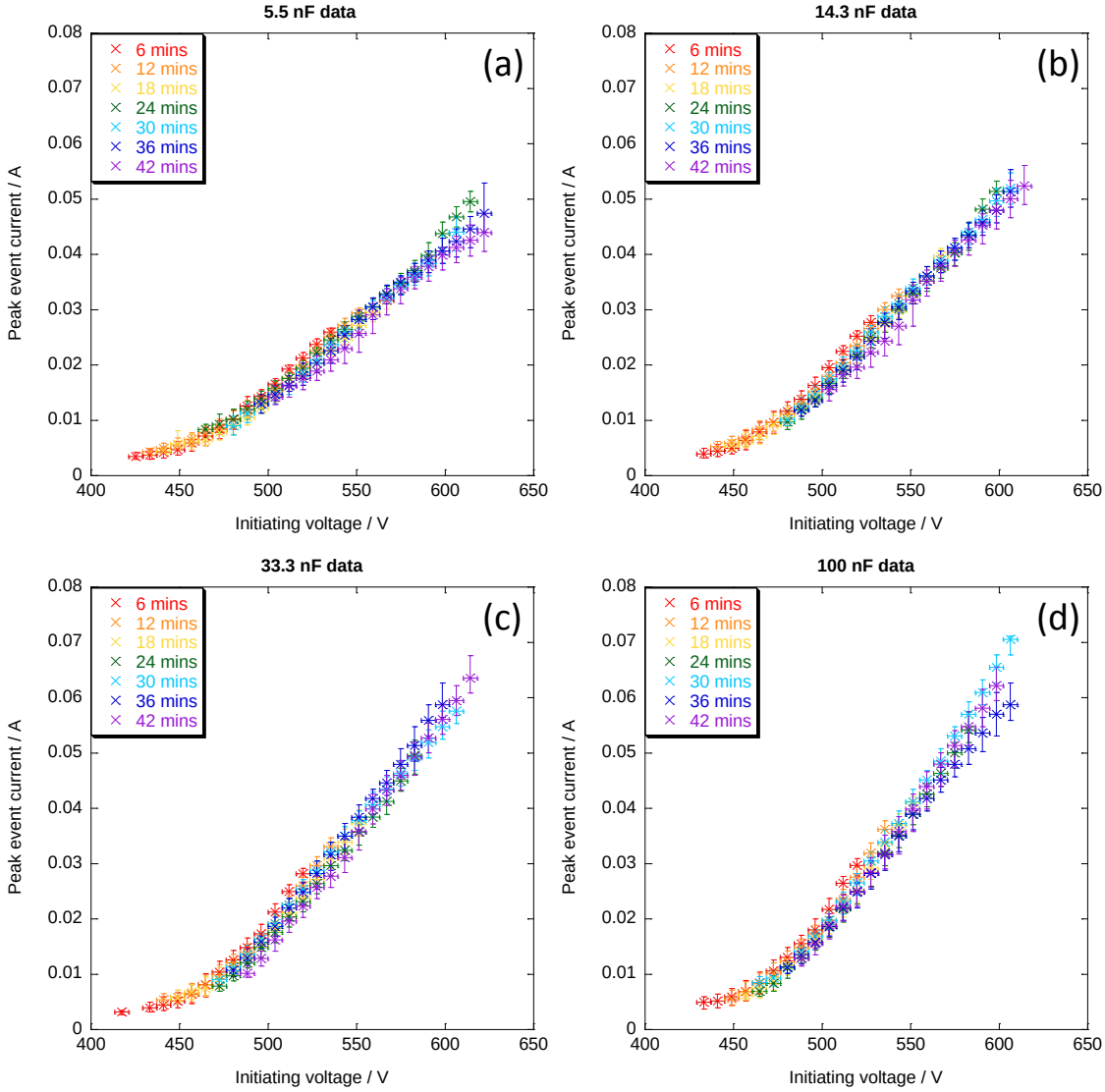

Figure 6.2: *Median values of I_{peak} as a function of V_{init}. A series is plotted in each panel for each coating thickness for (a) 5.5 nF data, (b) 14.3 nF data, (c) 33.3 nF data and (d) 100 nF data. Error bars in current represent the upper and lower quartiles of the peak current distribution. Voltage error bars represent the minimum resolved voltage shift in the experiment.*

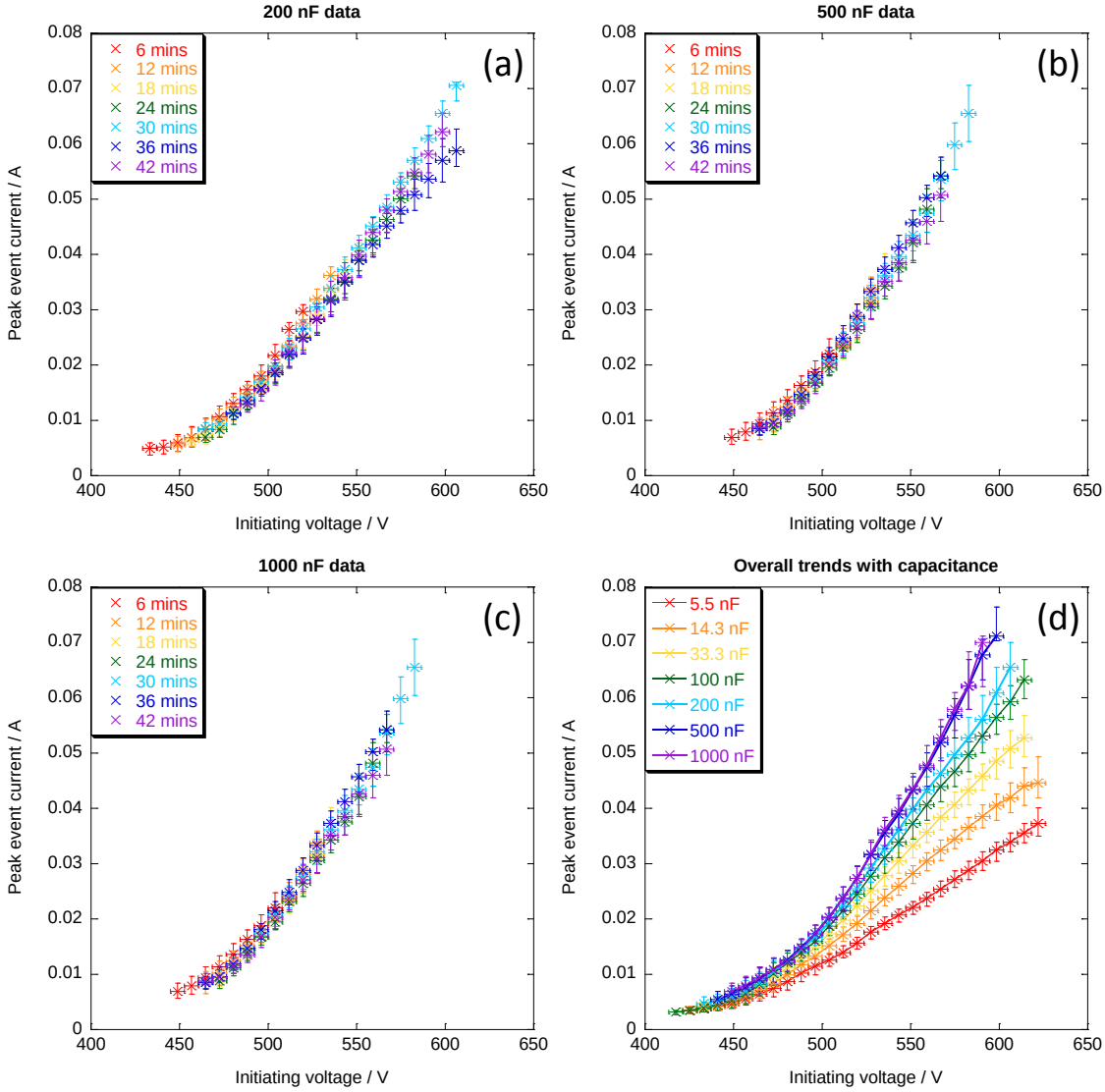

Figure 6.3: *Median values of I_{peak} as a function of V_{init}. A series is plotted in each panel for each coating thickness for (a) 200 nF data, (b) 500 nF data, (c) 1000 nF data and (d) overall data for all capacitances. Error bars in current represent the upper and lower quartiles of the peak current distribution. Voltage error bars represent the minimum resolved voltage shift in the experiment.*

the peak current without any strong influence of the existing coating thickness when plotted against V_{init}, this does not imply an independence of the discharges from the prior coating structure. Remembering the discussion of the likely probabilistic nature of breakdown event initiation, the probability of breakdown per unit time as a function of applied voltage will depend upon the existing coating thickness and structure. So in terms of the I_{peak} value reached, the existing coating determines the likely V_{init}, and thereafter the applied voltage determines the subsequent event development, up until the current peak is reached at any rate.

Such a dependence of I_{peak} on V_{init} might explain some of the literature results relating to bulk current and voltage measures. Arrabal et al found for processing of magnesium a significant 100 to 150 V decrease in applied voltage midway through deposition of coatings [**5**]. According to the authors this coincided with a transition of the processing to a 'soft sparking regime' with reduced apparent intensity of discharge activity. This would be consistent with the finding of this work about the dependence of discharge scale upon the applied voltage.

This does tend to lead into the question of why the I_{peak}–V_{init} relationship is influenced by the circuit capacitance. It has been stated numerous times that the purpose of the capacitance was to buffer the supply against the current loading of the event, by providing a reserve of charge and energy. This is the reason that the event development is influenced by the lower capacitances in particular.

As well as V_{init}, the voltage at the point of peak current, V_{peak}, was also measured, as is outlined in subsection A.1.15. The difference between V_{init} and V_{peak} can give an insight into the effects of increasing the circuit capacitance. Typical decreases for the different circuit capacitances are shown in Figure 6.4.

The plot tells two things, firstly that decreases in applied voltage as the event develops after initiation are probably responsible for the observed differences in rate of I_{peak} rise with V_{init}. Secondly, the still reasonably large voltage decreases seen with the 1000 nF capacitance would indicate that during bulk processing, when the voltage will remain essentially constant over event lifetimes, greater I_{peak} values still should probably be expected for any given V_{init}.

We are now in a position to understand the nature of the variation in the median I_{peak} values seen in Figure 5.5, panel (b). This can be explained using knowledge of two factors, firstly that the distribution of V_{init} values moves lower with increasing capacitance, as discussed in section 5.6. Secondly the increase in slope of the I_{peak}-V_{init} relationship with increased capacitance, caused by reductions in the voltage drop as the events develop.

For the thinner coatings (6 and 12 minutes), the median I_{peak} increases continuously with circuit capacitance. This is as the decrease in V_{init} with capacitance

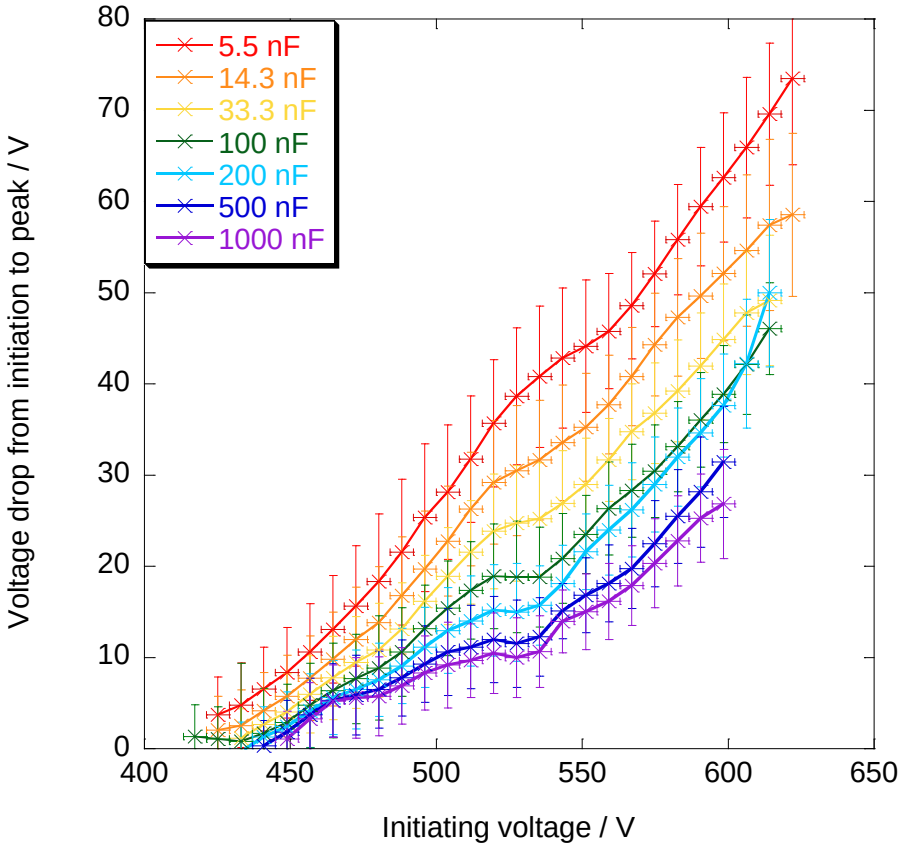

Figure 6.4: *Median differences between V_{peak} and V_{init} for the different circuit capacitances used, as a function of V_{init}. Error bars represent the upper and lower quartiles of the data at each V_{init} value.*

is low for the thin coatings, and the increased slope of the I_{peak}-V_{init} characteristic dominates.

As the coatings thicken, the V_{init} distributions are seen to be decreased more significantly with increasing capacitance (Figure 5.5, panel (a)). The I_{peak} values observed initially increase with capacitance as the slope of the I_{peak}–V_{init} characteristic increases. However, the rate of increase in the slope of the I_{peak}–V_{init} characteristic slows with increasing capacitance, as seen in Figure 6.3 panel (d), and at larger capacitances the shift to lower V_{init} values is large enough that it is not compensated for by the increased I_{peak}-V_{init} characteristic slope. This leads to the decrease in observed median I_{peak} for single discharge testing of thick coatings, for circuit capacitances above about 200 nF.

6.2 Discharge event scaling and average current development profiles for single discharge data.

During the computational methods discussion a procedure was outlined which allows the calculation of average current development profiles of discharge events, for times elapsed after initiation of the event, see section A.2. This analysis has so far been neglected, however it allows for a more visual understanding of the scaling behaviour of the discharge events.

Having established in the previous section that the I_{peak}–V_{init} characteristic is insensitive to coating thickness, to within the achieved experimental resolution, data used for calculation of average event development profiles will be averaged across the seven different thicknesses used. Calculated profiles and associated uncertainties are plotted in Figure 6.5 for the 1000 nF dataset.

With the exception of the smallest events, the shapes of the average discharge profiles remain similar as I_{peak} increases. A consequence of this is that d_{sing} scales in a similar fashion with voltage to I_{peak} (at least the median does). The scale of the uncertainty in the profiles is greatest around the peak current, though still of small enough magnitude that the peak values for each initiating voltage may be clearly differentiated.

The average profiles in Figure 6.5 are the average profiles for the median d_{sing} value at the relevant V_{init}. The average profiles for events of differing duration, within the subset of events for each V_{init}, are also of interest. This information is plotted in Figure 6.6. No systematic ordering of the different profile currents around the peak location is seen with total duration, and the profiles plotted all lie within about the standard error on the median d_{sing} profile.

The development up to the peak shows little variation, and the gradient of the

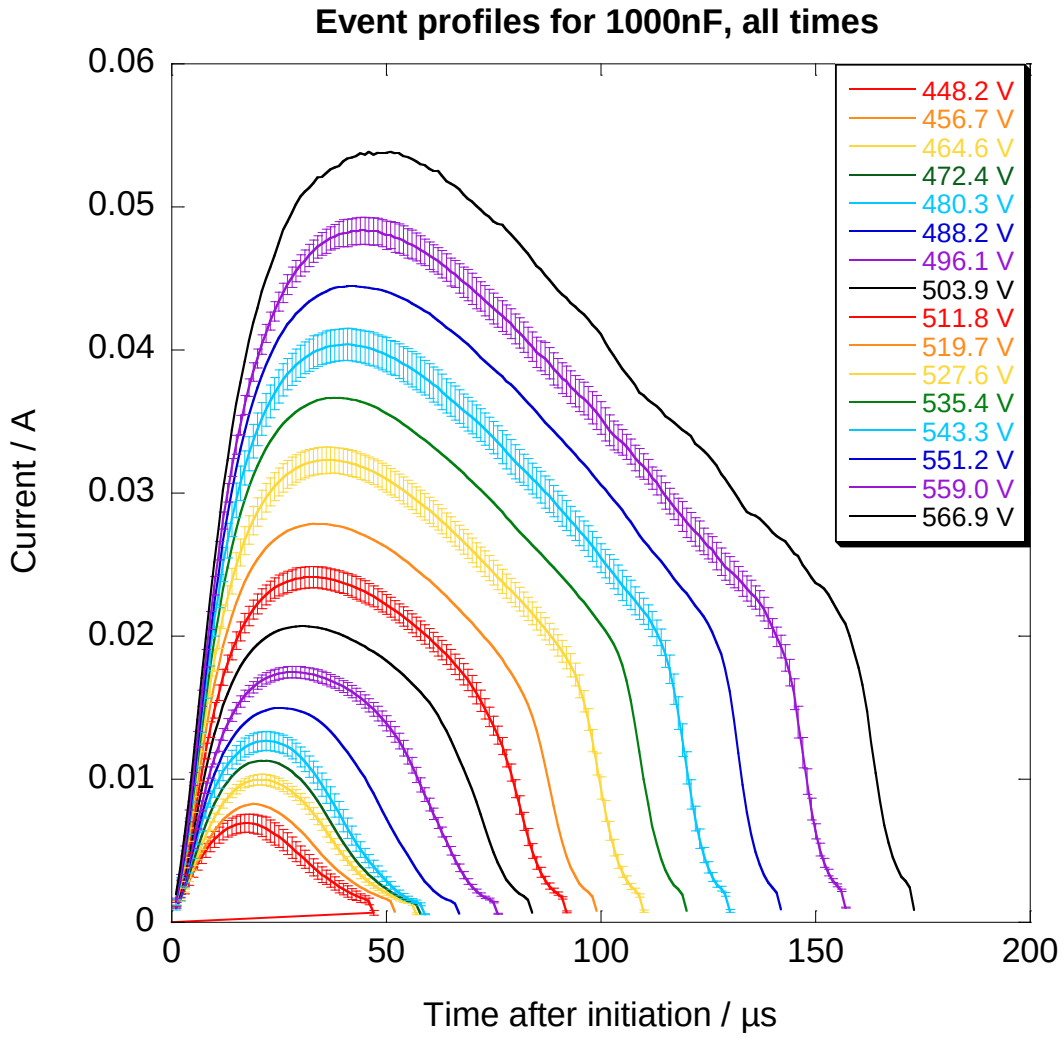

Figure 6.5: *Plot showing the averaged event development profiles for discharge events at a range of V_{init}. Profiles in each case are for the median d_{sing} within the specified V_{init} subset. Error bars plotted are the standard error on a single current measurement at that time after initiation of the event. Error bars are only plotted for every other data series to avoid overcrowding the figure.*

initial drop off after the peak appears similar in all cases. Much of the variation between the different durations observed for a specific V_{init} appears to be in the precise point during the initial region of decreasing current at which the final rapid drop off of current occurs.

The averaged voltage profiles were also calculated, however up until the point of event termination, no variation was seen for events which initiated at the same voltage but which continued for different durations. This is understandable considering the lack of significant deviations in the average current development profiles up until the termination point. It does indicate that the differences in event duration are probably not due to different behaviour of the applied voltage.

It is possible that the event termination is governed by the onset of some form of instability in the plasma bubble as it expands into the fluid, though there is insufficient data to test such a theory. What can be said reliably is that the event development is dominated by the applied voltage up until the point where the discharge current begins to drop rapidly.

6.3 Correlations between initiation voltage and event duration in single discharge data.

Given the scaling of events in both current and duration, it follows that there will also exist a correlation between V_{init} and the event duration, d_{sing}. The percentiles of d_{sing} at each V_{init} value for all coating process times, and with the 1000 nF circuit capacitance, are plotted in Figure 6.7.

The data in Figure 6.7 does show a strong correlation with voltage. The width of the distribution is observed to be relatively large than that of I_{peak} with V_{init}, especially towards the higher voltages (and hence larger events). This is likely a consequence of the uncertainty in the timing of the final collapse of the discharge current, as discussed with reference to Figure 6.6.

Having established that the discharge current signal scales in magnitude and duration with the voltage applied, the other properties derived from these properties, such as peak power and charge and energy transfer, will of course also show correlations with voltage. The other data presented in chapter 5 can therefore be rationalised along similar lines to the I_{peak} data.

As a final thought on the scaling of discharge events recorded during single discharge testing, the correlation between I_{peak} and d_{sing} will be considered. The percentiles of d_{sing} observed for 1 mA binning of I_{peak} values are plotted in Figure 6.8. A good correlation is seen, and there is no doubt that there is a strong likelihood of events which develop to greater I_{peak} enduring longer. It should be noted though

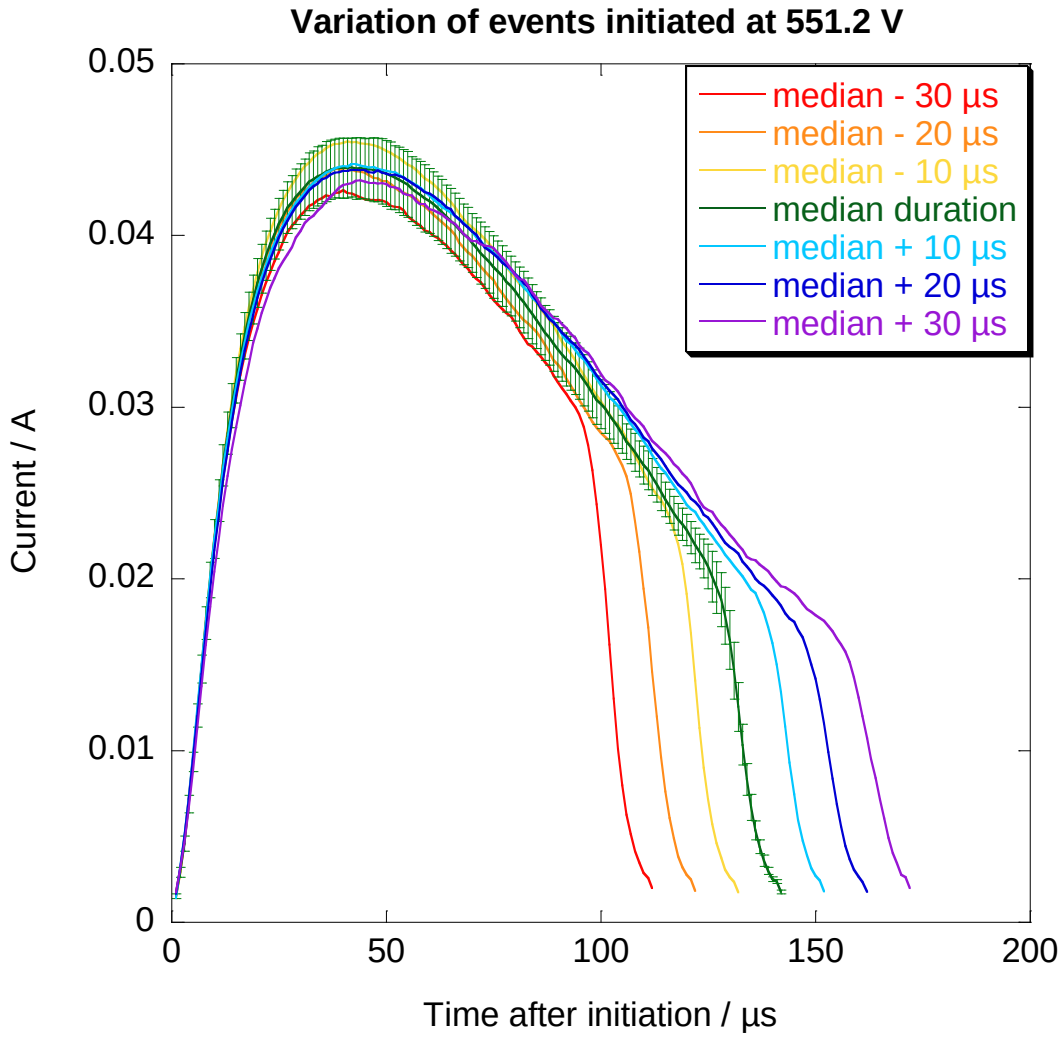

Figure 6.6: *Plot showing the averaged event development profiles for discharge events at 551.2 V. Profiles are shown for the median d_{sing} at this V_{init} and also for events within ±30 µs of the median. Error bars plotted are the standard error on a single measurement of the current at that time after initiation of the event, the error has only been plotted for the median duration profile.*

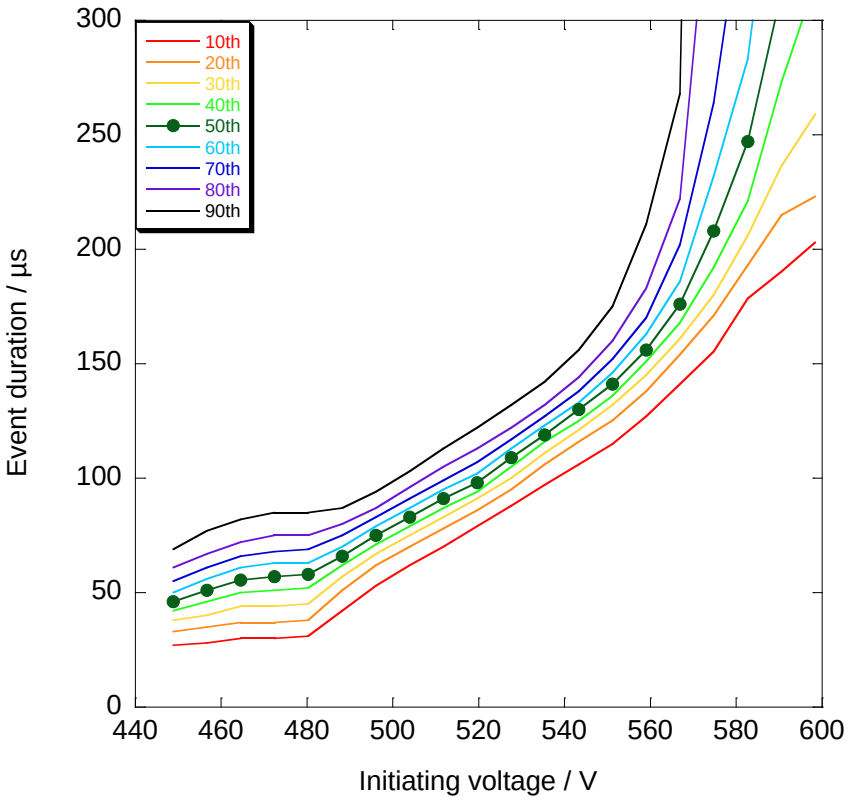

Figure 6.7: *Plot showing every tenth percentile of the distribution of d_{sing} at each V_{init}, for the 1000 nF circuit capacitance and including data from all coating thicknesses tested.*

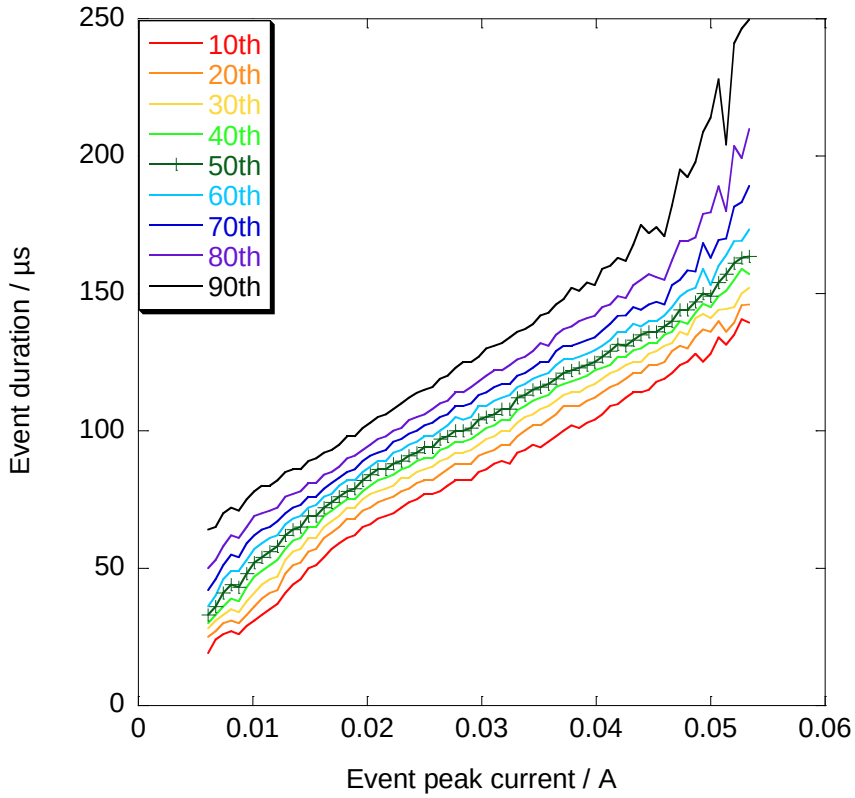

Figure 6.8: *Plot showing every tenth percentile of the distribution of d_{sing} for 1 mA binning of I_{peak} values, for the 1000 nF circuit capacitance and including data from all coating thicknesses tested.*

that the data indicates a reasonable range of d_{sing} at each I_{peak} value, an indication perhaps of the uncertainty in the exact point at which the discharge current finally collapses.

6.4 Correspondence to in-situ monitoring data.

Having established a relationship of the event properties to the applied voltage for single discharge experiments, we can now ask whether similar relationships hold for discharges recorded as part of bulk processing experiments. The degree of correspondence between the two datasets can also be assessed, as the scaling relations allow for the difference in the electrical conditions applied to be compensated for to a certain extent.

We shall begin by considering the correlation between I_{peak} and d_{sing}, plotted in Figure 6.8 for single discharge data with a 1000 nF capacitance. The median duration for each I_{peak} value, using 1 mA binning, is plotted for each 150 s monitored

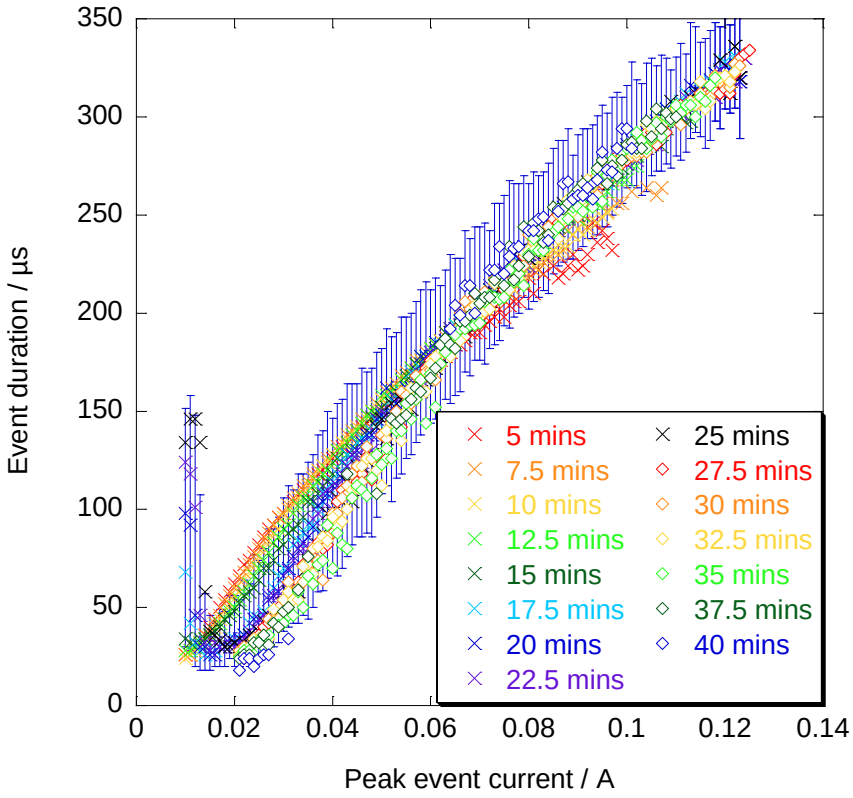

Figure 6.9: *Plot of the median d_{sing} as a function of I_{peak} for in-situ data. Error bars plotted for the 20 minute data series were typical, and represent the distance from the median to the upper and lower quartiles. Other error bars were not plotted for clarity of the median positions.*

period during in-situ experiments in Figure 6.9. The data for each time of processing refers to the 150 s up to the specified time, and includes data obtained during the specified time window.

There is a strong correlation evident in Figure 6.9 between I_{peak} and d_{sing} values. The correlation is also seen to be minimally affected by the time of processing, as was found for single discharge experiments. The largest deviation is seen for I_{peak} below about 40–50 mA, where the median d_{sing} values for the data corresponding to the first 15 minutes are seen to be slightly greater than for the data at subsequent times. Referring back to chapter 4, there was a change in the observed distributions of discharge properties between about 700 and 1000 s into processing. Whether the split seen in Figure 6.9 is related to this is not presently clear, though it would be tempting to make the association.

A comparison can be made between the in-situ data and the single discharge experiment based around the I_{peak}-d_{sing} correlation. Only the data from the 1000 nF

experiments will be used, as this was the least impacted by the voltage decreases inherent in the single discharge experiments. Data for all process times was considered together for both the single discharge and in-situ monitoring experiments. The comparison can be found in Figure 6.10.

Good agreement is seen between the two datasets, despite the major differences in electrical conditions used to generate them. The agreement is especially good for events which exceeded I_{peak} values above 30 mA. At lower I_{peak} values the single discharge data is found to lie at longer durations then the in-situ data. The exact cause of this, and the significance, is not clear at present, though it may be related to the different electrical conditions applied in each case.

In the single discharge experiments the voltage always decreased after initiation. How this could lead to longer lived discharges is unclear. In the in-situ experiments, any event was effectively in parallel with a large number of other active discharge events (on the large unmonitored area). If more discharges ignited during the course of an event, the additional pathways provided through the coating would tend to reduce current flow to all other active events slightly. This might give rise to a truncation of events in the in-situ monitoring experiment, and may explain the observed differences in Figure 6.10. Such effects of competition between active discharge events will be discussed further in section 6.5.

6.4.1 Correlations of initiating voltage and peak current during in-situ monitoring.

The occurrence of each discharge event as part of a larger set of active discharges during in-situ monitoring led to some significant deviations from the behaviour seen for single discharge events. A similar plot to Figure 6.10 is plotted for the correlation of V_{init} and I_{peak} in Figure 6.11.

Three things in particular are worth noting from the figure, firstly the median I_{peak} value from single discharge experiments is greater then the median I_{peak} from in-situ monitoring, especially at larger values of V_{init}. Secondly the distributions of I_{peak} for each V_{init} value are much wider for the in-situ data. Finally the lower end of the I_{peak} distribution shows no significant increase with V_{init} for in-situ experiments. The significance, or otherwise, of the slight downward shift of the distribution of I_{peak} values above 600 V is unclear. It is seen only for the 60^{th} percentile and lower, and is possibly indicative of a sharp rise in the number of simultaneously active events at large voltage. With the depression of I_{peak} values being due to the discharge interaction effects discussed in section 6.5. Whether this is the case or not, and whether the drop seen above 600 V is significant, is unclear at present.

Before discussing the possible reasons for the markedly different behaviour seen

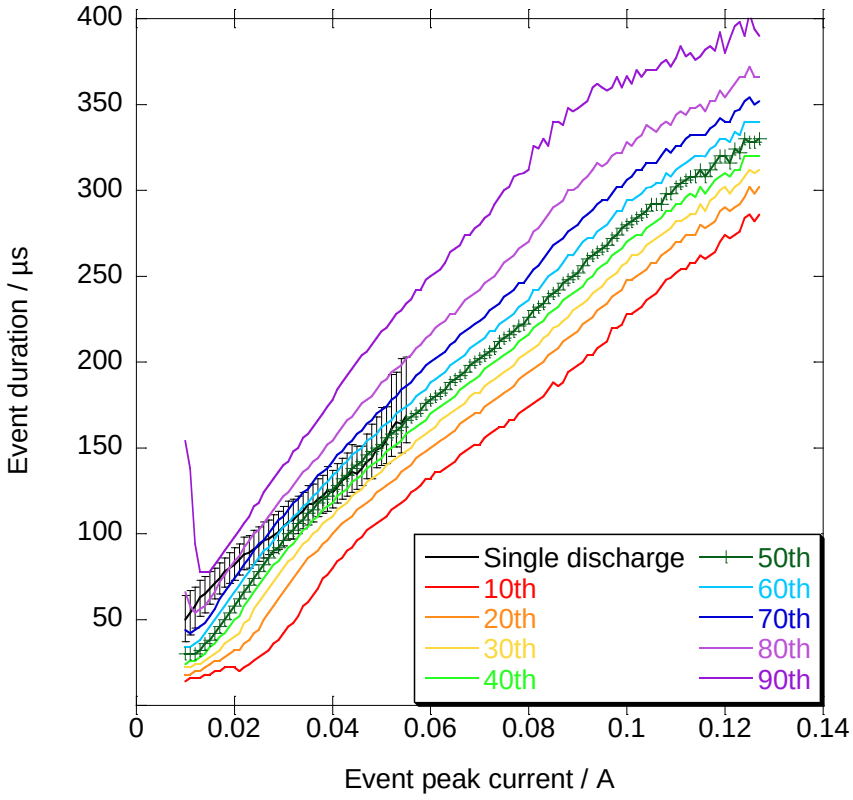

Figure 6.10: *Plot of every* 10^{th} *percentile of the* d_{sing} *distribution against* I_{peak} *with 1 mA binning, for the in-situ monitoring experiments. The median duration is plotted for the single discharge experiments with 1000 nF capacitor, and the error bars plotted represent upper and lower quartile of the* d_{sing} *distribution for the 1000 nF single discharge data within each* I_{peak} *bin.*

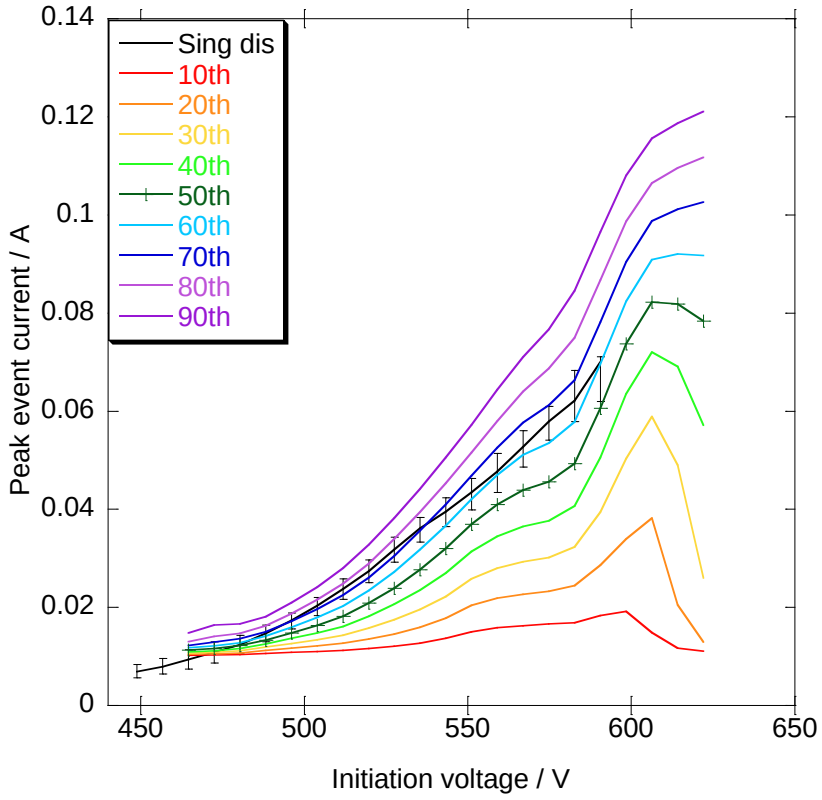

Figure 6.11: *Plot of every* 10^{th} *percentile of the* I_{peak} *distributions for each* V_{init}*, for the in-situ monitoring experiments. The median* I_{peak} *is plotted for the single discharge experiments with 1000 nF capacitor, and the error bars plotted represent upper and lower quartile of the 1000 nF single discharge* I_{peak} *distribution at each* V_{init}*.*

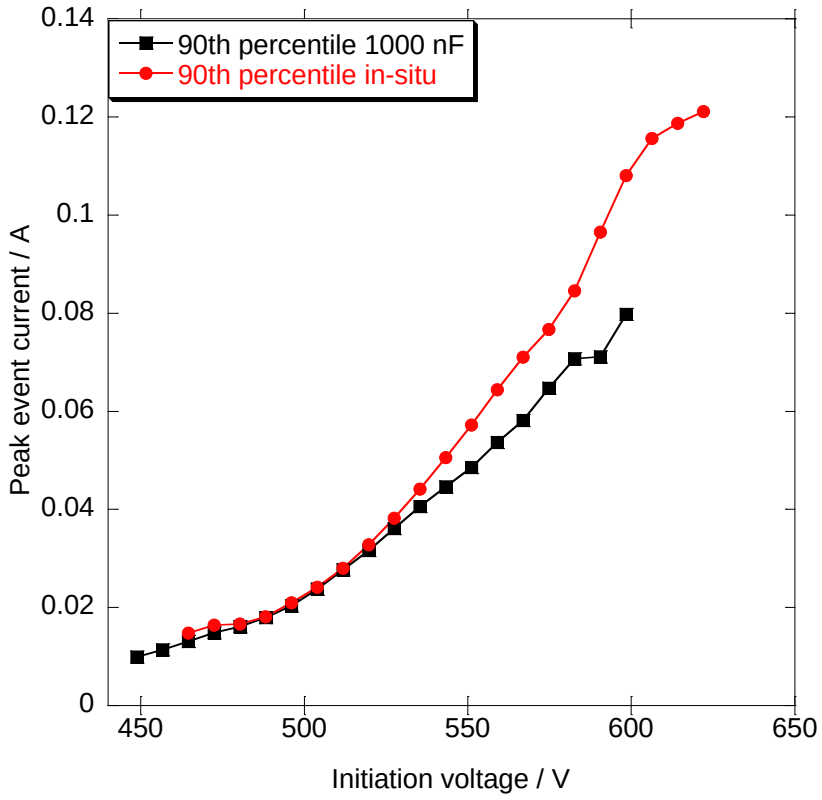

Figure 6.12: *Plot of the* 90^{th} *percentile of* I_{peak} *for each* V_{init} *for both the single discharge experiment with 1000 nF capacitance and the in-situ monitoring experiment.*

during in-situ monitoring experiments, the reader should examine the data plotted in Figure 6.12, which displays for both single discharge and in-situ datasets the value of the 90^{th} percentile of I_{peak} at each value of V_{init}. In this figure it can be seen that whilst practically identical up to about 525 V, the upper end of the I_{peak} distribution for the in-situ data lies at higher current than the single discharge data for further increases in V_{init}.

The difference in the trend seen for distributions of I_{peak} values with V_{init} between the single discharge and in-situ monitoring experiments is due to competition for current between concurrent discharge events in the bulk processing case. To help understand this it will be useful to re-cap what was found for the I_{peak}-V_{init} relationships as the capacitance was increased.

From panel d) of Figure 6.3 it can be seen that the increase in I_{peak} with V_{init} was more pronounced for larger capacitances. And it was then shown in Figure 6.4 that the decrease in voltage between the point of initiation and reaching peak current increased for decreases in circuit capacitance. This establishes that decreases in voltage over the initial period of the event development reduce the value of I_{peak}

reached. For the in-situ monitoring data, in which the voltage did not vary significantly between initiation and the peak in discharge current, it would be expected that I_{peak} values at a given V_{init} would be greater than for even the 1000 nF dataset from single discharge experiments. This is as moderate decreases in applied voltage, up to ~ 30 V, were seen for the 1000 nF dataset between event initiation and peak discharge current.

If we consider just the 90^{th} percentile of I_{peak} data at each V_{init}, which may be considered as an upper bound on the discharge current achievable at a given value of V_{init}, as in Figure 6.12, the expected trend is observed. This indicates that the maximum I_{peak} that can be reached by discharge events is determined by the applied voltage in both experiments. The enhancement of the 90^{th} percentile of the in-situ data with respect to the 1000 nF data seen in Figure 6.12 is due to the absence of a voltage decrease after event initiation in the in-situ case. The deviation becomes larger as V_{init} increases, as the decrease from V_{init} to V_{peak} for the 1000 nF single discharge data also becomes larger for greater V_{init}, as seen in Figure 6.4.

Having established that both physical systems have applied voltage as an upper bound on I_{peak}, the question remains as to why the distributions of I_{peak} with V_{init} are different within the context of bulk PEO processing. Two simplified models of discharge event interactions can aid this discussion. Both are simplistic, and neither represents an especially close analogy to the reality, as the actual interaction is likely closer to a mixture of the two viewpoints. On a basic level, the difference seen between single discharge and in-situ datasets arises because in the former the voltage is applied across a single event, whereas for the latter the voltage is applied in parallel across many discharge events.

6.5 Discharge event interactions during bulk PEO processing.

The first model considers a network of resistors connected in parallel. For a network of N resistors, each of an unspecified resistance R_j, with an imposed current of I_T, the current through each resistor will be given by the expression in Equation 6.1, with R_T the total resistance of the network. Examination of the current records throughout the preceding text of this work will show that the effective resistance of discharge events decreases from the initiation point to the peak current. Consider next a discharge event which initiates at a point in time when several other discharge events are already active across the sample surface. Assume further that the already active discharges were initiated before the new event, and have already reached a

stage of development at which they present a significantly less resistive path.

$$I_j = \frac{R_T I_T}{R_j} \tag{6.1}$$

To put some numbers on this, the median resistance at the peak for an event from single discharge testing with 1000 nF capacitance, initiated at 574.8 V, was $\sim 9500\ \Omega$. By contrast, at the early stages of a discharge event the dynamic resistance of the discharge is of the order several times $10^5\ \Omega$. It can be seen then that if another discharge event initiates whilst several, more developed, events are active, it will impact the total resistance, R_T, negligibly. The current drawn by the new event will also represent a small fraction of the total by Equation 6.1. This will reduce dramatically the energy input to the new event, and the development of the discharge will likely be curtailed with respect to an event initiated in isolation.

So whilst the maximum I_{peak} may be bounded by the applied voltage, the presence of concurrently active events across the sample surface will lead to a reduction in the power supplied to any subsequently initiated discharge events. The degree to which events are curtailed will be determined by the number and state of development of the already active discharge events. This sort of competition between discharge events could explain why the distribution of I_{peak} with V_{init} is so different between single discharge and in-situ experiments.

There are not usually multiple events active on the small monitored area, however it is being processed in parallel with an area ~ 100 times larger, and so there will be a large number of discharge events active on the unmonitored areas of the sample. By contrast an event initiated during single discharge testing has (more often than not) no competition from other events, which may be why a much tighter correlation is seen for I_{peak} and V_{init}.

That is one way to view the discharge interactions, but likely not the whole story and alternative views should be considered. Whilst the resistance of the actual discharge filaments is probably not large, the total contribution from the electrolyte when the current flows locally to a small area (the discharge plasma bubble) could be large. If the plasma bubble is assumed to be a perfect hemisphere, of radius r_P, on the surface of the coating. And if it is assumed that the counter-electrode is sufficiently distant and large that the current flow to the bubble may be considered to be perfectly radial, then the total resistance from the surface of the bubble to infinity is given by Equation 6.2.

$$R = \frac{\rho}{2\pi r_P} \tag{6.2}$$

The total potential difference between the bubble radius, r_P, and general radius r can be derived for specified discharge current I as in Equation 6.3.

$$\Delta V = \frac{I\rho}{2\pi}\left(\frac{1}{r_P} - \frac{1}{r}\right) \tag{6.3}$$

The diameters of discharge events from Matykina et al [**8**] and Yerokhin et al [**2, 7**] were of the order of several hundred μm. For the purposes of an estimate, assume a value of $r_P = 100$ μm, and take the discharge current to be 50 mA. The conductivity of the electrolyte used was measured to be 5.1 ± 0.1 mS.cm^{-1}, giving for the resistivity a value of $\rho \approx 2$ Ω.m. If we then use these values to estimate the potential drop between the plasma bubble surface and a radius 1 mm from the discharge site, the value obtained is $\delta V \approx 143$ V.

This is likely a serious overestimate, and the assumption of radial symmetry of the current to the plasma bubble is clearly inaccurate. The discussion does demonstrate that current flow to active discharges could influence the development of other events by reducing the effective potential difference at other regions of the coating. If breakdown did occur some distance from the active event, it would be at an effective voltage below the bulk applied potential, and would develop to lower current accordingly. Such effects cannot be distinguished in the in-situ data, as only the overall voltage could be measured.

Neither of these two examples is sophisticated enough to provide a sensible model for the circuit interactions of discharge events during PEO processing. The examples serve simply to illustrate some basic physical reasons why the distributions of I_{peak} as a function of V_{init} display such a wide spread, as is seen in Figure 6.11. The measured voltage between substrate and counter-electrode does not represent the absolute value of voltage driving individual events observed during in-situ monitoring, it can only tell the maximum driving force available to develop each event.

The exact reason why the voltage should determine an upper bound on the discharge current is not clear, however the applied voltage does establish an energy scale for the event, and the development of discharge events is likely to be linked to the energy that can be supplied by the external circuit. In this regard it is perhaps not surprising to find discharge event scale to be bounded by applied voltage.

6.6 Averaged profiles of discharge events recorded during in-situ monitoring experiments.

The averaged profiles for a selection of different possible event durations of discharges initiated at 559 V, during in-situ monitoring experiments, is presented in

Figure 6.13. The difference when compared to Figure 6.6 is pronounced. This gives an indication of the impact of competition with other active discharge events on the development of discharge events.

The event profiles have relatively larger standard error on a single current measurement then for the single discharge data. Scaling of the discharge event shape is also seen, reminiscent of Figure 6.5 for differing initiating voltages. Scaling of the peak current only continues up to an upper bound determined by the voltage, at which point event average profiles get no higher, only longer. This is seen in the longest average profiles plotted in Figure 6.13.

Similarity of the scaling behaviour below the upper bound of peak current to variations seen with applied voltage in single discharge experiments, is supportive of the view that the effective voltage driving any given event development is variable, and determined by the number and state of development of other discharge events active at unmonitored sites elsewhere on the substrate surface.

6.7 Estimation of discharge event physical scale.

The values of the discharge resistance at peak current, R_{peak}, were plotted in Figure 5.4 previously. The trends of R_{peak} with I_{peak} are re-plotted in Figure 6.14, though in this case each series represents data from all coatings for a specific value of the circuit capacitance. This data shows the same trend as was observed in Figure 5.4, and confirms that R_{peak} as a function of I_{peak} was not sensitive to the capacitance used during testing. Only data from the single discharge testing can be used for this purpose, this is due to the effects discussed in section 6.5. The resistance due to a single event, and the current flow to the event, cannot be determined for the in-situ experimental data, in which the voltage is applied in parallel across multiple active events at the same time.

A simple model already briefly discussed in section 6.5 can be applied to produce a crude estimate of the physical size of discharge events. Recall Equation 6.2 for the resistance for radial current flow to a hemispherical bubble. If it is assumed that at the point of peak current the conductivity of the plasma is much larger than that of the electrolyte, Equation 6.2 can be used to estimate a radius for the plasma bubble, using the R_{peak} values and the measured resistivity of the electrolyte used, $\rho \approx 2\ \Omega$.m. Results of such calculations are presented in Figure 6.15.

The assumption of much greater conductivity for the plasma may be considered in terms of reported conductivity values for partially ionised plasmas. Data from experiments on partially ionised caesium by Roehling [**50**], indicated $\sigma \approx 1$ S.cm^{-1} for a temperature of ~ 1800 K, falling rapidly as the temperature dropped, but not

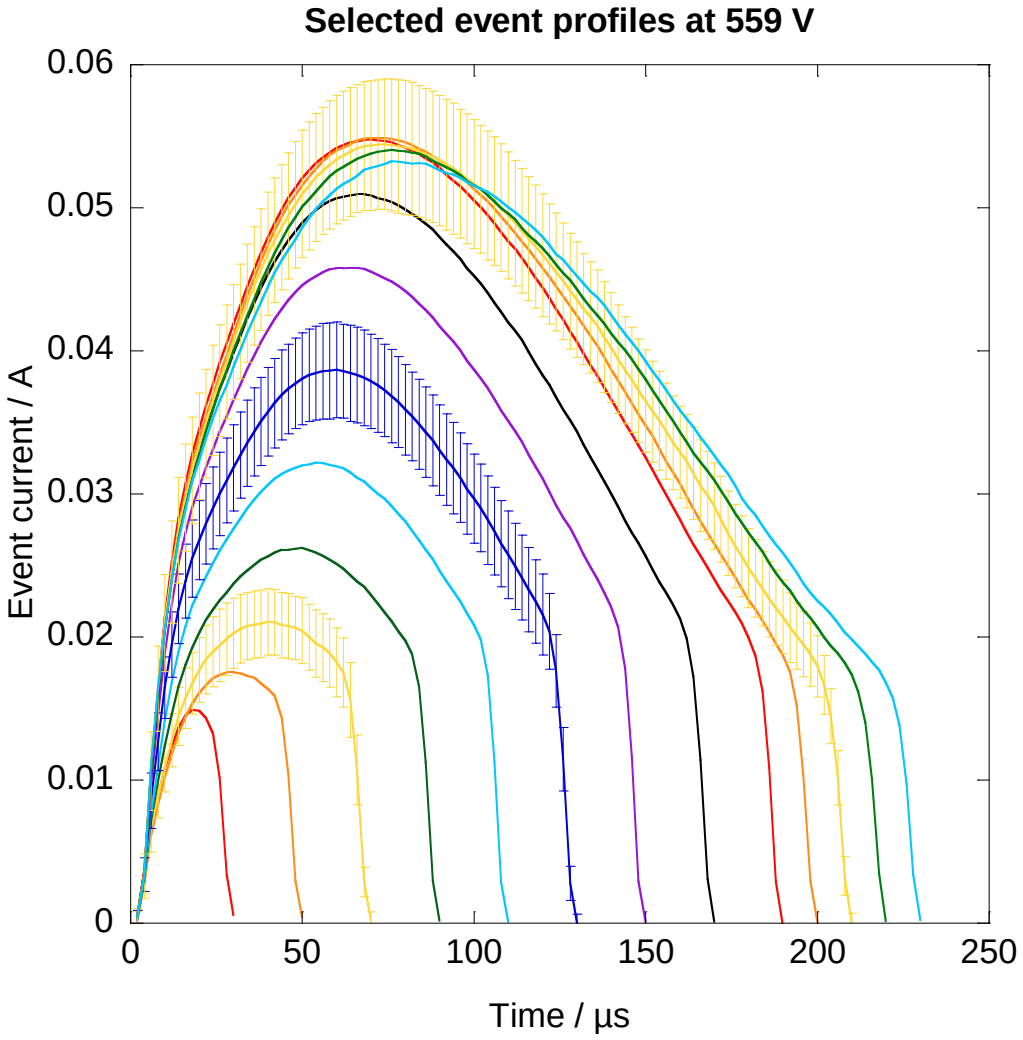

Figure 6.13: *Plot showing the averaged event development profiles for discharge events at 559 V, taken from in-situ monitoring data. A series of the observed event durations is plotted, and error bars plotted for selected series represent the standard error on a single measurement of current at the relevant time after initiation of an event with the respective duration. Not all error bars were plotted for clarity of the figure, those plotted are representative of the trends observed.*

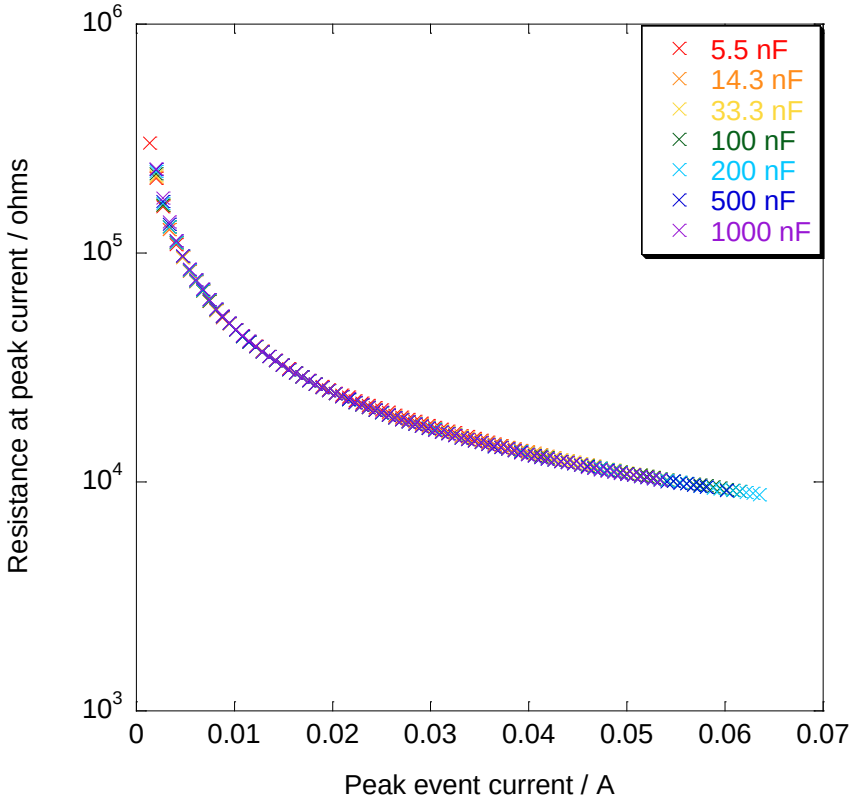

Figure 6.14: *Dynamic resistance of discharge events at the point of peak current, R_{peak}, as a function of I_{peak}, with bin width of* 676 μA. *The width of the distribution of R_{peak} values at each I_{peak} value was found to be too small to be resolved if plotted on the figure.*

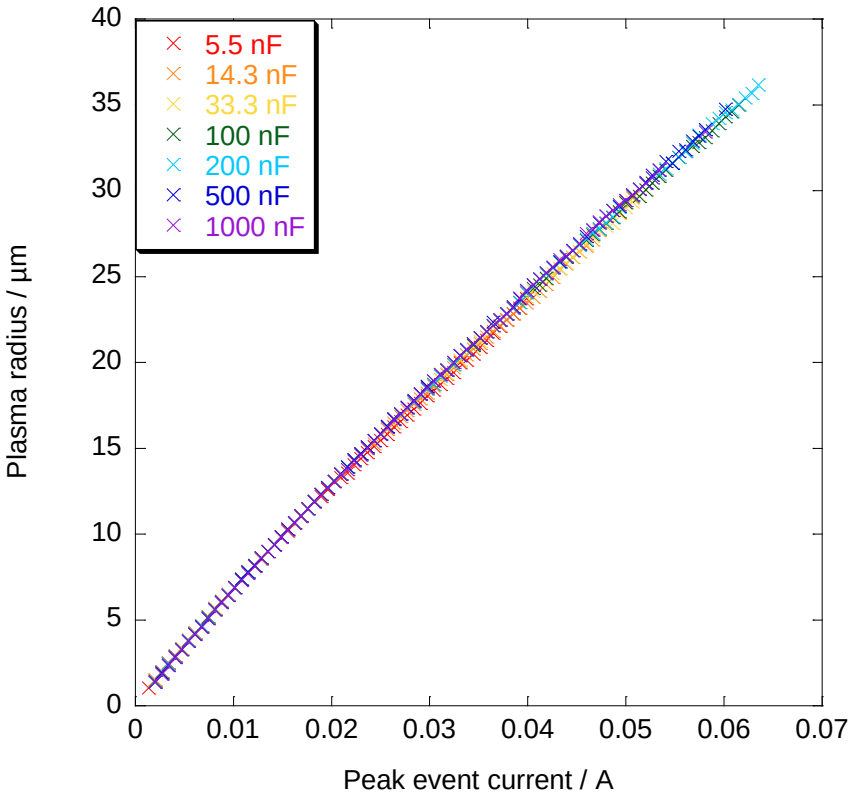

Figure 6.15: *Estimated radius of the plasma bubble, r_P, at the point of peak current as a function of discharge peak current, I_{peak}, with bin width of* 676 μA.

equal to the electrolyte conductivity of 5.1 ± 0.1 mS.cm^{-1} until a temperature of ~ 1300 K.

Kim and Kim calculated the conductivity of non-ideal aluminium [**51**] and non-ideal iron and nickel plasmas [**52**]. The lowest temperature for which they report values is 10 000 K for aluminium and 14 000 K for iron and nickel. For all three metals the authors report minimum conductivities of > 10 S.cm^{-1}, at least a thousand time greater then the electrolyte conductivity. The temperatures reported for PEO plasmas ranged from 3000 to 16 000 K [**1, 14, 15**], so the plasma conductivity has potential to be significantly greater than that of the electrolyte for at least part of the development of discharge events.

The values of radius estimated in Figure 6.15 are unlikely to be especially accurate, however they compare well with the reported scales of discharge plasmas reported in previous literature studies. Work by Matykina et al [**8**] and Yerokhin et al [**2, 7**], found the discharge diameter to be in the range of a few hundred μm (see subsection 2.1.4 for more discussion of literature values). The values of plasma radius estimated in Figure 6.15 are below these values, however these would represent the discharge scale at the peak current value. This occurs at a comparatively early stage of discharge development, no more than a quarter to a third of the way through many events (see Figure 6.5), and so discharge events would probably continue to expand beyond this point. The scale estimated in this fashion is in good agreement with the scale of a few hundred μm obtained from analysis of optical images. With more information about plasma electron temperature and density, potentially obtainable from time resolved spectroscopy of discharge events, the measured current signals could be used to develop a more physically realistic model of the discharge plasma. Such an undertaking is beyond what is possible with the information presently available.

Chapter 7

Conclusions

7.1 Characteristics of discharges.

The measured discharge characteristics presented in chapter 4, chapter 5 and chapter 6 are specific to the combination of substrate, power supply and electrolyte used in the present study. Without similar detailed information from another system it is not possible to say to what extent the present data may be taken as representative of wider PEO processing. Whilst the specific details will not be the same in other PEO systems, the general features observed and the scaling relationships obtained can allow some broad conclusions about PEO systems to be reached.

- At all times during PEO processing the discharge events are initiated across a range of voltages; no evidence was seen of a well defined breakdown voltage for discharging behaviour, even for a fixed coating thickness.
- Discharges occur across a range of scales in current, duration, power, energy dissipated and charge transferred, at all points during coating deposition.
- Current-time plots of PEO discharges display self-similar scaling between events which reached different peak discharge currents. This means that correlations are seen between peak current and total duration, and probably also physical size. The precise scaling of the typical discharge durations with the discharge peak current probably varies between processing systems, but the existence of such scaling behaviour would be expected for all PEO systems.
- The maximum scale of a PEO discharge event, in terms of electrical characteristics, is bounded by the applied voltage. The precise details of the relationship, for example the gradient of the correlation, would be assumed to be different for different substrates, electrolytes, or power supply systems,

but a limit on the maximum scale of the discharge events with voltage will probably apply to all systems.

- The initiation step of PEO discharge events has not been well resolved in the present work. Evidence is presented which is consistent with a probabilistic dependence of breakdown upon applied voltage. This manifested as a sensitivity of measured coating breakdown voltages to the rate of voltage increase during single discharge testing. Whilst the exact mechanism which leads to this behaviour cannot be determined from the present dataset, it is probable that similar behaviour would be observed for other PEO systems.

- The high degree of variability seen in the discharge characteristics demonstrates that large numbers of measurements are required in order to develop a reliable picture of discharge event behaviour in any given PEO processing system.

- No clear separation of the discharge events into different types, eg sparks, micro-arcs, arcs etc, was evident in the discharge characteristic measurements, or in the averaged current development profiles. The discharge events recorded formed a continuous range from small to large scale events, and the similar current development profiles at different event scales indicate strongly that the same physical factors are involved in the development of all discharge events. Such distinctions between different 'regimes' of discharge types should not be applied to the PEO process.

- The apparently longer lifetimes of discharges at longer processing times, when observed by eye or low speed optical imaging, is most probably the result of increased clustering and greater persistence of PEO discharges at, or close to, the same spatial location.

7.2 Effectiveness of the techniques presented

The two experimental methodologies presented for the quantitative investigation of PEO discharge events have been shown to allow measurement or calculation of many useful characteristics of discharge events.

- The 'in-situ monitoring' technique allows for the measurement of discharge event characteristics representative of PEO processing in the system under investigation. In the present work the majority of data obtained did not allow events smaller then 10 mA to be resolved. However, it was also shown that such a limit was not inherent to the procedure.

- The 'single discharge' technique allows for the study of discharge event behaviour in the absence of interactions with concurrently active discharge events elsewhere on the substrate. In particular this allows the relationship between event development and applied voltage to be studied. Such studies cannot be performed for the in-situ experiments as the precise electrical environment in which a recorded discharge occurs cannot be determined in the in-situ testing.

- The single discharge testing does not allow event characteristics representative of the bulk processing to be obtained, though event characteristic correlations between peak discharge current and event duration compare well with those obtained from in-situ experiments with the same electrolyte. Averaged current development profiles were also seen to present a close match to the in-situ dataset.

- Both methods presented in this work allow high data acquisition rates, and are easily adapted to facilitate multiple, rapid, repeats. This is a requirement for studying PEO discharges in any experimental system due to the high variability possible between any given discharge event and the next event to occur.

- Application to other PEO coating systems would require changes to be made to some of the experimental parameters. Mostly this would be superficial things such as the sizes of resistances and relative areas of samples. Slight adjustments to the computing procedures would probably also be required for the study of some alternative PEO processing systems.

7.3 Further work

There exists significant potential for further work, most importantly the application of the quantitative measurement techniques presented in this work to other systems of electrolyte, substrate and power supply. Such investigations will allow understanding to be developed of the connections between discharging behaviour and coating structure. The dependence of discharging behaviour upon the electrolyte composition and concentration could be studied. Studies of systems known to result in different phase compositions of coatings could be made, so that the hypothesis of a link between discharge event thermal heating intensity and relative phase proportions can be tested.

Development of a methodology to allow the probability of coating breakdown as a function of applied voltage to be reliably measured should be a priority of any

further work. Understanding the initiation step of the discharge events is a key aspect of discharge behaviour which was not well resolved in the present work.

Appendix A

Data analysis procedures for single discharge experiments

A.1 Single discharge data processing.

The processing of information recorded from single discharge testing will be described in this appendix. Algorithms for each task will be presented and described, and the operation of each upon a representative section of data illustrated with figures where appropriate. The example section was taken from testing of an 18 minute coating using a 200 nF capacitor, and the value of the current measurement resistor was 464 Ω. Calculations were performed using Matlab 7, and algorithms were written in the scripting language of that package. Pseudo-code will be used in preference to source code in this discussion for purposes of clarity.

A.1.1 Scaling of variables and calculation of the baseline current level.

The first procedure is to scale the raw data so that current and voltage data are in (S.I.) units. The data for voltage and current was in the form of vector arrays, with 10 million entries each. The current data was in the form of the voltage across the probe resistor, of magnitude R Ω, which was recorded using a 1× attenuation probe. The voltage data was recorded using a 100× attenuation probe.

The vector containing the voltage data was called A, and the vector containing the current B. The scaling used was as detailed in Equation A.1, in which the

subscript j refers to the j^{th} element of the relevant vector array.

$$\begin{aligned} V_j &= A_j \times 100 \quad \forall \quad j \\ I_j &= \frac{-B_j}{R} \quad \forall \quad j \end{aligned} \tag{A.1}$$

The minimum resolvable current step was determined according to Equation A.2. This results from the resistance, R, having been set to generate a signal from the current in the range 0 to 20 V. The factor of 127 results from the 8-bit digitisation of the data by the oscilloscope. I_{step} represents the minimum resolvable shift in the current signal. For the data section which will provide illustrative examples, $I_{step} = 340$ μA.

$$I_{step} = \frac{20/R}{127} \tag{A.2}$$

A sample of the correctly scaled current and voltage data is presented in Figure A.1. The form of the signal is of a low baseline current interrupted by discrete current peaks. These current peaks correspond to discharge events, and the correspondence of such current peaks to optical emission was previously established in a published article [**1**]. The voltage can also be seen to decrease slightly over the duration of the current peaks due to overloading of the power supply by the discharge event.

In the figure there is one event which appears as a superposition of two current peaks. Whether this represents a single event, or two separate events overlapping in time, is not resolvable from this data alone. Such event will not be discounted from consideration, but identification is required in order that later analyses can be restricted to single peak events if desired.

The approximate level of the baseline current seen in Figure A.1 is important for subsequent stages of processing. This was defined as the variable I_{base}. A histogram of all current values, with bins centred around integer multiples of I_{step}, was calculated; the most common value was assigned to be I_{base}. The distribution was sharply peaked, as can be seen in Figure A.2, which relates to the entire 10 s data segment from which the section in Figure A.1 was taken. It can be seen from this that $I_{base} = 680 \pm 340$ μA for this particular data section. It is worth noting that the baseline level is approximate, and calculated globally for a data segment of 10 million entries. In the example shown in Figure A.1 the baseline is running about $1 \times I_{step}$ above this level.

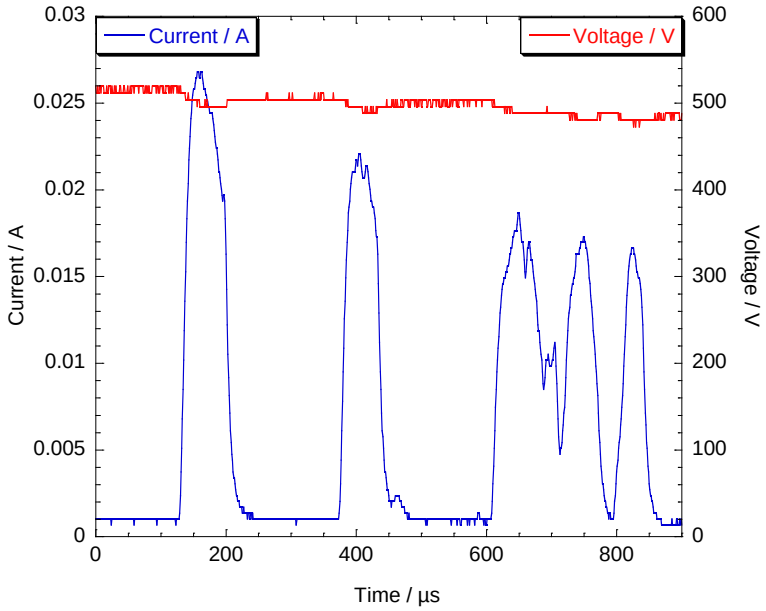

Figure A.1: *Sample of the correctly scaled current and voltage data from single discharge experiments. Data from an 18 minute coating tested with a 200 nF capacitor.*

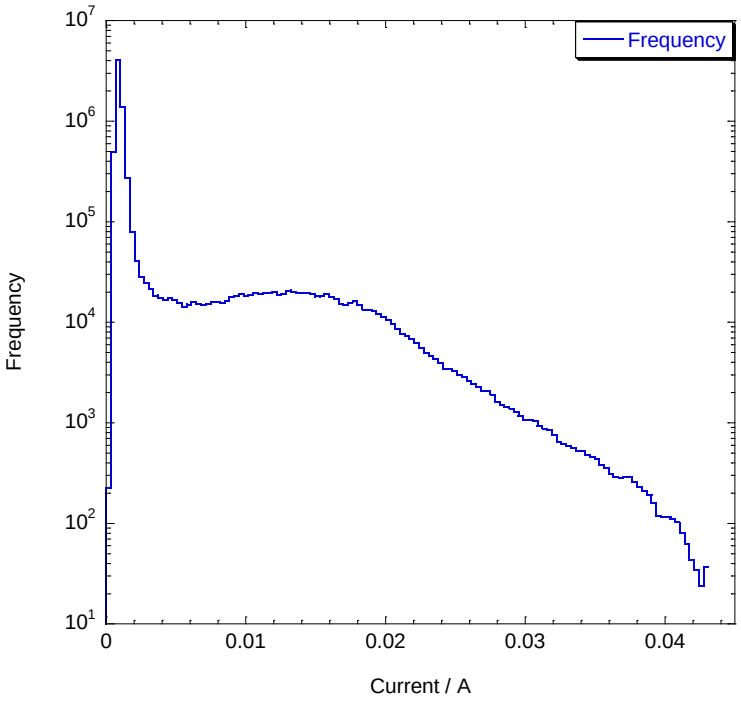

Figure A.2: *Histogram of all current values in one 10 s data record. The most common value is assigned to be* I_{base}.

A.1.2 Calculation of a gradient measure.

A measure of the gradient of the current data was required. The measure used was the 4^{th} order finite difference gradient, as defined for a function $f(t)$ by Equation A.3.

$$\frac{\mathrm{d}f}{\mathrm{d}t} = \frac{2}{3\delta t}\left[f(t+\delta t) - f(t-\delta t) - \frac{1}{8}(f(t+2\delta t) - f(t-2\delta t))\right] + O(\delta t^4)$$

then if F is a vector such that

$$F_j = f(j \times \delta t) \tag{A.3}$$

can write a measure of the gradient at the j^{th} entry as

$$\mathrm{d}F_j = \frac{2}{3\delta t}\left[F_{j+1} - F_{j-1} - \frac{1}{8}(F_{j+2} - F_{j-2})\right]$$

The gradient measure of the current data was calculated according to the procedure outlined in Algorithm 1. The first part of this procedure generates the gradient measure. The time step duration δt was omitted as the gradient measure was scaled to lie between -1 and 1 in the second part of the algorithm. This scaling of the gradient was performed to allow easy graphing on the same y-axis as logical variables. An example of the calculated current gradient measure $\mathrm{d}I$ is plotted in Figure A.3 for illustration.

Algorithm 1 *Calculation of gradient measure.*

N is total length of results vectors I_j and V_j

for $j = 3$ **to** $N - 2$ **do**

$$\mathrm{d}I_j \leftarrow \frac{2}{3}\left(I_{j+1} - I_{j-1} - \frac{1}{8}\left(I_{j+2} - I_{j-2}\right)\right)$$

end for

assign $\mathrm{d}I_{scale} \leftarrow$ maximum value of $\left|\mathrm{d}I_j\right|$

for all j **do**

$$\mathrm{d}I_j \leftarrow \frac{\mathrm{d}I_j}{\mathrm{d}I_{scale}}$$

end for

As can be seen from Figure A.3, the 8-bit nature of the data recorded by the oscilloscope leads to large fluctuations in the current gradient measure $\mathrm{d}I$. It is only when the current is changing rapidly that the gradient measure is useful. The $\mathrm{d}I$ vector will only be used for two purposes in the data processing as a result of this. The first use will be to identify the approximate locations and current values of stationary points (subsection A.1.3). The second use will be as part of the procedure for indexing of the rising and falling edges of current peaks.

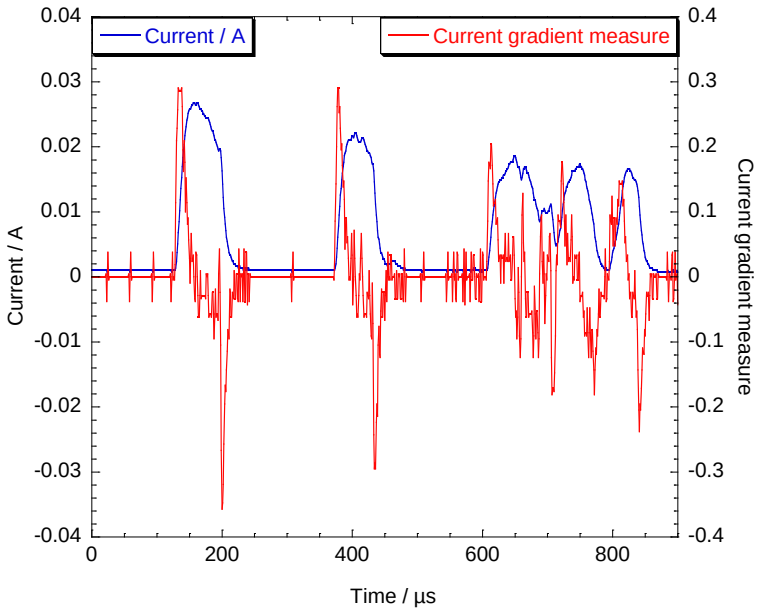

Figure A.3: *The representative section of experimental data, showing current and current gradient measure.*

A.1.3 Listing of current signal stationary points.

A listing of stationary points as defined by a change in the sign of the gradient measure, dI, was required. The procedure for compiling this list is detailed in Algorithm 2. In this algorithm, N is the total length of the I and V array vectors and *list* is an array of dimension N_{stat} row by 2 columns. The value N_{stat} is the total number of stationary points identified by the conditions detailed in Algorithm 2. The first column lists the locations, j, of stationary points and the second the corresponding current values I_j.

The algorithm passes through the current gradient measure, dI, and identifies when the gradient measure changes sign. When this happens, it is determined whether the implied zero is closer to dI_j or dI_{j-1}, and the appropriate values of index coordinate and corresponding current value are copied into the listing variable, *list*.

A.1.4 Determination of the initial current threshold.

A histogram of the current levels corresponding to stationary values is first generated. Such a plot is shown in Figure A.4. The first, and larger, peak corresponds to fluctuations around I_{base}. The second, lower peak corresponds approximately to the current peaks of discharge events.

The minima between the two peaks seen in Figure A.4 is found and set equal

Algorithm 2 *Listing of stationary current values.*

$m \leftarrow 0$
for $j = 1$ **to** N **do**
  if $\mathrm{d}I_j < 0$ **AND** $\mathrm{d}I_{j-1} \geq 0$ **then**
    $m \leftarrow m + 1$

    $x \leftarrow \dfrac{\mathrm{d}I_{j-1}}{\mathrm{d}I_{j-1} - \mathrm{d}I_j}$
    if $x > 0.5$ **then**
      $list_{m,1} \leftarrow j$
      $list_{m,2} \leftarrow I_j$
    else
      $list_{m,1} \leftarrow j - 1$
      $list_{m,2} \leftarrow I_{j-1}$
    end if
  else if $\mathrm{d}I_j > 0$ **AND** $\mathrm{d}I_{j-1} \leq 0$ **then**
    $m \leftarrow m + 1$

    $x \leftarrow \dfrac{\mathrm{d}I_{j-1}}{\mathrm{d}I_{j-1} - \mathrm{d}I_j}$
    if $x > 0.5$ **then**
      $list_{m,1} \leftarrow j$
      $list_{m,2} \leftarrow I_j$
    else
      $list_{m,1} \leftarrow j - 1$
      $list_{m,2} \leftarrow I_{j-1}$
    end if
  else
    do nothing
  end if
end for

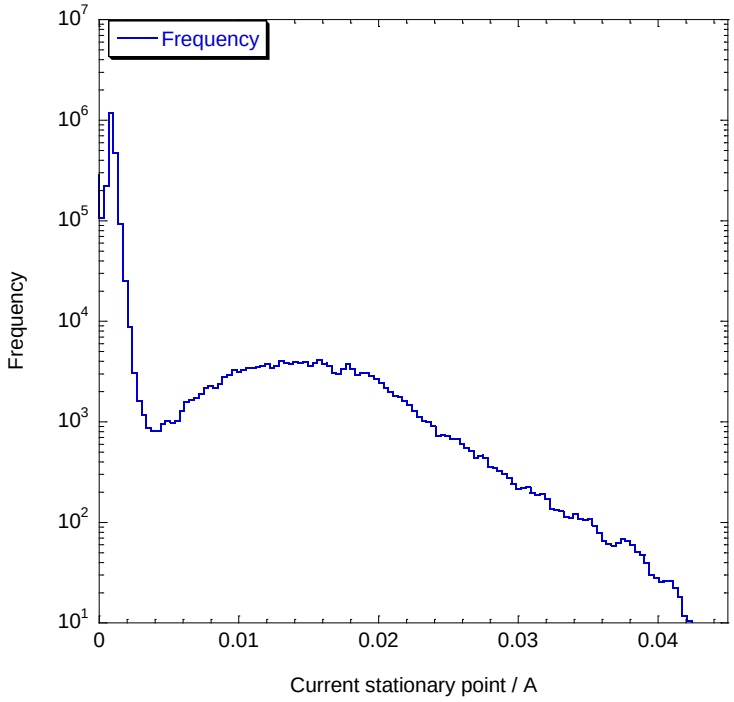

Figure A.4: *Histogram of stationary point values, frequency axis is logarithmic.*

to a threshold value, I_{thresh}. A minimum shift in the current required to identify a current peak, I_{shift}, is then defined on the basis of the values of I_{thresh}, I_{base} and I_{step}, according to Equation A.4.

$$\begin{gathered} I_{shift} = I_{thresh} - I_{base} \\ \text{if } I_{shift} < 5 \times I_{step} \text{ then instead let} \\ I_{shift} = 5 \times I_{step} \end{gathered} \tag{A.4}$$

It is required that I_{shift} be at least 5 times the minimum resolvable current shift, I_{shift}. This minimum is required in order to ensure reliable outcomes for the processing algorithms which index the locations of discharge events. I_{base} and I_{shift} are approximate only, and represent best estimates to begin the indexing process.

A.1.5 Preliminary indexing of regions of interest.

Identification of the locations of discharge events in the data is easily done by eye, but far too time consuming to make sufficient measurements manually. This next section of the data processing begins the process of indexing and listing the periods during which discharge events occurred.

The first step calculates an array vector, termed H, and the algorithm for this

is outlined in Algorithm 3. The algorithm starts with the variable *sum* set to zero. At every time point in the current record the *sum* variable is either set equal to zero if the current level is less then $I_{base} + I_{shift}$, or if this threshold is exceeded then *sum* is incremented by a quantity equal to the multiple of I_{step} by which I_j exceeds I_{base}. At each stage the present value of *sum* is set to be the value of H_j. A comparison of the reference section of data with the calculated H variable is presented in Figure A.5.

Algorithm 3 *Procedure to calculate variable H.*

$sum = 0$
for $j = 1$ **to** N **do**
  if $I_j > I_{base} + I_{shift}$ **then**
    $sum \leftarrow sum + \dfrac{I_j - I_{base}}{I_{step}}$
  else
    $sum \leftarrow 0$
  end if
  $H_j \leftarrow sum$
end for

introduce G, a logical index array vector
for all i **do**
  if $H_j > 128$ **then**
    $G_j = 1$
  end if
end for

for $j = N$ **to** 2 **do**
  if $G_j = 1$ **AND** $G_{j-1} = 0$ **AND** $H_{j-1} > 0$ **then**
    $G_{j-1} \leftarrow 1$
  end if
end for

After calculation of the H variable, indexing is begun by assigning the value 1 or 0 to entries of the vector G, depending on whether that time point is inside, or outside, a discharge event. This is initially done by assigning any point at which $H_j > 128$ to be part of a discharge event. The procedure then backtracks to the point at which H_j first exceeded 0, ie the point at which the threshold value of $I_{base} + I_{shift}$ was first exceeded. The outcome of this overall procedure is not displayed in another figure as it would provide no additional information over

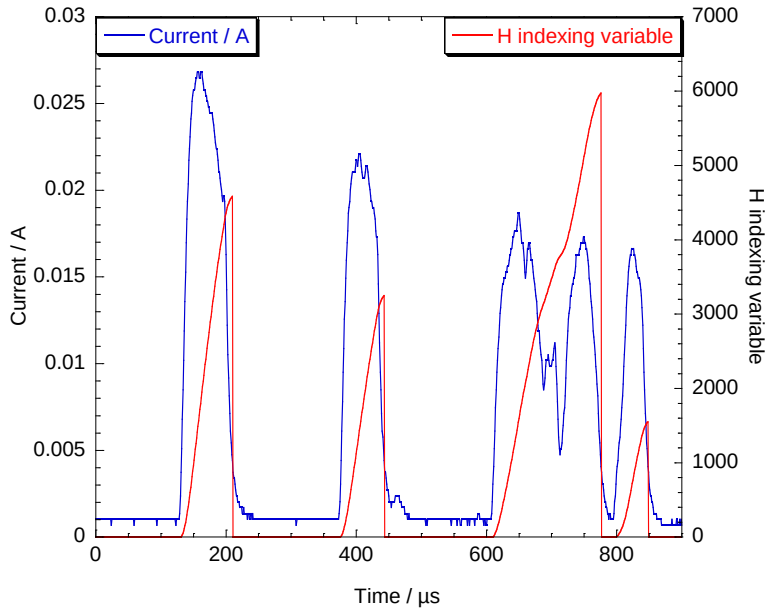

Figure A.5: *The representative section of experimental data, showing current and the indexing vector H.*

Figure A.5.

This might seem an unnecessarily complicated procedure to get to this point. Why not simply assign $G_j = 1$ at each point for which the current is above the threshold value? This would certainly be effective on the section shown in Figure A.5. The procedure outlined in Algorithm 3 was adopted because it performs better in certain situations, in particular with fluctuations in the recorded current signal which can occur around the same time as the current is passing up or down through the threshold value.

Using the H calculation procedure did not appreciably increase computation time, and helped reduce the number of mis-indexed regions identified via manual inspection. The chosen threshold of 128 means that an event which only exceeds the threshold value by $1 \times I_{step}$ would need to persist for a period in excess of $128 \times \delta t$ in order to be counted (δt = 1 μs for this work). A larger discharge would not need to persist for as long to register. In particular the value of 128 means that it is impossible for a spike which only lasted 1 sampling interval to register, as the maximum value with the 8-bit oscilloscope vertical resolution is $127 \times I_{step}$.

A.1.6 Extension of indexing to cover discharge event initiation.

By this stage all significant current peaks have been partially indexed. However, the point at which the current exceeds the threshold value is not the exact initiation point of the event. The falling edge of the discharge events is similarly excluded from the indexing at this stage.

The rising edge of the discharge event current peak can be included by consideration of $\mathrm{d}I$ around the initiating point. Recalling Figure A.3, the gradient measure was most accurate when the rate of change of current exceeded about $I_{step}/\delta t$. Typically this is the case during the initial rise, and terminal fall, of the discharge current. This allows the gradient measure $\mathrm{d}I$ to be useful when extending the indexing to cover the rising edge of the discharge.

Algorithm 4 *Procedure to extend the indexing to cover the discharge rising edge.*

```
for j = N to 2 do
  if G_j = 1 and G_{j-1} = 0 and dI_{j-1} ≥ 0 then
    G_{j-1} ← 1
  end if
end for
```

A procedure outlined in Algorithm 4 extends the discharge rising edge back in time to the point at which the gradient measure exceeds zero. This works well in most cases. However if there is a fluctuation on the rising edge of the discharge, and if this fluctuation is just below $I_{base} + I_{shift}$, then the rising edge below this value may not be indexed. This was not a common problem however, the discharge rising edge being about the most reproducible feature of the discharging behaviour, as shown in chapter 6. The output of data analysis up to this point can be seen in Figure A.6. It can be seen from the figure that the rising edge of the discharges is now accurately covered by the indexing, the falling edge of the discharge remains not indexed as yet.

A.1.7 Extension of falling edge to same current level as initiation

The first stage of extending indexing to the falling edge of the discharge involves extending the indexing to cover the discharge event until the current level has returned to within I_{step} of the starting current. The procedure for this is detailed in Algorithm 5. This works by scanning through the current record, and storing the current when the start of an indexed region is encountered as I_{temp}. A logical flag

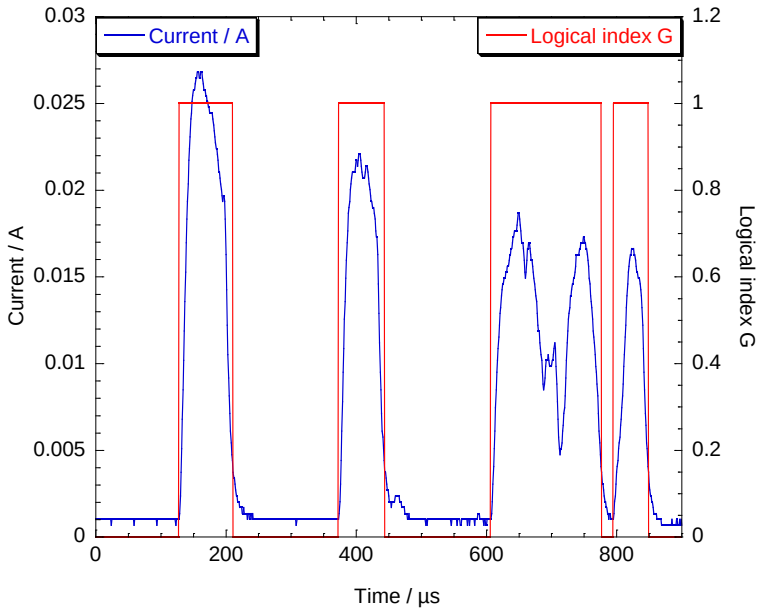

Figure A.6: *The representative section of experimental data, showing current and the logical indexing vector G.*

is also set to indicate that the algorithm is now in a region of interest. When the termination of the indexed region is reached, new points are added to the end until the current level, I_j, drops to within I_{step} of I_{temp}.

This procedure was adopted as it is effective when dealing with two sub-classes of event. Firstly of events which displayed a significant plateau region after the initial peak, but before a rapid final drop back to the baseline current. Secondly of events which had a two peak structure, with a minima just below the threshold current level, but still greater then the baseline current. It was necessary for such events to extend indexing in this manner prior to applying gradient conditions to ensure appropriate bounds on regions of interest.

A.1.8 Extension of index to cover falling edge.

After extending the indexed regions until the termination current is within I_{step} of the initiating current, the falling edge was further extended for those events which still show negative current gradient at the termination of the index. This procedure can be found in Algorithm 6, and is seen to be essentially similar to Algorithm 4.

The output of the indexing procedure at this point can be seen in Figure A.7. The indexing stored in the logical variable G can now be seen to encompass the discharge events in their entirety. The next task is to list the start and end points of regions of interest, so that subsequent procedures need only examine those sections

Algorithm 5 *Procedure to extend the falling edge until termination current is close to initiating.*

$I_{temp} \leftarrow 0$
$event \leftarrow 0$
for $j = 2$ **to** N **do**
  if $event = 0$ **then**
    if $G_j = 1$ **AND** $G_{j-1} = 0$ **then**
      $event \leftarrow 1$
      $I_{temp} \leftarrow I_j$
    end if
  else
    if $G_j = 0$ **AND** $G_{j-1} = 1$ **then**
      if $I_j - I_{temp} > I_{step}$ **then**
        $G_j \leftarrow 1$
      else
        $event \leftarrow 0$
      end if
    end if
  end if
end for

Algorithm 6 *Procedure to extend the falling edge whilst gradient is less then zero.*

for $j = 1$ **to** $N - 1$ **do**
  if $G_j = 1$ **AND** $G_{j+1} = 0$ **AND** $\mathrm{d}I_{j-1} \leq 0$ **then**
    $G_{j+1} \leftarrow 1$
  end if
end for

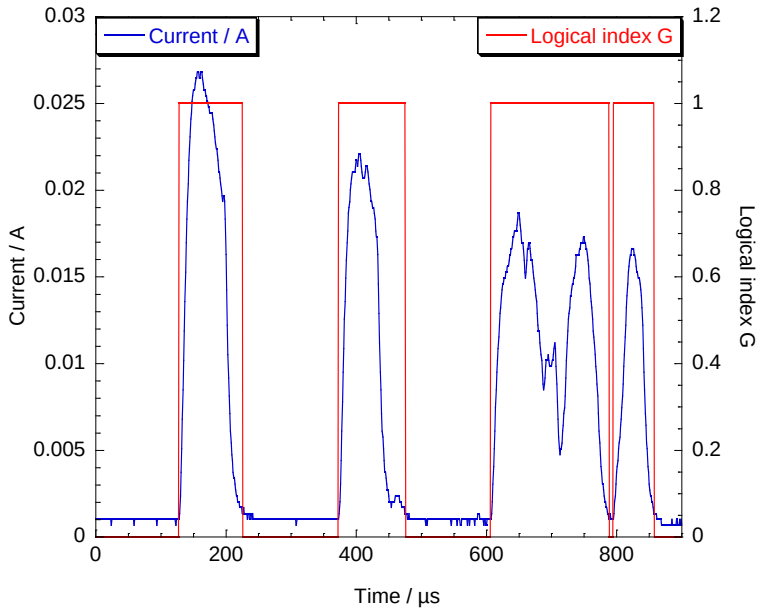

Figure A.7: *The representative section of experimental data, showing current and the logical indexing vector G.*

of the data which are of relevance. Before doing so, there is one further small procedure which is applied. Any points in the data for which $G_j = 0$ whilst $G_{j-1} = 1$ and $G_{j+1} = 1$ are set to be also equal to 1. This removes isolated points within indexed regions, however, if the un-indexed point represents a genuine separation of two events, then it will be later re-instated, subject to a locally derived current threshold. This seems perhaps a little long winded, however the procedure overall reduces the mis-identification of discharge events.

A.1.9 Listing of indexed regions.

The procedure for listing the coordinates of discharge initiation and termination points is given in Algorithm 7. This involves passing through the data, incrementing a running count whenever a discharge initiation is encountered, and listing the starting and ending coordinates of the indexed regions in an array, *index*, with dimension N_{event} by 3. N_{event} is the total number of indexed regions. The final row of *index* is removed prior to determination of N_{event} as quite often an event would commence just before the end of the recorded region, but would not terminate before the logging did. There are 3 columns in the variable *index*, the first is the event start coordinates and the second the end coordinates. The third will not be used until the internal peaks of indexed regions have been identified, and will represent the total number of current peaks within each indexed region, see subsection A.1.14

for further details.

Algorithm 7 *Procedure to list the starting and ending coordinates of indexed discharge events.*

$m \leftarrow 0$
for $j = 2$ **to** N **do**
  if $G_j = 1$ **AND** $G_{j-1} = 0$ **then**
    $m \leftarrow m + 1$
    $index_{m,1} \leftarrow j - 1$
  else if $G_j = 0$ **AND** $G_{j-1} = 1$ **then**
    $index_{m,2} \leftarrow j$
  else
    do nothing
  end if
end for
remove final row of the *index* variable
$N_{event} \leftarrow m - 1$

A.1.10 Removal of events of insufficient magnitude.

A few additional procedures are required before the data can be passed to the algorithm which will identify internal peaks and troughs. At the present stage of data processing, for the dataset from which the example data section is drawn, representing a 10 s test period of an 18 minute coating with a 200 nF circuit capacitance, the variable *index* contains 11640 rows, each corresponding to a discharge event.

Algorithm 8 *Procedure to remove events below a threshold magnitude of* $5I_{step}$.

for $j = 1$ **to** N_{event} **do**
  $I_{max} \leftarrow$ maximum I_m in the range $m = index_{j,1}$ to $index_{j,2}$
  $I_{min} \leftarrow$ minimum I_m in the range $m = index_{j,1}$ to $index_{j,2}$
  if $I_{max} - I_{min} < 5I_{step}$ **then**
    for all $index_{j,1} \geq m \leq index_{j,2}$ **do**
      $G_m \leftarrow 0$
    end for
  end if
end for

In some of the datasets, some of the events identified up to this point will have been incorrectly identified. So after the listing of indexed variables a subsequent

processing is applied to each of these regions. Any indexed discharge events which do not show a base to peak current variation of at least $5I_{step}$ are removed from the list, and the corresponding time points in the indexing variable G set equal to zero. This procedure is outlined in Algorithm 8. Typically by this stage this condition is not realised by more then a handful of the previously indexed events. For the example dataset, the *index* variable still contains 11640 rows after application of this condition.

A.1.11 Splitting of events which might be independent.

A routine is applied which causes a break in the indexing mid-way through any region which could conceivably be two or more independent regions, previously joined together either by a fluke of the prior conditions or explicitly when the isolated points were removed during subsection A.1.8. The procedure for this is presented in Algorithm 9.

Algorithm 9 *Procedure to separate possibly independent indexed regions.*

for $j = 1$ **to** N_{event} **do**
  $k \leftarrow index_{j,1}$
  $I_{temp} \leftarrow I_k$
  for $m = index_{j,1}$ **to** $index_{j,2}$ **do**
    if $I_m \leq I_{temp} + 1.1I_{step}$ **then**
      $G_m \leftarrow 0$
    end if
  end for
end for

The stated condition of $\leq I_{temp} + 1.1I_{step}$ is to ensure that anything within I_{step} of the initiating current level of the event, I_{temp} is indexed as not part of a discharge event. The factor of 1.1 not 1 is to ensure that errors arising from rounding error (I_{step} is stored only to finite precision) do not lead to a point remaining indexed when it is equal to $I_{temp} + I_{step}$ to within the measurement uncertainty, but not exactly equal. As far as a computer is concerned, $1.000 \neq 1.005$, experimentally they may be equivalent depending on the measurement uncertainty.

A.1.12 Finalising of indexing.

After the changes to the G logical index array in the previous subsections, the discharge listing variable *index* must be updated. This is according to Algorithm 7 as before. After this the number of rows in the *index* variable for the example

dataset has increased from 11 640 to 13 673. Not all of these new regions are sensible events however. A common problem results from slight fluctuations around the termination point of the discharge events. The application of the condition detailed in subsection A.1.11 can lead to such slight fluctuations, typically just after the main current drop on event termination, being split off as a separate event.

To remove such artefacts, the condition on event magnitudes described in subsection A.1.10 is re-applied. This is followed by a final application of the listing procedure of subsection A.1.9. After this, the final *index* variable for the example dataset contains 12 397 rows, each representing a discharge event.

A.1.13 Indexing of internal peaks.

Whilst the intent of the single discharge testing was to generate discharge events that were well separated and easily resolvable in time, the reality was not so simple. Single peak current events did dominate all single discharge datasets, so the name chosen is not completely spurious. However, multiple peak events, taking the form usually of two or more of the single peak events superimposed on top of each other, were often seen in the current records. It cannot be determined from the electrical data alone whether such multiple current peak events represented single discharge events showing significant fluctuation, or whether they represent concurrent operation of spatially distinct events. The latter possibility is more probable. In either case it is important that single and multiple peak events be distinguished so they can be treated separately during analysis of the discharge characteristics.

A procedure to identify whether indexed regions displayed significant internal structuring was developed, detailed in Algorithm 10. The output of this procedure is plotted for the by now familiar representative sample data in Figure A.8. The precise mechanics of the algorithm may benefit from additional explanation.

Recall that dI suffered from large fluctuations due to the 8-bit nature of the raw data (subsection A.1.4). This rendered it unusable except in regions where the current was changing rapidly. Unfortunately, the gradient measure was not reliable enough to be used for indexing of internal peaks within multiple peak discharge events.

An alternative procedure was developed instead, that presented in Algorithm 10. At the start of the event, the algorithm is looking for a current peak. The current peak magnitude, I_{peak}, and location, k_{peak}, are set to the initiation current of the event and the time coordinate respectively. For each subsequent time point in the indexed region, if I_m is greater than or equal to the currently stored I_{peak} value, then it is set to be the new I_{peak} value. The peak location, k_{peak}, is also updated to be m.

Algorithm 10 *Procedure to identify locally significant peaks and troughs within indexed regions.*

F is another indexing vector array, similar to G and H.

for $j = 1$ **to** N_{event} **do**
  $I_{max} \leftarrow$ maximum I_m in the range $m = index_{j,1}$ to $index_{j,2}$
  $I_{min} \leftarrow$ minimum I_m in the range $m = index_{j,1}$ to $index_{j,2}$
  $I_{scale} \leftarrow 0.2 \times (I_{max} - I_{min})$
  $k_{peak} \leftarrow index_{j,1}$, $k_{trough} \leftarrow index_{j,1}$
  $I_{peak} \leftarrow I_{k_{peak}}$, $I_{trough} \leftarrow I_{k_{trough}}$
  $seek_{peak} \leftarrow 1$, $seek_{trough} \leftarrow 0$
  if $I_{scale} < 5I_{step}$ **then**
    $I_{scale} \leftarrow 5I_{step}$
  end if
  for $m = index_{j,1}$ **to** $index_{j,2}$ **do**
    if $seek_{peak} = 1$ **then**
      if $I_m \geq I_{peak}$ **then**
        $I_{peak} \leftarrow I_m$
        $k_{peak} \leftarrow m$
      else if $I_m < I_{peak} - I_{scale}$ **then**
        $F_{k_{peak}} \leftarrow 1.0$
        $seek_{peak} \leftarrow 0$, $seek_{trough} \leftarrow 1$
        $k_{trough} \leftarrow m$
        $I_{trough} \leftarrow I_m$
      end if
    else if $seek_{trough} = 1$ **then**
      if $I_m \leq I_{trough}$ **then**
        $I_{trough} \leftarrow I_m$
        $k_{trough} \leftarrow m$
      else if $I_m > I_{trough} + I_{scale}$ **then**
        $F_{k_{trough}} \leftarrow 0.5$
        $seek_{trough} \leftarrow 0$, $seek_{peak} \leftarrow 1$
        $k_{peak} \leftarrow m$
        $I_{peak} \leftarrow I_m$
      end if
    end if
  end for
end for

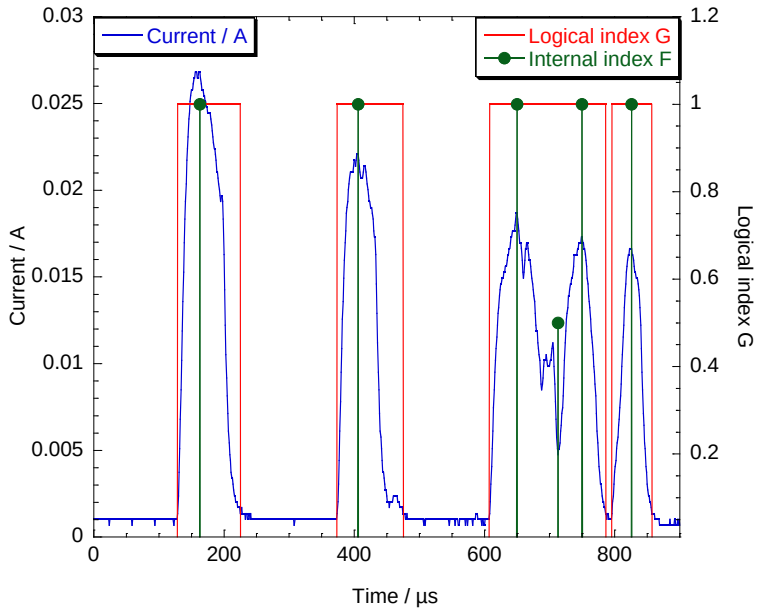

Figure A.8: *The representative section of experimental data, showing current, logical indexing vector G and internal peak indexing vector F.*

This continues until I_m, has dropped to a less then $I_{peak} - I_{scale}$. I_{scale} is whichever is largest out of 20% of the discharge event base-peak magnitude, or $5I_{step}$. When this occurs, the coordinate stored in k_{peak} is assigned to be the location of a current peak by assigning the corresponding entry in the indexing vector F to have the value 1.0. The logical variables $seek_{peak}$ and $seek_{trough}$ are then updated to indicate the algorithm should start looking for a trough in the current. The storage variables I_{trough} and k_{trough} are re-initialised to the present I_m and m values.

The trough seeking procedure is identical except that I_{trough} is updated to be the lowest encountered current value, with k_{trough} the corresponding coordinate. The trough is marked when I_m has increased to more then I_{scale} above the recorded I_{trough} value. The trough is marked by the value 0.5 at the corresponding position of F. The algorithm is then set to look for another peak location and the I_{peak} and k_{peak} values re-initialised.

This process repeats until the end of the indexed region is reached. So a single peak event would have a single marked peak, whilst a two peak event would have two marked peaks and a single marked trough between them. A double peak event is seen in Figure A.8. Despite there being several dips of current on the falling edge of the first peak, it can be seen that only one is marked as a trough by the algorithm. This is because the other dips are not followed by an increase greater then I_{scale}.

Setting the threshold I_{scale} to be 20% of the base to peak current magnitude of the indexed region represents an arbitrary selection on the author's part. There was no particular reason to choose this value beyond utility and that the results looked sensible when examined manually. The 20% of local maximum variation used to assign peaks or troughs should be borne in mind when considering the processed data.

A.1.14 Generation of separate list of single peak events.

In order to separate the analysis of single and multiple peak current events, it is required to create a separate listing array which contains only single peak events, *index_sing*. The procedure is detailed in Algorithm 11. The total number of single peak events was then assigned to be N_{single}.

For the dataset from which examples were drawn (18 minute coating, 200 nF circuit capacitance), there were in total 12397 discharge events, and 9491 single peak events. The single current peak discharge events represented $\approx 76.6\%$ of all events recorded in that particular 10 s interval. Complete listing of the fraction of events which were single peak may be found in Table 5.3.

A.1.15 Measurement of the characteristics of single discharges.

The results for all single peak events were measured first. The results were stored in a results array, termed *results_sing*, which was of dimension N_{single} by 17. The 17 stored measurements were as detailed in Table A.1.

The first 3 columns of the *results_sing* array are concerned with the integer indexing coordinates of the initiation of the discharge, k_{start}, the peak location as determined from the vector F, k_{peak}, and the termination point of the discharge, k_{end}. These are not terribly interesting, but were stored as they might be of potential use for subsequent analyses.

The duration ,d_{sing}, was calculated as the difference between termination and initiation coordinates, multiplied by the sampling interval, $\delta t = 1$ μs. The rise time to peak current, d_{rise}, was calculated in similar fashion from the difference between k_{peak} and k_{start}. The fall time from peak current, d_{fall}, was from the difference between k_{end} and k_{peak}.

Initiating voltage, V_{init}, was defined to be the voltage at the initiation point of each discharge event. The mean voltage, V_{mean}, over the event duration was calculated as the arithmetic mean of the V_j for $k_{start} \leq j \geq k_{end}$. The mean current, I_{mean}, was calculated in the same fashion from $I_j - I_{base}$.

Algorithm 11 *Procedure to generate a new listing variable relating only to single peak discharge events.*

first fill in the 3rd column of *index* vector
with the number of internal peaks in each indexed region

for $j = 1$ **to** N_{event} **do**
  $tally \leftarrow 0$
  for $m = index_{j,1}$ **to** $index_{j,2}$ **do**
    if $F_m = 1.0$ **then**
      $tally \leftarrow tally + 1$
    end if
  end for
  $index_{j,3} \leftarrow tally$
end for

create the listing array for single peak events $index\_sing$

$m \leftarrow 0$
for $j = 1$ **to** N_{event} **do**
  if $index_{j,3} = 1$ **then**
    $m \leftarrow m + 1$
    for all $1 \geq k \leq 3$ **do**
      $index\_sing_{m,k} \leftarrow index_{j,k}$
    end for
  end if
end for
let $N_{single} \leftarrow m$

Column	Measurement	Symbol	Unit
1	Initiation coordinate	k_{start}	integer
2	Peak current coordinate	k_{peak}	integer
3	Termination coordinate	k_{end}	integer
4	Event duration	d_{sing}	s
5	Rise time to peak current	d_{rise}	s
6	Fall time from peak current	d_{fall}	s
7	Initiating voltage	V_{init}	V
8	Mean voltage during event	V_{mean}	V
9	Mean current during event	I_{mean}	A
10	Peak current during event	I_{peak}	A
11	Voltage at peak current	V_{peak}	V
12	Peak instantaneous power	P_{peak}	W
13	Dynamic resistance at peak current	R_{peak}	Ω
14	Event width at half maximum current	d_{half}	s
15	Event width at quarter maximum current	d_{quart}	s
16	Total charge passed	Q_{sing}	C
17	Total energy transferred	E_{sing}	J

Table A.1: *Properties measured for the single peak discharge events.*

Columns 10–13 represent the electrical properties of the discharge at the time the peak current was reached. The peak current was defined as $I_{peak} = I_{k_{peak}} - I_{base}$, the voltage at peak current was defined as $V_{peak} = V_{k_{peak}}$, the peak instantaneous power of the discharge was defined to be $P_{peak} = I_{peak} \times V_{peak}$ and the resistance at peak current as $R_{peak} = V_{peak}/I_{peak}$. The resistance at peak current was the lowest dynamic resistance displayed by the test system during each discharge event.

The widths at half and quarter maximum current were calculated according to the procedure detailed in Algorithm 12. Linear interpolation was applied to estimate the points when the discharge current rose through, and then fell below the half or quarter maximum current. Linear interpolation was used in this case to estimate the implied width at half or quarter maximum current, as the current was usually changing rapidly at these points.

The final two measurements were the total charge passed, Q_{sing}, and the total energy transfer by the discharge, E_{sing}. Q_{sing} was calculated as the numerical trapezium rule integral of $\delta t.(I_j - I_{base})$ for the duration of the discharge event. E_{sing} was calculated as the numerical trapezium rule integral of $\delta t.(I_j - I_{base}).V_j$ for the duration of the discharge event.

A.1.16 Measurement of the characteristics of all discharge events.

The results for all indexed discharge events were measured last. The results were stored in a results array, termed $results\_all$, which was of dimension N_{event} by 16. The 16 stored measurements were as detailed in Table A.2.

The initiation coordinate, k_{start}, and the termination coordinate, k_{end}, were the same as for the single peak discharge events. The event duration, d_{event}, was defined to be $\delta t.(k_{end} - k_{start})$. The end to start event separation, d_sep_{es}, is the time difference between the start of the event and the termination of the previous event. The start to start event separation, d_sep_{ss}, is the time difference between the start of the current event and the initiation of the previous event.

Event initiating voltage, V_{init}, is again the voltage at initiation of the discharge. The mean voltage and current over the event, V_{mean} and I_{mean}, were calculated as for the single peak events.

The peak current, I_{peak}, was the maximum value of $I_j - I_{base}$ reached during the discharge event. The peak power, P_{peak}, was the maximum value of $V_j.(I_j - I_{base})$ observed over the event. Total charge passed, Q_{event}, and total energy transferred, E_{event}, were calculated in the same fashion as Q_{sing} and E_{sing} for the single peak events.

The number of internal peaks during the discharge event, N_{int}, was simply the

Algorithm 12 *Procedure to estimate the half / quarter width (d_{half} / d_{quart}) of events.*

$I_{temp} \leftarrow 0.5$ **OR** 0.25
$seek \leftarrow 1$
$k_{rise} \leftarrow k_{start}$
for $j = k_{start}$ **to** k_{peak} **do**
  if $seek = 1$ **then**
    if $I_j - I_{base} \geq I_{temp}$ **AND** $I_{j-1} - I_{base} < I_{temp}$ **then**

$$k_{rise} \leftarrow (j-1) + \frac{I_{temp} - I_{j-1}}{I_j - I_{j-1}}$$

      $seek \leftarrow 0$
    end if
  end if
end for

$seek \leftarrow 1$
$k_{fall} \leftarrow k_{end}$
for $j = k_{end}$ **to** k_{peak} **do**
  if $seek = 1$ **then**
    if $I_j - I_{base} \geq I_{temp}$ **AND** $I_{j+1} - I_{base} < I_{temp}$ **then**

$$k_{rise} \leftarrow j + \frac{I_{temp} - I_j}{I_{j+1} - I_j}$$

      $seek \leftarrow 0$
    end if
  end if
end for
d_{half} **OR** $d_{quart} \leftarrow \delta t.(k_{fall} - k_{rise})$

Column	Measurement	Symbol	Unit
1	Initiation coordinate	k_{start}	integer
2	Termination coordinate	k_{end}	integer
3	Event duration	d_{event}	s
4	Separation (end of one to start of next)	d_sep_{es}	s
5	Separation (start of one to start of next)	d_sep_{ss}	s
6	Initiating voltage	V_{init}	V
7	Mean voltage during event	V_{mean}	V
8	Mean current during event	I_{mean}	A
9	Peak current during event	I_{peak}	A
10	Peak instantaneous power	P_{peak}	W
11	Total charge passed	Q_{event}	C
12	Total energy transferred	E_{event}	J
13	Number of internal peaks	N_{int}	integer
14	Duration per internal peak	d_{norm}	s
15	Charge per internal peak	Q_{norm}	C
16	Energy per internal peak	E_{norm}	J

Table A.2: *Properties measured for all indexed discharge events.*

total number of internal peaks indexed between the initiation and termination of the discharge event. Duration per internal peak was calculated as $d_{norm} = d_{event}/N_{int}$, and represents the event duration normalised to the number of peaks indexed. The charge per internal peak, Q_{norm}, and the energy per peak, E_{norm}, were calculated in the same fashion.

A.2 Estimation of the event current development profiles.

It was observed, during many hours examining the current data and the output of various indexing conditions and procedures, that the current-time profiles of discharge events have a tendency to be a certain shape. Hardly any two events follow the exact same current development profile, however the overall trend is that discharge events appear to have a certain shape, which changes only slightly as the events scale to larger currents.

Quantifying this requires a measure of the average discharge current development to be calculated. This was only done for the single peak discharge events. The average development was calculated for each distinct combination of V_{init} and

d_{sing}. A calculation was also made of the standard error at each point in the event development.

It was first required to know the number of events which occurred for each combination of V_{init} and d_{sing}. Remember that these variables can only really take discrete values as the data recorded was digital and sampled. An array was calculated to store the numbers for each combination, N^{prof}, with dimensions 128 by 300 entries. The procedure for doing this is outlined in Algorithm 13.

Algorithm 13 *Procedure to calculate the number of events at each combination of* V_{init} *and* d_{sing}.

$V_{step} \leftarrow \dfrac{1000}{127}$

$\delta t \leftarrow 10^{-6}$

N^{prof} is a 2 dimensional array, 128 by 300, initialised to hold zeros.

for all single peak events **do**

  $j \leftarrow \dfrac{V_{init}}{V_{step}} + 1$

  $m \leftarrow \dfrac{d_{sing}}{\delta t} + 1$

  if $m \leq 300$ **then**

    $N^{prof}_{j,m} \leftarrow N^{prof}_{j,m} + 1$

  end if

end for

The dimension with 128 entries corresponded to the 128 distinct values in the range 0 to 1000 V which the 8-bit voltage data could assume. The 300 entry dimension corresponds to the possible duration values. Events longer than 300 samples, or 300 μs, are technically possible, but rare for single peak events and so not included in this particular calculation.

Once the number at each combination has been calculated, the averaged profiles can be estimated according to the procedure presented in Algorithm 14. The profiles are stored in a 3 dimensional array of dimension 300 by 128 by 300. The first dimension holds the averaged profiles as a function of time, the second two dimensions correspond to the two dimensions of the numbers array, N^{prof}.

The array I^{prof} then holds the averaged current profiles, and V^{prof} the average voltage variation after initiation, which will be of interest subsequently. Once a voltage and duration are specified, the remaining variation in the array represents the averaged profile of a discharge event at the specified voltage which lasted the specified duration.

The averaged profiles, I^{prof} and V^{prof}, were then used to calculate the standard

Algorithm 14 *Procedure to estimate the averaged event development profiles.*

for all single peak events **do**

$j \leftarrow \dfrac{V_{init}}{V_{step}} + 1$

$m \leftarrow \dfrac{d_{sing}}{\delta t} + 1$

if $m \leq 300$ **then**

$n \leftarrow 0$

$cyc = k_{cyc}$

for $p = k_{start}$ **to** k_{end} **do**

$n = 1 + 1$

$I^{prof}_{n,j,m} \leftarrow I^{prof}_{n,j,m} + \dfrac{1}{N^{prof}_{j,m}} \times I^{adj}_{p,cyc}$

$V^{prof}_{n,j,m} \leftarrow V^{prof}_{n,j,m} + \dfrac{1}{N^{prof}_{j,m}} \times V_{p,cyc}$

end for

end if

end for

errors at each time point in the averaged profiles and for each combination of voltage and event duration. The procedure is fundamentally similar to Algorithm 14, and the standard errors were stored in the arrays σI^{prof} and σV^{prof}. An example of one such averaged current profile, calculated from the 10 s data segment referred to for examples, is displayed in Figure A.9.

This particular example was calculated from just 47 events which occurred at a voltage of 528 V, however the standard error on a single current measurement is seen to be low compared to the event magnitude.

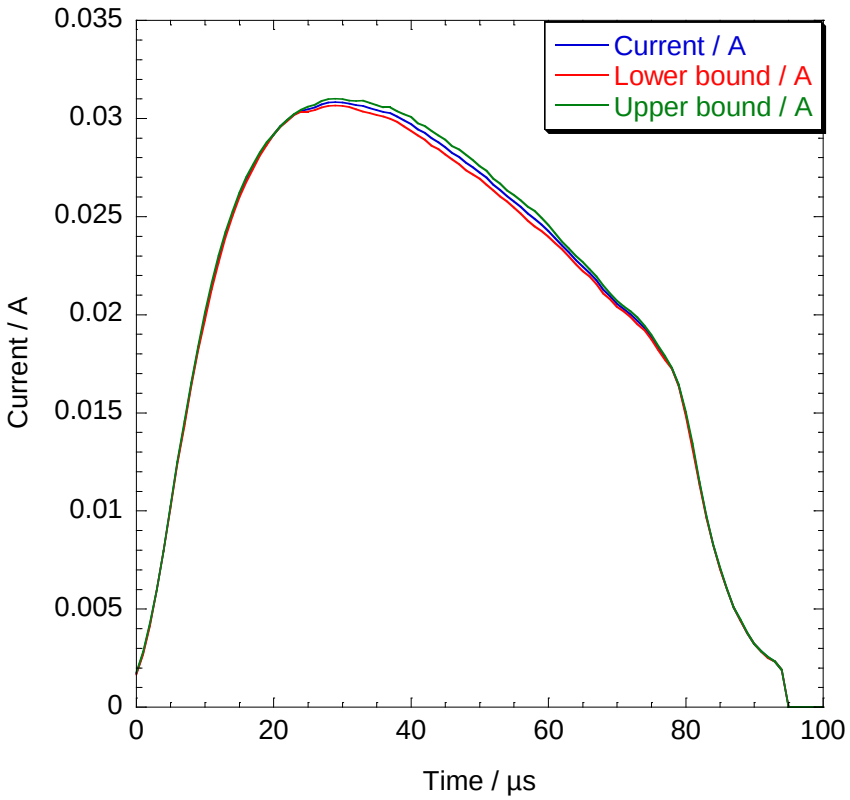

Figure A.9: *One example of the averaged profiles calculated, the lower and upper bounds represent the standard error. This represents an event initiated at 528 V.*

Appendix B

Data analysis procedures for in-situ discharge monitoring experiments.

Whilst similar in many respects to the processing of data from single discharge experiments, the data from in-situ monitoring required slightly different analysis. This was in part due to the requirement that the signal from the current probe be corrected for the distortion resulting from LR droop.

B.1 Correction for current probe frequency effects.

The current during in-situ discharge monitoring experiments was measured using a Tektronix P6021 current probe and a Picoscope 5203 digital oscilloscope. The current probe was non-contact, relying on the electrical induction. As mentioned in section 3.2, four loops of the signal wire were passed through the current probe, giving an effective resolution of 2 mV per 1 mA. The probe is designed to be used with periodic signals, and the lower bandwidth cut off specified by the manufacturer was 400 Hz.

Even signals at greater then 400 Hz will suffer from distortions, especially if the signals contain sections where the current signal is not changing in time. For example a square wave signal will show exponential LR decay of the current indicated by the probe during the period of constant current.

The discharge events were detected as short pulses, with a total duration short enough that detection by the probe was not problematic. However the LR decay over the peak of the event, when the current gradient was low, led to distortion of the

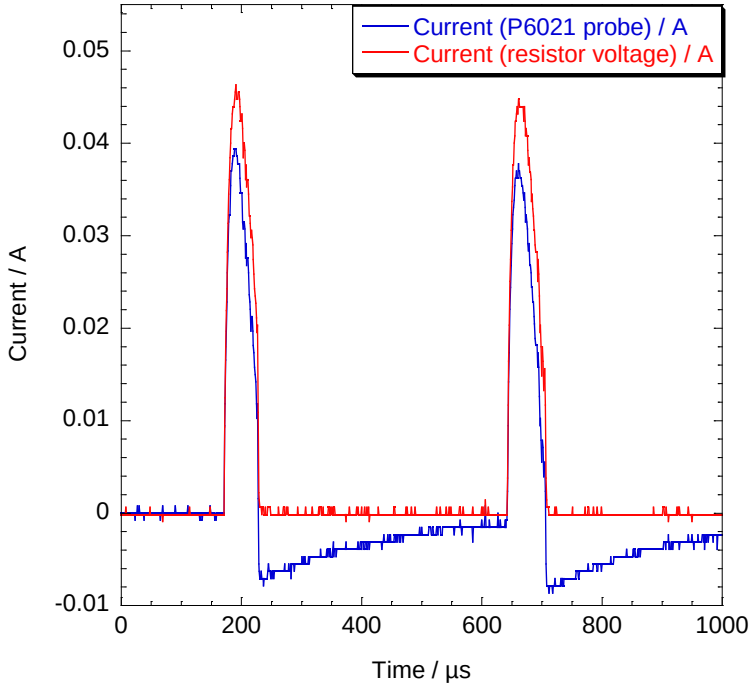

Figure B.1: *Example of the distortion to measured current signal from the Tektronix P6021 current probe. For comparison the current measured from the voltage over a known series resistance is also displayed.*

current signal. Subsequently during the falling edge of the event, the current signal overshoots the zero level, before slowly decaying back towards zero. An example of this behaviour is displayed in Figure B.1.

The section of data shown in Figure B.1 shows a section of current data recorded in two ways, firstly using the Tektronix P6021 current probe and secondly using the voltage over a known series resistor. This data was taken from a section of the calibration data, obtained as described in subsection 3.4.2. The analysis of this data to develop the correction procedure for the current probe is described in the following sections.

B.1.1 Mathematical basis of the signal correction procedure.

The calibration data was used to generate a frequency domain function which could be applied to correct the data from the current probe. The current record of the discharge events consists of a series of short, uncorrelated, pulses of current. If the Fourier transform of these pulses were (individually) taken it would be found

to contain components across a range of frequencies. The lower band cut off for the current probe is 400 Hz, this does not mean that the probe does not detect frequencies below that (any non-DC components will couple to an extent), but below the cut off the frequency components of the signal suffer distortions in both amplitude and phase. It is these distortions in the low frequency components of the signal which cause the problems visible in Figure B.1, and which must be removed from the signal to obtain the discharge currents accurately.

The first step is to find sections within the calibration data which can be considered to be independent. As can be seen in Figure B.1, after each discharge event the current probe signal overshoots the zero level before it begins to decay upwards back to zero. Any section of data which begins with the initiation of a discharge event, and ends with the return of the current probe signal back to the zero level can be considered independent, as subsequent discharge events are not impacted by the signal of previous events. By contrast, if a discharge event initiates before the current probe signal has returned to zero, then the starting level of the new discharge is influenced by the previous events and hence cannot be considered independent.

A sample of the current record from the resistor will be referred to as I_j^{res} and from the current probe as I_j^{probe}. If an independent section of current data is considered, of total length N_{ind} samples, then the Discrete Fourier Transform (DFT) can be determined as in Equation B.1.

$$\tilde{x}_k = \sum_{j=1}^{N_{ind}} x_j \exp\left(\frac{-2\pi i\,(j-1)\,(k-1)}{N_{ind}}\right) \tag{B.1}$$

In practical terms if the signal under consideration returns to zero after a finite duration, then that signal can be padded with zeros (by adding them to the end) to increase N_{ind}. This padding is required to ensure the DFT represents an approximation to the Fourier transform (which is like a Fourier series of infinite period). If the signal is not padded with zeros then the DFT is an approximation to the Fourier series of the signal instead, if it were to be repeated with period equal to the signal length.

It will be assumed that the period of zero signal after the current pulse is sufficient that calculation of the DFT yields an approximation to the Fourier transform of the transient signal. If the DFT is calculated for both I_j^{res} and I_j^{probe}, then the ratio of the components $\tilde{I}_k^{res}$ and $\tilde{I}_k^{probe}$ can be taken according to Equation B.2 to give an estimation of the amplitude ratio and phase shift between components of the signal and the current probe response. The vector FR is a complex number, the components of which then represent an approximation to the frequency response of

the current probe and wire coil system.

$$FR_k = \frac{\tilde{I}_k^{res}}{\tilde{I}_k^{probe}} \tag{B.2}$$

The calculated frequency response function, FR, can then be used to estimate the probe response to an applied signal, or in this case to estimate the signal which gives rise to a certain response from the current probe. This is done by taking the DFT of the probe signal to yield $\tilde{I}_k^{probe}$, multiplying each component by the corresponding value of FR, then taking the inverse DFT to yield an estimate of the true current signal, with I_j^{corr} representing the corrected current signal, calculated according to Equation B.3.

$$I_j^{corr} = \frac{1}{N_{ind}} \sum_{k=1}^{N_{ind}} \left(\tilde{I}_k^{probe} \times FR_k \right) \exp\left(\frac{(2\pi i \,(j-1)\,(k-1))}{N_{ind}} \right) \tag{B.3}$$

This procedure suffers from many problems when implemented on the in-situ monitoring data. The correction is sensitive to the quality of the FR function which can be calculated from the calibration data. The measured signals both have errors associated with them, low level noise, and the 8-bit digitisation makes the data seem stepped. The 8-bit and stepped nature of data introduces sometimes severe fluctuations in the regions of the DFT corresponding to high frequency components.

The extent to which the DFT can be taken as an approximation of the Fourier transform is to a degree dependent upon the number of zeros with which the signal is padded. More zeros after the signal itself is generally going to represent a better approximation to the Fourier transform (effectively extending the periodicity towards infinity). However in practice the extent of such padding is limited by the requirements of computing time, and in this case a balance had to be struck between robustness of the correction and the time required.

In the following sections the procedures applied to estimate the probe frequency response function will be outlined, and the limitations discussed in greater detail. The quality of the FR function generated will be tested by application back to the raw calibration data and calculation of the deviation of I^{corr} from I^{res}.

B.1.2 Scaling of variables and determination of threshold values.

In the in-situ logging, data analysis will focus upon the periods of positive sample polarity. These represent roughly two thirds of each cycle of 20 ms. With sampling every 2 μs this is 10 000 samples per process cycle, and approximately 6600 samples during positive polarity. Discharging activity never extended to the end of positive

polarity, and generally there was an appreciable period of zero activity between cessation of discharge activity and the voltage passing through zero.

In light of the requirement that the processing not take an infeasible period of time, it was decided not to pad the signal data from each positive cycle beyond that already provided by the natural quenching of discharge activity. It was also decided that any interpolation of the FR function would be undesirable. The regions of interest in the calibration data then represented those sections of data with length 6600 samples and which could be considered to be independent. As discussed previously, for a section to be independent it is required that both the start and end of the section have zero value of both the current probe signal and the gradient of the current probe signal. This allows estimation of a frequency response of the current probe, FR, which can be applied to the experimental data without interpolation.

The raw data from which the calibration is to be calculated required scaling, and determination of threshold values prior to indexing of regions of interest. This was done in a broadly similar fashion to the single discharge case, though sufficient differences exist between the procedures to be worth repeating some elements. The vector containing the current probe data was called A in this case, corresponding to the first channel of the oscilloscope, the vector B was the voltage over the 200 Ω resistor. The scaling was as detailed in Equation B.4.

$$\begin{aligned} I_j^{probe} &= A_j \times 0.5 \quad \forall \quad j \\ I_j^{res} &= \frac{B_j}{200} \quad \forall \quad j \end{aligned} \tag{B.4}$$

The minimum detectable current shifts for each current record were also defined, according to Equation B.5. A gradient measure was also calculated for the I_j^{res}, using the same procedure as detailed in subsection A.1.2. This gradient measure, $\mathrm{d}I_j^{res}$, was again used to compile a list of stationary points, as in subsection A.1.3, and a histogram of the current values at stationary points calculated. The baseline level, I_{base}, was defined as before, and so were the threshold value, I_{thresh} and the minimum shift I_{shift}. All three refer only to the current data obtained from the resistor measurement.

$$\begin{aligned} I_{step}^{probe} &= \frac{100 \times 10^{-3}}{127} \\ I_{step}^{res} &= \frac{20/200}{127} \end{aligned} \tag{B.5}$$

One variable calculated during this stage of the procedure, which has no analogy for single discharge processing, was a running average of the current probe signal,

covering the current sample and 9 previous samples. This was defined according to Algorithm 15, in which N is again the total record length. This vector will be later used as part of a condition to determine whether the current probe signal has returned to zero signal.

Algorithm 15 *Calculation of current probe signal running average.*

I^{avg} is a vector of length N, initialised to contain all zeros

for all $10 \geq j \leq N$ **do**
  for $m = 0$ **to** 9 **do**
    $I_j^{avg} \leftarrow I_j^{avg} + 0.1 I_{j-m}^{probe}$
  end for
end for

B.1.3 Indexing of independent regions.

The indexing of 6600 sample independent regions is required in order that the frequency response of the current probe can be determined. Many parts of this procedure are sufficiently similar to many of the elements of the single discharge event indexing that detailed textual descriptions and illustrative examples will not be provided in this case. The important difference is that this procedure is trying to identify regions which begin with initiation of a discharge event at a time when I_j^{probe} is equal to zero, and terminate when the probe current has again returned to zero. As is evident from Figure B.1, this often did not occur until some time after termination of the actual event, and sometimes another event would initiate before I_j^{probe} was again zero. Two events whose signals in the current probe record overlapped in this fashion cannot be regarded as independent signals since the first has influenced the starting signal level of the second. The initial identification of discharge events was as detailed in Algorithm 16.

Up to this point the indexing procedure is similar to that adopted for single discharge data. Now the process diverges significantly as the indexing must be extended from the start of each discharge event up until the point where the subsequent recorded data may once again be considered independent of the proceeding signal. The procedure to extend the tail ends of regions indexed in the G variable is detailed in Algorithm 17.

One feature of the procedure which requires clarification is why the next 30 samples worth of data were automatically set as true after the start of each discharge event. This was because the running average, I_j^{avg}, would pass through zero value around the endpoint of the discharge event, however this happened as the current

Algorithm 16 *Initial identification of discharge events.*

G will again denote a logical indexing vector, initialised to all zeros

for $j = 1$ **to** N **do**
  if $I_j^{res} > I_{base} + I_{shift}$ **then**
    $G_j \leftarrow 1$
  end if
end for

extension of indexing to cover the rising discharge edge

for $j = N$ **to** 2 **do**
  if $G_j = 1$ **AND** $G_{j-1} = 0$ **AND** $\mathrm{d}I_{j-1}^{res} > 0$ **then**
    $G_{j-1} \leftarrow 1$
  end if
end for

probe signal, I_j^{probe} was overshooting the zero level. Conditions to account for this which were based around the 4^{th} order finite difference gradient of I_j^{probe} were found to be inadequate. The addition of the next 30 samples after the currently indexed termination of regions, which prior to this condition is the point where I_j^{probe} drops below $I_{base} + I_{shift}$, enabled this problematic region to be removed from consideration. From this point onwards the extension of indexing in vector G to cover up until I_j^{probe} returns to zero can be performed without concern over mis-identification.

The regions of independent signal held in G can now be listed in variable *index* using a listing routine identical to that detailed in subsection A.1.9, with the listing variable having the same structure as in that subsection. After listing, any identified regions over which the maximum to minimum variation in I_j^{probe} is less than $5I_{step}^{probe}$ are removed from the indexing vector G by setting all associated $G_j = 0$. A short representative section showing this indexing is displayed in Figure B.2.

B.1.4 Final identification of usable sections and calculation of frequency response function.

The final task before the estimation of the frequency response of the current probe is to identify sections of 6600 samples duration which start and end in regions where $G_j = 0$, and in which some discharge events were included. This procedure is outlined in Algorithm 18.

Algorithm 17 *Extension of the indexing to cover entire independent regions.*

need to locate all end-points in the current indexing
let N_{event} denote the number of regions indexed in G
list end points in vector $list$, of length N_{event}

$m \leftarrow 0$
for $j = 2$ **to** N **do**
  if $G_j = 0$ **AND** $G_{j-1} = 1$ **then**
    $m \leftarrow m + 1$
    $list_m \leftarrow j$
  end if
end for

extend indexing at all endpoints by 30 samples

for $j = 1$ **to** N_{event} **do**
  for all $list_j \geq m \leq list_j + 30$ **do**
    $G_m \leftarrow 1$
  end for
end for

extend indexing to point where subsequent data is independent

for $j = 2$ **to** N **do**
  if $G_{j-1} = 1$ **AND** $G_j = 0$ **AND** $I_j^{avg} \leq 0 - 0.25 I_{step}^{probe}$ **then**
    $G_i \leftarrow 1$
  end if
end for

Algorithm 18 *Identification and listing of usable regions.*

let G^{use} denote a second logical index vector, length N
$N_{scale} \leftarrow 6600$

for $j = 2$ **to** $N - N_{scale}$ **do**
  $temp \leftarrow G^{use}_{j-1} + G^{use}_{j} + G^{use}_{j+1}$
  if $temp = 0$ **AND** $G_j = 0$ **AND** $G_{j+N_{scale}-1} = 0$ **then**
    if $G_m = 1$ at some point between $m = j$ and $m = j + N_{scale} - 1$ **then**
      for all $j \geq m \leq j + N_{scale} - 1$ **do**
        $G^{use}_m \leftarrow 1$
      end for
    end if
  end if
end for

now list start and end coordinates of usable regions
use listing array $index^{use}$ for this purpose

$m \leftarrow 0$
for $j = 2$ **to** N **do**
  if $G^{use}_j = 1$ **AND** $G^{use}_{j-1} = 0$ **then**
    $m \leftarrow m + 1$
    $index^{use}_{m,1} \leftarrow j - 1$
  else if $G^{use}_j = 0$ **AND** $G^{use}_{j-1} = 1$ **then**
    $index^{use}_{m,2} \leftarrow j$
  end if
end for

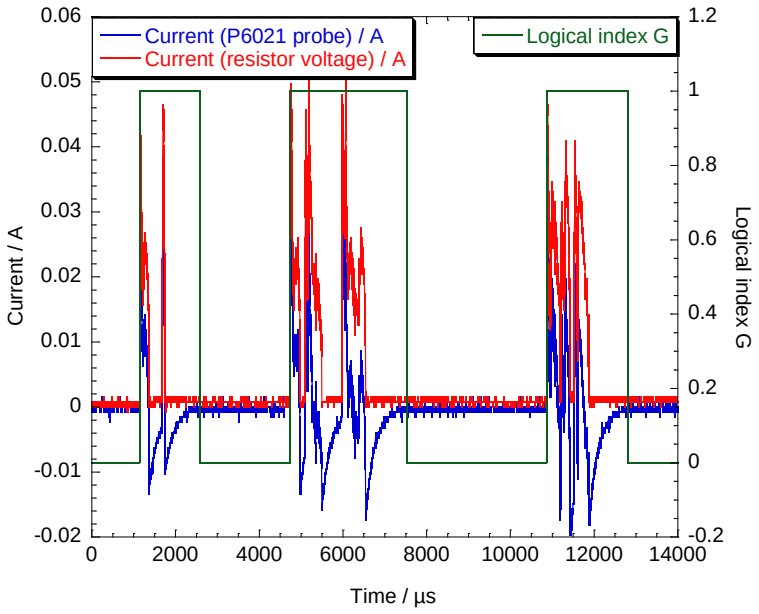

Figure B.2: *Example of the indexing of regions which may be considered related by the current probe signal, I_j^{probe}. Three separate independent blocks of discharge activity can be seen.*

The procedure finds regions of 6600 samples in length which start and end from $I_j^{probe} = 0$, and which contain at least one discharge event. These regions can be used to estimate the frequency response by calculating the DFT of both I^{probe} and I^{res}. The DFT was calculated using the fast Fourier transform algorithm supplied with the Matlab 7 software package. For each usable region identified, the ratio between $\tilde{I}_k^{res}$ and $\tilde{I}_k^{probe}$ was taken for all k. All such estimated frequency responses were stored, and then used to calculate an averaged frequency response from all the usable regions. The procedure for this is outlined in Algorithm 19.

In total there were 2101 usable regions, and an averaged frequency response function was calculated from these. This was done by calculation of the mean FR_k value for each k. The averaged frequency response function will be termed fr from now onwards. The frequency response function contains unique information only up to the Nyquist frequency, 250 kHz in this case. At most frequencies the function is essentially uninteresting, with amplitude close to 1, and phase shift close to zero. At lower frequencies the amplitude ratio and phase shifts become large. It is these lower frequency components of the signal which require correction in the current probe data. The amplitude and phase angle of the function fr and a function of frequency are presented in Figure B.3.

Algorithm 19 *Calculation of the frequency response function.*

N_{use} is the number of usable regions identified

$\mathcal{F}[X]$ will indicate the fast Fourier transform of vector X

I^R indicates the current probe response vector in usable region

I^S indicates the series resistor current probe in usable region

for $j = 1$ **to** N_{use} **do**

$p \leftarrow 0$

for $m = index_{j,1}^{use}$ **to** $index_{j,2}^{use}$ **do**

$p \leftarrow p + 1$

$I_p^R \leftarrow I_m^{probe}$

$I_p^S \leftarrow I_m^{res}$

end for

$\tilde{I}^R \leftarrow \mathcal{F}\left[I^R\right]$

$\tilde{I}^S \leftarrow \mathcal{F}\left[I^S\right]$

let FR be the frequency response data array, dimension 6600 rows and N_{use} columns

for $m = 1$ **to** N_{scale} **do**

$FR_{m,j} \leftarrow \dfrac{I_m^S}{I_m^R}$

end for

end for

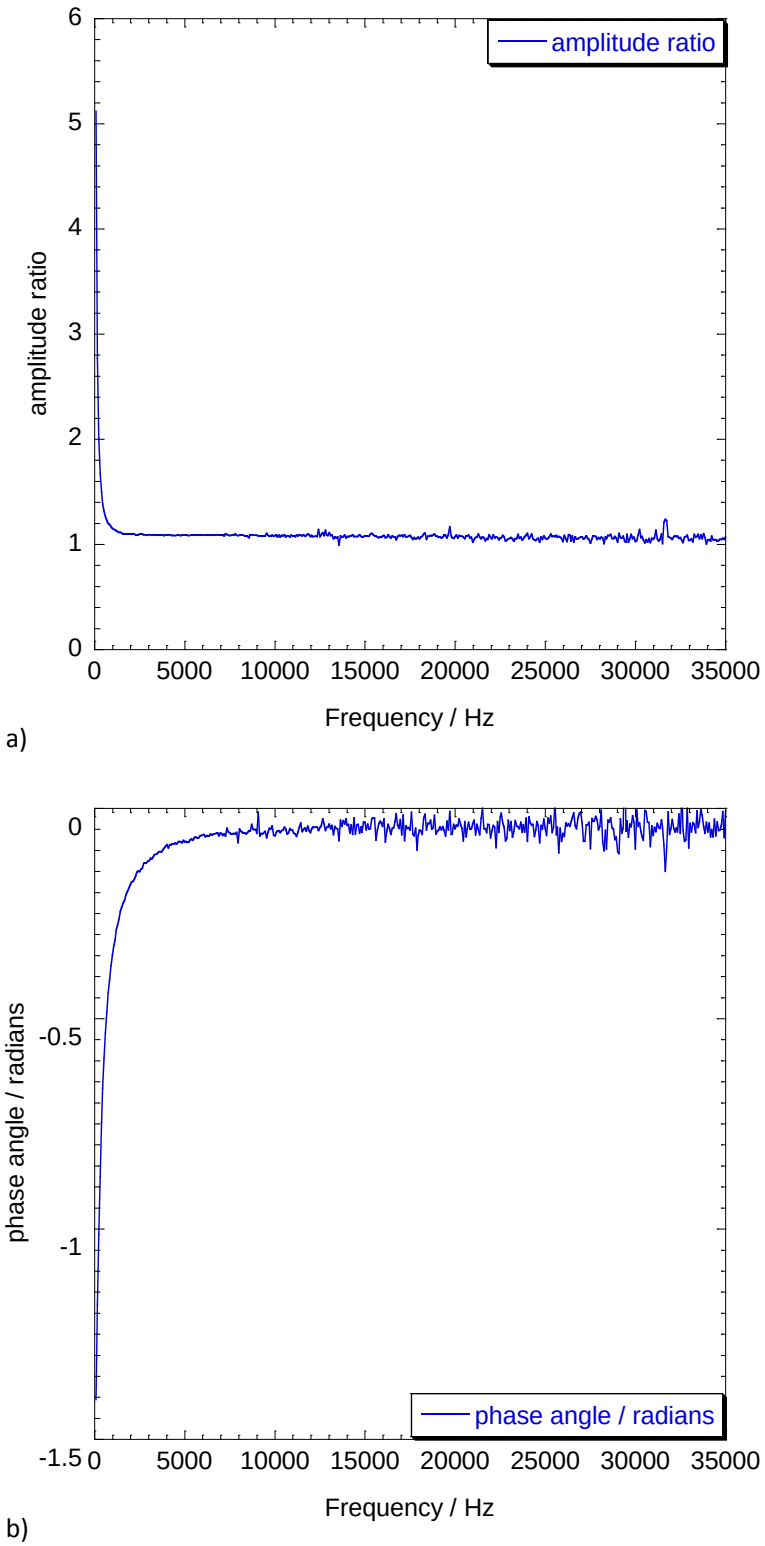

Figure B.3: *The low frequency end of the frequency response function, fr, calculated for the current probe from the calibration data.*

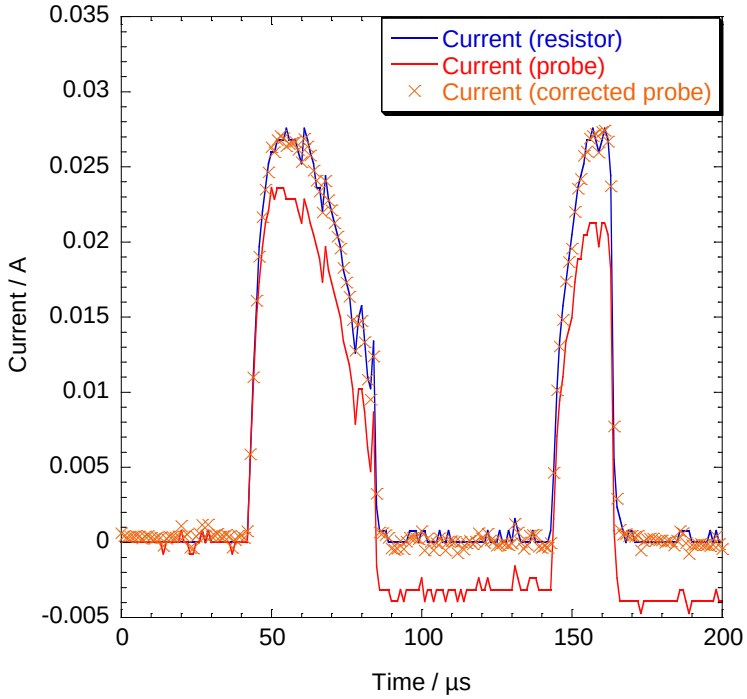

Figure B.4: *Section of calibration data showing the current measured via a known resistance, using the current probe, and the corrected current probe signal.*

B.2 Validation of correction procedure and estimation of uncertainty.

The best measure of the quality of the averaged frequency response function obtained is to apply it back to the calibration data so the corrected data and actual signal may be directly compared. This was done for all 2101 sections of usable calibration data. Each section of current probe data, I^{probe}, was converted to the frequency domain by application of the FFT. Each frequency element, $\tilde{I}_k^{probe}$, was multiplied by the corresponding entry in the frequency response, fr_k. The resulting vector was returned to the time domain by application of the inverse FFT, and again referred to as I^{corr}. The values of I^{probe}, I^{res} and I^{corr} for one section of data are plotted in Figure B.4.

From Figure B.4 is it clear that the response function fr obtained is adequate but imperfect. It is therefore important to quantify the extent of uncertainty expected when it is used during processing of the in-situ monitoring experiments, for which there will be not in general be a more directly measured current signal to compare against. The difference $I_j^{res} - I_j^{corr}$ was calculated for each of the calibration regions to give an estimation of the error in the procedure. Once all the errors

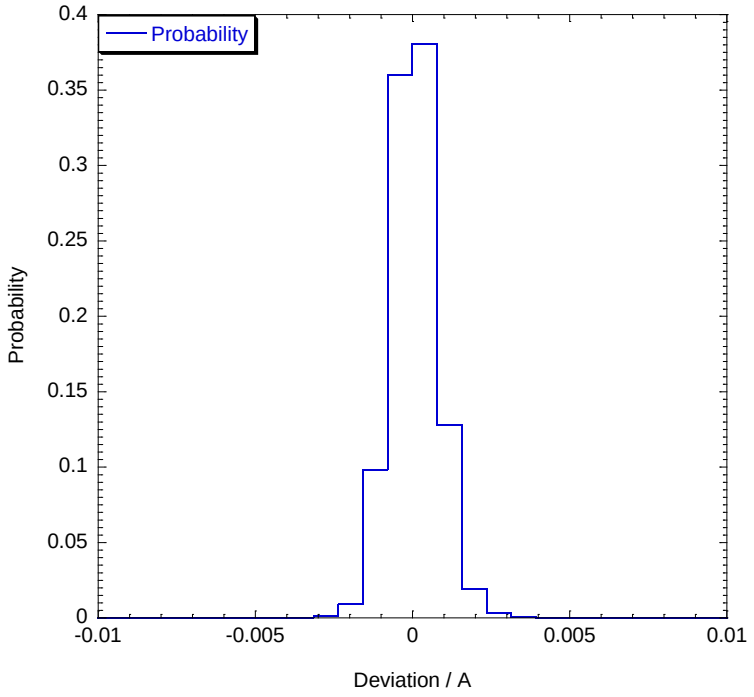

Figure B.5: *Histogram of the deviations of corrected current probe signal, I^{corr}, from the current measured from voltage over a known resistor, I^{res}. Bin width used was 790 μA.*

were compiled, a histogram of the deviations seen was produced, this is presented in Figure B.5. The bin width used was 790 μA, which was the minimum resolvable shift in the original 8-bit signal from the current probe with range $\pm$ 100 mA.

The distribution is seen to be quite sharply peaked about zero, but extends with significant probability to several mA of deviation. A standard error may be estimated from the data by calculating the mean of the squared deviations and taking the square root, which yields $\sigma_{\mathrm{I}} = 620$ μA. However this estimate includes all data within the calibration regions, and is likely skewed by the large number of samples at which both signals were essentially zero. This represents an over-estimate of the procedure reliability.

A better measure may be obtained by considering only those deviations at samples where I^{res} was more than $5I^{res}_{step}$. This results in a larger standard error estimate of $\sigma_{\mathrm{I}} = 750$ μA. This is comparable to the minimum resolvable shift in the original current probe data, it is slightly less though, so the value of $I^{probe}_{step} = 790$ μA should be adopted as the error estimate. The procedure is seen therefore to be adequate for measurements of discharge properties to within the experimental limitations. However it should be appreciated that whilst the correction performance is gener-

ally good, there are aberrations for a minority of discharge events. The maximum deviation observed was ≈ 8 mA. Therefore any one single measurement from such corrected data should not be relied upon, large numbers however should ensure reliable conclusions can be reached.

B.3 Correction of current signal for in-situ monitoring experiments.

Before discharge events can be indexed and measured, the current probe signal must be corrected for the inductive droop effects discussed in section B.1. An example of the raw data from in-situ monitoring experiments, for a single period of positive polarity, is shown in Figure B.6. Several prominent current peaks are evident, corresponding to discharge events on the small monitored area. The baseline current level of the current probe signal requires correction before any further progress can be made in measuring the properties of the discharge events. The data plotted in Figure B.6 has already been scaled from the raw results vectors, according to the relations $I_j = 0.5A_j$ and $V_j = 100B_j$, where A and B are again the first and second data channels of the oscilloscope used.

The first and most obvious task is to identify the locations of the periods of positive sample polarity within the current and voltage records. This must be done in order to allow sections of 6600 samples duration to be isolated and corrected for the current probe inductance effects. This was relatively simple and the procedure is detailed in Algorithm 20. This procedure resulted in the vector G^P holding the value of 1 for regions of total duration 6600 samples each, and each starting from the point at which the voltage exceeded 10V.

Before application of the FFT algorithm the regions of positive polarity were copied into an array, I^{resp} ('resp' for 'response' of the current probe), with dimension 6600 rows and N_P columns. N_P is the total number of regions of positive polarity. Each region was then separately converted to the frequency domain by application of the FFT algorithm, each frequency element multiplied by the corresponding entry in the frequency response function, fr, and then converted back to the time domain and copied into the relevant column of the array I^{sig} ('sig' for 'signal'). The procedure for the correction is detailed in Algorithm 21. V^{sig} is an array analogous to I^{sig} and containing the corresponding voltage data.

After the procedure from Algorithm 21 has been executed, the in-situ monitoring data has the typical appearance as displayed in Figure B.7. The serious distortion of the baseline level due to LR droop of the current probe signal has been removed. There is an important question remaining about the baseline current level however.

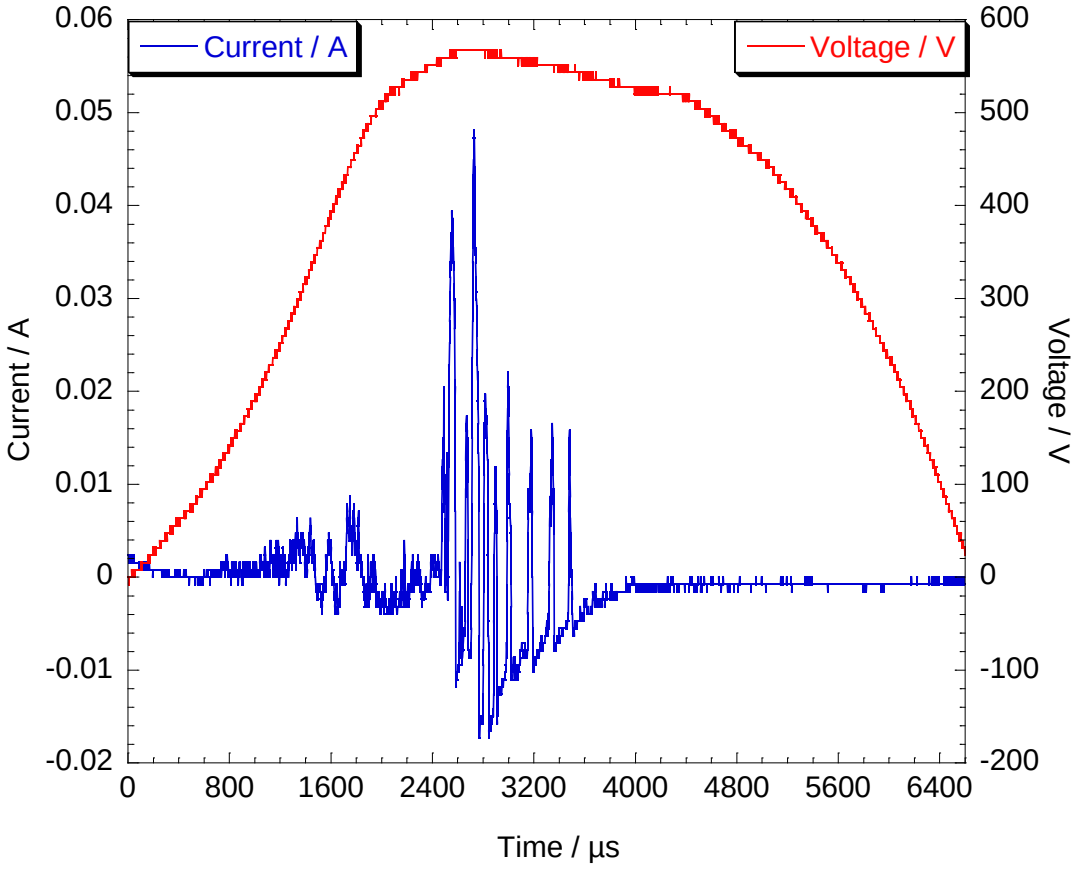

Figure B.6: *Example of the raw data from a single positive period during in-situ discharge monitoring.*

Algorithm 20 *Identification of the positive periods of process cycles.*

N is again vector length and $N_{scale} = 6600$
G^P will be used as logical indexing vector
$seek \leftarrow 0$
for $j = 2$ **to** N **do**
  if $seek = 1$ **AND** $V_j > 10$ **AND** $V_{j-1} < 10$ **then**
    $seek \leftarrow 0$
    for all $j \geq m \leq j + N_{scale} - 1$ **do**
      $G^P_m \leftarrow 1$
    end for
  else if $seek = 0$ **AND** $V_j < 0$ **then**
    $seek \leftarrow 1$
  end if
end for

Algorithm 21 *Correction of the current signal.*

$m \leftarrow 0$
for $j = 2$ **to** N **do**
  if $G_j^P = 1$ **AND** $G_{j-1}^P = 0$ **then**
    $m \leftarrow m + 1$
    $p \leftarrow 0$
    for all $j \geq n \leq j + N_{scale} - 1$ **do**
      $p \leftarrow p + 1$
      $I_p^{resp} \leftarrow I_n$
      $V_p^{sig} \leftarrow V_n$
    end for
  end if
end for
apply signal correction procedure
for $j = 1$ **to** N_P **do**
  for all $1 \geq m \leq N_{scale}$ **do**
    $I_m^{temp} \leftarrow I_{m,j}^{resp}$
  end for

  $\tilde{I}^{temp} \leftarrow \mathcal{F}\left[I^{temp}\right]$
  for all $1 \geq k \leq N_{scale}$ **do**
    $\tilde{I}_k^{temp} \leftarrow \tilde{I}_k^{temp} \times fr_k$
  end for

  $I^{temp} \leftarrow \mathcal{F}^{-1}\left[\tilde{I}^{temp}\right]$
  for all $1 \geq m \leq N_{scale}$ **do**
    $I_{m,j}^{sig} \leftarrow I_m^{temp}$
  end for
end for

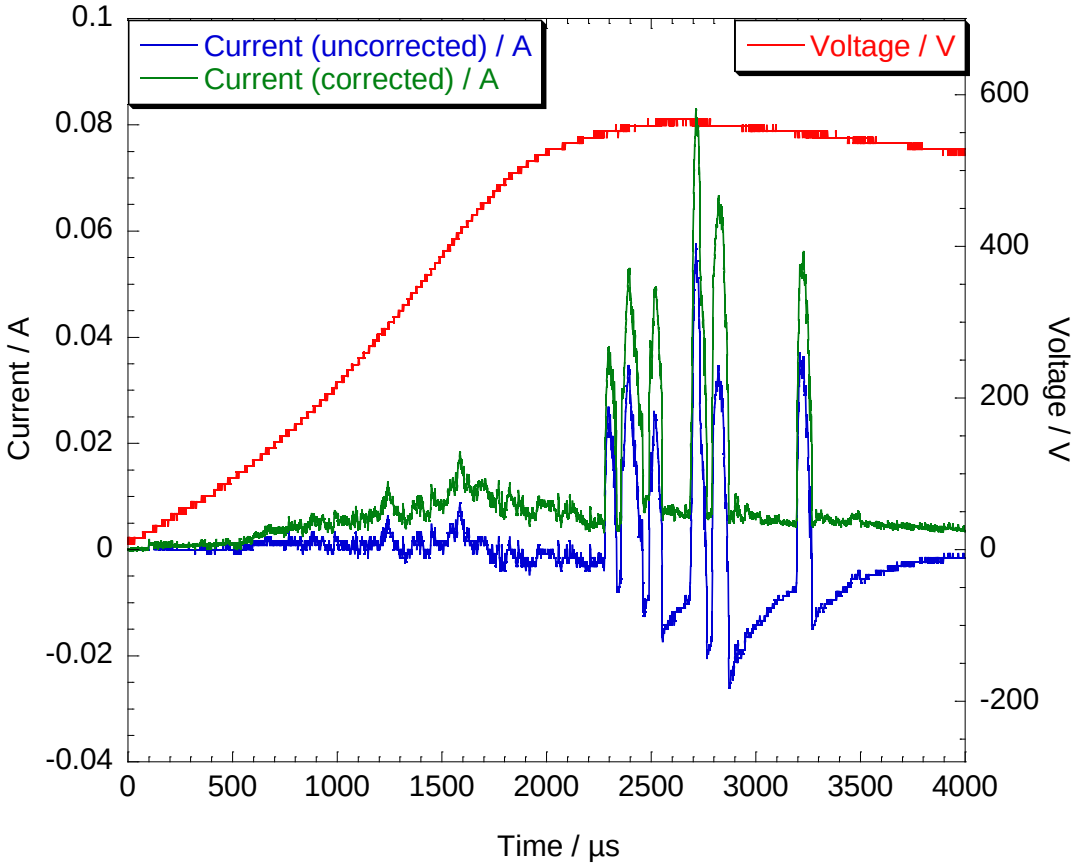

Figure B.7: *Comparison of the uncorrected and corrected current signal. Note that the full 6600 sample region is not displayed to allow better resolution of discharge features during the active period.*

After application of the current signal correction, the discharge events appear to be superposed upon an underlying low level hump in the current response. This could represent a variation in the baseline non-discharge current as the voltage is increased, or it could be an error resulting from the correction procedure. This issue will be discussed in subsection B.3.1.

The section shown will be re-used throughout the following discussion to illustrate the various stages in processing. This particular section is from about 3 minutes into processing of sample Al_04, with two 500 μm wires forming the small monitored area.

B.3.1 Variation of the baseline current during each cycle.

The issue of the baseline level is interesting, however it is unlikely to influence the eventually measured discharge event properties for two reasons. Firstly if it is an error then it is on a much longer timescale then any discharge event, and secondly because the current level at the start of the discharge event must be subtracted from current during the event in order to measure the event properties accurately. Even so, it was possible to resolve the issue of whether the current hump represented a genuine signal or not using a modification of the standard in-situ monitoring experiment.

As was mentioned in section 3.1, the power unit does not generate the voltage bias seen during processing. The positive bias is the result of interaction between power supply and the sample-electrolyte system. This fact can be exploited to allow limited operation of the in-situ monitoring experiments using a known resistance in place of the current probe, to obtain more reliable information about the small area current. This is accomplished by connecting the output bar to ground and the counter-electrode to the supply output. The output bar now being grounded allows resistor based current measurement without having to float the oscilloscope to 600 V. Incidentally this is the reason why a non-contact current probe was used for the in-situ monitoring generally.

This geometry has a major flaw which means it cannot be used for long periods, which is that with the counter-electrode connected to the output, the bulk of the electrolyte is raised to high voltages, meaning that such experiments cannot be run with the normal processing tank, and the electrolyte cannot be passed through the heat exchanger without developing a short circuit to ground through the chilled water system. As a result, long processing periods would overheat. Nonetheless, by reversing the output and running a short period of processing in an electrically isolated insert tank, it was possible to obtain data about the current through the small monitored area which required no correction.

Examination of this data revealed that an increase in the baseline current with applied voltage is a real feature of the processing. This can be seen in Figure B.8 and Figure B.9. One figure shows a cycle displaying large events, the other only small discharge events of a few mA at peak. Compared to the current data in Figure B.7, the hump is of lower magnitude, however this is probably because the data in Figure B.8 and Figure B.9 are from a sample with only a single 500 μm wire as small area.

The underlying hump shape visible Figure B.7 is obscured by roughness of the current signal. This does not represent noise however, as the signal is cleaner when the voltage is lower. The roughness possibly arises from a number of overlapping

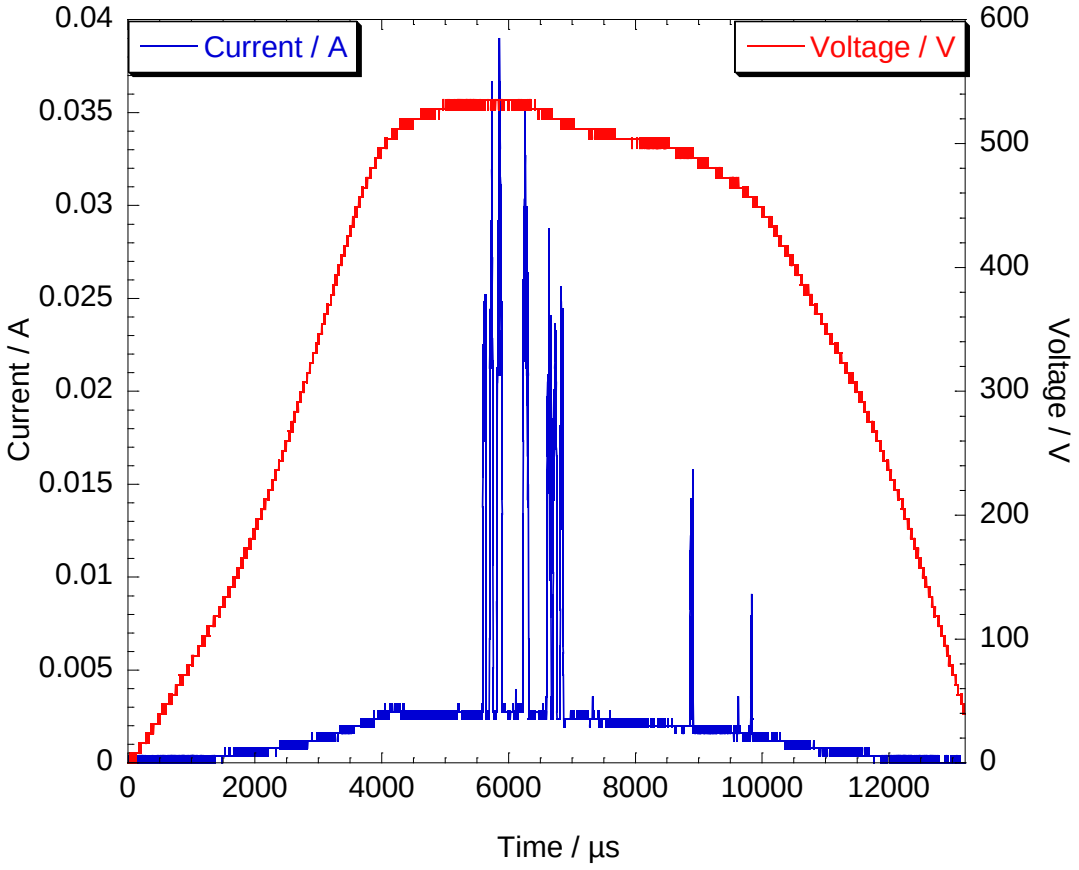

Figure B.8: *Example of data from a more reliable current measurement during in-situ monitoring, showing a cycle containing large discharge events.*

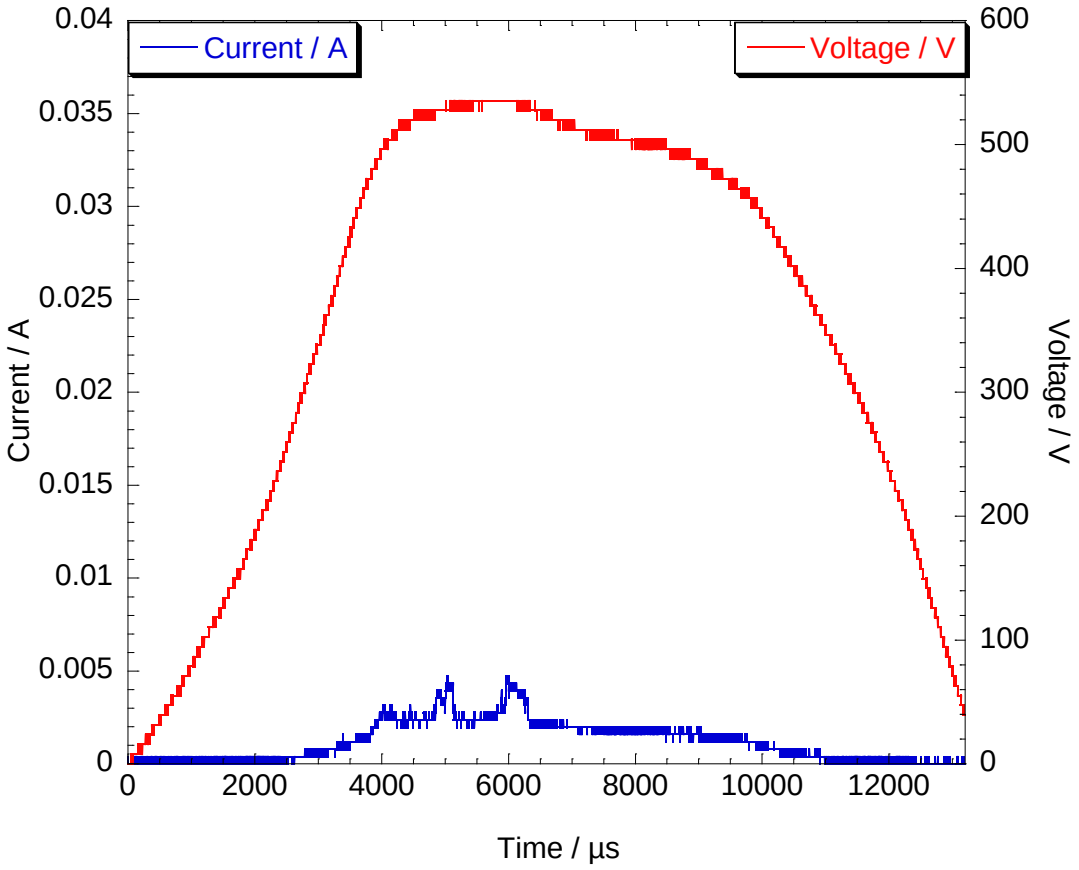

Figure B.9: *Example of data from a more reliable current measurement during in-situ monitoring, showing a cycle during which small amplitude events are visible.*

small discharge events, such as those visible in Figure B.9. In general a limitation of the in-situ monitoring technique as it will be presented here is that small discharge events ($\leq$ 10 mA) cannot be reliably measured once the current probe signal correction has been applied. This is also a result of using small monitored areas which turned out to be still too large to reliably separate out the smallest of discharge events.

This independent confirmation of the presence of a current hump underlying the signals of discharge events in the small area current response should hopefully reassure the reader of the reliability of the current signal correction procedure. In contrast to single discharge experiments, during which the background current level varied little due to the comparatively small changes in applied voltage, the baseline current changes over the course of each cycle during in-situ monitoring. This baseline current must be determined before indexing of regions of interest can

proceed.

B.4 Adjustment for the baseline current level.

Determination of the baseline current level at each point during a process cycle is not easy. Such a background can only really be obtained from cycles in which no discharge events are observed. Determining which cycles contain discharge events before being in a position to even index discharge event signals leads into a circular argument. As such the determination of the baseline current waveform is inexact, and involves several assumptions. The first part of the procedure determines which process cycles (columns of I^{sig}) are likely to be suitable for estimation of the baseline.

The first stage is to compile a list of the maximum current values during each cycle, a subsidiary list is then compiled of all the maximum current values which are below 40 mA. This list is stored as a vector, I^{max}. The selection of 40 mA as a cut off for this stage was arbitrary, and made by the author as it worked reasonably well in testing. In the 20 s segment from which the example plotted in Figure B.7 was taken, the vector I^{max} had 369 entries, out of 998 process cycles in the entire segment.

The vector I^{max} is then used to generate a histogram of the maximum current during each cycle, using binning of 1 mA. The histogram was then used to determine the mode value of the maximum current for those cycles without large scale discharging activity. The mode value plus 2 mA was termed I_{cyc}, and was used in determination of the baseline current. In the example 20 s segment the value of the threshold I_{cyc} was 16 mA. The baseline current variation was then estimated according to Algorithm 22, in which the background current level is stored in the vector I^{back}, and N_{cyc} is the total number of process cycles in the segment, which was 998 for the example considered.

Vector I^{back} now contains an estimate of the baseline current variation during each process cycle (of positive polarity and starting from when the voltage exceeded 10 V). This is assuming that the baseline current level varies only slowly over each 20 s data segment. The baseline current variation determined for the example segment was calculated from 161 cycles out of 998 overall, and can be seen in Figure B.10. This background variation was then subtracted from each column of the array I^{sig} to yield another array, I^{adj} (in which adj stand for adjusted), and therefore from each process cycle in the data segment. The appearance of the example section after this adjustment is presented in Figure B.11.

It can be seen in Figure B.11 that the adjustment is far from perfect. It does however remove most of the effect of the current hump upon which the signals of

Algorithm 22 *Estimation of the cycle baseline current variation.*

the number of cycles which meet condition to be included is pre-determined and stored as the variable N_{count}

for $j = 1$ **to** N_{cyc} **do**

$I_{peak} \leftarrow$ maximum current value in column j of array I^{sig}

if $I_{peak} \leq I_{cyc}$ **then**

for all $1 \geq m \leq N_{scale}$ **do**

$$I_m^{back} \leftarrow I_m^{back} + \frac{1}{N_{count}} \times I_{m,j}^{sig}$$

end for

end if

end for

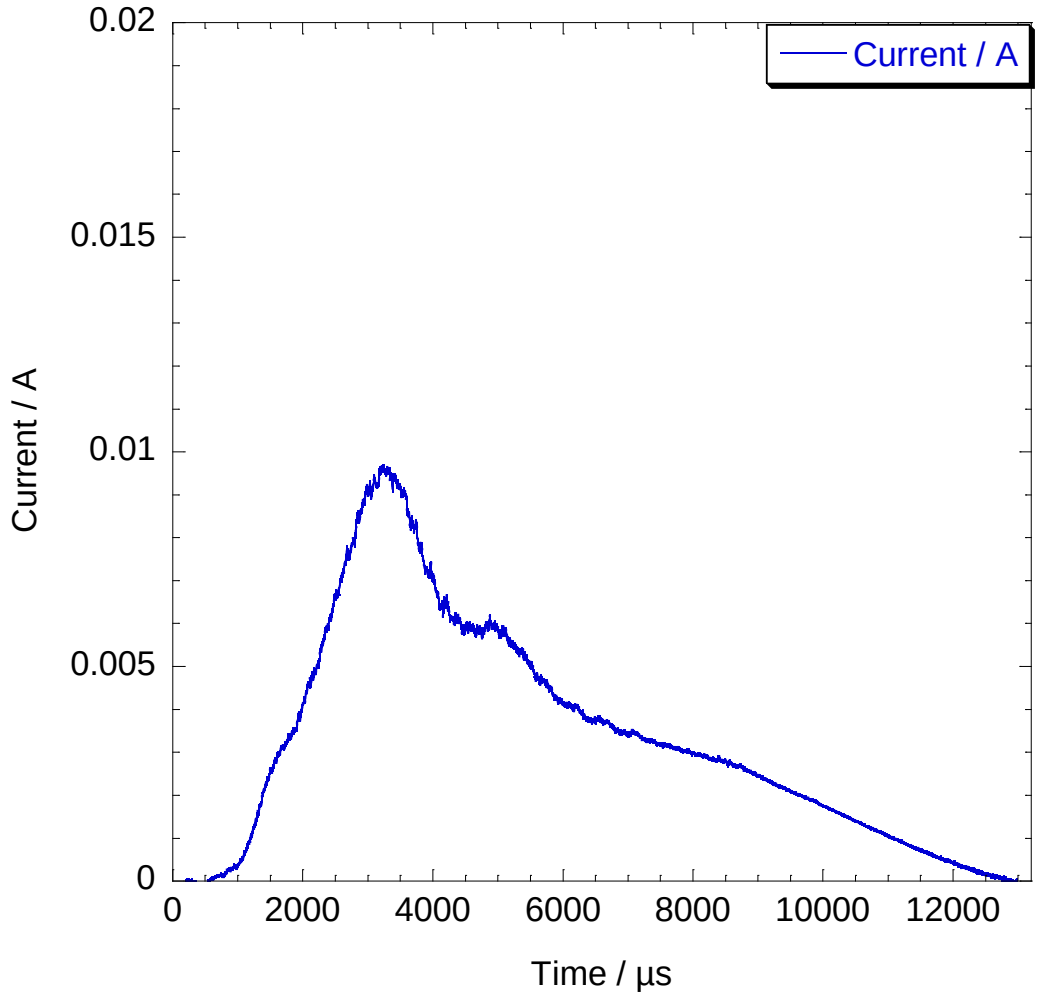

Figure B.10: *The estimated current background variation, I^{back}, calculated from all the cycles in the 20 s example segment.*

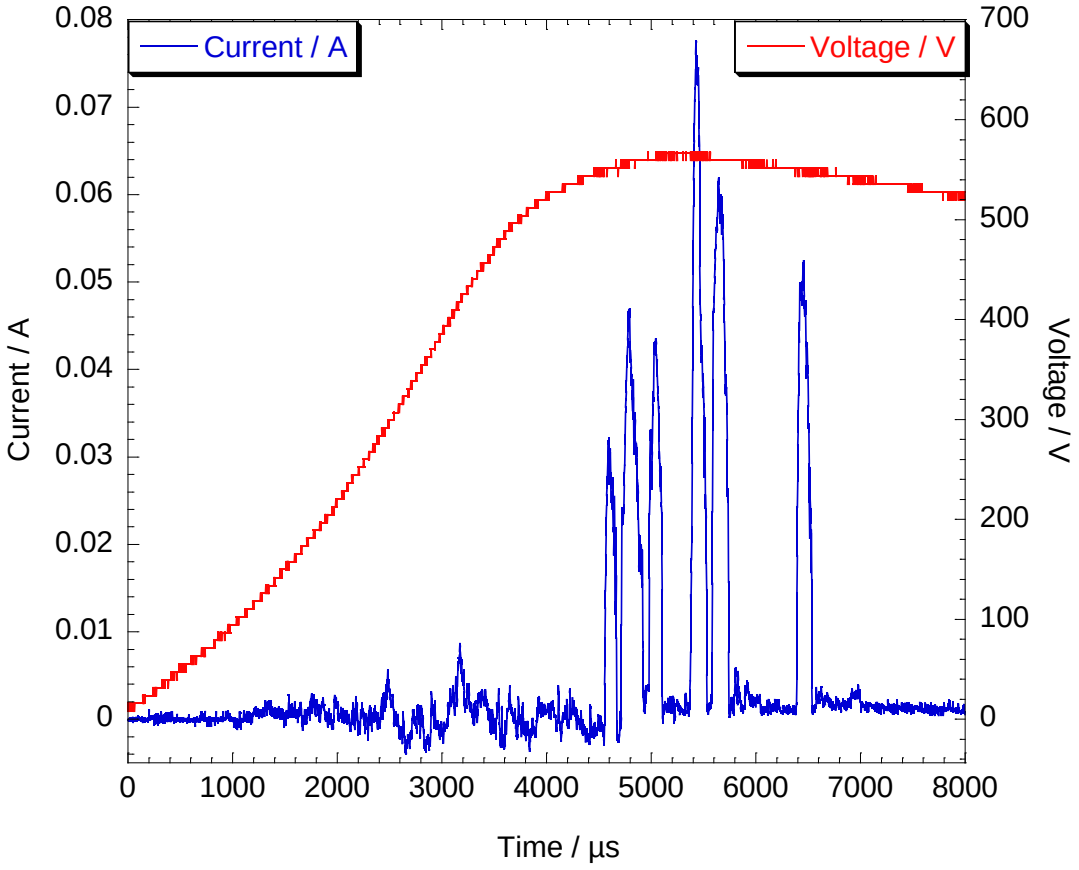

Figure B.11: *The current and voltage signals after adjustment to remove the estimated background current variation.*

discharge events are superimposed. The current data stored in the array I^{adj} is now as suitable as it can reasonably be made for identification of current peaks corresponding to discharge events. Of course, the much greater degree of pre-processing to get the data to this point (as well as additional errors incurred from the nature of the experiment itself) when compared to the single discharge experiments means that the data from in-situ monitoring may only be used to identify and provide information about the larger discharge events. The technique itself as presented here is limited by the experimental choice of samples and the equipment utilised, with suitable refinements the methodology could easily provide better resolution and hence be used to isolate smaller events.

B.5 Identification and listing of discharge event locations.

As for single discharge data, the first stage of indexing is to estimate gradient measures and current thresholds for use in locating discharge events. These processes deviate significantly from those used for single discharge data, though many common procedures exist.

For the in-situ monitoring data two gradient measures are calculated. The first order forward difference gradient was calculated according to Equation B.6 from the adjusted current record, I^{adj}, and stored in an array termed $\mathrm{d}I^f$ of same dimension as I^{adj}. In similar fashion the centred second order finite difference gradient was calculated using I^{adj} and according to Equation B.7, this was stored in array $\mathrm{d}I^c$. These two different gradient measures were used for different purposes in the following processing. The 4^{th} order finite difference was not used as in subsection A.1.2 as the extensive pre-processing means that the current data for in-situ monitoring is substantially more challenging to index, and better results were obtained using these two gradient measures in tandem.

$$\frac{\mathrm{d}f}{\mathrm{d}t} = \frac{f(t+\delta t) - f(t)}{\delta t} + O(\delta t)$$

then if F is a vector where

$$F_j = f(j \times \delta t) \tag{B.6}$$

then can write a measure of the gradient at the j^{th} entry as

$$\mathrm{d}F_j^f = \frac{F_{j+1} - F_j}{\delta t}$$

$$\frac{\mathrm{d}f}{\mathrm{d}t} = \frac{f(t+\delta t) - f(t-\delta t)}{2\delta t} + O\left(\delta t^2\right) \text{ then if F is a vector where}$$
$$F_j = f(j \times \delta t)$$
$$\text{then can write a measure of the gradient at the } j^{th} \text{ entry as} \tag{B.7}$$
$$\mathrm{d}F_j^c = \frac{F_{j+1} - F_{j-1}}{2\delta t}$$

B.5.1 Determination of the current threshold.

As was the case for single discharge data, a threshold value for regions of elevated current to be indexed as part of a discharge event must be estimated. However, as has been often mentioned, the more variable nature of the data during each processing cycle, means that in this case the current threshold is a vector of length N_{scale}, allowing different levels of current shift to be indexed as a discharge event in different regions of each process cycle. This is of course sensitive to the more global behaviour in the 20 s recorded segment in which a cycle occurred.

The stationary points of the current, as estimated from the gradient measure $\mathrm{d}I^c$, were calculated according to Algorithm 23, in which *list* is an array of 2 columns and N_{stat} rows. N_{stat} again refers to the total number of stationary points identified in the current record I^{adj}. One important difference from the single discharge case is that the coordinate assigned to each stationary point is a local coordinate to the previously identified 6600 sample region in which the stationary point lies. The local nature of the stationary point coordinates will be utilised later.

Once the listing of stationary points is completed, the determination of the current threshold may proceed. Threshold current values are calculated for different parts of each process cycle, and the cycle is broken down into 66 evenly spaced subregions of 100 samples for this purpose. In this context I^{thresh} will represent a vector of 66 entries, one entry to hold the threshold value for each part of the processing cycle. The vector I^{bins} is a list of bin midpoints for calculating histograms, running from -20 mA to +150 mA with spacing $I_{step} = 0.79$ mA. The total number of bins is termed N_{bins}. The procedure for calculating I^{thresh} is detailed in Algorithm 24.

The procedure of Algorithm 24 is similar to the threshold determination of single discharge events detailed in subsection A.1.4. However it is separately carried out for each small section of the process cycle. In each 100 sample subregion the threshold is defined as either the minimum between the fluctuation about the baseline at that point and a second peak, or if that does not exist the maximum value at which a stationary point in $\mathrm{d}I^c$ was observed. A minimum value of 5 mA is accepted for the local value of I^{thresh}. The I^{thresh} vector is then smoothed over a period of 3

Algorithm 23 *Generation of list of stationary current values.*

$p \leftarrow 0$
for $j = 1$ **to** N_{cyc} **do**
  for $m = 2$ **t** N_{scale} **do**
    if $(\mathrm{d}I^c_{m,j} < 0$ **AND** $\mathrm{d}I^c_{m-1,j} > 0)$ **OR** $(\mathrm{d}I^c_{m,j} > 0$ **AND** $\mathrm{d}I^c_{m-1,j} < 0)$ **then**
      $p \leftarrow p + 1$
      if $\mid \mathrm{d}I^c_{m,j} \mid < \mid \mathrm{d}I^c_{m-1,j} \mid$ **then**
        $list_{p,1} \leftarrow I^{sig}_{m,j}$
        $list_{p,2} \leftarrow m$
      else
        $list_{p,1} \leftarrow I^{sig}_{m-1,j}$
        $list_{p,2} \leftarrow m - 1$
      end if
    end if
  end for
end for

samples, and a condition applied that at no point can the local value be less than two thirds of the maximum I^{thresh} value.

After that, the vector I^{thresh} is padded to make it N_{scale} values in total length. The threshold vector is calculated with respect to the entire 20 s data segment, and then applied to each cycle individually. An example of the threshold level vector, plotted with the example cycle for comparison, is found in Figure B.12. The current threshold is seen to show slight increases in value during parts of the cycle which had a tendency to be noisier, within the approximately 1000 cycles in the respective 20 s segment of the recording. These are only small increases, however it was found in practice to dramatically reduce the number of artefacts in the discharge indexing.

As was discussed before, the 'noisy' period towards the start of each cycle is probably not noise, but rather many very small discharge events which overlap. Nonetheless, the experimental set-up used could not resolve these events properly, and so the indexing algorithms should not be identifying such small fluctuations as discharge events, as the data obtained would contain no sensible information.

B.5.2 Initial indexing and listing of discharge events.

The initial indexing was simple, with a sample being assigned as part of a discharge event if the current was in excess of, or equal to, the local current threshold. This was done for each column of the current array I^{adj}. The indexing was stored in a logical array, termed G, of equivalent dimensions to I^{adj}, with a value of 1 indicating

Algorithm 24 *Estimation of current threshold values for each point in the process cycle.*

for $j = 1$ **to** $\frac{N_{scale}}{100}$ **do**
  let $temp$ be a temporary listing vector used in computation
  $p \leftarrow 0$
  $k_{start} \leftarrow (j-1) \times 100 + 1$
  $k_{end} \leftarrow j \times 100$
  for $m = 1$ **to** N_{stat} **do**
    if $list_{m,2} > k_{start}$ **AND** $list_{m,2} \leq k_{end}$ **then**
      $p \leftarrow p + 1$
      $temp_p \leftarrow list_{m,1}$
    end if
  end for
  $hist \leftarrow$ calculated histogram of values stored in $temp$ with bins centred around I^{bins} values
  $k_{max} \leftarrow$ coordinate of maximum value of $hist_p$ for $1 \geq p \leq N_{bins}$
  $seek \leftarrow 1$
  for $m = k_{max}$ **to** $N_{bins} - 1$ **do**
    if $seek = 1$ **then**
      if $hist_m = 0$ **OR** $hist_m < hist_{m+1}$ **then**
        $I_j^{thresh} \leftarrow I_m^{bins}$
      end if
    end if
  end for
  if $I_j^{thresh} < 5 \times 10^{-3}$ **then**
    $I_j^{thresh} \leftarrow 5 \times 10^{-3}$
  end if
end for
$temp = I^{thresh}$
for all $2 \geq j \leq \frac{N_{scale}}{100} - 1$ **do**
  $I_j^{thresh} \leftarrow \frac{1}{3}\left(temp_{j-1} + temp_j + temp_{j+1}\right)$
end for
$I_{max}^{thresh} \leftarrow$ maximum value stored in I^{thresh}
for all $1 \geq j \leq \frac{N_{scale}}{100}$ **do**
  if $I_j^{thresh} < \frac{2}{3} I_{max}^{thresh}$ **then**
    $I_j^{thresh} \leftarrow \frac{2}{3} I_{max}^{thresh}$
  end if
end for

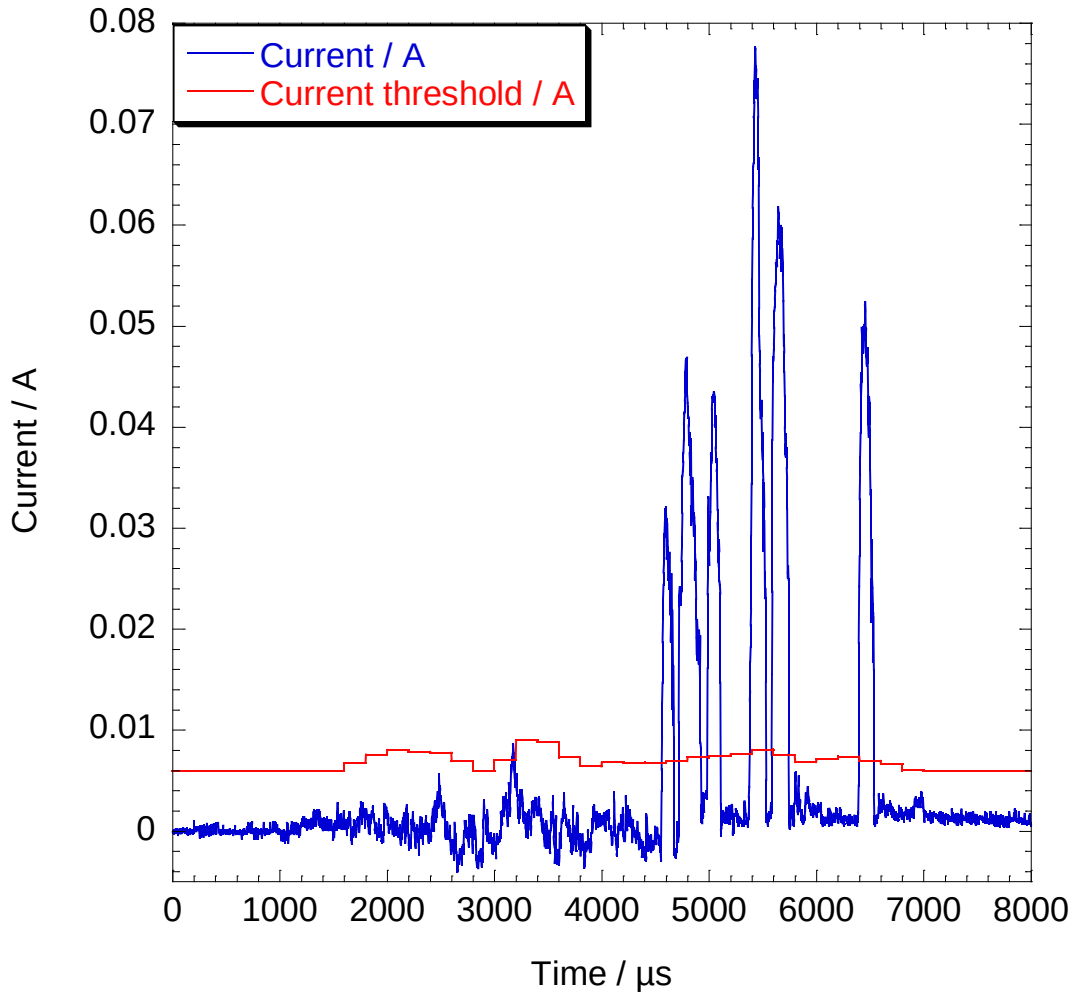

Figure B.12: *The current threshold for the 20 s data segment from which our example cycle is drawn, plotted for comparison with the example cycle current signal.*

Column	Measurement	Symbol	Unit
1	Cycle number	k_{cyc}	integer
2	Initiation coordinate within cycle	k_{start}	integer
3	Termination coordinate within cycle	k_{end}	integer
4	Initiation current level	I_{start}	A
5	Termination current level	I_{end}	A
6	Average baseline current	I_{base}	A
7	Peak current minus averaged baseline	I_{peak}	A

Table B.1: *Properties stored in the columns of the listing array index.*

inside an event and the value 0 outside. A figure representing the output of this procedure will not be produced, as it should be evident from inspection of Figure B.12 which parts of the example cycle will be indexed as above the threshold, I^{thresh}.

In the section which will follow, a process which will be repeated often is the listing of discharge event locations, as indexed in array G, and the measurement of some selected properties of the events as currently indexed. The list will be in the form of an array termed *index*, of dimension 7 columns and N_{event} rows. The details of which measures will be stored in which column of the listing variable are shown in Table B.1. These measurements were used primarily to allow for screening conditions to be applied to the listed discharge events at various points during indexing.

The procedure for generating the *index* array is outlined in Algorithm 25. This procedure will be referred to many times later on in the indexing process. The first three columns allow the event to be located by listing first the cycle within the wider 20 s segment in which the event occurs, then the local coordinates of initiation and termination of the event within the specified process cycle.

Knowledge of the initiation and termination currents is an important quality control measure. Whilst the baseline level is varying all the time slightly, if the indexed start and end currents differ by much more than a few times $I_{step} = 0.79$ mA, it likely indicates a problem with the indexing of that event. The average of the start and end currents defines a local baseline level for current, which can be used to estimate the current level due to the discharge alone. The maximum current shift due to the discharge event is important, as events which demonstrate too low a level of current variation are unlikely to be reliably indexed discharge events. After application of the initial indexing and listing, in the 20 s segment from which the example section is drawn there were 6766 discharge events indexed.

Algorithm 25 *Generation of listing array of indexed discharge events.*

$p \leftarrow 0$
$seek \leftarrow 0$
for $j = 1$ **to** N_{cyc} **do**
  for $m = 2$ **to** N_{scale} **do**
    if $seek = false$ **then**
      if $G_{m,j} = 1$ **AND** $G_{m-1,j} = 0$ **then**
        $p \leftarrow p + 1$
        $seek \leftarrow 1$
        $index_{p,1} \leftarrow j$
        $index_{p,2} \leftarrow m$
        $index_{p,4} \leftarrow I_{m,j}^{adj}$
      end if
    else
      if $G_{m,j} = 0$ **AND** $G_{m-1,j} = 1$ **then**
        $seek \leftarrow 1$
        $index_{p,3} \leftarrow j - 1$
        $index_{p,5} \leftarrow I_{m-1,j}^{adj}$
      end if
    end if
  end for
end for
for $j = 1$ **to** N_{event} **do**
  $index_{j,6} \leftarrow \dfrac{index_{j,4} + index_{j,5}}{2}$
  $I_{max} \leftarrow$ maximum value of $I_{m,j}^{adj}$ over range $index_{j,2} \geq m \leq index_{j,3}$
  $index_{j,7} \leftarrow I_{max} - index_{j,6}$
end for

B.5.3 Common procedures for finalisation of indexing.

The listing procedure detailed in Algorithm 25 is one example of a repeated procedure during indexing of discharge event current signatures. There were three other commonly repeated procedures, and these will detailed and explained before their usage in finalising the indexing of discharge events is outlined in subsection B.5.4.

B.5.3.1 Splitting of independent peaks.

As was discussed in subsection B.5.1, the estimation of a baseline current variation was vital, but far from perfect. One way in which it was often found to fail was the case of two large and clearly distinct current peaks, separated by a period of a few tens of μs of baseline current which was locally in excess of the previously estimated baseline level. This can occur in a number of ways. Firstly every cycle was different and the baseline level did vary. Secondly the procedure used to correct the current probe signal for inductance effects was also not perfect.

Algorithm 26 *Splitting of independent peaks separated by higher than usual baseline current.*

for $j = 1$ **to** N_{event} **do**
  $I_{max} \leftarrow$ maximum value of $I^{adj}_{m,p}$ for $p = index_{j,1}$ and $index_{j,2} \leq m \leq index_{j,3}$
  $I_{temp} \leftarrow I^{thresh}_{index_{j,2}}$
  if $0.1 \times I_{max} > I_{temp}$ **then**
    $cycle \leftarrow index_{j,1}$
    for $m = index_{j,2}$ **to** $index_{j,3}$ **do**
      if $I^{adj}_{m,cycle} < 0.1 \times I_{max}$ **then**
        $G_{m,cycle \leftarrow 0}$
      end if
    end for
  end if
end for

In these situations the large peaks separated by baseline current slightly above the initial threshold level will all be indexed as a single event. To eliminate such artefacts a procedure and set of conditions were developed which allow the current peaks to be separated. This procedure is detailed in Algorithm 26, and was executed at several stages during processing of the data.

The splitting procedure takes 10% of the maximum current shift, from the initiating current to the peak current, as an alternative threshold value, if that 10% value is greater than the local current threshold stored in the vector I^{thresh}. This will allow plateau regions between independent current peaks, where the plateau

region of baseline current is unusually high and not identified correctly. The initial threshold value was no more than a guess to begin with, and cannot be guaranteed to be accurate during every process cycle.

The application of the splitting procedure will of course affect indexing of many events (by reducing the extent of indexing of rising and falling edges in many cases). However in practice its use is always coupled to other routines designed to extend discharge event indexing of the rising and falling edges, so such problems are compensated for. That said, all elements of the data processing are imperfect, and small numbers of artefacts are unavoidable in a dataset of many hundreds of thousands of discharge events.

B.5.3.2 Extension of rising / falling discharge edge.

The rising and falling edges of indexing of discharge events were extended according to conditions applied to the gradient measures $\mathrm{d}I^f$ and $\mathrm{d}I^c$ calculated before. The procedure was applied several times to both rising and falling discharge edges, and is detailed in Algorithm 27.

The variable *sense* takes the value either 1 or -1 depending on whether the falling or rising edge respectively is being extended. The gradient threshold $\mathrm{d}I_{thresh} = (0.5 \times 10^{-3})/\delta t$, with $\delta t = 2$ μs, is used during the procedure as a threshold value. If the magnitude of the gradient falls below this value then the initiation / termination point of the discharge event is deemed to have been reached.

B.5.3.3 Extension of rising / falling edge until close to ending / starting current level.

Another procedure carried over from the single discharge case, with suitable modifications, was the extension of the falling edge to within a certain current of the initiation level. For the in-situ monitoring data it was also required to extend the rising edge to within a certain current of the termination current. This procedure was required as fluctuations and plateaus in discharge event signals meant it was reasonably common for only one out of the initiation or termination points to be readily located.

In such cases application of the procedure detailed in Algorithm 28 for $sense = 1$ and Algorithm 29 for $sense = -1$, usually allowed the indexing to be extended such that subsequent application of the gradient measure based procedure of subsubsection B.5.3.2 allowed correct determination of start and end locations. This procedure again can be conducted in either sense depending on whether it is desired to extend the indexing of rising or falling discharge edges.

The procedure in Algorithm 28, for the positive sense, starts from just before

Algorithm 27 *Extension of rising/falling discharge edge according to current gradient measures.*

$sense \leftarrow 1$ for falling edge **OR** -1 for rising edge
if $sense = 1$ **then**
  for $j = 1$ **to** N_{cyc} **do**
    for $m = 1$ **to** $N_{scale} - 1$ **do**
      if $G_{m,j} = 1$ **AND** $G_{m+1,j} = 0$ **then**
        if $\mathrm{d}I^{f}_{m+1,j} < -\mathrm{d}I_{thresh}$ **OR** $\mathrm{d}I^{c}_{m+1,j} < -\mathrm{d}I_{thresh}$ **then**
          $G_{m+1,j} \leftarrow 1$
        end if
      end if
    end for
  end for
else
  for $j = 1$ **to** N_{cyc} **do**
    for $m = N_{scale}$ **to** 2 **do**
      if $G_{m,j} = 1$ **AND** $G_{m-1,j} = 0$ **then**
        if $\mathrm{d}I^{f}_{m-1,j} > \mathrm{d}I_{thresh}$ **OR** $\mathrm{d}I^{c}_{m-1,j} > \mathrm{d}I_{thresh}$ **then**
          $G_{m-1,j} \leftarrow 1$
        end if
      end if
    end for
  end for
end if

Algorithm 28 *Extension of rising/falling discharge edge according to termination/initiation current level.*

let $sense \leftarrow 1$ for falling edge extension
for $j = 1$ **to** N_{event} **do**
  $I_{temp} \leftarrow index_{j,4}$
  if $I_{temp} < 0$ **then**
    $I_{temp} \leftarrow 0$
  end if
  $I_{max} \leftarrow$ maximum value of $I_{m,p}^{adj}$ for $p = index_{j,1}$ and $index_{j,2} \leq m \leq index_{j,3}$
  $I_{return} \leftarrow 0.1\times$ larger of $I_{max} - index_{j,4}$ **OR** $I_{max} - index_{j,5}$
  if $I_{return} < 3 \times 10^{-3}$ **then**
    $I_{return} \leftarrow 3 \times 10^{-3}$
  end if
  $seek \leftarrow 1$
  $m \leftarrow index_{j,3} - 2$
  $cyc \leftarrow index_{j,1}$
  while $m \leq N_{scale}$ **AND** $seek = 1$ **do**
    if $G_{m,cyc} = 0$ **then**
      if $I_{j,cyc}^{adj} - I_{temp} \geq I_{return}$ **then**
        $G_{m,cyc} \leftarrow 1$
      else
        $seek \leftarrow 0$
      end if
    end if
  end while
end for

Algorithm 29 *Extension of rising/falling discharge edge according to termination/initiation current level.*

let $sense \leftarrow -1$ for rising edge extension
for $j = 1$ **to** N_{event} **do**
  $I_{temp} \leftarrow index_{j,5}$
  if $I_{temp} < 0$ **then**
    $I_{temp} \leftarrow 0$
  end if
  $I_{max} \leftarrow$ maximum value of $I^{adj}_{m,p}$ for $p = index_{j,1}$ and $index_{j,2} \leq m \leq index_{j,3}$
  $I_{return} \leftarrow 0.1\times$ larger of $I_{max} - index_{j,4}$ **OR** $I_{max} - index_{j,5}$
  if $I_{return} < 3 \times 10^{-3}$ **then**
    $I_{return} \leftarrow 3 \times 10^{-3}$
  end if
  $seek \leftarrow 1$
  $m \leftarrow index_{j,2} + 2$
  $cyc \leftarrow index_{j,1}$
  while $m > 0$ **AND** $seek = 1$ **do**
    if $G_{m,cyc} = 0$ **then**
      if $I^{adj}_{j,cyc} - I_{temp} \geq I_{return}$ **then**
        $G_{m,cyc} \leftarrow 1$
      else
        $seek \leftarrow 0$
      end if
    end if
  end while
end for

the presently indexed termination point. When a point not indexed as within the discharge is encountered it is tested to see whether the current is within I_{return} of the initiating current value. I_{return} is set for each discharge event as either 10% of the base to peak current difference or 3 mA, whichever is greater. The net result is that samples neighbouring the previously indexed discharge falling edge are added to the event until the current level condition is met. The function is similar in the negative sense for extension of the discharge rising edge 29.

B.5.4 Finalisation of discharge event indexing.

Now that the repeated procedures have been detailed, discussion may return to the processing of the in-situ monitoring data. At the end of subsection B.5.2 the initial indexing had been performed, and the listing procedure of Algorithm 25 executed once. At this stage there were 6766 regions identified in the 20 s segment from which our example data is taken.

The next stage is to execute Algorithm 26 to split up any peaks separated by baseline current plateaus which locally exceed I^{thresh}. This increases the number of indexed regions to 6770 as some regions are split into two or more separate regions. This is followed by application of the gradient measure based extension of discharge falling edge by application of Algorithm 27 with $sense = 1$.

After extension of the discharge falling edges the number of regions indexed has fallen to 6676, this is due to events which dip just below the local current threshold being merged once the falling edges are extended. This is followed by the gradient procedure with $sense = -1$ to extend the rising edges according to the gradient measures.

The application of the gradient based extension, after the splitting procedure, should allow the current initiation and termination points to be located. After this portion of the processing, the listing procedure of Algorithm 25 must be executed to update the discharge listing variable $index$. After the listing has been refreshed the number of indexed regions has fallen to 5747 for the example segment, the result of extending the rising edges backwards has been the merging of regions initially mis-identified as separate regions.

Having executed the gradient based edge extension procedures at least once, it is likely that most events presently indexed will have either the initiation or termination point identified correctly. Many events will now already be perfectly well indexed. The indexing for events not correctly identified yet can be improved by application of Algorithm 28 with $sense = 1$ to extend the discharge falling edges. This merges more regions, resulting in 5536 regions indexed after the procedure.

After extending the falling edges, the indexed rising edges must also be forced

to be consistent with the falling edges, and so Algorithm 29 is executed again with $sense = -1$. This must be followed by application of the listing procedure, Algorithm 25, and it is found for our example 20 s segment that the number of indexed regions has been reduced to 5484 by merging of some regions.

This is followed by a repeat application of Algorithm 27 with $sense = 1$ and then again with $sense = -1$. After this procedure the reduction of regions by mergers is much smaller, falling slightly to 5469. This is an indication of the fact that by this point the majority of discharge events are properly identified.

There will still be problem regions however. In particular some more complicated discharge events which showed local troughs or plateaus near to the local value of I^{thresh} will only in the previous step have had indexing extended down to the baseline level, on one out of the rising or falling edges. For this reason the extension of both ends of indexing according to Algorithm 28 and 29 is repeated first for $sense = 1$ and then after the listing procedure (Algorithm 25) has been executed once again, for $sense = -1$. This reduces the number of regions by only 4 to 5465, again this indicates the low level of correction required to the indexing of most discharge events by this point in the process.

One problem with these processing procedures is that whilst aiming to remove one set of artefacts, one can inadvertently create others. Repeated application of the extension procedures will have helped with many types of discharge, but some peaks will have been merged which should not have been. This is corrected for with one final stage of indexing. First the splitting procedure of Algorithm 26 is applied, then the extension of indexing by gradient, Algorithm 27, is applied for both $sense = 1$ and $sense = -1$. This increases the number of indexed regions slightly, to 5471.

B.5.5 Removal of indexed events unlikely to be reliable.

Out of the 5471 indexed regions in the 20 s example segment considered here, most can reliably be termed as corresponding to discharge events. Many however will not. The limitations of the experimental set-up and data pre-processing were discussed in some detail previously. For this reason the author decided to focus investigations of the in-situ monitoring data only on events which exceeded 10 mA from base to peak. Events which were less than 6 samples in duration were also removed from consideration if they were less than 20 mA from base to peak. An example of the output of the indexing procedures is presented in Figure B.13 for the example cycle that has been considered.

These self imposed limitations reduce the number of indexed regions to be considered considerably, to just 3997 for the 20 s example segment. Such limitations

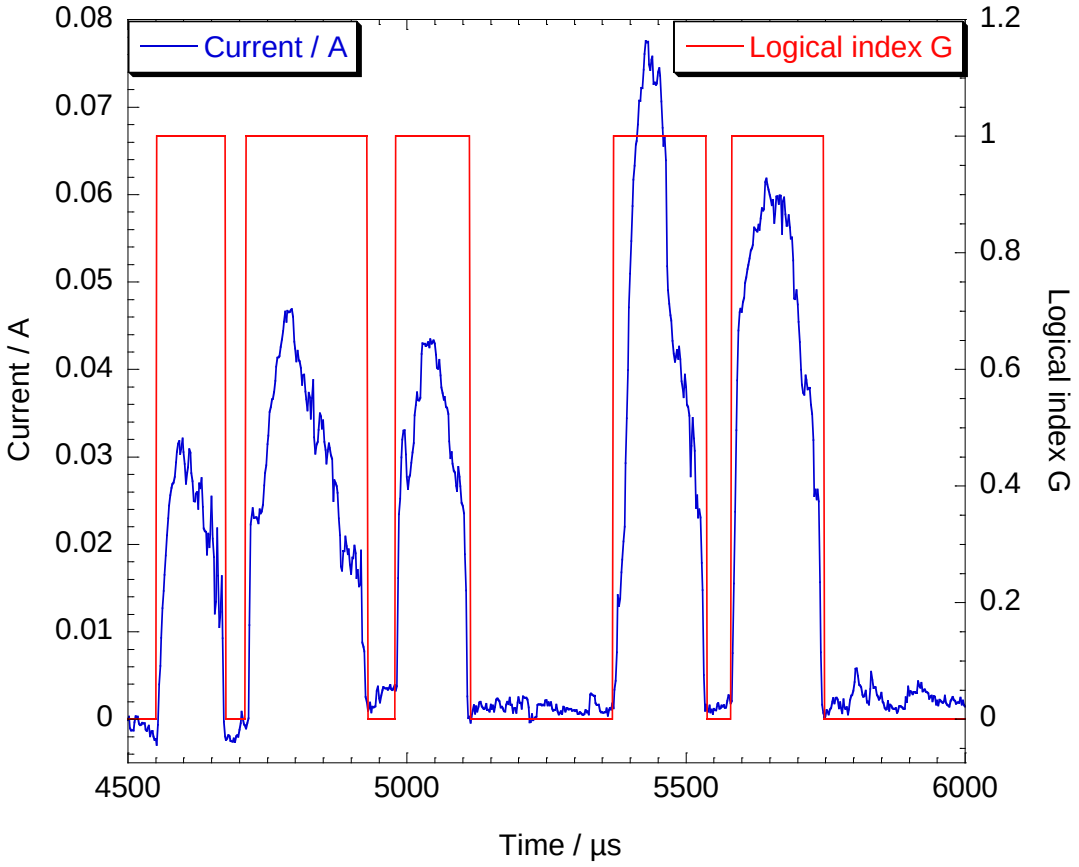

Figure B.13: *Example of the completed indexing for a zoomed-in section of the example cycle.*

must be borne in mind when considering the experimental data which will be presented later on. It is the authors feeling that it is better to draw the line high, so that one can be certain that what is measured can be relied upon as representative of the subset of events to which consideration was restricted, if nothing else.

The in-situ monitoring experiments in the present case only allow the properties, distributions and numbers of events more than about 10 mA to be reliably measured. Even this still represents a big step forward in the understanding of PEO processing, and furthermore the presently imposed limits are not in any sense fundamental limits on the technique, just the equipment and samples utilised in the present work.

B.6 Indexing of internal peaks.

As for the single discharge data, many of the discharge events identified displayed multiple current peaks without a return to the baseline current level. It cannot be determined whether such events are one single event or two concurrent events which overlap in time, so it is important to determine the number of current peaks during each discharge event. This allows consideration to be restricted to only events which were composed of a single current peak for certain discussions.

The procedure adopted was in this case exactly identical to that adopted for single discharge data, and detailed in subsection A.1.13, with only two differences. The first was that the array G, the second indexing array F and the current data I^{adj} were all arrays instead of simple vectors. The second relates to the minimum shift required for indexing a peak or trough in the current signal.

The nature of the experiment, which involved both the measurement of small current signals indirectly about 1 metre from a 10 kW power unit, and extensive pre-processing, meant that in-situ monitoring data was subject to larger levels of noise and fluctuations than the single discharge data. For this reason the shift required to identify peaks or troughs in Algorithm 10, I_{scale}, was for the in-situ monitoring data set to a larger fraction of the discharge peak current. I_{scale} was set equal to the larger out of 50% of the base to peak current variation or 5 mA for each indexed event.

B.7 Measurement of discharge event properties.

Measurements of discharge properties may now be made, however first it will be required to extend the listing variable *index* to encompass a greater range of simple measurements. The additional properties added are listed, along with the original

Column	Measurement	Symbol	Unit
1	Cycle number	k_{cyc}	integer
2	Initiation coordinate within cycle	k_{start}	integer
3	Termination coordinate within cycle	k_{end}	integer
4	Initiation current level	I_{start}	A
5	Termination current level	I_{end}	A
6	Average baseline current	I_{base}	A
7	Peak current minus averaged baseline	I_{peak}	A
8	Number of internal peaks	N_{int}	integer
9	Coordinate of first peak	k_{peak}	integer
10	Did current exceed range?	max	logical

Table B.2: *Measurements stored in the columns of the listing array index when extended prior to discharge property measurements.*

measures, in Table B.2.

The number of internal peaks, N_{int}, was calculated by counting the number of internal peaks indexed in the vector F for each discharge event between k_{start} and k_{end}. The coordinate of the first peak, k_{peak}, is self explanatory.

The final measurement, max, refers to a problem which did occasionally arise with the current probe date correction routine. The oscilloscope range was from -100 to +100 mA, if the raw current probe data signal, I^{resp}, exceeded this range during a process cycle, then that cycle is unusable. This is because the signal during that period will be truncated, and the signal correction procedure will not function correctly.

The variable max was set equal to 1 if the maximum value of I^{resp} was less than the range, and 0 otherwise. The events during cycles for which $max = 0$ were not removed from the listing variable $index$, even though they were not usable for current measurements. This was because events which occurred during such cycles may still be used for measurements of initiating voltage and discharge event duration, though they must be excluded from consideration for many of the discharge event properties. The flag variable, max, can be used to screen these events out in the relevant contexts. In the main text, unless explicitly stated it should be assumed that data is from single peak events with $max = 1$.

Column	Measurement	Symbol	Unit
1	Cycle number	k_{cyc}	integer
2	Initiation coordinate within cycle	k_{start}	integer
3	Termination coordinate within cycle	k_{end}	integer
4	Peak coordinate	k_{peak}	integer
5	Initiation current level	I_{start}	A
6	Termination current level	I_{end}	A
7	Average baseline current	I_{base}	A
8	Current at peak location	I_{peak}	A
9	Maximum current reached	I_{max}	A
10	Duration of event	d_{sing}	s
11	Initiating voltage	V_{init}	V
12	Voltage at peak location	V_{peak}	V
13	Average voltage over event	V_{avg}	V
14	Power at peak location	P_{peak}	W
15	Energy transferred	E_{sing}	J
16	Charge transferred	Q_{sing}	C
17	Did current exceed range?	max	logical

Table B.3: *Properties measured for the single peak discharge events.*

B.7.1 Measurement of single peak discharge event properties.

The measurements for single peak events were stored in an array termed $result\_sing$, of dimension 17 columns and N_{sing} rows. Where N_{sing} is the total number of single peak events listed in the expanded *index* array, identified by requiring the measure N_{int} in the expanded list array to be equal to 1. The number of single peak events in the example 20 s segment was 3617, out of 3997 indexed discharge events in total. A description of the properties measured and stored in each column if the $result\_sing$ array is presented in Table B.3.

The cycle number, k_{cyc}, and the initiation and termination coordinates, k_{start} and k_{end}, are stored so that the event location in the data can be found if required. The peak coordinate, k_{peak}, is the location at which the array $F_{m,j}$ holds the value 1 for $j = k_{cyc}$ and $k_{start} \leq m \leq k_{end}$.

Initiation current, I_{start}, is the current value at indexed start of the discharge event. The termination current, I_{end}, is the same for the indexed end of the event. The average baseline current, calculated as $I_{base} = 0.5\,(I_{start} + I_{end})$, is used as a baseline level for calculation of other current measures. The peak current, I_{peak}, is

the current at k_{peak}, minus I_{base}. The maximum current reached , I_{max},should be identical to the peak current, but is calculated differently as a check. I_{max} is found as the maximum value of $I^{adj}_{m,j}$ for $j = k_{cyc}$ and $k_{start} \leq m \leq k_{end}$, minus I_{base}.

The duration of the event, d_{sing}, is taken as the difference between k_{start} and k_{end}, multiplied by the sampling interval, $\delta t = 2$ μs. The initiating voltage, V_{init}, is the voltage at the start of the discharge event. The voltage at peak, V_{peak}, is simply the voltage at k_{peak} during the process cycle k_{cyc}. The average voltage across the event, V_{avg}, is the average of $V_{m,j}$ for $j = k_{cyc}$ and $k_{start} \leq m \leq k_{end}$.

Power at peak location was found as $P_{peak} = I_{peak} \times V_{peak}$. The energy transferred, E_{sing}, was found as the trapezium rule integral of the quantity $\delta t \times \left(I^{adj}_{m,j} - I_{base}\right) \times V_{m,j}$ for $j = k_{cyc}$ and $k_{start} \leq m \leq k_{end}$. The charge transferred, Q_{sing}, was calculated in the same fashion for the quantity $\delta t \times \left(I^{adj}_{m,j} - I_{base}\right)$. The flag of whether the current data is usable, max, is the same as it was stored in the expanded *index* listing variable.

B.7.2 Measurement of all discharge event properties.

Whilst the primary focus of the analysis will be on the single peak discharge events, due to the likelihood that multiple peak events represent concurrent discharges on the monitored area, the properties of all the indexed events are useful for some purposes, and were in any event calculated for completeness of the dataset.

These measurements were made for every indexed discharge event, not just the multiple peak events (ie all the single peak events are included in this array also). The measurements were stored in an array termed $result\_all$, with dimension 15 columns and N_{event} rows. The properties which were measured were as outlined in Table B.4.

Many of these properties are exactly as for the single peak events. N_{peak} is the number of internal peaks indexed for the discharge event, which was predominantly 1, but went up to 7 for one event in the example 20 s segment. The maximum current and power, I_{max} and P_{max}, are used in this case, as for multiple peak events only the first peak location is indexed, and that might not be the largest peak in that event.

B.8 Estimation of the event current development profiles.

The procedure used to calculate the average current development profiles for single peak events were identical to those applied to the single discharge data, and detailed

Column	Measurement	Symbol	Unit
1	Cycle number	k_{cyc}	integer
2	Initiation coordinate within cycle	k_{start}	integer
3	Termination coordinate within cycle	k_{end}	integer
4	Number of internal peaks	N_{peak}	integer
5	Initiation current level	I_{start}	A
6	Termination current level	I_{end}	A
7	Average baseline current	I_{base}	A
8	Maximum current reached	I_{max}	A
9	Duration of event	d_{event}	s
10	Initiating voltage	V_{init}	V
11	Average voltage over event	V_{avg}	V
12	Maximum power reached	P_{max}	W
13	Energy transferred	E_{event}	J
14	Charge transferred	Q_{event}	C
15	Did current exceed range?	max	logical

Table B.4: *Properties measured for all indexed discharge events.*

in section A.2. The average shapes by d_{sing} and V_{init} were used to aid discussions of correlations between d_{sing} and other properties such as I_{peak}. See chapter 6 for further details.

Note on the Bibliography

As was discussed in chapter 2, several references were made to interesting values which were quoted by other authors with reference to publications not available to this author. The references to which this applies are [**19, 21, 23, 24, 25, 26, 27**].

Bibliography

[1] C. S. Dunleavy, I. O. Golosnoy, J. A. Curran, and T. W. Clyne. Characterisation of discharge events during plasma electrolytic oxidation. *Surface and Coatings Technology*, 203:3410–3419, 2009.

[2] A. L. Yerokhin, L. O. Snizhko, N. L. Gurevina, A. Leyland, A. Pilkington, and A. Matthews. Discharge characterization in plasma electrolytic oxidation of aluminium. *Journal of Physics D: Applied Physics*, 36:2110–2120, 2003.

[3] G. Sundararajan and L. Rama Krishna. Mechanisms underlying the formation of thick alumina coatings through the MAO coating technology. *Surface and Coatings Technology*, 167:269–277, 2003.

[4] J. A. Curran and T. W. Clyne. Thermo–physical properties of plasma electrolytic oxide coatings on aluminium. *Surface and Coatings Technology*, 199:168–176, 2005.

[5] R. Arrabal, E. Matykina, T. Hashimoto, P. Skeldon, and G. E. Thompson. Characterization of AC PEO coatings on magnesium alloys. *Surface and Coatings Technology*, 203:2207–2220, 2009.

[6] J. A. Curran and T. W. Clyne. Porosity in plasma electrolytic oxide coatings. *Acta Materialia*, 54:1985–1993, 2006.

[7] A. L. Yerokhin, L. O. Snizhko, N. L. Gurevina, A. Leyland, A. Pilkington, and A. Matthews. Spatial characteristics of discharge phenomena in plasma electrolytic oxidation of aluminium alloy. *Surface and Coatings Technology*, 177–178:779–783, 2004.

[8] E. Matykina, A. Berkani, P. Skeldon, and G. E. Thompson. Real–time imaging of coating growth during plasma electrolytic oxidation of titanium. *Electrochimica Acta*, 53:1987–1994, 2007.

[9] S. Moon and Y. Jeong. Generation mechanism of microdischarges during plasma electrolytic oxidation of Al in aqueous solutions. *Corrosion Science*, 51:1506–41512, 2009.

[10] B. Kasalica, M. Petkovic, S. Belca, S. Stojadinovic, and Lj Zekovic. Electronic transitions during plasma electrolytic oxidation of aluminium. *Surface and Coatings Technology*, 203:3000–3004, 2009.

[11] V. Kadary and N. Klein. Electrical breakdown I. During the anodic growth of tantalum pentoxide. *Journal of the Electrochemical Society: Solid–State Science and Technology*, 127:139–151, 1980.

[12] N. Klein, V. Moskovici, and V. Kadary. Electrical breakdown II. During the anodic growth of aluminium oxide. *Journal of the Electrochemical Society: Solid–State Science and Technology*, 127:152–155, 1980.

[13] T. B. Van, S. D. Brown, and G. P. Wirtz. Mechanism of anodic spark deposition. *Ceramic Bulletin*, 56:563–566, 1977.

[14] M. D. Klapkiv, H. M. Nykyforchyn, and V. M. Posuvailo. Spectral analysis of an electrolytic plasma in the process of synthesis of aluminium oxide. *Materials Science*, 30:333–343, 1994.

[15] R. O. Hussein, X. Nie, D. O. Northwood, A. Yerokhin, and A. Matthews. Spectroscopic study of electrolytic plasma and discharging behaviour during the plasma electrolytic oxidation (PEO) process. *Journal of Physics D: Applied Physics*, 43:1–13, 2010.

[16] F. Jaspard-Mecuson, T. Czerwiec, G. Henrion, T. Belmonte, L. Dujardin, A. Viola, and J. Beauvir. Tailored aluminium oxide layers by bipolar current adjustment in the plasma electrolytic oxidation (PEO) process. *Surface and Coatings Technology*, 201:8677–8682, 2007.

[17] F. Mecuson, T. Czerwiec, T. Belmonte, L. Dujardin, A. Viola, and G. Henrion. Diagnostics of an electrolytic microarc process for aluminium alloy oxidation. *Surface and Coatings Technology*, 200:804–808, 2005.

[18] O. P. Terleeva, V. I. Belevantsev, and A. I. Slonova. Types of discharges in electrochemical microplasma processes. *Protection of Metals*, 39:50–54, 2003.

[19] V. V. Bakovets, O. V. Polyakov, and I. P. Dolgovesova. *Plazmenno-elektroliticheskaya obrabotka metallov (Electrolytic-plasma treatment of metals)*, page 20. Novosibirsk: Nauka. Sib. Otd., 1991.

[20] B. H. Long, H. H. Wu, B. Y. Long, J. B. Wang, N. D Wang, X. Y. Lu, Z. S. Jin, and Y. Z. Bai. Characteristics of electric parameters in aluminium alloy MAO coating process. *Journal of Physics D: Applied Physics*, 38:3491–3496, 2005.

[21] L. A. Snezhko and V. I. Chernenko. N.a. *Elektron. obrabotka materialov*, 2:25, 1983.

[22] S. V. Gnedenkov, O. A. Khrisanfova, A. G. Zavidnaya, S. L. Sinebrukhov, A. N. Kovryanov, T. M. Scorobogatova, and P. S. Gordienko. Production of hard and heat–resistant coatings on aluminium using a plasma micro–discharge. *Surface and Coatings Technology*, 123:24–28, 2000.

[23] P. S. Gordienko and S. V. Gnedenkov. *Microarc oxidation of titanium and its alloys*. Vladivostok, 1997.

[24] O. A. Golovanova and A. M. Sizikov. N.a. *Izvestiya Vuzov. Khimiya i Khimicheskaya Tekhnologiya*, 39:85, 1996.

[25] L. T. Bugaenko, E. G. Volf, and E. P. Kalyazin. *Mikrorazryad v kondensirovannoi faze na ventil nykh anodakh (Microdischarge in condensed phase on rectifying anodes)*, page 8. Moscow, 1990.

[26] L. A. Snezhko. N.a. In *Abstracts of papers, respublikanskii nauchno-tekhnicheskii seminar "Anod-88" (Republic scientific-technical seminar "Anode-88")*, page 77, Kazan, 1988.

[27] G. A. Markov and M. K. Mironova. *Mikrodugovoe oksidirovanie alyuminiya i ego splanov v kontsentrirovannoi sernoi kislote. (Microarc oxidation of aluminium and its alloys in concentrated sulfuric acid)*, chapter 2. VINITI, Novosibirsk, 1988.

[28] F. Monfort, A. Berkani, E. Matykina, P. Skeldon, G. E. Thompson, H. Habazaki, and K. Shimizu. Development of anodic coatings on aluminium under sparking conditions in silicate electrolyte. *Corrosion Science*, 49:672–693, 2007.

[29] H. Kalkanci and S. C. Kurnaz. The effect of process parameters on mullite–based plasma electrolytic oxide coatings. *Surface and Coatings Technology*, 203:15–22, 2008.

[30] F. Y. Jin, K. Wang, M. Zhu, L. R. Shen, J. Li, H. H. Hong, and P. K. Chu. Infrared reflection by alumina films produced on aluminium alloy by plasma electrolytic oxidation. *Materials Chemistry and Physics*, 114:398–401, 2009.

[31] R. Arrabal, E. Matykina, F. Viejo, P. Skeldon, G. E. Thompson, and M. C. Merino. AC plasma electrolytic oxidation of magnesium with zirconia nanoparticles. *Applied Surface Science*, 254:6937–6942, 2008.

[32] R. Arrabal, E. Matykina, P. Skeldon, G. E. Thompson, and A. Pardo. Transport of species during plasma electrolytic oxidation of WE43-T6 magnesium alloy. *Journal of The Electrochemical Society*, 155:C101–C111, 2008.

[33] A. L. Yerokhin, A. Shatrov, P. Samsonov, P. Shashkov, A. Pilkington, A. Leyland, and A. Matthews. Oxide ceramic coatings on aluminium alloys produced by a pulsed bipolar plasma electrolytic oxidation process. *Surface and Coatings Technology*, 199:150–157, 2005.

[34] D. J. Shen, Y. L. Wang, P. Nash, and G. Z. Xing. Microstructure, temperature estimation and thermal shock resistance of PEO ceramic coatings on aluminium. *Journal of Materials Processing Technology*, 205:477–481, 2008.

[35] Y. Guan, Y. Xia, and G. Li. Growth mechanism and corrosion behaviour of ceramic coatings on aluminium produced by autocontrol AC pulse PEO. *Surface and Coatings Technology*, 202:4602–4612, 2008.

[36] W. C. Gu, G. H. Lv, H. Chen, G. L. Chen, W. R. Feng, and S. Z. Yang. Characterisation of ceramic coatings produced by plasma electrolytic oxidation of aluminium alloy. *Materials Science and Engineering A*, 447:158–162, 2007.

[37] W. Xue, Z. Deng, Y. Lai, and R. Chen. Analysis of phase distribution for ceramic coatings formed by microarc oxidation on aluminium Alloy. *Journal of the American Ceramic Society*, 81:1365–1368, 1998.

[38] T. H. Teh, A. Berkani, S. Mato, P. Skeldon, G. E. Thompson, H. Habazaki, and K. Shimizu. Initial stages of plasma electrolytic oxidation of titanium. *Corrosion Science*, 45:2757–2768, 2003.

[39] E. Matykina, R. Arrabal, P. Skeldon, and G. E. Thompson. Transmission electron microscopy of coatings formed by plasma electrolytic oxidation of titanium. *Acta Biomaterialia*, 5:1356–1366, 2009.

[40] W. Dietzel, M. Klapkiv, H. Nykyforchyn, and V. Psuvailo. Porosity and corrosion properties of electrolyte plasma coatings on magnesium alloys. *Materials Science*, 40:585–590, 2004.

[41] G. Lv, W. Gu, H. Chen, W. Feng, M. Latif Khosa, L. Li, E. Niu, G. Zhang, and S. Z. Yang. Characteristic of ceramic coatings on aluminium by plasma

electrolytic oxidation in silicate and phosphate electrolyte. *Applied Surface Science*, 253:2947–2952, 2006.

[42] Y. J. Guan and Y. Xia. Correlation between discharging property and coatings microstructure during plasma electrolytic oxidation. *Transactions of Nonferrous Metals Society of China*, 16:1097–1102, 2006.

[43] F. Monfort, A. Berkani, E. Matykina, P. Skeldon, G. E. Thompson, H. Habazaki, and K. Shimizu. A tracer study of oxide growth during spark anodizing of aluminium. *Journal of The Electrochemical Society*, 152:C382–C387, 2005.

[44] R. H. U. Khan, A. L. Yerokhin, and A. Matthews. Structural characteristics and residual stresses in oxide films produced on Ti by pulsed unipolar plasma electrolytic oxidation. *Philosophical Magazine*, 88:795–807, 2008.

[45] I. Levin and D. Brandon. Metastable alumina polymorphs: Crystal structures and transition sequences. *Journal of the American Ceramic Society*, 81:1995–2012, 1998.

[46] V. Jayaram and C. G. Levi. The structure of delta-alumina evolved from the melt and the gamma to delta transformation. *Acta Metallurgica*, 37:569–578, 1989.

[47] C. S. John, N. C. M. Alma, and G. R. Hays. Characterization of transitional alumina by solid state magic angle spinning aluminium nmr. *Applied Catalysis*, 6:341–346, 1983.

[48] K. J. Morrissey, K. K. Czanderna, R. P. Merril, and C. B. Carter. Transition alumina structures studied using HREM. *Ultramicroscopy*, 18:379–386, 1985.

[49] E. Matykina, G. Douchet, F. Monfort, A. Berkani, P. Skeldon, and G. E. Thompson. Destruction of coating material during spark anodizing of titanium. *Electrochimica Acta*, 51:4709–4715, 2006.

[50] D. Roehling. The electrical resistivity of a partially ionized cesium plasma. *Advanced Energy Conversion*, 3:69–76, 1963.

[51] D. K. Kim and I. Kim. Calculation of ionization balance and electrical conductivity in nonideal aluminium plasma. *Physical Review E*, 68, 2003.

[52] D. K. Kim and I. Kim. Electrical conductivities of nonideal iron and nickel plasmas. *Contributions to Plasma Physics*, 47:173–176, 2007.